# Machine learning methods for automatic crop classification and prediction of yields on a large scale

Walid Hammache

## To cite this version:

Walid Hammache. Machine learning methods for automatic crop classification and prediction of yields on a large scale. Artificial Intelligence [cs.AI]. Université Paris-Saclay, 2022. English. NNT : 2022UPAST127 . tel-03988943

HAL Id: tel-03988943
https://theses.hal.science/tel-03988943

Submitted on 14 Feb 2023

# Méthodes d'apprentissage statistique pour la classification automatique des cultures et la prévision de rendement à grande échelle

*Machine learning methods for automatic crop classification and prediction of yields on a large scale*

**Thèse de doctorat de l'université Paris-Saclay**

École doctorale n° 573, interfaces : matériaux, systèmes, usages (INTERFACES)
Spécialité de doctorat : Mathématiques appliquées
Graduate School : Sciences de l'ingénierie et des systèmes
Référent : CentraleSupélec

Thèse préparée dans l'unité de recherche **MICS (Université Paris-Saclay, CentraleSupélec)**, sous la direction de **Paul-Henry Cournède**, Professeur, CentraleSupélec, Université Paris-Saclay, et la co-supervision de **Théophile Lohier**, Docteur, Entreprise Cybeletech

**Thèse soutenue à Gif-Sur-Yvette (CentraleSupélec), le 9 Décembre 2022, par**

## Walid HAMMACHE

### Composition du jury

Membres du jury avec voix délibérative

| | |
|---|---|
| **Céline Hudelot**<br>Professeur, CentraleSupélec, Université Paris-Saclay | Présidente |
| **Adel Hafiane**<br>Maître de conférences HDR, INSA Centre Val de Loire | Rapporteur & Examinateur |
| **Xiaopeng Zhang**<br>Professeur, Institute of Automation, Chinese Academy of Sciences | Rapporteur & Examinateur |

THESE DE DOCTORAT

NNT : 2022UPAST127

# Résumé

La principale thématique étudiée dans ce travail concerne l'identification des types de cultures à l'aide d'imagerie satellite radar en utilisant des modèles d'apprentissage statistique. L'identification des types de cultures permet le suivi automatique de la couverture du sol et l'estimation des surfaces plantées, mais peut aussi être indirectement utile dans plusieurs applicatifs, par exemple en termes d'amélioration de la prévision des rendements agricoles résultant d'une meilleure connaissance des surfaces plantées, c'est l'autre sujet qui sera traité dans le présent travail.

Développer un outil de reconnaissance automatique et à grande échelle des cultures peut créer une valeur ajoutée considérable dans le monde agricole actuel, de plus en plus demandeur de technologies innovantes. Les besoins de travailler sur un outil d'identification des cultures sont multiples. Une application concrète consiste à pouvoir estimer les surfaces globales cultivées pour une culture donnée à l'échelle d'un bassin de production ou d'exploitations agricoles. Cela intéresse les différents acteurs: l'agriculteur, pour simplifier ses tâches administratives de déclaration, les transformateurs, pour une meilleure logistique et planification des collectes, des assureurs, pour une meilleure évaluation de l'exposition au risque, ou pour un état, pour anticiper les situations de pénurie.

Pour ces travaux, nous avons pu compter sur un allié majeur, l'imagerie satellitaire qui fournit des images multi-temporelles à haute résolution offrant une réelle opportunité de suivre l'évolution des propriétés réflectives des plantes au cours de leur croissance, en fonction des variations liées à la phénologie et au pédoclimat. Dans notre travail, nous utilisons des données issues de l'imagerie de télédétection radar assurant une indépendance vis-à-vis des conditions climatiques, plus précisément, les images du satellite Sentinel-1 caractérisées par une résolution spatiale acceptable et une résolution temporelle relativement réduite de l'ordre de quelques jours.

Notre approche pour la reconnaissance des cultures est basée sur l'utilisation de la dynamique de croissance des plantes pouvant être capturée par l'imagerie satellite pour discriminer les cultures. Il s'agit d'une approche basée sur les pixels pour laquelle nous avons choisi d'utiliser deux modèles supervisés d'apprentissage statistique, les réseaux de neurones récurrents LSTM (Long Short-Term Memory) et les réseaux de convolution CNN (Convolutional Neural Network). Notre approche est conçue de telle sorte que le modèle puisse produire une évaluation du couvert végétal sans avoir à labelliser des parcelles en début de campagne, opération très complexe à réaliser. Nous avons donc cherché à calibrer les modèles en utilisant les données des campagnes précédentes.

Nous proposons une méthode dans laquelle le développement phénologique de la plante est considéré pour l'identifier en utilisant le concept du temps thermique. Cela permet de compenser la variabilité inter-annuelle, qu'elle soit pédo-climatique, liée aux caractéristiques de la culture comme la résistance aux épisodes de gel, ou due aux pratiques culturales. Cette idée a été motivée par le fait qu'a priori, indépendamment des facteurs précédemment cités, un stade phénologique d'une culture donnée est atteint à un niveau donné d'accumulation de température, donc de temps thermique, assurant la robustesse de la variation inter-annuelle de la dynamique de développement des cultures.

L'identification des cultures peut servir plusieurs applications, comme l'amélioration des prévisions de rendement résultant d'une meilleure connaissance des surfaces plantées. C'est une autre thématique de recherche de notre thèse. La reconnaissance des cultures peut constituer un élément essentiel dans le processus visant à obtenir des prévisions de rendements agricoles les plus précis possible. En identifiant le type de culture dans le champ, nous connaissons les caractéristiques phénotypiques de cette culture pour pouvoir estimer les paramètres biophysiques, ce qui, couplé aux données pédoclimatiques et aux pratiques culturales, nous permet d'aller vers une prévision précise des rendements agricoles en utilisant les modèles de croissance des plantes, les méthodes de calibration et d'assimilation de données.

Cette méthodologie pour la prévision des rendements à l'échelle de la parcelle ou de la région est également étudiée dans cette thèse. En effet, la connaissance anticipée des rendements agricoles est un enjeu majeur en agriculture: dans un bassin de production, pour le chef de silo afin de prévoir la logistique de culture et de stockage des grains ou à plus grande échelle, pour anticiper les crises agricoles. Dans ce contexte, nous avons commencé par évaluer le potentiel de l'imagerie radar pour le développement de modèles statistiques permettant l'estimation des variables biophysiques des plantes telles que la biomasse. Nous avons également proposé un outil permettant de conseiller le positionnement des points de mesure dans les parcelles agricole en fonction des hétérogénéités intra-parcellaires et en utilisant un clustering non supervisé de type K-means de la dynamique de la réponse radar de chaque pixel.

Ensuite, nous présentons une mise en œuvre des méthodes d'assimilation de données pour montrer comment elles peuvent être utilisées pour améliorer les pouvoirs prédictifs des modèles de croissance des plantes. Nous utilisons un algorithme d'assimilation de données basé sur le filtre particulaire par convolution appliqué à un modèle mécaniste de croissance du blé dérivé du modèle STICS.

**Mots-clés:** Reconnaissance des cultures, Propriétés réflectives des plantes, Télédétection radar, Sentinel-1, Temps Thermique, Réseaux de neurones récurrent LSTM, Réseaux de convolution CNN, Biomasse, Prévision des réndements, Assimilation de données.

# Abstract

The main thematic studied in this work concerns the identification of crop types using radar satellite imagery by using statistical learning models. Crop type identification allows the automatic monitoring of land cover and the estimation of planted areas, but can also be indirectly useful in several applications, for example in terms of improving the prediction of agricultural yields resulting from a better knowledge of planted areas, this is the other topic that will be addressed in this work.

Developing an automatic and large-scale crop recognition tool can create considerable added value in today's agricultural world, more and more in demand of innovative technologies. The needs to work on a crop identification tool are multiple. A concrete application consists in being able to estimate the global cultivated areas for a given crop at the scale of a production basin or agricultural exploitation. This interests the different actors: the farmer, to simplify his administrative tasks of declaration, the transformers, for a better logistics and planning of collections, the insurers, for a better evaluation of the exposure to the risk, or for a state, to anticipate the situations of penury.

For these works, we could count on a major ally, the satellite imagery which provides multi-temporal images with high resolution offering a real opportunity to track the evolution of the reflective properties of plants during their growth, according to the variations related to the phenology and the pedoclimate. In our works, we use data from radar remote sensing imagery ensuring independence from climatic conditions, more precisely, images from the Sentinel-1 satellite characterized by an acceptable spatial resolution and a relatively reduced temporal resolution of a few days.

Our approach for crop recognition is based on the use of plant growth dynamics that can be captured by satellite imagery to discriminate crops. It is a pixel-based approach for which we have chosen to use two supervised statistical learning models, Long Short-Term Memory (LSTM) recurrent neural networks and Convolutional Neural Network (CNN).

Our approach is designed so that the model can produce a vegetation coverage assessment without having to label parcels at the beginning of the season, which is a very complex operation to perform. We, therefore, sought to calibrate the models using data from previous seasons. We propose a method in which the phenological development of the plant is considered to identify its species using the concept of thermal time. This allows compensating the inter-annual variability, whether it is pedo-climatic, related to the characteristics of the crop such as the resistance to frost episodes, or due to the cultivation practices. This idea was motivated by the fact that a priori, independently of the above-mentioned factors, a phenological stage of a given crop is reached at a given level of temperature accumulation, thus of thermal time, ensuring the robustness of the inter-annual variation of the crop development dynamics.

Crop type identification can be useful for several applications, such as improving yield forecasting through a better knowledge of the planted areas. This is another research theme of our thesis. Crop recognition can be an essential element in the process of obtaining the most accurate crop yield forecasts possible. By identifying the type of crop in the field, we know the phenotypic characteristics of that crop to be able to estimate the biophysical parameters, which, coupled with soil-climate data and cultivation practices, allows us to move towards accurate crop yield forecasting using plant growth models, calibration and data assimilation methods. This methodology for yield forecasting at the scale of the parcel or the region is also studied in this thesis. The anticipated knowledge of agricultural yields is a major challenge in agriculture: in a production basin, for the silo manager to predict the logistics of cultivation and storage of grains or on a larger scale, to anticipate agricultural crises. In this context, we started by evaluating the potential of radar imagery for the development of statistical models allowing the estimation of plant biophysical variables such as biomass. We also proposed a tool allowing to recommend the positioning of measurement points in agricultural parcels according to intra-parcel heterogeneities and using an unsupervised K-means clustering of the radar response dynamics of each pixel.

Next, we present an implementation of data assimilation methods to show how they can be used to improve the predictive powers of plant growth models. We use a data assimilation algorithm based on the particle convolution filter applied to a mechanistic wheat growth model derived from the STICS model.

**Keywords:** Crop Recognition, Plant's Reflective Properties, Rradar Remote Sensing, Sentinel-1 SAR data, Thermal Time, Long Short-Term Memory recurrent neural networks, Convolutional Neural Networks, biomass, crops yield forecasting, Data Assimilation.

# Contents

# Introduction

CRop type identification is a key issue in automatic land cover monitoring and to improve yield prediction in agriculture, thanks to a better knowledge of the planted areas.

The objective of our work is to contribute, through **mathematical modeling, statistical analysis, computer science frameworks, and remote sensing**, to answer some of today's agricultural challenges. Two main topics, jointly linked, are addressed in this manuscript: **crop type identification** at the scale of the production basin and agricultural farms, and large-scale agricultural **yield forecasting**. It should be noted that our work concerns mainly the field of crops with an annual cycle such as wheat, barley, maize, beet, and rapeseed. As an indication, government data on cultivation practices in France indicates that the crops mentioned above, in addition to sunflower and protein peas, occupy an average of 66% of the cropland.

The needs to work on a crop identification tool are multiple. One concrete application consists in being able to estimate the overall cultivated areas for a given crop at the scale of a production basin or agricultural farms, thus allowing to replace conventional farmers declarations and enrich the agricultural surface databases. For instance, farmers may inform their cooperatives or the agricultural actors who transform their crops about the surfaces of production. This declarative process is not always precise and it causes a heavy administrative charge that could be reduced.

Reciprocally, all the actors of the agricultural transformation chains are interested in being able to evaluate more accurately and automatically, the surface areas cultivated in each parcel or farm, and this, as early as possible before harvest. It may help silo managers to have a better visibility of the crop rotation in their production basin, and consequently on the logistics to implement. In fact, in a storage organism or an agricultural cooperative, evaluating the crop productions that will be received a few weeks or even months before harvest allows the silo manager to prepare the collection plan and the logistics dedicated to grain storage. For example, it is important to optimize the filling of the cells as a half-empty silo represents an economic loss that can be significant. This task relies on strong constraints, since silos are assigned to the storage of specific crops, with a given variety and quality: not all qualities and/or cultivars can be combined in one silo. Similarly, the need to estimate in advance the crop type that will be available may be relevant for mills managers, in particular for cereals, there is a need to adjust the mill according to the expected crop type and to adjust their offers to the region's crop rotation. Another example concerns agricultural insurers, to check the cultivated areas and adapt their offers as well as exposition to risk according to the crop rotation characteristics of a given production basin.

In another perspective, a pixel-based crop type recognition approach in a production basin combined with relevant indicators allows detecting crop surfaces that have not correctly emerged. For example, for rapeseed that did not emerge properly because of a severe drought, the farmer can replant with another crop like wheat instead.

Moreover, crop recognition may also be indirectly useful for certain applications. For instance, for harvest monitoring of a given crop, such as beet for which harvesting can last a considerable time, crop recognition may constitute the first brick to delimit the beet parcels in a given area, before using other techniques, such as the satellite imagery signal analysis, to assess the beet harvesting progress.

We illustrated the interest of crop type recognition for the evaluation of planted areas in a given year and derived applications, but it can also help for a better management of the crop rotation of agricultural parcels. Knowing the history of crop rotation allows the control of crops combinations and the qualification of the risks related to diseases (mycotoxins, fusarium, etc.) and bio-aggressors (weeds, slugs, etc.) [Legrand et al., 2017] [Maiorano et al., 2008] [Peters et al., 2003]. For instance, a parcel in which corn was sown during the previous season and had another major crop, like wheat, for the following season presents a risk related to contamination with mycotoxins [Maiorano et al., 2008] [Fischer et al., 2002]. They are toxic fungal metabolites occurring pre and post-harvest and result in reduced nutritional value and possible risks for human and animal health, a risk that must be identified. An interesting document on the agricultural advice magazine ”perspectives agricoles” [1] gives some information on the impact of previous crop corn on fusarium. Also, the article from ”lafranceagricole” [2] presents table showing that the risk of developing mycotoxins is more or less critical according to the previous crop. Readers can find further information on the effect of prior crops on diseases in [Desgranges et al., 2007].

In addition, the control of crop rotation must allow for a reduction in the use of phytopharmaceutical products, either to reduce the impact of these products or to conform to particular specifications. This is achieved in two manners: directly, by introducing crops that consume fewer phytopharmaceutical products than those already present in the rotation, such as the introduction of corn in rapeseed/wheat/barley rotations, or the introduction of alfalfa in corn/wheat rotations; or indirectly, by introducing crops with different development cycles from those already present, thus disrupting the development of bio-aggressors.

The challenge is therefore to know the crop combination of the previous and current seasons, and even older ones, and to draw up a sort of parcel typologies in order to establish a filter by crop rotation history to anticipate and make the cropping system less vulnerable to such risks.

---

[1] https://www.perspectives-agricoles.com/file/galleryelement/pj/8c/65/a6/cf/315_2530984742270309649.pdf.

[2] https://www.lafranceagricole.fr/article/mycotoxines-des-risques-ane-pas-sous-estimer-1,0,442503861.html.

In the same idea, crop type recognition can also help guide the decision of which crops to plant. For example, introducing an oilseed (such as rapeseed), beets, or sunflowers, which are so-called ”break crops” (tête d’assolement in french), in a cereal rotation (wheat, barley, ...) can improve the yields/quality of cereals.

More generally, cultivated land monitoring and crop rotation management are key factors from the point of view of sustainability: the intensification of agricultural productions and disrespect of the principle of crop rotation in some areas can be threatening for agricultural ecosystems [Geiger et al., 2010] [Duflot et al., 2022], and a better monitoring could help in controlling some agricultural practices. Hence the importance of working on tools that provide advice on which rotations to establish and/or help detect the combinations of rotations conducted. Obviously, crop rotation is also guided by the soil and climate conditions in the region of interest, the existence of structured agricultural sectors, or individual farmers’ choices.

Crop recognition is an essential component in yield forecasting. Actually, by identifying the type of crop in a field, we can refer to the corresponding knowledge on the phenotype characteristics of this crop to be able to estimate the biophysical parameters, which, coupled with the pedoclimatic data and the cultural practices in place (sowing, fertilization, irrigation, etc.), are key elements for the accurate forecasting of yields using plant growth models - more particularly the so called mechanistic models - calibration and data assimilation methods which will be evoked in our work.

In fact, the anticipated knowledge of crop yields is a major challenge in agriculture: in a production basin, for the silo manager to forecast the logistics of farming and grain storage and for the insurers about the adaptation of their strategies and offers according to the typologies of the yields, with regard to the previously mentioned aspects; at the level of a country, to anticipate agricultural crises or even food crises in the poorest countries. Better production anticipation is also essential for different players in agricultural raw material markets.

The issue of agricultural yield prediction has been widely surveyed by the specialized scientific community. It is a crucial subject that remains quite challenging due to the necessity to take into account the impact of a multitude of factors related to the phenotype and genotype of plants as well as environmental context, but also the interaction of these factors. With this in mind, the classical approach for the forecasting of agricultural yields in a broad sense (in terms of quantity but also the quality and environment) is the modeling of plant growth by agro-environmental models. Globally, these models simulate the behavior of the pedolimatic environmental context in interaction with the plant’s development dynamics and cultivation practices. The most advanced models intend to address the diversity of environmental variations under a wide range of contexts, such as APSIM ([Keating et al., 2003]) or STICS ([Brisson et al., 2003, Brisson et al., 2008]), which will be evoked in our thesis work. Document [Jin et al., 2018a] includes a complete synthesis of plant growth models and their development over time but also a review with a more historical aspect of agricultural systems modeling, in general, is carried out in work [Jones et al., 2017].

Let us note that another type of approach, which has expanded with the advent and progress of the artificial intelligence domain, is based on the use of machine learning models in forecasting agricultural yields. We can mention for instance the works [Romero et al., 2013] and [Chu and Yu, 2020]. Readers may refer to the work of [van Klompenburg et al., 2020] for a complete review of the machine learning models and features used in crop yield prediction studies.

In the present work, we propose investigating how to crop above-ground biomass (also known as above-ground dry matter) can be estimated from radar remote sensing data using some simple machine learning models. Biomass, measured in weight per surface unit, is directly involved in the yield, and its creation in plants is done according to the following process: solar radiation is intercepted by the foliage and transformed during photosynthesis into above-ground biomass allocated to the different claimant organs during crop growth [Brisson et al., 2008].

More generally, the estimation of plant biophysical variables such as leaf area index (LAI) or biomass from satellite observation data is a research topic that has received a lot of focus boosted by the considerable advances in satellite imagery in terms of availability and quality. In current research works, remote sensing data can most often be optical as in [Guerif et al., 1988], and more recent works like in [Dong et al., 2020], or from radar as in [Mansaray et al., 2020]. The use of radar data has been well-reviewed in [Steele-Dunne et al., 2017] and more references will be given in the present document, particularly in section 3.1.1. The combination of both technologies has also been exploited as in [Forkuor et al., 2020], as well as the use of one of these technologies in combination with other imaging sources such as airborne LiDAR data [Fassnacht et al., 2021].

In the same scope, we propose an implementation case of the methods known as data assimilation in our thesis work. These approaches can significantly improve the predictive power of plant growth models by correcting the calibration of the latter using field observation data.

Actually, Even with the considerable advances in the matter, it remains rather complex to have agro-environmental plant growth models that characterize the different varieties under the full diversity of agronomic and environmental contexts [Chen and Cournède, 2014].
Various works aim to model the plant's growth by considering the sub-optimal environmental growth conditions in the development processes. For example, [Fowler et al., 1999] evokes the case of the extreme temperatures and proposes a functional model that conforms to the known low-temperature responses of cereals and in which equations taking into account low-temperature stress are built. In the works of [Tardieu, 2003], the genetic variability of responses to water stress and consideration of these deficits in plant growth modeling are studied.
More globally, the challenge of designing models for varietal characterization under any context and environment has allowed significant advances in the elaboration of robust models integrating more biological understanding. The works of [Yin and Struik, 2010] provide a complete synthesis review. In these works, the authors start from the statement that current crop model parameters may have little biological meaning. They outlined the possibility of making

plant growth models less empirical by incorporating ecophysiological comprehension. They also present further progress in modeling crop genotype-phenotype relationships and suggest ways to link crop modeling with biochemical modeling and genomics.

However, considering all the mechanisms mentioned above can engender complex models that would require a lot of experimental data with a high cost and reliability, usually not sufficient. Because in effect, the lack of sufficient reliable experimental data permitting to constrain the plant growth model is the main factor, leading to yield prediction quality that is not always satisfying. Considering the data specific to these different contexts by means of assimilation of observation data [Dowd, 2007, Wikle and Berliner, 2007a] makes it possible to correct the calibration of crop models during the growing season and thus provide a much more reliable forecast. Readers can refer to the work of [Delécolle et al., 1992] where several kinds of crop models are described, and specific methods are detailed for introducing remotely sensed information into models. Besides, works of [Dorigo et al., 2007] can constitute an overview of different methods used to obtain biophysical and biochemical canopy state variables from optical remote sensing data. The authors retrace the different processes developed to retrieve canopy state variables from optical remote sensing data and assimilate them into agro-environmental models.

The general principle of data assimilation consists in updating the calibration of a model each time new experimental data is available. It is a statistical approach allowing to refine the learning of the model parameters dynamically. It fits naturally into the so-called Bayesian formalism and most of the time involves the use of powerful algorithms such as sequential Monte Carlo methods [Del Moral, 2004, Arnaud Doucet and Gordon, 2001]. The initial probability distributions are sampled using particles, then propagating them independently through the model equations and selecting them according to their relevance to the experimental data. Note that the work of [Makowski et al., 2004] to improve the accuracy of winter-wheat biomass production and grain protein content models is among the first works to update predictions within the framework of a Bayesian formalism.

In all these perspectives and objectives, we have been able to count on a major ally, satellite imagery, more particularly the one based on radar technology ensuring a certain independence from climatic hazards. Remote sensing technologies provide high resolution multi-temporal images offering a real opportunity to track the evolution of plant reflective spectral properties during their growth process, depending on the variations related to phenology and pedoclimate.

Two major types of sensors for land surface observation have been mentioned: optical multispectral sensors, operating in a varied spectrum from the visible to the infrared and allowing the acquisition of images of a quality close to visual perception (typically, one can perfectly distinguish the contours, with details, of the imaged agricultural parcels), however, these sensors have a major drawback, their sensitivities to cloud cover, which makes their exploitation arduous under severe cloud cover. Radar sensors, operating by emitting and receiving electromagnetic waves, are insensitive to clouds, which allows the acquisition of relatively high resolution images at regular time intervals, even if the images acquired are more delicate to interpret and noisier than optical imagery. In addition, radar sensors allow day and night image acquisition, as they do not depend on the illumination of the observed surfaces (hence the qualification of an active sensor, while optical sensors are passive sensors depending on the illumination of the sun). In our work, we use data imagery from the Sentinel-1 satellite, launched by the European Space Agency as part of the European Copernicus mission, offering a spatial resolution of about 10 meters and a rather reduced temporal resolution of a few days.

The objective of this PhD work is the identification of crop types from radar imagery. We propose an approach that takes as input a time series of Sentinel-1 radar satellite images acquired over the area of interest and returns a label associated with a given crop type for each pixel covering the area (of an extent depending on the spatial resolution of the pixel). The approach is conceived such that the models can produce an evaluation of the cropland cover without having to label parcels at the beginning of the campaign. In other words, we want to calibrate the model using historical data from previous campaigns and other locations, which is what we will call the inter-annual approach in our manuscript.

Another situation to identify the types of crops covering a given production basin is to have the location and the type of crop of a few parcels located in the same production basin at the beginning of each farming campaign (or at the latest a few days before the desired moment of prediction). We then train supervised statistical learning models on these parcels to use them in the prediction of the rest of the parcels within the basin, this is what we will call the intra-annual approach in our manuscript. However, to implement such a process is not obvious from a logistical point of view. In fact, having training parcels requires either being in contact with farmers who tell us what they have sown in each campaign, or going out into the field to manually label a certain number of parcels. To all this is added an additional level of difficulty, the training data collected must ensure a certain level of variability, because depending on the cultural practices, such as the choice of sowing periods, sowing method (tilling, no-till, direct seeding), weeding method, fertilization, phytosanitary treatments, irrigation, etc., the development of a given crop may be different from one exploitation to another, or even from one parcel to another [Wang et al., 2021] [Tomaz et al., 2021].

To remedy all these obstacles, the approach we propose allows us to produce an evaluation of cropland cover through statistical models trained on crop occupation data from previous farming seasons, data that are reasonably easy to acquire.

In such an approach, a first natural intuition would be to rely on the dynamics, expressed in calendar time, of the radar response scattered from the fields of a given crop, thus forming a kind of signature characteristic of this crop type, which can be used to identify it in each agricultural campaign. However, this growth dynamic of the concerned crop can vary from one campaign to another and is strongly guided by the pedoclimatic environment, cultural practices (sowing date, different fertilization applications, irrigation, etc.) as well as the characteristics of the crop itself, such as its resistance to extreme frosts. Therefore, the characteristic signature given by the dynamic in calendar time of the radar response can be very different from one campaign to another, either with the same evolutionary dynamic but shifted in time, or with a quite different dynamic evolution.

Many works based on the phenological development of plants to identify their types exist. For instance, [Peña-Barragán et al., 2011] in a supervised approach combining object-based image analysis and decision tree algorithms, the authors rely on plant phenology, through different vegetation indices and textural features extracted from optical remote-sensing imagery, to field-based identification of the most important crops types in Yolo County, California. The authors highlighted the importance of crop development monitoring using satellite images at distinct growth stages for discriminating crop types. In another study, [Serra and Pons, 2008] presented an approach for mapping and monitoring temporal signatures of six agricultural categories over four seasons (from 2002 to 2005) in irrigated areas located in Spain. They proposed a hybrid classifier for crop identification and characterization of the temporal dynamics using optical Landsat satellite time-series images. They concluded, amongst other things, the importance of a multi-temporal approach, allowing to take into account the crop phenology for such applications.

In this context, we propose an approach in which the phenological development of the plant is considered to identify its species. Instead of using calendar time series of the radar response, we proposed to use time series guided by the thermal time to readjust the shift and/or difference in the dynamics of the radar response allowing a better synchronization of the radar backscatter evolution between the several years. This idea is motivated by the fact that a priori, independently from the pedoclimatic conditions, the cultivation practices or the crops' degree of resistance, a phenological stage of a given crop is reached at a given level of temperature accumulation, hence of thermal time, ensuring the robustness of the inter-annual variation of crop development dynamics.

For this work, we rely on machine learning models. An important part of the use of machine learning models for classification of time-series optical data in large area land cover characterization and mapping are reviewed in [Gómez et al., 2016]. The considerable advances in the availability, but also in both spatial and temporal resolutions of satellite imagery allow their use for land cover monitoring, and more particularly for crop types mapping at large scale [Inglada et al., 2017][Matton et al., 2015][Vuolo et al., 2018]. In terms of pixel-based supervised machine learning models, the well-known Support Vector Machines (SVM) and Random Forests (RF) are widely used [Khatami et al., 2016]. Nevertheless, These models have a major inconvenience, the temporality aspect of the satellite images time-series is not considered thus preventing the evolutionary dynamics of plants from being taken into account in their type identification. Some works have tried to overcome this drawback by temporal features extraction before making classification, as in [Valero et al., 2016] where the authors propose to use a set of statistical indicators extracted from the temporal evolution of the Normalized Difference Vegetation Index (NDVI), like the maximum or average values, to feed an RF classifier, in addition to the satellite images. However, it was shown that the performance gain of such operations remains very slight [Pelletier et al., 2016], in addition to the data preparation cost that might be involved.

The question of the portability of a model for crop identification using Sentinel-1 imagery learnt in a production basin/region A to a production basin/region B is also addressed in our work. Indeed, in order to explore whether a model trained on data from a given region remains valid in another region, a study aiming to evaluate the effect of the pedoclimatic conditions which characterize a given region on the radar response was carried out on the soft winter wheat crop as a pilot crop.

This manuscript is composed of four chapters and is organized as follows: a first chapter, in which a description of the remote sensing data used in this work is given, followed by a second chapter, in which the statistical approaches proposed for crop identification based on time series of radar images are detailed. The third chapter is a bridge between the previous chapter on crop recognition and the last chapter on data assimilation. It contains two chapters, the first chapter in which we present some approaches allowing the estimation of a biophysical variable of critical importance for plants, the biomass, from radar remote sensing data, followed by a second chapter in which we propose a tool intended for positioning the field measurement points of these biophysical variables, still using radar images. The fourth and last chapter deals with the implementation of data assimilation methods intended to improve the predictive power of plant growth models, in the particular case of soft winter wheat. Details of the different chapters composing this manuscript are given hereafter.

**Chapter 1 :**

- This chapter aims to describe the Sentinel-1 remote sensing radar data that we will use in our work, on the aspects that concern their operating mode as well as the series of operations that compose the pre-processing chain necessary to prepare these data to be operational. We will then carry out a study aimed at evaluating, by analysis of variance (ANOVA), the impact of the variation of a satellite remote sensing factor identified as important, the incidence angle, in addition to the variation of pedoclimatic conditions from one production basin to another, on the radar response in interaction with the vegetation cover. An experimental plan to study the effect of these factors at a specific date, but also over the entire agricultural campaign, is established.

**Chapter 2 :**

- In this chapter, the proposed approach for crop recognition using time series of satellite images will be detailed. We will start by describing the research problem based on a first application case on corn crop in the United States. A mathematical formulation of the prediction problem will be proposed, followed by details of our main contribution in which it is proposed to take into account the phenological development of plants, which is strongly dependent on climate, by means of thermal time for inter-annual modeling of identification of crop types. We will then present the supervised statistical learning models used: a long short-term memory (LSTM) recurrent model and a convolutional neural network model (CNN). The functioning of these models as well as the approaches proposed to use these models in the context of crop identification at the pixel level of the satellite image will be discussed. We will then embark on the experimental phase in which all the results obtained will be presented. We will start by presenting the preliminary results obtained with an LSTM model on corn over the United States data sets. We will then present the study areas in France as well as the results obtained with the intra-annual modeling as a proof of concept, and the inter-annual modeling to evaluate the contribution of thermal time and the performance of the trained models, we will focus on a few types of major crops: soft winter wheat, winter rapeseed, and beet. Finally, We will conclude with a discussion.

**Chapter 3 :**

- Chapter 3.1 tackles the issue of estimating plant biophysical variables (biomass, leaf area index, etc.) from remote sensing data. We will present how, based on Sentinel-1 radar data and biomass data of the different soft winter wheat compartments, measured in the field within experimental parcels in France, we have fitted simple supervised statistical models and evaluated their capacity to estimate these biomass through validation data. The objective here is to evaluate the opportunities that radar data can offer for these types of needs.
- Chapter 3.2 presents a tool that we propose to define the positioning of measurement points of a given biophysical variable in an agricultural field according to the intra-parcel heterogeneities. We will present an approach to use unsupervised K-means clustering of radar response signatures in winter rapeseed experimental parcels located in the Beauce region of France, over the 2019/2020 cropping campaign.

**Chapter 4 :**

- This chapter is an implementation of data assimilation methods aimed at improving the predictive power of models by successive updates of their calibration each time observation data are available, applied to a mechanistic model simulating plant growth. We will start by recalling the operating principle of mechanistic plant growth models adapted to the case of winter wheat. We will then discuss the filtering approach used in the framework of a general state-space model. We will discuss the so-called filtering problems, the convolution particle filter (CPF) methods based on Sequential Monte Carlo (SMC) methods, and the adapted algorithms. We will then switch to an application case of these methods, in which we evaluate the performance of the CPF-based data assimilation algorithm applied to the mechanistic winter wheat growth model, employing simulated above-ground biomass data. The objective is to calibrate the soil parameterization of the model using these synthetic simulated biomass data. We also investigate the importance of the moment of observation as well as having more observations data for model calibration.

# Chapter 1

# Radar remote sensing for crop monitoring and interaction with vegetation

## 1.1 SAR radar satellite data

The main remote sensing technology used in our work is radar imaging (Radar : for Radio detection and ranging), more particularly, Sentinel-1 at C-Band (around 6cm of wavelength) Synthetic Aperture Radar (SAR), launched by the European Space Agency as part of the European Copernicus mission and having the advantage of providing images in all weather conditions, day and night.

Sentinel-1A was launched on 3 April 2014 and Sentinel-1B on 25 April 2016. Sentinel-1 Radar had a 12-day acquisition period from March 2015 to August 2016 when Sentinel-1A was operating alone, and it has been decreased to 6 days since September 2016 by combining the Sentinel-1A and 1B acquisitions.

Radar operates by emitting impulses in the centimeter wavelengths and measures the backscattered energy (waves), and the waves can be transmitted and received in two trajectories: vertical and horizontal, as shown in figure 1.1. The operating principle of an imaging radar is schematized in figure 1.2 [1].

The radar response, known in a more technical term as backscatter, is influenced in Sentinel-1 images by the characteristics of the imaged target, in addition to the characteristics of the emitted electromagnetic wave. For instance, when the imaged targets are plants, the signal is strongly impacted by the biomass of the plants, the signal changes as the biomass evolves during the plants' growth cycle. More details on what drives the radar response will be given

---

[1] Basic image credit: Lucas Ternynck - satellite icon by Jose Luis Algara - tree icon by James Keuning, Cours de Télédétection Radar, septembre 2013, Ecole Nationale des Sciences Géographiques, image amended by Walid Hammache.

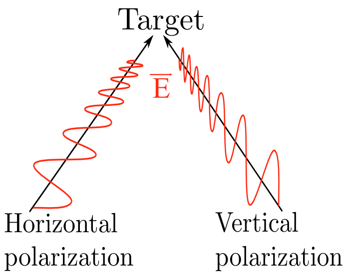

*Figure 1.1:* ***Electromagnetic wave: vertical and horizontal trajectories.***

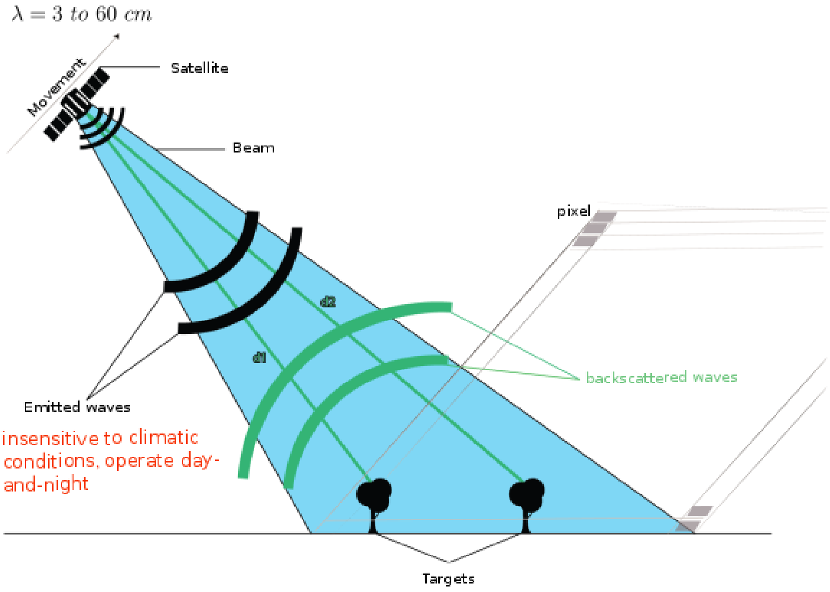

*Figure 1.2:* ***Operating mode illustration of an imaging radar.***

later, particularly in the section 1.1.2.

We access the Sentinel-1 mission data provided by the European Space Agency (ESA) through the Copernicus open access hub. For the purposes of our research, an automated pipeline to download the raw images was developed, in addition to the deployment of appropriate storage logistics, to ensure real-time interaction with our models in the framework of our various applications.

Sentinel-1 provides C-Band (corresponding to a radar wavelength of about 5.6 cm) SAR data in interferometric wide swath (IW) mode which is the main acquisition mode over land. Data is acquired in three swaths for 250km in total using the Terrain Observation with Progressive Scanning SAR (TOPSAR) imaging technique. This mode provides dual-polarization VV and VH images at a spatial resolution of 10 meters (V for vertical trajectory, H for horizontal trajectory. The first letter corresponds to the emission and the second one is for the reception). We use level-1 Ground Range Detected (GRD) processed product consisting of focused SAR data, multi-looked, and projected to ground range using an Earth ellipsoid model.

Once the Sentinel-1 raw data are loaded, and in order to make images exploitable for our analyses, pre-processing operations are achieved. The corresponding tools were implemented and the steps involved in these operations are detailed, in the next paragraph.

### 1.1.1 SAR radar images pre-processing

Some indispensable processing operations are applied to Sentinel-1 raw data, using the ESA Sentinel-1 Toolbox (S1TBX) deployed on Sentinel Application Platform (SNAP).[2]

Without going into too many details of radar imagery, we would like to explain some specific treatments, in particular speckle filtering, as it allows to see in a concrete way the direct impact of such a treatment on the radar response, the main data sources of our work.

#### Thermal noise removal

Thermal noise suppression is performed using the reference table of noise (Lookup Table - LUT) for each set of measurement data provided in Sentinel-1 Level 1 products.

#### Orbit information update

The orbit state vectors provided in the Sentinel-1 product metadata are generally not accurate and can be refined with the accurate orbit files that are available a few days after product generation. The orbit files provide accurate information about the satellite's position and velocity. The orbit information of image acquisition is then updated in the product metadata.

#### Radiometric calibration

The radiometric calibration of SAR images aims at converting the digital values recorded by the sensor, i.e., the intensity values, which contain uncorrected radiometric biases, into a physical variable: the backscatter coefficient $\sigma^0$, which is directly related to the radar backscatter of the imaged target. This operation allows a quantitative use of radar images and is also necessary to be able to compare SAR images acquired with different sensors, under different acquisition modes, or acquired from the same sensor but at different times. Readers may refer to [Laur et al., 2004] [Rosich and Meadows, 2004] for a detailed description of the radiometric calibration of SAR products.

In the case of Sentinel-1 data, this operation, which is actually quite complex, is simplified by the availability of Look Up Table (LUT) denoted $A_\sigma$, included within the Sentinel-1 GRD product used in our work, and providing the necessary information to convert the radar intensity into the backscatter coefficient [Miranda and Meadows, 2015].

In fact, at pixel scale, the radiometric calibration is applied according to Equation (1.1)

$$\sigma^0 = \frac{DN^2}{A_\sigma^2} \tag{1.1}$$

where $DN$ is the pixel digital value and is equal to the pixel amplitude in the case of GRD products.

Furthermore, the backscatter coefficient is defined from a simplified form of the radar equation (in which some non-radiometric corrections have already been made in Sentinel-1 GRD

---

[2] https://step.esa.int/main/toolboxes/snap/

products) as follows [Miranda and Meadows, 2015]:

$$\sigma^0 = \frac{DN^2}{A_{dn}^2.K} sin(\alpha) \tag{1.2}$$

where $\alpha$ is the radar incidence angle, $K$ is the absolute calibration constant (calculated during the satellite commissioning phase and calibrated using knowledge of homogeneous areas, such as forests), and $A_{dn}$ is the Look Up Table (LUT) scaling applied to generate S1 level-1 product from initial internal S1 products (allowing to avoid saturation of both brighter and darker targets, and at the same time to reduce measurement errors).
Therefore, from (1.1) and (1.2) , $A_\sigma$ is defined as:

$$A_\sigma = \sqrt{\frac{A_{dn}^2.K}{sin(\alpha)}} \tag{1.3}$$

We can see that this radiometric calibration depends mainly on the calibration constant and the incidence angle.

So far, we have mentioned radiometric calibration to extract the backscatter coefficient $\sigma^0$ for which the area normalization is aligned with the ground range plane, thanks to the angle of incidence. However, other backscatter coefficients, denoted $\beta^0$ and $\gamma^0$, can be used for areas of interest with significant slope effects, through the local incidence angle. Since the majority of the areas of interest in our work have a relatively flat topography, we will use S1 data that are calibrated without taking into account the slope effect.

To complete this step, note that the LUT scale provides the absolute values of $\sigma^0$. It is however recommended to convert these values into decibels (db) in order to reduce the range of variation of the values of $\sigma^0$ by the following formula:

$$\sigma_{db}^0 = 10.\log_{10}.\sigma^0 \tag{1.4}$$

A question is naturally raised during the radiometric calibration phase of the SAR data for the different applications studied in our thesis work: do we need to calibrate data acquired in different locations in the same way? For example, shall we calibrate a radar image acquired in Africa or in America in the same way as an image acquired in metropolitan France ?
Our description of the calibration presented above allows us to answer positively from a radiometric calibration viewpoint. It is indeed the whole purpose of radiometric calibration to ensure comparability of the data. However, it only remains valid for areas with homogeneous topography. As explained above, for areas with significant slope effects, specific backscatter coefficients shall be used.

However, it should be noted that this calibration is in no way a correction of the angle of incidence. Radar backscatter varies with the angle of incidence as well as the characteristics of the electromagnetic waves (mainly polarization and wavelength), the climate, and the properties of the imaged targets. Therefore, and knowing that the incidence angle varies between 30 and 45 degrees in the Sentinel-1 IW GRD images used in this thesis, as shown in Figure 1.3, the

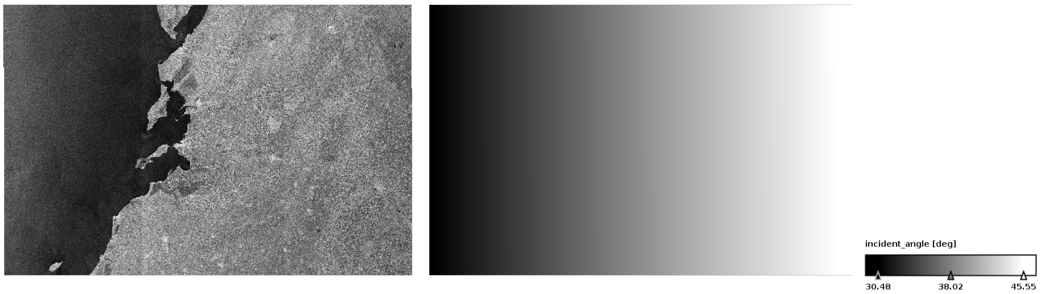

*(a)* *(b)*

*Figure 1.3:* ***Range of incidence angle variations in degrees (b) within a Sentinel-1 IW GRD product example (a).***

effect of the variation of the incidence angle on the radar response in the agricultural areas that we are interested in, as well as its impact on the performance of our statistical models, will be studied in detail in Subsection 1.1.2.

### Speckle filtering

SAR radar data are exposed to the speckle effect [Lee, 1986]. This is a phenomenon that results in high variability of radar response from one pixel to another in a homogeneous area. In fact, if we assume that there are different elementary targets within a given pixel, the radar response within that pixel is the sum of the responses of these elementary targets. This summation induces an interference phenomenon that can be constructive or destructive [Elachi, 1988] (it depends on the wavelength and distances between the different elementary targets and the radar antenna, in addition to the target characteristics). The image is then strongly granulated, with a visual pepper and salt effect as shown in figure 1.4, which makes the interpretation and analysis of the different image characteristics quite complicated. The reader can refer to the book [S. Lee, 2009], section Polarimetric SAR Speckle Statistics, for more details on speckle formation, effect, and its statistical property. To reduce this speckle and improve radiometric resolution, filtering is applied by averaging several pixels. In our study, we apply Lee Sigma filter [Lee et al., 2009] ($7 * 7$ local window, $3 * 3$ target window, and sigma of $0.9$) which is implemented in S1TBX. This filter is a good compromise between the preservation of polarimetric information and radiometric resolution [Cazals, 2017] [Boutarfa et al., 2013], so we have a clearer interpretation of features in SAR radar images.

Let us highlight that speckle reduction is crucial in providing exploitable and interpretable radar images and therefore has been the subject of considerable research work. Since the first pioneer works of lee [Lee, 1983], new approaches have emerged to reduce noise in SAR products. one of the most performing is the so-called patch-based approaches, which rely on the search for similar local configurations within the images and can efficiently replace more complex models using the statistical distribution of images. One can mention the works [Tupin et al., 2019], which constitutes a global review of such patch-based approaches. Further, the considerable recent advances in the machine learning field, particularly in deep learning, allowed the recourse to these approaches for speckle reduction. Works [Fracastoro et al., 2020] provides extensive reviews of deep learning for SAR image restoration. Those of [Denis et al., 2021] also evoke the most recent works as well as the principal research perspectives for the use of deep-learning in SAR product ”despeckling”. Moreover, an interest in combining both approaches based on similar local configurations and deep learning models such as CNNs has emerged. In this context, works [Denis et al., 2019] explores different strategies that can be used.

However, supervised approaches based on deep learning models are often confronted with a significant blocking point, lack of training speckle-free data. This issue has therefore been the subject of several research works. For instance, in paper [Dalsasso et al., 2020], the authors have presented two main strategies for speckle reduction in SAR images. The first one consists of using a convolutional pre-trained natural images denoising, combined with Gaussian denoisers [Deledalle et al., 2017] to consider the noise generated by the speckle. The second strategy consists of form scratch convolutional network training with SAR data generated by multi-temporal multi looking of a time series images at the same areas, followed by a denoising step with Gaussian denoisers. Besides, noisy images are synthetically simulated with a statistical speckle model [Goodman, 1976] to obtain the necessary samples for supervised learning. This latter work served as a basis for the development of the SAR2SAR algorithm [Dalsasso et al., 2021a], in which the synthetically generated input data in [Dalsasso et al., 2020] were t a later stage replaced by real SAR acquisitions, allowing learning of the spatial correlation introduced by the processing steps of these acquisitions, and achieving a clear improvement over existing despeckling algorithms. This work has also been adapted to filter Sentinel 1 GRD images [Gasnier et al., 2021] [Dalsasso et al., 2021b].

### Range Doppler Terrain Correction

Due to the side-looking geometry of radar imagery and the topographical variations in the monitored area, some geometric distortions may appear in the Sentinel-1 data. Terrain corrections are intended to compensate for these distortions so that the geometric representation of the image is as close as possible to reality on the ground. For this correction, we use the Range Doppler ortho-rectification method [Small and Schubert, 2019] for geocoding SAR scenes from images in radar geometry. The digital elevation model (DEM) used is that of the NASA Shuttle Radar Topography Mission (SRTM) at 30 m of spatial resolution. The images used in our work are projected on the WGS84 ellipsoid and expressed in Lat/Long geographic coordinate system. They can also be expressed in Universal Transverse Mercator (UTM) coordinate system to have pixel sizes in meters instead of degrees, this will depend on the different needs in our work (to have pixel sizes of $10m * 10m$, to be in adequacy with the Sentinel-2 optical images pixel size,. . . ).

Finally, the sequence of all these previous steps is summarized in Figure 1.5.

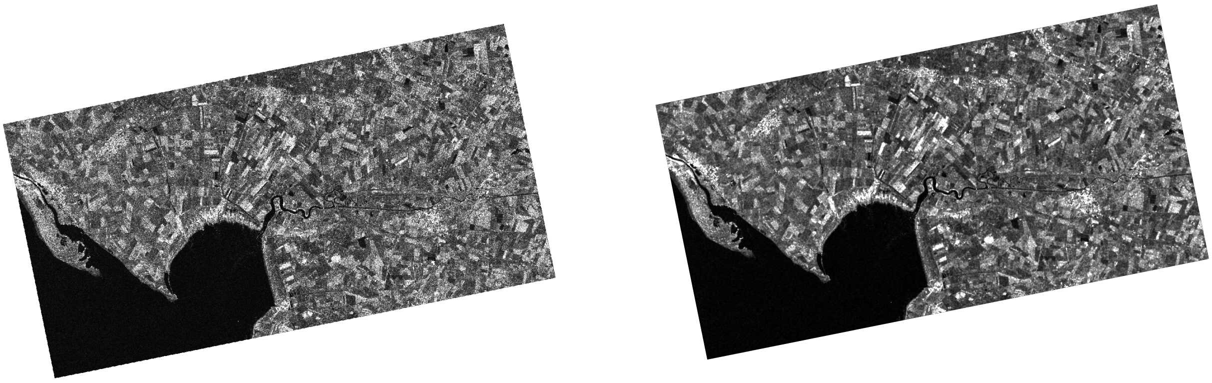

*(a) VH polarization before speckle reduction, highly granulated Sentinel-1 product example.*

*(b) VH polarization after reduction of speckle leading to a much less granular Sentinel-1 product.*

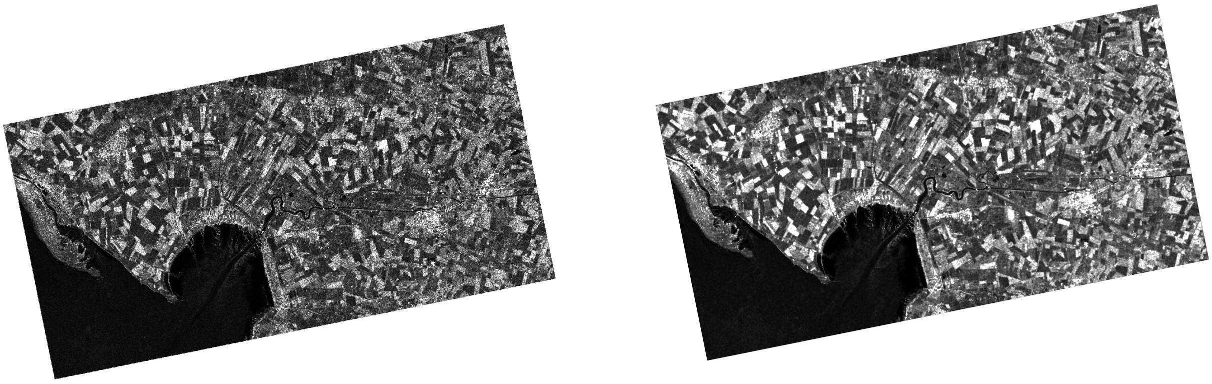

*(c) VV polarization before speckle reduction, highly granulated Sentinel-1 product example.*

*(d) VV polarization after reduction of speckle leading to a much less granular Sentinel-1 product.*

*Figure 1.4: A demonstration of the effect of the speckle reduction operation on both $\sigma^0_{VV}$ and $\sigma^0_{VH}$ polarizations of an example Sentinel-1 product covering southwest France acquired in June 2018. Lee Sigma filter [Lee et al., 2009] with $7 * 7$ local window size, $3 * 3$ target window size and sigma of $0.9$ is applied.*

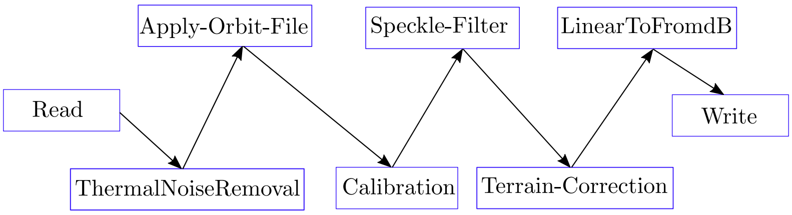

*Figure 1.5: Sequence of the preprocessing phases of the Sentinel-1 radar images.*

### 1.1.2 Effect of the variation in incidence angle on backscatter: a study on soft winter wheat parcels in France

As mentioned in 1.2, the incidence angle varies from about $30$ to $45$ degrees within a Sentinel-1 product. The objective of this chapter is therefore to study the effect of this variation on the radar response from agricultural areas. Note that, within the same Sentinel-1 product, different areas located at different incidence angles of this product have most likely different pedoclimatic (soil and climate) conditions. Therefore, what will be really assessed in the present study is the effect of the interaction between incidence angles and pedoclimate on radar backscatter.

To statistically assess the variability in radar backscatter between incidence angles, as well as between studied areas with different pedoclimatic conditions, a one-factor analysis of variance (one-way ANOVA) test was applied to every radar polarization ($\sigma^0_{VH}$, $\sigma^0_{VV}$ and the ratio $\sigma^0_{VH}/\sigma^0_{VV}$), the goal being to assess the statistical differences of the group sample (pixels in our case study) means, in addition to the analysis that can be carried out directly from the boxplots, in which it can be complex to draw direct conclusions when working with a large number of samples. The method for this analysis will be presented in the following.

For this survey, the following experimental test plan has been defined:

**Step 1- Impact, at a fixed date, of the variation of incidence angles and pedoclimatic factors on the same crop type pixels radar response:**

We selected Sentinel-1 products acquired at a given date, as well as multiple areas of interest, located at different incidence angles within these Sentinel-1 products. Afterward, in each of these areas of interest, and using the French national land use database (registre parcellaire graphique - RPG) in France, we automatically selected all parcels of the same given crop type intending to exclude as much as possible the variability related to phenology in radar signal. The aim here is to study the radar response variability within the pixels of this same crop in each selected area of interest.

We first chose to study the impact of the interaction between incidence angles and pedoclimate on radar backscatter as a single factor, before studying in a second time the impact of the two incidence angles and pedoclimate factors of variation separately. For that purpose, the following sub-tests configurations shall be considered:

> **Step 1 (a)- Impact of incidence angles and pedoclimate interaction as a single factor of variation:**
>
> Within one Sentinel-1 product acquired at a given date, three different zones are selected. These three zones are chosen so that they correspond to different incidence angles on the Sentinel-1 product, in addition to being geographically distant to assure different pedoclimates. The objective is to study the impact of the interaction of both incidence angles and pedoclimatic conditions with the radar response.

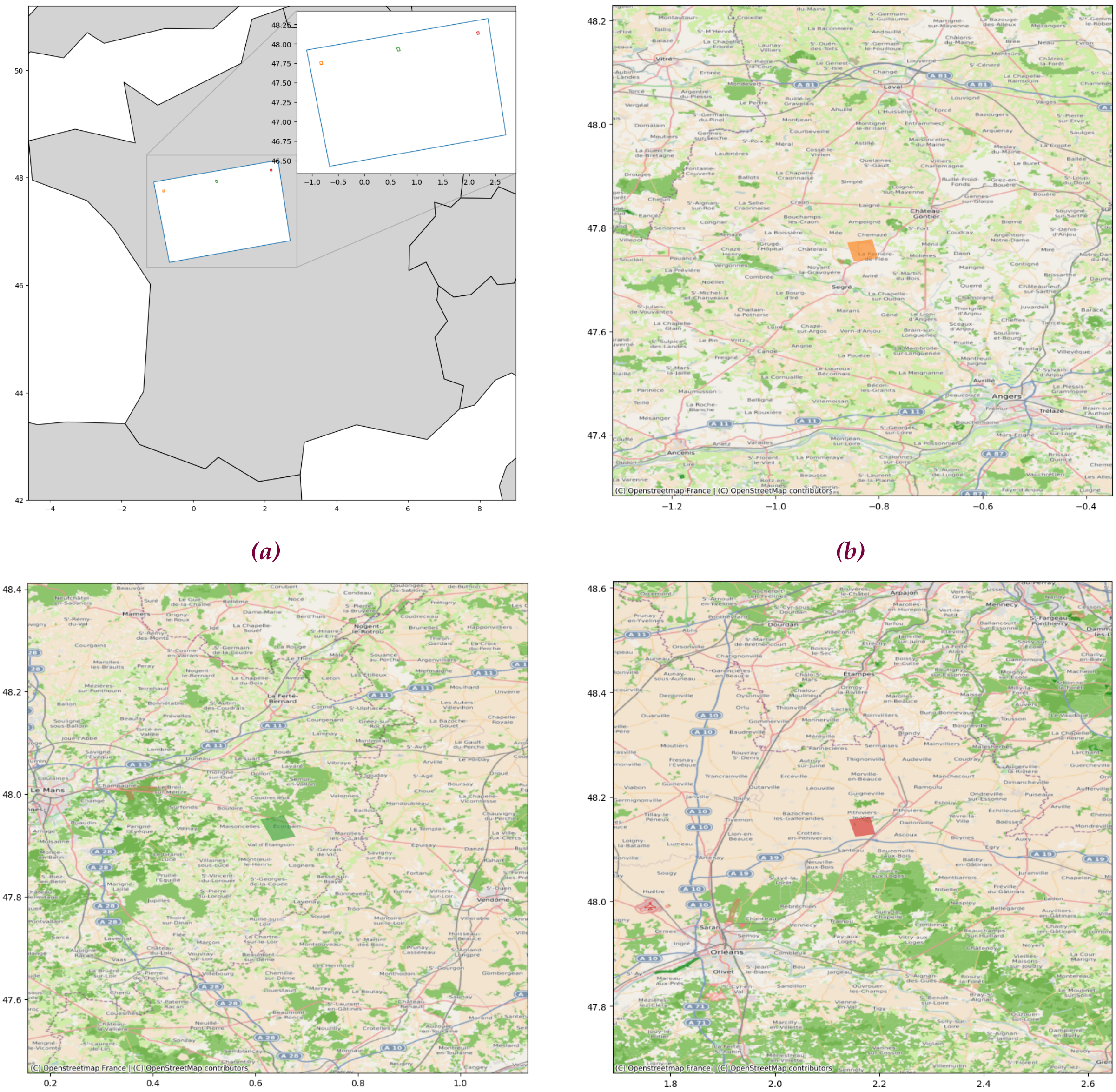

*(a)* *(b)*

*(c)* *(d)*

*Figure 1.6:* ***Location of study areas: (a) Geographic coordinate of the used sentinel-1 product (in the blue rectangle) acquired on May 08, 2018 in the center of France. The locations of the areas of interest with different incidence angles are indicated by the orange, green and red colored boxes. (b) Geographic location of the study area with an average incidence angle of about 31 degrees. (c) Geographic location of the study area within an average incidence angle of about 38 degrees. (d) Geographic location of the study area with an average incidence angle of about 45 degrees. In the whole manuscript, unless otherwise indicated, the maps are projected on the ellipsoid WGS84 (latitude/longitude in decimal degrees, EPSG:4326) coordinate reference system.***

**Step 1 (b)- Impact of incidence angle variation under similar pedoclimatic conditions:**

Within two (or more) different Sentinel-1 products, acquired on the same date, two (or more) different zones are selected. The selected areas are close (to ensure similar soil-climate conditions), but this time they are at totally different incidence angles. In these conditions, we can study the impact of different incidence angles on the radar response.

**Step 1 (c)- Impact of pedoclimate variation under similar incidence angles:**

Two (or more) areas are chosen with the same angle of incidence, but far away enough from each other so that they may have different pedoclimatic conditions. This way, we study the effect of the pedoclimatic conditions on the radar response.

**Step 2- Impact, during the crop growth cycle, of the variation of incidence angles and pedoclimatic factors on the same crop pixels radar backscatter:**

The effects of the angle of incidence and, potentially, of soil-climate conditions are studied over a farming season this time. We are therefore working on time series of Sentinel-1 products, the objective being to evaluate the impact of these two factors during the complete crop growth cycle.

### One-way ANOVA analysis

One-way ANOVA is a parametric statistical test that uses a test of significance to determine whether the population means of a quantitative variable (radar backscatter in our research case) for a given factor (incidence angles and/or pedoclimat here) are significantly different. It relies on the normality assumption of the underlying distributions and consistent variances across the different conditions. However, ANOVA was shown to be relatively robust to departures from these hypotheses [Schmider et al., 2010].

Suppose we have $k$ regions with different incidence angles and/or soil-climates conditions and want to compare their respective sample means $\bar{x}_i$, $i = 1, \ldots, k$. We then consider the following hypotheses:

$$\begin{cases} \mathcal{H}_0 : & \bar{x}_1 = \bar{x}_2 = \ldots = \bar{x}_k \text{ (null hypothesis);} \\ \mathcal{H}_1 : & \exists 1 \leq i, i' \leq k : \bar{x}_i \neq \bar{x}_{i'} \text{ (alternative hypothesis).} \end{cases}$$

The objective of the ANOVA is to compare the variation between groups (of different incidence angles and/or pedoclimat) with the variation within each group (different observation areas) by analyzing their respective variances.

The following test statistic, denoted by $F_s$, is then computed:

$$F_s = \frac{\text{between-groups variance } (\text{Var}_{\text{between}})}{\text{within-groups variance } (\text{Var}_{\text{within}})}$$

where:

$$\text{Var}_{\text{between}} = \frac{\text{between-groups sum of squares}}{\text{between-groups degrees of freedom}} = \frac{\sum\limits_{i=1}^{k} n_i \cdot (\bar{x}_i - \bar{x})^2}{k-1}$$

and:

$$\text{Var}_{\text{within}} = \frac{\text{within-groups sum of squares}}{\text{within-groups degrees of freedom}} = \frac{\sum_{i=1}^{k} \sum_{j=1}^{n_i} (x_{ij} - \bar{x})^2}{n-k}$$

$n$ is the total number of observations, $n_i$ is the total number of observation in region $i$ and $\bar{x}$ is the mean of all observations, also called the grand mean.

Under the null hypothesis $\mathcal{H}_0$, the statistic $F_s$ follows an $F$ distribution $F(k-1, n-k)$.
$\mathcal{H}_0$ is rejected if $F_s > F_{(\alpha,k-1,n-k)}$, where $F_{(\alpha,k-1,n-k)}$ is the critical F-value for a given significance level $\alpha$ for $F(k-1, n-k)$, such that $\mathbb{P}_{\mathcal{H}_0}(F_s > F_{(\alpha,k-1,n-k)}) \leq \alpha$.
Here we set the value of $\alpha$ to $0.05$, $F_{(\alpha,k-1,n-k)}$ can be obtained from the $F$ distribution table [Dodge, 2008].

In addition to this one-way ANOVA analysis, we applied an additional test, a post-hoc Tukey-Kramer test also called Tukey's Minimum Significant Difference (MSD) test, which aims to evaluate significant pairwise group differences (see Algorithm 1).

**Algorithm 1:** Tukey's Minimum Significant Difference test

```
Result: Minimum Significant Difference
scroll through the Studentized range table to find the critical value statistic $Q_{[\alpha,k,df_w]}$
  depending on the critical threshold $\alpha$ (that we will set to 0.05), the number of groups
  to be compared $k$, and the within-group degrees of freedom $df_w$ (equal to the
  difference between the total number of observation and $k$);
compute the Minimum Significant Difference for groups $i, j$ $MSD_{i,j} = Q_{[\alpha,k,df_w]}\sqrt{\frac{MS_w}{\bar{n}}}$,
  where $\bar{n}$ is the mean of the number of observations of both groups, $MS_w$ is the mean
  square within groups (can be directly extracted from the one-way ANOVA results);
calculate the difference of the means $MD_{i,j} = |\bar{x_i} - \bar{x_j}|$, with $\bar{x_i}$, $\bar{x_j}$ the means of groups
  $i$ and $j$;
if $MD_{i,j} >= MSD_{i,j}$ then
    the mean difference between groups $i$ and $j$ is significant;
else
    the mean difference is not significant;
end
```

### Experimental test plan: Step 1 (a)- Impact of incidence angles and pedoclimatic conditions as a single factor of variation:

The location of the Sentinel-1 study product was chosen somewhat arbitrarily. The product is located in the center-west of France ( 1.6a). The choice of the date of acquisition of the product was made so as to have a study crop at booting/heading (beginning of the reproductive phase) to ensure a significant contribution in the radar signal. The date of May 8, 2018 was chosen for the S1 product, with the intention of working with a winter crop (sufficiently advanced in growth on this date).

Three sub-study areas were then selected: one at the left end of the S1 product with a low incidence angle (about 30 degrees, 1.6b), another at the right end of the S1 product with a high incidence angle (about 45 degrees, 1.6d), and a third area in the center with an intermediate incidence angle (about 38 degrees, 1.6c).

The choice of the crop to be studied was based on the total surface areas occupied within the areas of interest, the objective is to ensure as much representativity as possible through a greater coverage. As shown in figure 1.7, soft winter wheat (Blé Tendre d'Hiver in French - BTH) is the crop that covers the largest surface in the areas of interest, so parcels of this crop were selected for our study.

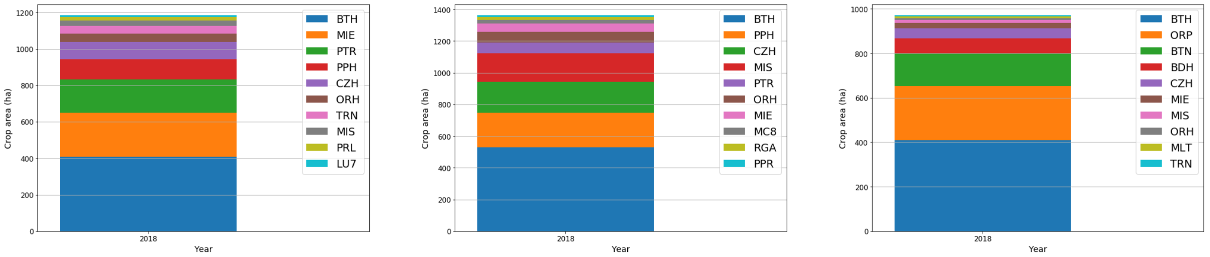

*(a) Crop representativity in the area with an average incidence angle of* $31.47$ *degrees.*

*(b) Crop representativity in the area with an average incidence angle of* $38.76$ *degrees.*

*(c) Crop representativity in the area with an average incidence angle of* $45.19$ *degrees.*

***Figure 1.7:** Total occupation of the cultivated surface of the most frequent crops in the three studied areas in the year 2018. The crop codes are in accordance with the RPG naming system (BTH for Blé Tendre d'Hiver, soft winter wheat).*

In each area of interest, the BTH parcels are automatically extracted from the RPG. Figure 1.8 shows the coordinates and contours of these parcels. The variation of the radar backscatter in each studied sub-area of soft winter wheat parcels is displayed in figure 1.9, for each of the radar polarizations as well as for the ratio band. In this figure 1.9, we can clearly observe, for the set of three polarizations, a monotony or a uniformity in the variation between the different angles of incidence.

Figure 1.10 displays the results of this comparative study. It can be seen that for the two polarizations $\sigma^0_{VH}$ and $\sigma^0_{VV}$, there is variability in the distributions of the radar response with the mean incidence angle at which the study parcels are located. This variability is however re-

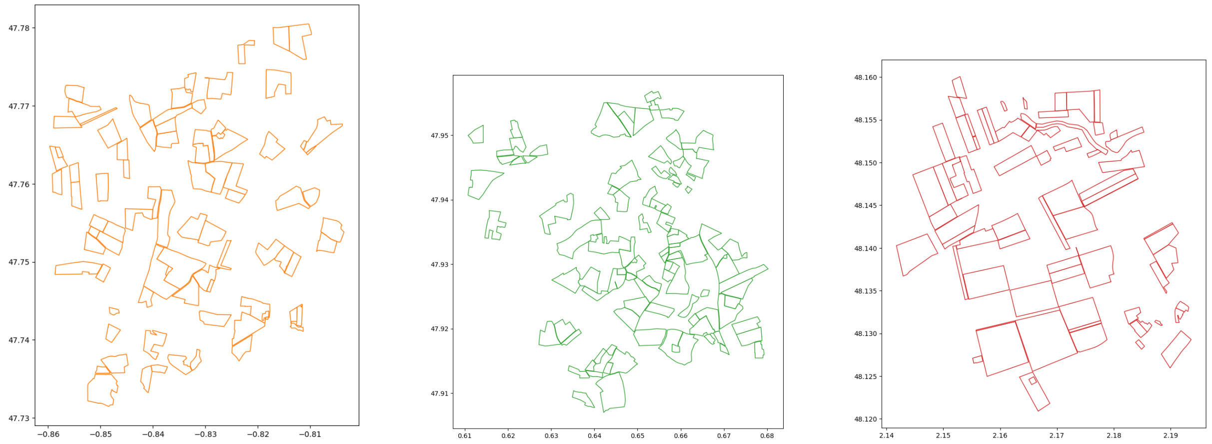

***(a)** Soft winter wheat parcels, average incidence angle of* $31.47$ ***degrees.***

***(b)** Soft winter wheat parcels, average incidence angle of* $38.76$ ***degrees.***

***(c)** Soft winter wheat parcels, average incidence angle of* $45.19$ ***degrees.***

***Figure 1.8:** Coordinates and contours of soft winter wheat parcels, automatically extracted from the RPG, using the areas of interest bounding boxes.*

duced for the ratio $\sigma^0_{VH}/\sigma^0_{VV}$ band. Below, we analyze in more detail whether this diminution is significant enough to reduce the differences in the backscatter means or not with the analysis of variance tests.

In order to evaluate more precisely the differences in backscatter distributions with respect to incidence angles/pedoclimatic conditions interaction, we look at the results of the analysis of variance presented in table 1.1. We observe that the means of the Sentinel-1 radar response across the three backscatter bands over the different groups of incidence angles/pedoclimate are significantly different (p-value significantly lower than $\alpha = 0.05$).

Also, the results of the Tukey-Kramer test presented below in the table 1.2 indicate that the backscatter means are different for each two group pairs [incidence/pedoclimate group $i$ and incidence/pedoclimate group $j$].

It can also be mentioned, based on these Tukey-Kramer test results, that for this case study, even if we observe a decrease in backscatter variability on the ratio $\sigma^0_{VH}/\sigma^0_{VV}$ band in the boxplot 1.10, the sample means remain significantly different.

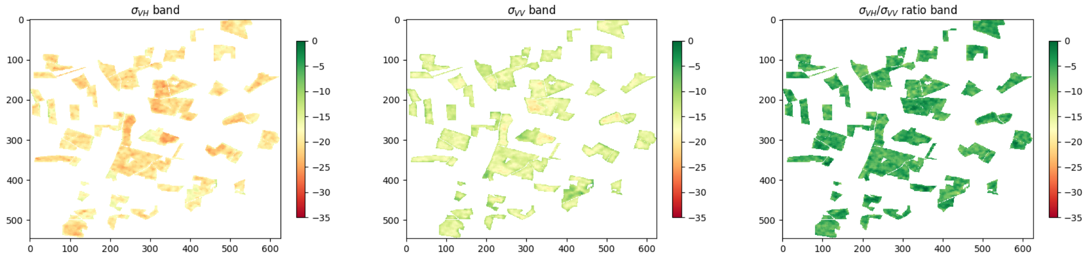

*(a) variation of backscatter in parcels with mean incidence angle of* $31.47$ *degrees.*

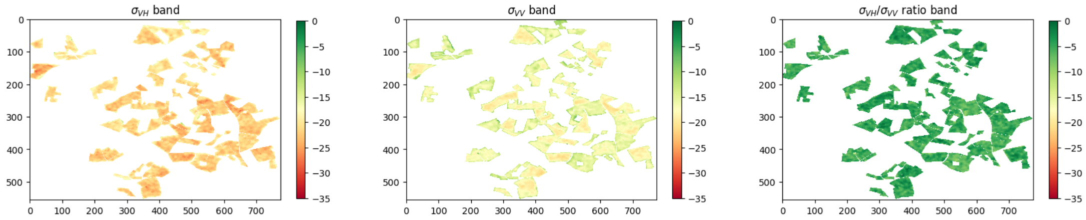

*(b) variation of backscatter in parcels with mean incidence angle of* $38.76$ *degrees.*

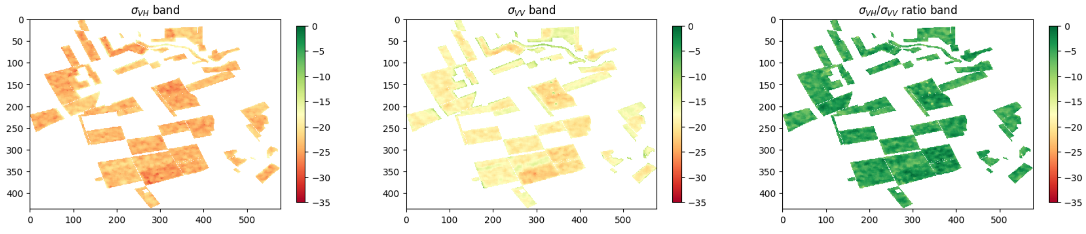

*(c) variation of backscatter in parcels with mean incidence angle of* $45.19$ *degrees.*

***Figure 1.9:*** ***Soft winter wheat parcels pixels variation of backscatter (in decibels) for the bands*** $\sigma^0_{VH}$, $\sigma^0_{VV}$ ***and the ratio*** $\sigma^0_{VH}/\sigma^0_{VV}$.

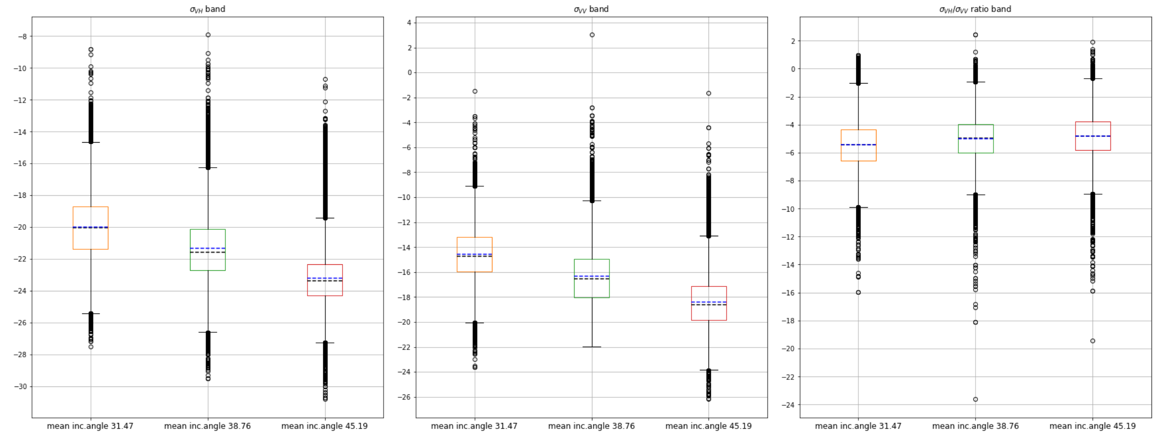

***Figure 1.10:*** ***Boxplots of polarizations*** $\sigma^0_{VH}$, $\sigma^0_{VV}$ ***and the ratio*** $\sigma^0_{VH}/\sigma^0_{VV}$ ***for soft winter wheat parcels and for different incidence angles. The black dashed lines represent the medians and those in blue represent the mean values.***

***Table 1.1:*** ***One-way ANOVA test statistics for the three bands $\sigma^0_{VH}$, $\sigma^0_{VV}$ and $\sigma^0_{VH}/\sigma^0_{VV}$, applied to the Step 1 of the proposed experimental test plan. It is indicated in the table that p-value $< \alpha = 0.05$, but in reality the p-value is far smaller in this test case.***

| | | $\sigma^0_{VH}$ | | | | $\sigma^0_{VV}$ | | | | $\sigma^0_{VH}/\sigma^0_{VV}$ | | | |
|---|---|---|---|---|---|---|---|---|---|---|---|---|---|
| | d.f | sum of squares | mean square | $F_s$ | p-value | sum of squares | mean square | $F_s$ | p-value | sum of squares | mean square | $F_s$ | p-value |
| among groups | 2 | 358041.56 | 179020.78 | 45882.44 | $< 0.05$ | 5.11e+05 | 255763.35 | 51607.55 | $< 0.05$ | 15513.81 | 7756.90 | 3146.58 | $< 0.05$ |
| within groups | 229967 | 897268.49 | 3.90 | | | 1.13e+06 | 4.95 | | | 566910.42 | 2.46 | | |
| total | 229969 | | | | | | | | | | | | |

***Table 1.2:*** ***Tukey-Kramer test statistics for the three bands $\sigma^0_{VH}$, $\sigma^0_{VV}$ and $\sigma^0_{VH}/\sigma^0_{VV}$, applied to the Step 1 of the proposed experimental test plan. critical $Q_{[\alpha,k,df_w]} = 3.31451$, $\sigma^0_{VH} MS_w = 3.90$, $\sigma^0_{VV} MS_w = 4.95$ and $\sigma^0_{VH}/\sigma^0_{VV} MS_w = 2.46$. We refer to algorithm 1 for the notations. We denote the incidence angles/pedoclimate interaction by "interact" in the table.***

| | $\sigma^0_{VH}$ | | | $\sigma^0_{VV}$ | | | $\sigma^0_{VH}/\sigma^0_{VV}$ | | |
|---|---|---|---|---|---|---|---|---|---|
| pair of groups | $MD_{i,j}$ | $MSD_{i,j}$ | reject | $MD_{i,j}$ | $MSD_{i,j}$ | reject | $MD_{i,j}$ | $MSD_{i,j}$ | reject |
| interact1-interact2 | 1.3248 | 0.0229 | True | 1.7918 | 0.0259 | True | 0.467 | 0.0182 | True |
| interact1-interact3 | 1.8804 | 0.0231 | True | 2.0553 | 0.0261 | True | 0.175 | 0.0184 | True |
| interact2-interact3 | 3.2052 | 0.0249 | True | 3.8472 | 0.0280 | True | 0.642 | 0.0197 | True |

### Experimental test plan: Step 1 (b)- Impact of the variation in incidence angle under similar pedoclimatic conditions:

For this test, parcels of soft winter wheat are selected in two different areas, close enough to ensure similar pedoclimatic conditions, but at different angles of incidence in terms of image coverage, at the same date of acquisition. To obtain such a configuration, two different Sentinel-1 products must be used this time. The ideal configuration would have been to have two adjacent (side-by-side) products on exactly the same date. However, the acquisition mode of the used Sentinel-1 images (Ground Range Detected (GRD), Interferometric Wide (IW) acquisition mode) implies that such a configuration is not possible. There are two possibilities in this case:

- Work with two distinct, partially overlapping Sentinel-1 products which are on the same orbit direction (ascending for example) but with a 24-hour acquisition time delay. See Figure 1.11 (a) for an illustration.
- Work with two distinct Sentinel-1 products, which may have partial overlapping points, acquired on the same calendar date, but with an acquisition delay of about 12 hours and two different orbit directions (ascending for the first one, descending for the second one). See Figure 1.11 (b) for an illustration.

Tests on the study of the Sentinel-1 radar signatures were done, and we found that the variability produced by a different orbit direction (e.g., ascending and descending) is important compared to the variability produced by a one-day shift with the same orbit direction. In addition, studies such as [Wood et al., 2002] pointed to the possibility that early morning dew is often present on the crop canopy at the time of the satellite overpass, which can impact the radar response of these crops and which must be taken into account in the processing of the information provided by the radar signal. In fact, they observed an increase of the order of 2 to 4 db in radar backscatter when dew was present on the crop canopy, which can be consequent. Moreover, [Brisco et al., 1993] hypothesized that the formation of dew on the crop canopy likely has an effect on backscatter similar to rainfall, this may lead us to expect an increase in radar backscatter at times of heavy rainfall. It will be evoked in this manuscript.

For all these reasons, and to reduce the effect of any factor, external to the characteristics of the electromagnetic waves and the imaged target (the crop), we decided to work with Sentinel-1 images having the same orbit directions (ascending, whenever possible, to reduce the effect of early morning dew), despite the one day delay.

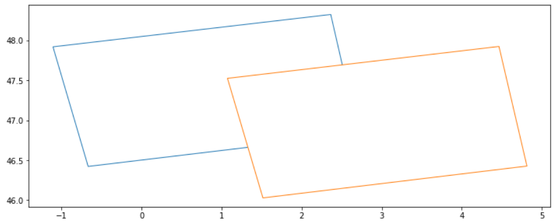

*(a) Neighboring Sentinel-1 products with the same orbit direction (ascending). The product in blue is acquired on day $j$ at approximately 5:00 PM, the one in orange is acquired at about $j + 24$ hours, also at approximately 5:00 PM.*

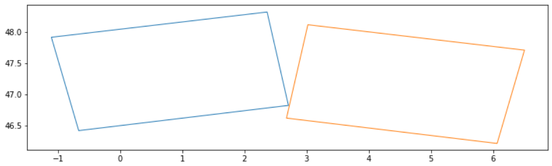

*(b) Neighbouring Sentinel-1 products acquired on the same day $j$, but with a 12 hour time lag. The product in orange is acquired on day $j$ at approximately 5:00 AM, with a descending orbit, the one in blue is acquired about 12 hours later, at approximately 5:00 PM, with an ascending orbit.*

***Figure 1.11:* Possible configurations for two neighbouring Sentinel-1 products at a given date.**

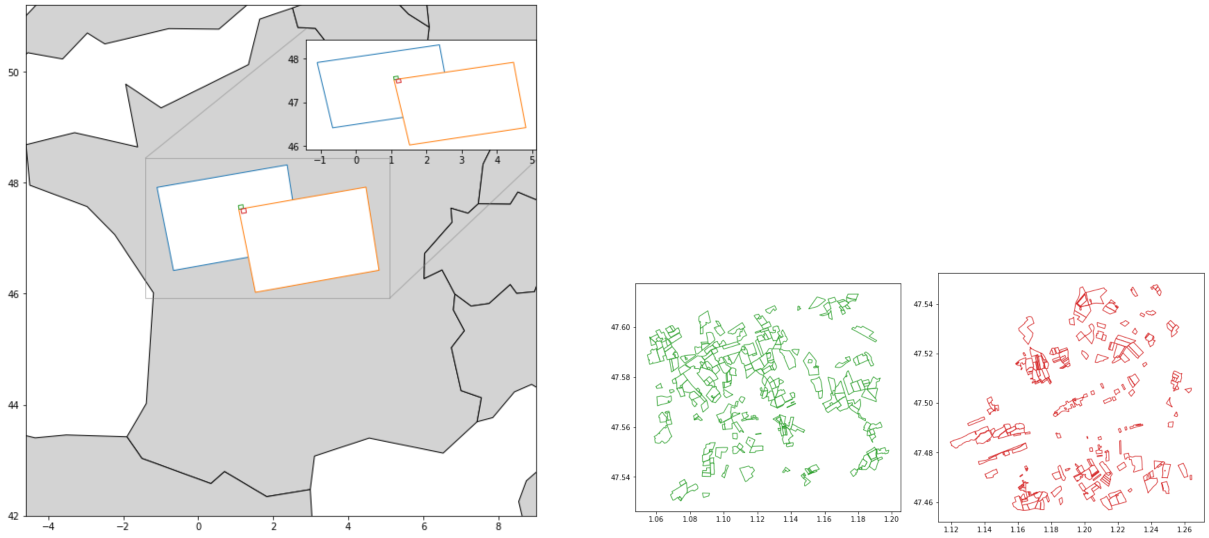

*(a)* *(b)*

***Figure 1.12:* Step 1-b of the experimental test plan, location of study areas: (a) geographic coordinate of the used sentinel-1 products (product acquired on May 08, 2018 in blue rectangle and the one acquired on May 09, 2019 in orange rectangle) in the center of France. The location of the areas of interest with similar pedoclimatic conditions and at different angles of incidence is indicated by the green and red colored boxes. (b) coordinates and contours of soft winter wheat parcels, automatically extracted from the RPG, using the areas of interest bounding boxes.**

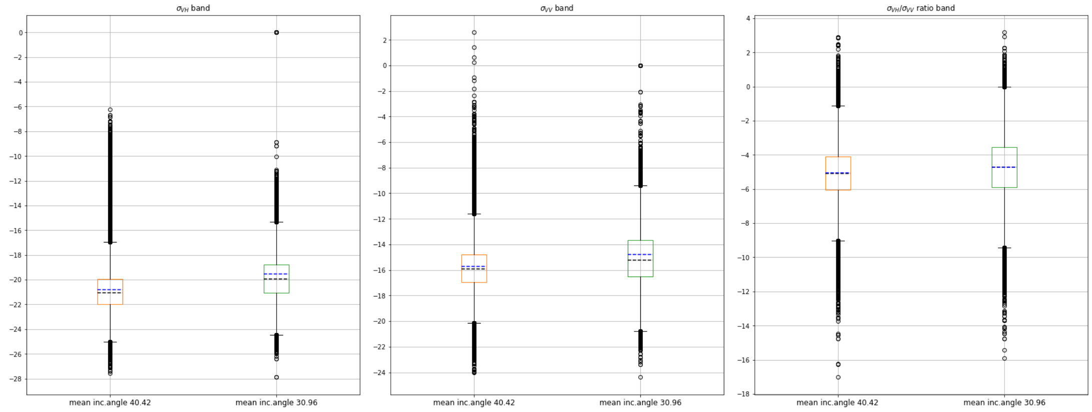

*Figure 1.14:* ***Boxplot of the variation of the radar response of the of soft winter wheat parcels for both mean incidence angles areas, for $\sigma^0_{VH}$, $\sigma^0_{VV}$ and the ratio $\sigma^0_{VH}/\sigma^0_{VV}$ polarizations. The black dashed lines represent the medians and those in blue represent the mean values.***

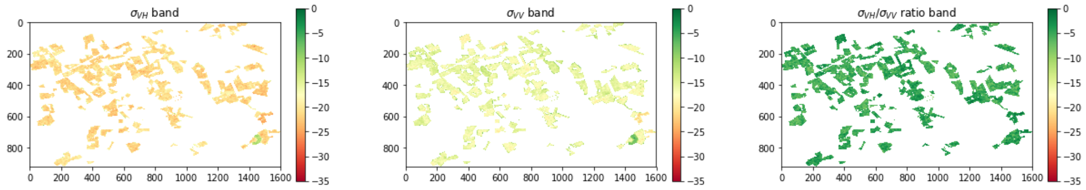

*(a)* ***variation of backscatter in parcels with mean incidence angle of*** $40.42$ ***degrees.***

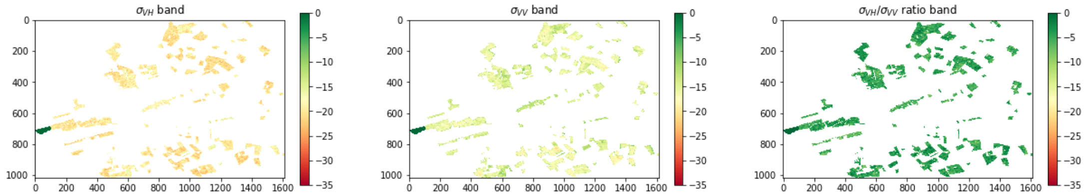

*(b)* ***variation of backscatter in parcels with mean incidence angle of*** $30.96$ ***degrees.***

*Figure 1.13:* ***Soft winter wheat parcels pixels variation of backscatter (in decibels) for the bands $\sigma^0_{VH}$, $\sigma^0_{VV}$ and the ratio $\sigma^0_{VH}/\sigma^0_{VV}$.***

In this case study, it is complex to have more than two areas with the same pedoclimatic conditions and different angles of incidence for a given date. We, therefore, restrict ourselves in this phase of the test plan to two study areas. Therefore, to evaluate whether or not the difference in the means of the two groups with different incidence angles is significant, the parametric Student's t-test is used this time.

This test uses as test statistic the ratio between the difference in the means of the two groups and the standard error of the means difference (equation (1.5)).

$$t = \frac{\bar{x}_1 - \bar{x}_2}{s \cdot \sqrt{\frac{1}{n_1} + \frac{1}{n_2}}} \tag{1.5}$$

Where $s$ is the standard deviation of the backscatter measurements among the two areas with different mean incidence angles (equation 1.6). $s_1$ and $s_2$ are the respective standard deviations

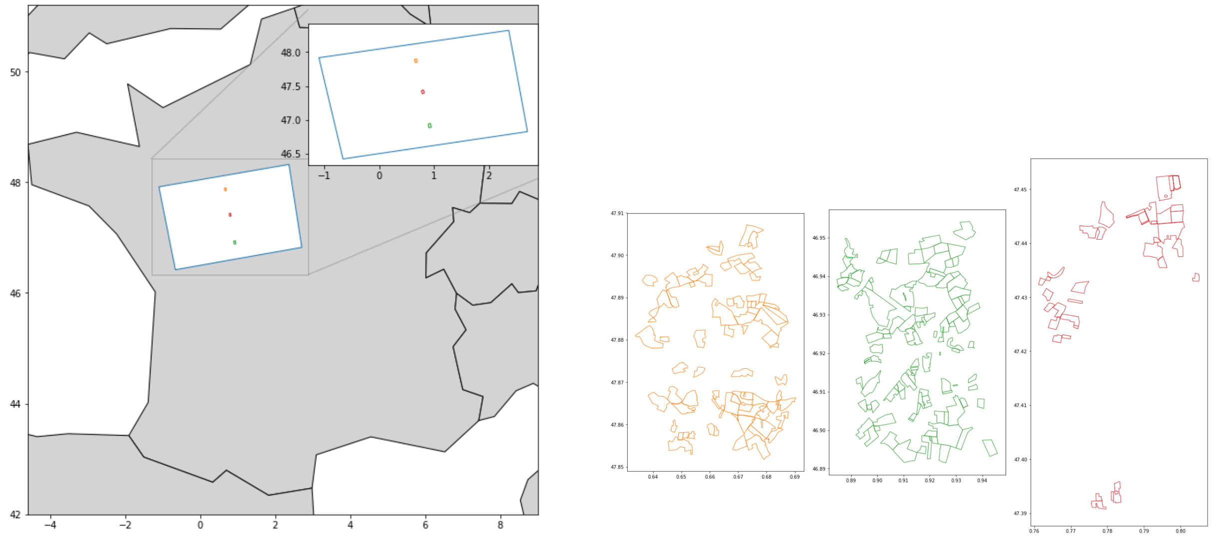

*(a)* *(b)*

**Figure 1.15:** ***Step 1-c of the experimental test plan, location of study areas: (a) geographic coordinate of the used sentinel-1 product(in the blue rectangle) acquired on May 08, 2018 in the center of France. The location of the areas of interest located on the same incidence angles in different pedoclimatic conditions is indicated by the orange, green and red boxes. (b) coordinates and contours of soft winter wheat parcels, automatically extracted from the RPG, using the areas of interest bounding boxes.***

of the samples, of respective sizes $n_1$ and $n_2$, for each incidence angle area.

$$s = \sqrt{\frac{(n_1 - 1) \cdot {s_1}^2 + (n_2 - 1) \cdot {s_2}^2}{n_1 + n_2 - 2}} \tag{1.6}$$

In this step 2.b of the present experimental plan, the Student's t-test results, for each of the three Sentinel-1 radar bands are $(t = 172.16, p - value < \alpha = 0.05)$ for the $\sigma^0_{VH}$ band measurement, $(t = 129.21, p - value < \alpha = 0.05)$ for the $\sigma^0_{VV}$ band and $(t = 70.94, p - value < \alpha = 0.05)$ for the ratio $\sigma^0_{VH}/\sigma^0_{VV}$ band.
This probability being very low, $\mathcal{H}_0$ is rejected, and the differences in the means are therefore considered significant across the three bands when comparing the two studied areas.

### Experimental test plan: Step 1 (c)- Impact of pedoclimate variation under similar incidence angles:

We now aim to study the effect of the variation in pedoclimatic conditions on the radar response of crops. We continue our study on soft winter wheat parcels located in central France. Within a Sentinel-1 product acquired on May 8, 2018, we selected three areas located on the same incidence angles but, this time, sufficiently distanced so that they have the highest possible probability of having different soil and climate conditions. The location of the study areas is detailed in Figure 1.15.

Base on a first analysis of the 1.17 boxplots, we can already observe a quasi-similar behavior of the two bands $\sigma^0_{VH}$ and $\sigma^0_{VV}$ in the three different studied areas. On these same bands,

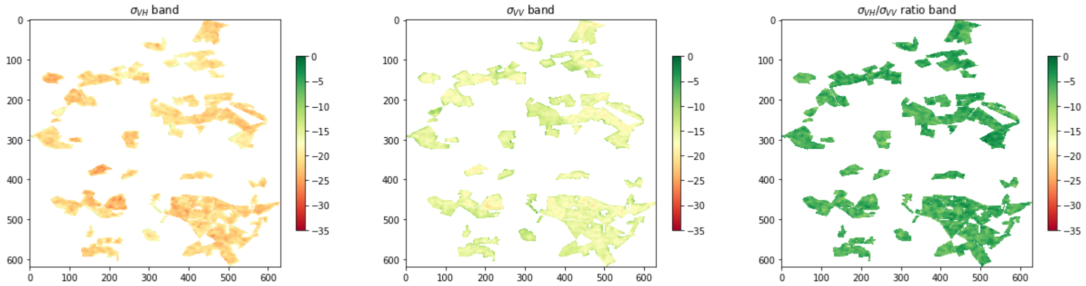

*(a) Variation of backscatter in parcels with mean incidence angle of* $38.8$ *degrees and the first pedoclimatic condition.*

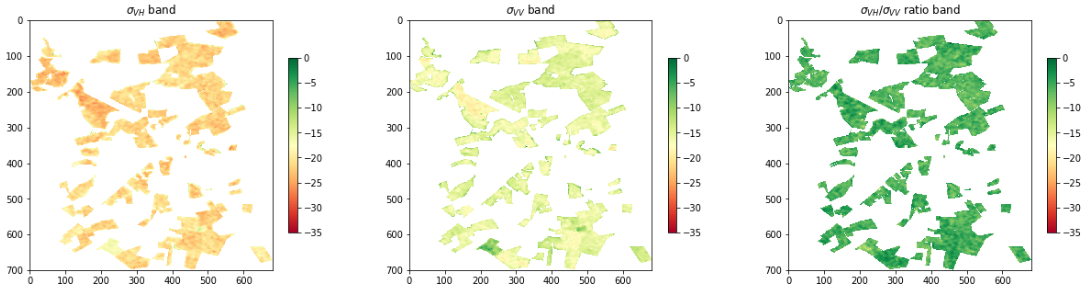

*(b) Variation of backscatter in parcels with mean incidence angle of* $38.8$ *degrees and the second pedoclimatic condition.*

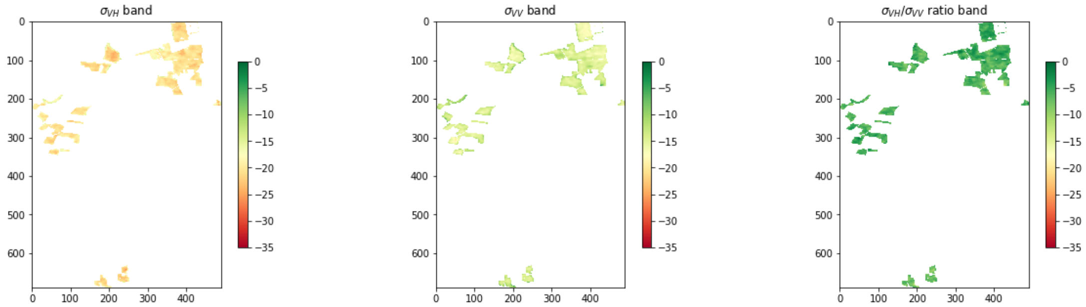

*(c) Variation of backscatter in parcels with a mean incidence angle of* $38.8$ *degrees and third pedoclimatic condition.*

*Figure 1.16: Step 1-c of the experimental test plan: soft winter wheat parcels pixels variation of backscatter (in decibels) for the bands* $\sigma^0_{VH}$, $\sigma^0_{VV}$ *and the ratio* $\sigma^0_{VH}/\sigma^0_{VV}$.

variability in the backscatter distributions can also be observed, which can be significant. Nevertheless, one has the impression that this variability is reduced by the ratio $\sigma^0_{VH}/\sigma^0_{VV}$ band, more particularly on the two green and red areas in the boxplot.

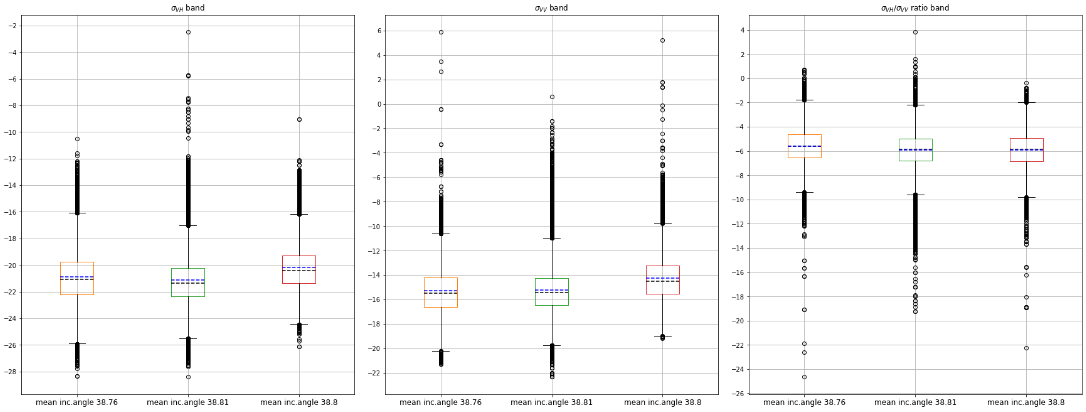

*Figure 1.17:* ***Step 1-c of the experimental test plan: boxplots of the variation in the radar response of the soft winter wheat parcels in areas with different pedoclimatic conditions, for the $\sigma^0_{VH}$, $\sigma^0_{VV}$ and the ratio $\sigma^0_{VH}/\sigma^0_{VV}$ polarizations. The black dashed lines represent the medians and those in blue represent the mean values.***

The results of a more detailed variance analysis with a one-way ANOVA test are presented in table 1.3. The means of the backscatter distributions are significantly heterogeneous, for all three bands ($p - value < \alpha = 0.05$). For each band, the average backscatter differs according to the pedoclimatic conditions, we can therefore conclude that, in our case study, the pedoclimatic conditions have played a role in the way the crop interacted with the Sentinel-1 radar.

*Table 1.3:* ***One-way ANOVA test statistics for three bands $\sigma^0_{VH}$, $\sigma^0_{VV}$ and $\sigma^0_{VH}/\sigma^0_{VV}$, applied to the step (1.c) of the proposed experimental test plan. It is indicated in the table that p-value $< \alpha = 0.05$, but in reality the p-values are far smaller in this study case.***

| | | $\sigma^0_{VH}$ | | | | $\sigma^0_{VV}$ | | | | $\sigma^0_{VH}/\sigma^0_{VV}$ | | | |
|---|---|---|---|---|---|---|---|---|---|---|---|---|---|
| | d.f | sum of squares | mean square | $F_s$ | p-value | sum of squares | mean square | $F_s$ | p-value | sum of squares | mean square | $F_s$ | p-value |
| among groups | 2 | 16911.25 | 8455.63 | 2302.88 | < 0.05 | 19146.41 | 9573.20 | 2510.52 | < 0.05 | 4217.50 | 2108.75 | 1030.57 | < 0.05 |
| within groups | 220318 | 808955.81 | 3.67 | | | 840122.84 | 3.81 | | | 450813.17 | 2.05 | | |
| total | 220320 | | | | | | | | | | | | |

Even with the results of the ANOVA test, we still opted to apply Tukey-Kramer test with the intention of trying to understand, by pair of pedoclimatic areas, which class mean is significantly different from the others. The results are presented in table 1.4. The results of this test are consistent with our first impressions derived from the boxplots 1.17. The differences of the backscatter means are, pair by pair, significantly different for the $\sigma^0_{VH}$ and $\sigma^0_{VV}$ bands

($MD_{i,j} > MSD_{i,j}$), and it is true over the three areas of interest. On the other hand, the results show that for the [pedoclimat2 area - pedoclimat3 area] pair (green and red-colored boxes), the difference in means is not significant for the ratio $\sigma^0_{VH}/\sigma^0_{VV}$ band, which was already revealed by the boxplots 1.17.

***Table 1.4:*** ***Tukey-Kramer test statistics for three bands $\sigma^0_{VH}$, $\sigma^0_{VV}$ and $\sigma^0_{VH}/\sigma^0_{VV}$, applied on the step (1.c) of the proposed experimental test plan. critical $Q_{[\alpha,k,df_w]} = 3.31452$, $\sigma^0_{VH}MS_w = 3.67$, $\sigma^0_{VV}MS_w = 3.81$ and $\sigma^0_{VH}/\sigma^0_{VV}MS_w = 2.05$. We refer to the algorithm 1 for notations.***

| | $\sigma^0_{VH}$ | | | $\sigma^0_{VV}$ | | | $\sigma^0_{VH}/\sigma^0_{VV}$ | | |
|---|---|---|---|---|---|---|---|---|---|
| pair of groups | $MD_{i,j}$ | $MSD_{i,j}$ | reject | $MD_{i,j}$ | $MSD_{i,j}$ | reject | $MD_{i,j}$ | $MSD_{i,j}$ | reject |
| pedoclimat1-pedoclimat2 | 0.2297 | 0.02 | True | 0.0555 | 0.0204 | True | 0.2852 | 0.0149 | True |
| pedoclimat1-pedoclimat3 | 0.7417 | 0.028 | True | 1.0445 | 0.0289 | True | 0.3027 | 0.0211 | True |
| pedoclimat2-pedoclimat3 | 0.9714 | 0.024 | True | 0.989 | .0244 | True | 0.0176 | 0.0178 | **False** |

At this stage, the insights that can be drawn from our study are the following: **the angles of incidence and the pedoclimatic conditions may play a role in the way the imaged target, agricultural areas in our case, interacts with the radar satellite antenna**, as well as the other factors whose impact is already known and which depend on the characteristics of the electromagnetic wave (wavelength or polarisation) or those of the imaged target.

Therefore, when we work with Sentinel-1 radar data in our different models, **we believe that it is necessary, as far as possible, to take into account the incidence angle and pedoclimatic conditions. One way of doing this would be to limit the scope of validity of the developed models to a given pedoclimate, region, or range of incidence angles.**

However, taking into account pedoclimatic conditions seems achievable by limiting the validity range of a given model to a specific region, for example, but it seems less feasible or intuitive in terms of incidence angles because, in the case of Sentinel-1 images, the field of variation of incidence angles within a given product can be relatively large (as seen in 1.1.1 ). Without forgetting the difficulties that the acquisition mode of Sentinel-1 images can generate: typically, when working with time series of images with reduced time steps (less than 12 days for example), or when working on large areas of interest covering a wide range of incidence angles, it can be complex to form the desired time series in such a way that it remains valid over an extensive range of incidence angles.

### Experimental test plan: Step 2- Impact, during the crop growth cycle, of the variation of incidence angles and pedoclimate factors on radar backscatter, for the same crop pixel

In this part of the test plan, by working on a time series of sentinel-1 images covering the main stages of the plant's growth cycle, we aim to study and evaluate how one or all of the investigated factors impact the radar backscatter during key moments of the crop growth cycle. Soft winter wheat is still used as a test crop for consistency with the previous steps of the proposed experimental test.

Contrary to the Step-1 of the above-proposed experimental plan, this analysis will be based on the interpretations of the graphs of radar backscatter evolution during the growth cycle of soft winter wheat, consolidated by graphs of temperature and rainfall data presented in figure 1.18.

*Table 1.5:* ***Sentinel-1 images time series***

| Campaign | SAR Sentinel-1 acquisition dates |
|---|---|
| 2017/2018 | November 09, 21; December 03, 15, 27;<br>January 08, 20; February 01, 13, 25;<br>March 09, 21; April 02, 14, 26;<br>May 08, 20; June 01, 13, 25;<br>July 07, 19, 31. |

The time series of Sentinel-1 images was chosen so that all the images cover the same geographical footprint (the same one we worked on within the Step 1 of our test plan, Fig. 1.6) at each acquisition date, the objective being to remain on the same angle of incidence at each date for each study area, which is very important for carrying out our study. Likewise, each area within a given average angle of incidence is characterized by a given pedoclimate.

We have therefore defined a time step of 12 days for images from the beginning of November to the end of July of the 2017/2018 soft winter wheat crop campaign, this time step guarantees us coverage of the same geographical footprint at each date. Table 1.5 shows the set of images used.

The daily resampled climate data used are derived from ERA5 dataset [Hersbach et al., 2020], which consists of a reanalysis[3] dataset, hourly evaluating the most common weather features on a regular grid with a spatial resolution of $0.25° \times 0.25°$.

The daily surface[4] soil moisture content, one of the main pedological factors affecting vegetation backscattering, is used in this work. the data are obtained from the European Space Agency's Climate Change Initiative for Soil Moisture (ESA CCI SM) project [Gruber et al., 2019, Gruber et al., 2017, Dorigo et al., 2017] with models based on the harmonization and

---

[3] reanalysis technique gives a numerical description of the recent climatic data, produced by combining models with observations

[4] The surface layer is conventionally considered to be within 2 to 5 cm [Ulaby, 1982]

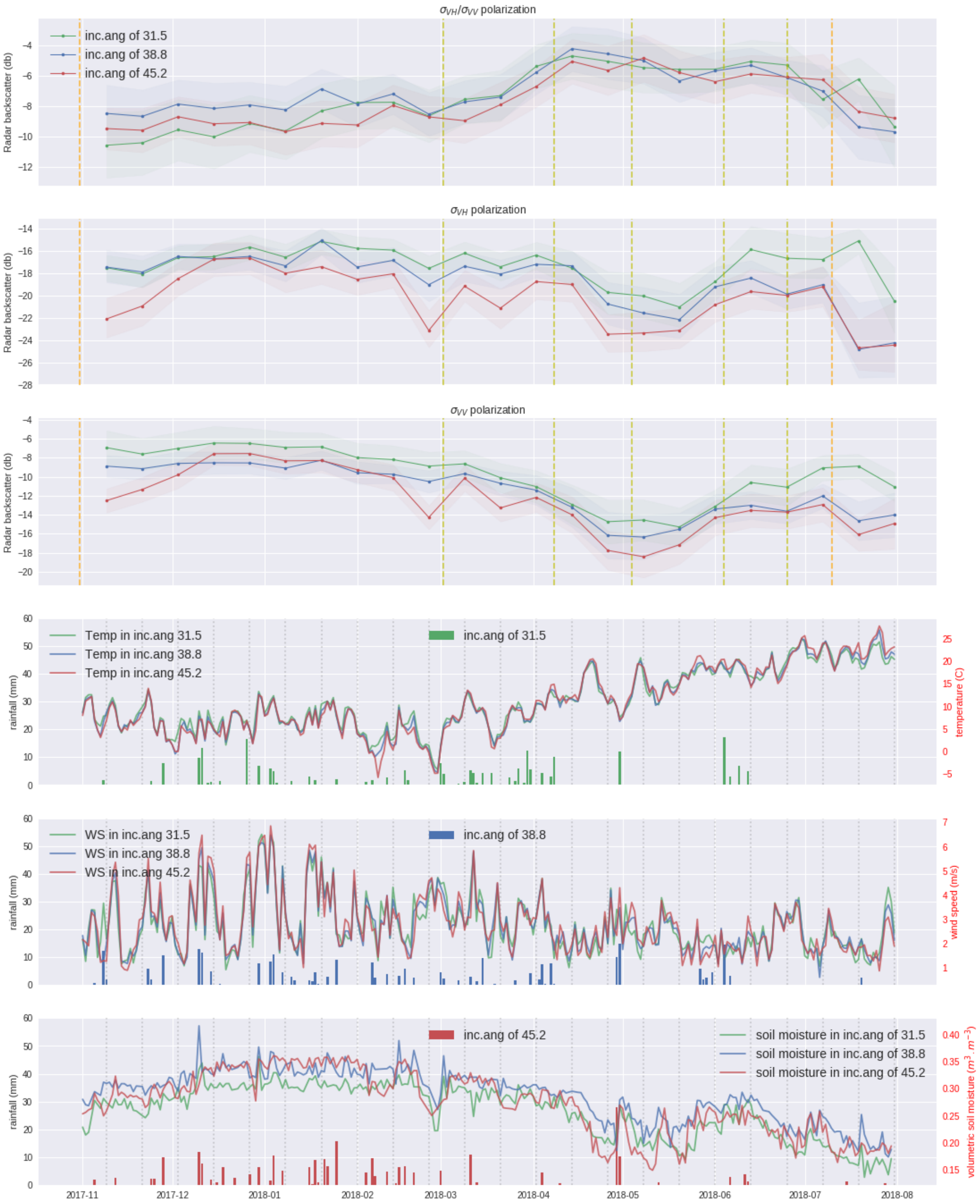

*Figure 1.18:* ***Temporal evolution of the radar signal in the bands $\sigma^0_{VH}/\sigma^0_{VV}$, $\sigma^0_{VH}$ and $\sigma^0_{VV}$, average daily temperature (°C), wind speed $(m \cdot s^{-1})$ at the height of 2 m above the surface, volumetric soil moisture $(m^3.m^{-3})$ at 2 cm depth and precipitation (mm) in the three studied areas, each is characterized by a given angle of incidence and a specific pedoclimate. Approximate periods around the dates of sowing, harvesting, and the main growth stages of wheat from March 2018 (early tillering, stem elongation, second node, flowering and senescence) are indicated respectively by the two orange and yellow vertical dashed lines. The grey dotted vertical lines in the climate data graphs correspond to the acquisition date of the images.***

fusion of soil moisture data retrieved from several satellites with active or passive sensors. These data are sampled on a regular spatial grid of 0.25° (around 25 km) and considered in $m^3.m^{-3}$ volumetric unit.

We can observe similar evolution profiles for all three bands with differences in the magnitude of the backscatter dynamics over the three study areas. We can also see, and in coherence with what was observed in the first part of the elaborated experimental plan, that the differences are reduced by the ratio band compared to the other two bands. Also, it can be noted that these differences remain relatively stable over time.

From the viewpoint of the particular sensitivity of a given band to the interaction between incidence angles/pedoclimate and given the backscatter differences that appear in the graphs, it can be said that the $\sigma^0_{VH}$ band is slightly more sensitive to this interaction compared to the $\sigma^0_{VV}$ band, this is best seen from the early tillering to the second node stages between early March and early May. This is an observation that remains valid for our case study and can in no way be generalized.

The radar signal that the imaged crop returns to the satellite antenna is a composite of the response of the canopy, that of the soil more or less attenuated by the canopy, and finally the response of the crop-soil composite. It appears that the contribution of each of the three elements mentioned above can be driven by the characteristics of the electromagnetic wave: wavelength, polarization, but also the angle of incidence from which the target is imaged ([Ulaby, 1982], [Ferrazzoli et al., 1997]).
Indeed, in a very interesting paper [Blaes et al., 2006] identified some of the most appropriate configurations (in terms of polarization and incidence angles) for monitoring maize by maximizing the sensitivity of the signal to plant growth while reducing the contribution of soil moisture in this signal. Using a discrete radiative transfer model to simulate maize backscatter, they showed that in simple VV and HH polarizations, the sensitivity of the signal to soil moisture is reduced at high incidence angles. Moreover, the configuration that is the least dependent on soil moisture variation throughout the growing season appears to be the HH polarization at high incidence angles. Also, they identified the VV/VH ratio calculated at high incidence angles (about 45 degrees) as the most appropriate index for monitoring maize growth due to its low sensitivity to soil moisture. Finally, the VV/HH index, at low incidence angles, was chosen to detect maize emergence due to its sensitivity at early stages and its low sensitivity to soil moisture variation.
What emerges from this study, carried out on maize (which remains relatively close to wheat) under fixed soil conditions (especially soil moisture), and knowing that in reality, this soil moisture varies throughout the growth cycle of the plant as can be seen on the surface soil moisture evolution plot in figure 1.18, we can realize the importance of choosing the angle of incidence for better monitoring of the crops, by minimizing as much as possible the contribution of soil moisture in the radar signal.

Gradual analysis of radar signals can be carried out to explain/interpret certain behaviors at given time periods.

Rainfall just before a given acquisition date may partially explain an increase, even slight, in the radar signal as reported in [Veloso et al., 2017]. Indeed, this can be seen in our case study, in the $\sigma^0_{VH}$ and $\sigma^0_{VV}$ bands, over the first four acquisition dates (much more pronounced on the red signal corresponding to the area with an angle of incidence of about 45 degrees), this is due to the fact that at this period the plants are in the germination/emergence stages, the effect of soil characteristics (more particularly roughness and water content) is dominant in the response of the imaged targets.

Both the $\sigma^0_{VH}$ and $\sigma^0_{VV}$ bands recorded a brutal drop in backscatter on the acquisition date corresponding to 25 February 2018, which is typical behavior for a frozen episode release according to the literature as in [Veloso et al., 2017] and [Khaldoune et al., 2011]. This observation is valid for all three areas, but with varying magnitudes. In fact, this drop is clearly more marked in the region with an angle of incidence of 45 degrees, because the frozen episode was stronger in this region compared to the other two regions (difference of around 5 °C) according to the temperature curve around 10 February 2018.
However, even though the same frost event occurred again around February 28, with almost the same temperature and over all three studied areas this time, there was no such abrupt drop in the radar signal, but just a much smaller drop which is seen on the acquisition date of March 21, 2018 (visible especially in the signal of the region with an angle of incidence of 45 degrees in red color).

Several assumptions may justify a different time behavior of the radar response after a period of frost, one of the possibilities is that the impact of a frost episode becomes less important at a more advanced stage of growth where the structure/volume of the plant has evolved (we move from the early tillering stage to the ear at 1cm stage in our case study). Another is that an additional factor (climatic or otherwise) is involved in addition to frost in producing such a severe signal drop. For example, on the graphs of the climatic data in figure 1.18 above, we can see that the wind was stronger at the time of the second frost episode compared to the first one, which may impact the orientation at the canopy level. We can also see a strong decrease in relative humidity just before the second frost episode as opposed to the first one. This remains suppositions because studying in detail what guides the dynamics of backscatter is not a simple task. We will try to provide more detail in the remainder of this document.

Moreover, It can be seen that, unlike the two $\sigma^0_{VH}$ and $\sigma^0_{VV}$ bands with trajectories that are somewhat unstable and complex to interpret, the ratio band reproduces the wheat growth cycle well, with a relatively stable phase corresponding to the period between sowing and the start of tillering (early March), then a slight increase from the latter to flowering, before starting to decrease gradually, characterizing the start of senescence around mid-June.

Finally, as a recap synthesis, we feel that the following conclusions can be drawn from this part of our work:

- With the perspective of developing machine learning models, notably for crop type recognition, using S1 radar imagery data, we proposed an experimental scheme with the primary objective of identifying the extent of validity of these models depending on some factors of variation of the radar response that we deemed most influential: incidence angle and pedoclimate. Statistical tests of variance revealed that, for the most optimal results, the field of validity of a model built based on S1 data should, as far as possible, be limited to a given region with a given pedoclimate and/or range of incidence angles.
- Also, based on state-of-the-art elements, we have seen what may drive the dynamics of radar backscatter in interaction with vegetation. We have drawn up interpretations of certain behaviors of the radar signal when confronted with rainfall or frost episodes. This study has also allowed us to see the added value that the ratio polarization can provide to our developed machine learning models using this type of imaging data, which can constitute an interesting additional feature.

# Chapter 2

# Crop type identification with deep learning using multi-temporal satellite images

## 2.1 Research problem introduction

Identifying crops from remote sensing images can help automatic land cover monitoring and serve several purposes. For example, it can be used for the large-scale estimation of the overall area of a given planted crop. The potential benefits are numerous, first in terms of yield prediction, with a better knowledge of the planted areas. The anticipated evaluation of agricultural yields is a major challenge in agriculture: in a production basin, to forecast the logistics of farming and grain storage; at the level of a country, to anticipate agricultural crises or even food crises in the poorest countries. Better anticipation is also essential for insurers or players in agricultural raw material markets. The monitoring of cropland use gives also another interesting perspective from the point of view of sustainability: the intensification of agricultural productions and disrespect of the principle of crop rotation in some areas can be threatening for agricultural ecosystems, and better monitoring could help to control agricultural practices, as underlined in the introduction of this manuscript.

Every plant type has a growth dynamics characterized by different phenological stages from emergence to maturity. During these successive development steps, plants change their reflective spectral properties [Thenkabail et al., 2000], which can be observed using remote sensing, and more precisely with backscattering in the case of radar. This dynamics can be thought of as a specific signature of the crop, as illustrated in Fig. 2.1, and can thus be used to identify crop types.

Fig. 2.2 represents a composite of both VV and VH polarizations of a Sentinel-1 product acquired at different observation times in South Dakota (USA) and illustrates the evolution of crop spectral properties in different parcels during plant growth cycle.

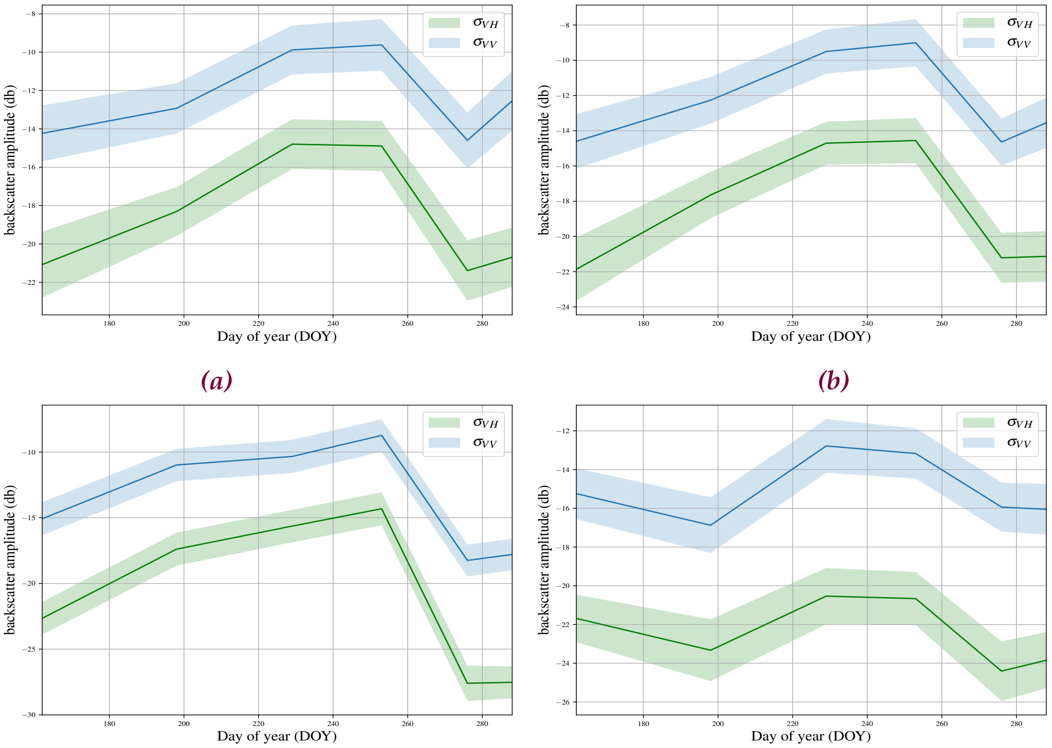

*(a)* *(b)*

*(c)* *(d)*

*Figure 2.1:* ***Evolution of the means (plus or minus one standard deviation) of radar dual polarization backscatters $\sigma^0_{VV}$ and $\sigma^0_{VH}$, from June 11, 2016 to October 15, 2016, in two parcels of corn (a) and (b), a parcel of soybean (c), and a parcel of spring wheat (d) in South Dakota, USA. It can be observed that the two parcels of corn share comparable profiles of backscatter dynamics while differing significantly from those of soybean and even more spring wheat.***

In this section, we propose an approach allowing the identification of major crop types by satellite imagery. In a pixel-based system, the temporal evolution of the radar signal is used to identify the type of crop covering this pixel. These dynamics will be compared to the specific signatures characterizing each crop type, illustrated in figure 2.1 for some crops and learned by machine learning models. For this purpose, we used the long short-term memory (LSTM) Recurrent Neural Networks (RNNs), well adapted to the modeling of time series data, and Convolutional Neural Networks (CNNs), widely used to process imagery data and for which we propose a pixel transformation allowing to consider both temporal and spectral dimensions of satellite images.

We have evaluated the proposed approach in two situations:

- Intra-annual crop recognition, in which we extrapolate, within the same agricultural season, a model trained from a limited number of pixels to the whole area of interest. Concretely, knowing the crops in a subset of parcels in a production basin, for a given agricultural season, we aim at determining the crop type coverage of the remaining parcels in the production basin, for the same season.
- Inter-annual crop recognition, dictated by the difficulties of obtaining training data at

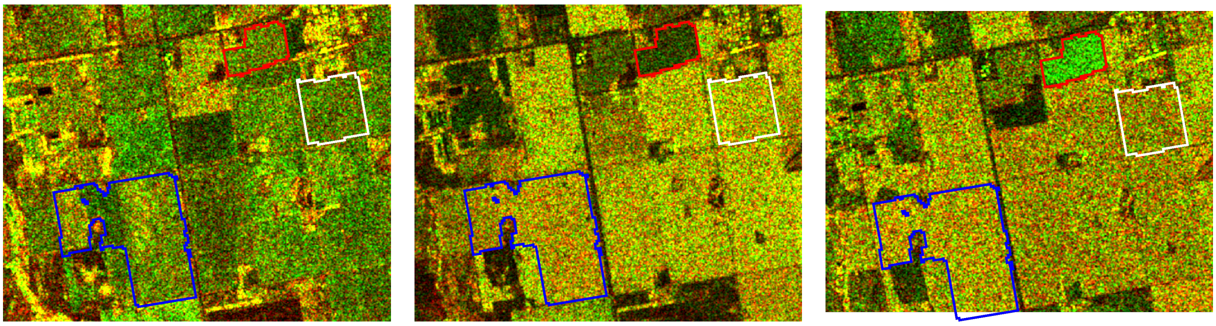

*(a) June 11, 2016* *(b) July 17, 2016* *(c) August 17, 2016*

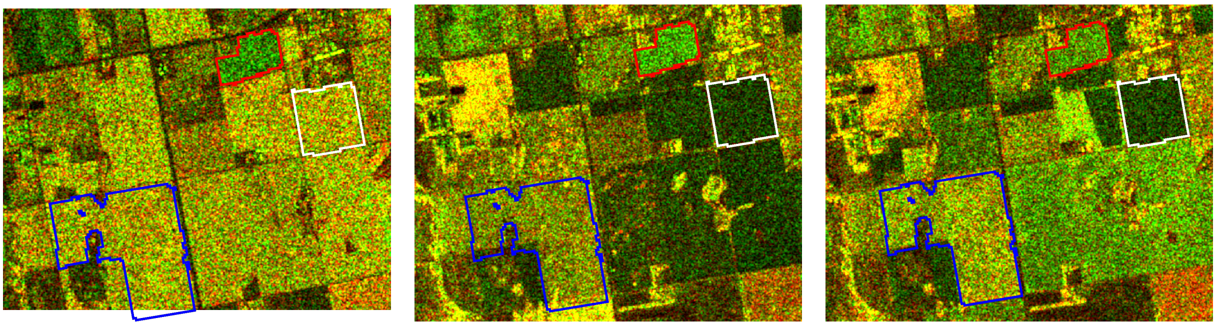

*(d) September 10, 2016* *(e) October 03, 2016* *(f) October 15, 2016*

***Figure 2.2:* Sentinel-1 images combining $\sigma^0_{VV}$ and $\sigma^0_{VH}$ polarizations, acquired at six observation times covering parts of both Jerauld and Sanborne counties in U.S. South Dakota state. For illustration purposes, we delineate some specific fields: one corn parcel in blue, one soybean parcel in white, and one spring wheat parcel in red. We can clearly observe color changes in these reference parcels at different dates, which illustrates the variation in the radar response of imaged targets due to the phenological development of plants.**

> the beginning of each agricultural season. We want a model to predict an evaluation of crop rotation without having to manually label and/or request a set of parcels from agricultural partners at the beginning of each season. In other words, we want to calibrate the model from historical data of previous crop campaigns and extrapolate to new crop seasons. In this inter-annual recognition approach, we proposed a new approach integrating the phenological development of plants through the concept of thermal time. Thermal time allows to compensate and readjust the potential discrepancies in the radar signatures due to intra-annual variability related to different factors such as pedoclimate, plant characteristics such as frost episodes resistance, and crop practices.

We will use data sets from two different locations to test the proposed approaches. The first one is located in the United States, for which a national database of crop rotation is available with agricultural campaigns that can go back two years (if $n$ is the current season, years $n-1$ and $n-2$ are available). The second data set, more consequent and on which more experiments will be done, is located in France. For this second data set, a database of the crop rotation of the previous campaigns is available, with a 2 years delay (if $n$ is the current season, years up to $n-2$ are available).

With these data sets, we will principally try to answer the following questions: How to formalize mathematically the training and inference problems in the proposed supervised approach? How is the satellite image time series transformed for an alignment according to thermal times instead of an alignment on image acquisition calendar times? And how, for both intra- and inter-annual situations, these satellite image time series and the land cover training data can serve as inputs to both LSTM and CNN models?.

## 2.2 First study areas and data sets

The first data sets for which we opted at the beginning of our work were in the United States. Such a choice was mainly dictated by the availability of cropland cover databases corresponding to the dates of availability of the radar (Sentinel-1) and optical (Sentinel-2, Landsat-8) images.

In fact, the cropland cover data required for the training of our supervised learning models are widely available from the US Cropland Data Layers (CDL) database of the National Agricultural Statistics Service (NASS) of the US Department of Agriculture (USDA) through the web service called CropScape. Data up to year $n-1$ are provided with a spatial resolution of 30 meters, $n$ being the current year.
These data are generated from classification models [Han et al., 2012] using satellite imagery from the Advanced Wide Field Sensor (AWiFS) and LandsatTM 5 and ETM+ 7. For the ground truth data, multiple data sources are used: USDA agricultural programs with experimental parcels reporting crop types and crop management, information from the annual NASS surveys (more precisely the June Agricultural Survey - JAS data), and the U.S. Geological Survey's National Land Cover Data-sets (NLCD). The latter is based on Landsat with a spatial resolution of 30 meters and provides descriptive data for land surface characteristics such as thematic class (e.g. urban, agricultural and forest) and percentage of forest cover.
Fig.2.3 shows an example of a CDL raster in the U.S. Midwest, commonly known as the ”Corn Belt”, a region in which corn is the prevalent crop, and this is precisely the crop with which we decided to start our work (a sort of pilot crop), the idea being to become familiar with satellite imagery while starting to develop our models.

On the other hand, and knowing that the first Sentinel-1 (resp. Sentinel-2 and Landsat-8) acquisitions started from year 2015 (a few years before for Landsat-8 but with a less interesting spatial resolution and repeating cycle compared to Sentinel products), the CDL database was, to our knowledge, the only massive and freely accessible database allowing at least two years of cropland cover data. The French Registre Parcellaire Graphique (RPG) data already mentioned in Section 1.1.2, and that will be described in more detail later in this document (which will serve as the main basis for our learning data) has, unlike the CDL, a latency of two years (data up to year $n-2$ available in year $n$).

The first U.S. area of interest which is denoted by $U.S.A_1$ covers parts of both Jerauld and Sanborne counties in South Dakota, spreading over a surface of 14000 hectares.

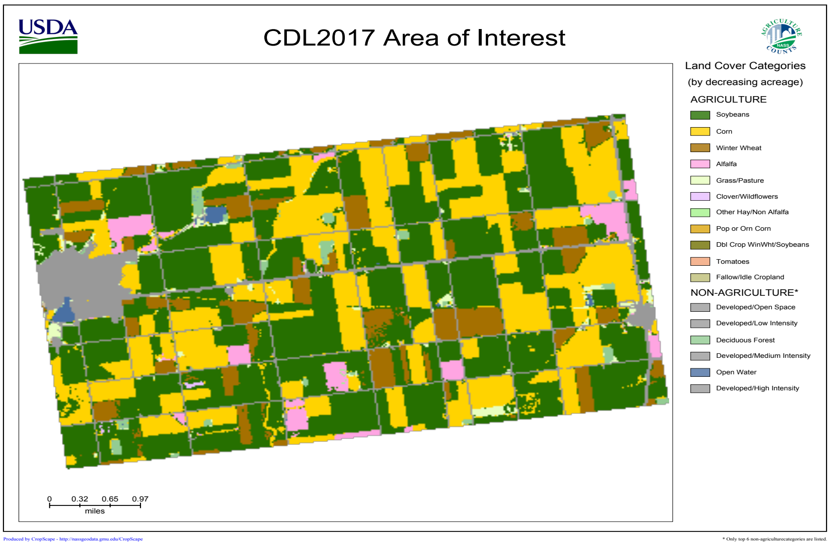

Produced by CropScape - http://nassgeodata.gmu.edu/CropScape

* Only top 6 non-agriculturecategories are listed.

*Figure 2.3:* ***Preview example of crop type information (as well as other land cover classes) in an area of interest in the U.S. Corn Belt. The data was produced thanks to the CropScape web service.***

We worked with all the exploitable Sentinel-1 images acquired in 2015, 2016, and 2017 and covering $U.S.A_1$ during a large part of the corn growth cycle (from June to the end of October/beginning of November) as reported in Table 2.1.

## 2.3 Methodology

### 2.3.1 Mathematical representation of the training data

Let $k$, $1 \leq k \leq N$, represent the index of the scenario under investigation (a scenario corresponding in our case to a cropping season and a location as introduced by [Kang et al., 2011]. For example, if we work in a single geographic region, over three different years, the total number of scenarios $N$ is then equal to 3.

*Table 2.1:* ***Sentinel-1 acquisition dates in the $A_1$ area of interest***

| Area of interest | Year | Sentinel-1 acquisition dates |
|---|---|---|
| test area $A_1$ | 2015 | June 05, 12, 24; July 23, 30; August 11, 16, 23; September 04, 09, 16, 21; October 03, 27. |
| | 2016 | June 06, 11, 30; July 05, 17, 24, 29; August 05, 10, 17, 22, 29; September 03, 10, 15, 22, 28; October 03, 10, 15, 22, 27. |
| | 2017 | June 07, 12, 24; July 01, 06, 30; August 06, 18, 23; September 04, 11, 16; October 05, 10, 17, 22, 29. |

Let $\left(t_o^k\right)$, $1 \leq o \leq \mathcal{T}_k$, be the observation times for scenario $k$ and $\mathcal{T}_k$ the total number of observation times for scenario $k$.
For each scenario, the area of interest is characterized at time step $t_o^k$ by the observation vector $(x_1^k(t_o^k), \ldots, x_{m_k}^k(t_o^k))$, where $m_k$ is the number of pixels in the corresponding zone, and $x_i^k(t_o^k) \in \prod_{j=1}^{p}[a_j, b_j]$, where $1 \leq i \leq m_k$, $p$ is the number of spectral bands of the satellite and $[a_j; b_j]$ is the range of variation of each band.

We note that in the case of optical satellite data, values of reflectance vary between $a_j = 0$ and $b_j = 1$. In the case of Sentinel-1 SAR data which contains dual polarization backscatter $\sigma_{VV}^0$ and $\sigma_{VH}^0$, the number of bands is thus $p = 2$ ($p = 3$ if one adds the ratio band $\sigma_{VH}^0/\sigma_{VV}^0$). For this kind of data, to estimate the backscatter range of variations is less intuitive, values of both $VV$ and $VH$ polarizations do not have the same magnitude, it depends on the crop type and more generally, on the target of radar satellite.
We will denote in what follows $\Omega_r = [a_{VV}; b_{VV}] \times [a_{VH}; b_{VH}] \times [a_{VH/VV}; b_{VH/VV}]$, the 3-dimensional space corresponding to the ranges of variation of the dual-polarization and the ratio radar data.

Let $X_i^k = (x_i^k(t_1^k), \ldots, x_i^k(t_{\mathcal{T}_k}^k)) \in \mathcal{X}_k$ with $\mathcal{X}_k = \Omega_r^{\mathcal{T}_k}$. To each $X_i^k$ is associated a ground truth data output $Y_i^k \in \mathcal{Y}$, $\mathcal{Y} = \{0, \ldots, q\} \subset \mathbb{N}$, $q$ is the number of crops to classify, with therefore $q + 1$ classes, 0 corresponding to none of the $q$ crops. For the particular case of a binary model (for example only identifying all corn crops), $q = 1$, and we take $Y_i^k = 1$ for the crop of interest and $0$ otherwise.

$(X_i^k, Y_i^k)_{1 \leq i \leq m_k}$ form the training data set for scenario $k$ and we define the prediction function $f$ as follows :

$$
\begin{aligned}
f \colon \mathcal{X}_k &\to \mathcal{Y} \\
X_i^k &\mapsto \widehat{Y}_i
\end{aligned}
$$

### 2.3.2 Use of the Thermal Time

A key point of our methodology is that we do not align the sequential data of the different data sets (corresponding to the different scenarios) according to the calendar time, but according to the thermal time.
Indeed, there is a difficulty to generalize from one scenario to another, if we choose the calendar time as the reference to make coincide the different data sets (coming from different scenarios). We explain this difficulty by the variability of temperature dynamics across seasons and locations, while it is the main driver of plant development [Ritchie and Nesmith, 2015]: two similar dates can thus represent very different development stages for crops.

The temperature variation during crop development can be measured by a widely used concept: thermal time. In its simplest formulation, it is expressed in growing degree-days (GDD) and corresponds to the accumulated daily temperature since emergence above a threshold temperature (see for example a detailed calculation for sugar beet in [Lemaire et al., 2009] or for rapeseed in [Jullien et al., 2011]).

Even if the scientific literature suggests taking emergence day as a starting day for the calculation of the accumulated daily temperature [McMaster and Wilhelm, 1997], the sowing date is used instead for thermal time initialization, since this information is most likely to be available in agricultural statistics compared to the emergence date which is not usually available. Except for extraordinary conditions (mainly cultural practices and pedoclimatic conditions affect the time between sowing and emergence), the impact of such an approximation is thought to be minimal, since, in normal conditions, the time span between planting and emergence is relatively short (about 30-90 accumulated GDD (in degrees Celsius) [Angel et al., 2017] for corn, which corresponds to 5-15 days).
Nevertheless, it is necessary to keep in mind this approximation since the satellite signal is affected by crop growth only after emergence, and the potential differences between sowing and emergence in different scenarios (location × year, as described in Section 2.3.1) will affect the whole growth dynamic.

In this document, we rely on the most commonly corn GDD evaluation method explained in [McMaster and Wilhelm, 1997] where it is considered that GDDs are only accumulated when daily temperature condition are optimal for corn development (between $10°C$ and $30°C$, from [Cross and Zuber, 1972]). Daily thermal time accumulation on day $t$ is thus given by:

$$\Delta_{TT}(t) = \max\left[\min\left(\frac{T_{Max}(t) + T_{Min}(t)}{2}; 30\right) - 10; 0\right] \tag{2.1}$$

where $T_{Max}(t)$ and $T_{Min}(t)$ are the daily maximum and minimum air temperatures on day $t$.

The thermal time on day $t$ is simply the accumulation of $GDD$ since planting date:

$$TT(t) = \sum_{i=1}^{t} \Delta_{TT}(i),$$

where day 1 corresponding to the planting date.

In [Angel et al., 2017, Cross and Zuber, 1972, Abendroth et al., 2011], field studies were carried out to evaluate the relationship between accumulated daily temperature and corn development stage. [Angel et al., 2017] underlines the two most important stages in corn growth development: Silking (also called R1) when flowering begins (a stage very sensitive to extreme values of temperature), and Maturity (R6) when kernel moisture is relatively high and no more water or nutrient input is needed. We refer to [Angel et al., 2017] to estimate the values of accumulated GDD for Silking and Maturity stages of corn in our studied experimental areas.

Temperature data are obtained from the US National Oceanic and Atmospheric Administration (NOAA). Corn planting dates in the studied areas are estimated thanks to data from the Risk Management Agency of the U.S. Department of Agriculture (USDA).

Fig. 2.4 shows the evolution of thermal time as a function of calendar time (Day of Year (DOY)) for corn over three years, 2015 and 2016 in studied test area $A_1$ and 2017 in studied test area $A_2$. Estimation of temperature accumulation for two important corn development stages, Silking (R1 stage) and Maturity (R6 stage), are represented by red and black dotted lines respectively

[Angel et al., 2017]. These curves illustrate that for different years and/or different locations, reference phenological development stages are reached on very different days, for the same crop.

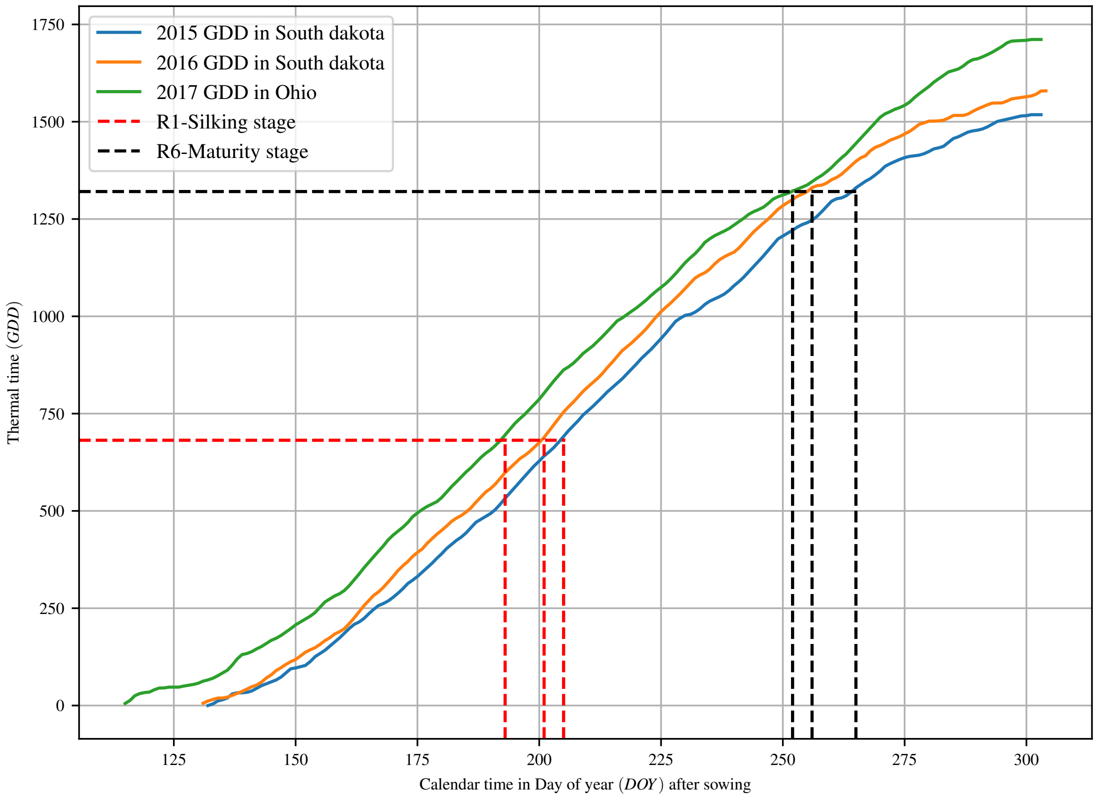

***Figure 2.4:*** ***Evolution of corn thermal time (growing degree day (GDD)) according to calendar time (Day of Year (DOY)) with*** $T_{Base} = 10°C$ ***and*** $T_{Treshold} = 30°C$ ***in three years,*** $2015$ ***and*** $2016$ ***in South Dakota and*** $2017$ ***in Ohio. Corn estimated temperature accumulation of Silking and Maturity stages are represented by red and black dotted lines, respectively.***

We thus map the sequence of data $X_i^k = (x_i^k(t_1^k), \dots, x_i^k(t_{\mathcal{T}_k}^k)) \in \mathcal{X}^k$ onto a sequence defined for periods of constant GDD. This constant thermal time step will be denoted by $\alpha$.

For scenario $k$, $TT_k(t_{\mathcal{T}_k}^k)$ corresponds to the final thermal time of acquisition, and the number of periods for scenario $k$ is thus given by $N_k = \lceil TT_k(t_{\mathcal{T}_k})/\alpha \rceil$.

Formally, we define the mapping from the calendar time sequence to the thermal time sequence as follows:

First, $\forall o, 1 \leq o \leq \mathcal{T}_k$, we define $\psi_k(o)$ such that $\psi_k(o)$ represents the index of the defined thermal time periods in which fall the observation at time $t_o^k$.

Using this correspondence, we can now define a map $\Psi_k$ from $\mathcal{X}_k = \Omega_r^{\mathcal{T}_k}$ into $\tilde{\mathcal{X}}_k = \Omega_r^{N_k}$ which to $X_i^k = (x_i^k(t_1^k), \dots, x_i^k(t_{\mathcal{T}_k})) \in \mathcal{X}_k$ maps $\tilde{X}_i^k \in \tilde{\mathcal{X}}_k$ as follows: $\forall j, 1 \leq j \leq N_k$, the $j$-th component of $\tilde{X}_i^k$ denoted $\left[\tilde{X}_i^k\right]_j$ is given by:

$$\left[\tilde{X}_i^k\right]_j = \begin{cases} x_i^k(t_l^k) \text{ if there exists } l \text{ such that } \psi_k(l) = j \\ \\ 0 \text{ otherwise} \end{cases}$$

In what follows, the zeros will be handled as missing data. Observation vectors can also be interpolated instead of having null missing data.
Furthermore, if it happens that $\phi_k(l_1) = \phi_k(l_2) = j$ for $l_1 \neq l_2$, then the average of the values $x_i(t_{l_1}^k)$ and $x_i(t_{l_2}^k)$ will be chosen, and similarly for more indices.

Note that for the example of corn, the thermal time between sowing and maturity exceeds 1000 GDD. The choice of the value of $\alpha$ can be adapted according to the difference in thermal time between image acquisitions.

For each scenario $k$, our training data are now given by $(\tilde{X}_i^k, Y_i^k)_{1 \leq i \leq m_k}$ and we define the prediction function $\tilde{f}$ as follows:

$$\begin{aligned} \tilde{f} \colon \tilde{\mathcal{X}}_k &\to \mathcal{Y} \\ \tilde{X}_i^k &\mapsto \widehat{Y}_i \end{aligned}$$

The approach we have already proposed and described aims to align a time series of satellite images with dates chosen "à priori" on a thermal time grid by calculating the thermal times corresponding to each date in the time series.
Such an approach can be seen from another angle by taking the opposite procedure as follows: for a given crop, the most important phenological growth stages are fixed, the thermal times corresponding to each phenological stage are then calculated (for this, we can refer to the scientific literature), which will generate a time series of thermal times, then the satellite images that coincide with the dates of each thermal time are identified and collected.
This latter approach, in which the temporality is guided by the plant's growth stages, allows for more implementation comfort and shorter time series, and in the same manner as above, the training data can be mathematically formulated as follows:

for a given crop type $c$, $TT_c(p)$, $1 \leq p \leq \mathcal{P}$ where $\mathcal{P}$ is the number of phenological stages maintained for the crop $c$, represents the thermal time that the plant is expected to reach at growth stage $p$.

Under scenario $k$, $(d^k(TT_c(1)), \ldots, (d^k(TT_c(\mathcal{P})))$ represents the vector of the calendar dates corresponding to the thermal time series formed by the sequence of $TT_c(p)$.

The $j$-th component of the resulting observation time series can then be defined by $\left[X'^k_i\right]_j$ with $1 \leq j \leq \mathcal{P}$ and $1 \leq i \leq m_k$, where:

$$\left[X'^k_i\right]_j = x_i^k(d^k(TT_c(j))),$$

or when not available, by finding $t_{l_j}^k$ as close as possible to $d^k(TT_c(j))$.

### 2.3.3 Supervised deep learning models: Neural Networks

A neural network (NN) is a powerful type of model $f$ of the form $f : \mathbb{R}^{dim_x} \rightarrow \mathbb{R}^{dim_{\widehat{y}}}$ such that $\widehat{y} = f(x, \theta)$ where $x \in \mathbb{R}^{dim_x}$ and $\widehat{y} \in \mathbb{R}^{dim_{\widehat{y}}}$ are input and output vectors, respectively. For a dataset of input-output couples $(x_i, y_i)_i$, training an NN corresponds to adjusting parameters $\theta$ such that $f$ be the best approximation of $E(Y|X)$, where $(X, Y)$ is the random vector corresponding to the input-output couple.

We briefly describe below the basic concepts underlying modeling by NNs, an in-depth comprehensive presentation can be found for example in [Goodfellow et al., 2016].

The most fundamental form of neural networks are Multilayer Perceptrons (MLPs), they are formed by a sequence of hidden layers connecting an input layer to an output layer.
Each layer $l$ is characterized by the number of neurons that we denote $n_l$, nonlinear activation function $f_l : \mathbb{R}^{n_l} \rightarrow \mathbb{R}^{n_l}$, and parameters $\theta_l = (W_l, b_l)$, where $W_l \in \mathbb{R}^{n_{l-1} \times n_l}$, $b_l \in \mathbb{R}^{n_l}$ are the weight matrix and bias vector respectively.

Input information propagates through these hidden layers (where the output of one layer represents the input of the next hidden or output layer) by activation of an affine transformation as follows :

$$h_l = f_l(W_l.h_{l-1} + b_l) \tag{2.2}$$

where $h_{l-1}$ is the output vector from the previous layer $l-1$, this process is called forward propagation. The difference between the predicted output $\widehat{y}$ and the real output $y$ is quantified through a loss function $\mathcal{L}$ which will be minimized by optimization algorithms like stochastic gradient descent algorithms, with gradients of the loss function computed by back-propagation [Ruder, 2017].

A particular architecture of neural networks, the Recurrent Neural Networks (RNNs), are adapted to the modelling of time series data. They were introduced in [Rumelhart et al., 1986] and different variants have been proposed such as for example [Elman, 1990].

In RNNs, a time dimension is added to the layer of classical NNs, the network parameters will then be expressed by $\theta_l = (W_l, \bar{W}_l, b_l)$ where $\bar{W}_l \in \mathbb{R}^{n_l \times n_l}$ is the weight matrix connecting the temporal sequences, known as the recurrent weights. Information propagates through hidden layers as follows: $h_l(t) = f_l(W_l.h_{l-1}(t) + \bar{W}_l.h_l(t-1) + b_l)$, where $h_l(t)$ is the output of layer $l$ at observation time $t$ (e.g. in the case of a network with a single hidden layer, $h_{l-1}(t)$ will be $x(t)$). This process is applied recursively incrementally with $t, 1 \leq t \leq \mathcal{T}$ with the same weights at each time step. More details on RNNs can be found in [Graves, 2012].

Such an architecture is well adapted for a multi-temporal sequence of satellite images, the use of information at the previous observation time $t-1$, in addition to the one at $t$ allows us to better take into account the variation in the reflective spectral properties of the crop during its growth cycle.

### 2.3.4 Long Short-Term Memory network

A particular architecture of RNNs known as Long Short Term Memory network (LSTM), introduced by Hochreiter and Schmidhuber [Hochreiter and Schmidhuber, 1997], has shown its effectiveness in learning long-term dependencies compared to classical RNNs.
An LSTM block, showed in Fig. 2.5, replaces the classical RNN unit: a simple nonlinear activation is applied to the affine transformation of inputs. It has a more complex but efficient system to propagate information, and moreover largely solves the issues of vanishing and exploding gradients, as detailed in [Hochreiter et al., 2001] and [Bengio et al., 1994].

Our models will rely on the variant called the standard extended LSTM ([Gers, 2001]), an improved version of the LSTM networks in their initial form, which had only two weighted gates, input gate, and output gate. Indeed, two major modifications have been added to the basic LSTM networks, as explained and evaluated in [Gers et al., 2000] and [Gers et al., 2002]: a forget gate allows an updating of the cells by forgetting previous information, and weighted connections from the cells to the different gates of an LSTM block, called ”peephole connections”, are designed to allow all gates to inspect current cell state, even in the case where the output gates are closed (which means that the output activation is close to zero).

This standard extended form seems to be a good compromise between relative simplicity and efficiency and has given good results in different applications, such as for learning context free languages ([Gers and Schmidhuber, 2001]), handwriting recognition (as in [Graves et al., 2007]), speech recognition ([Graves et al., 2013]), or also more recent applications in sequence-to-sequence models to generate captions for videos ([Venugopalan et al., 2015]) and images generation ([Gregor et al., 2015]).

The key idea in an LSTM memory block is the memory cell, whose activation is called the cell state $c_t$, acting as a memory of relevant information and allowing it to persist as long as possible (hence the ”long term memory” name): they prevent error signals from degrading quickly because they ”propagate over time”.
The flow of information in this block is controlled through sigmoid gating as follows: in layer $l$ and at time $t$, cell state $c_t^l$ is updated by adding the **forget gate** $f_t$ multiplied by the cell state at previous time $c_{t-1}^l$ and an external **input gate** $i_t$ multiplied by the non-linearly activated (generally by $tanh$) new candidate information $\widetilde{c}_t^l$. The output $h_t^l$ of the LSTM block will be non-linearly activated, usually by $tanh(c_t^l)$ and controlled by an additional **output gate** $o_t$.

Note that for reasons of clarity, the observation vector of the scenario $k$ which was denoted by $(x_1^k(t_o^k), \ldots, x_{m_k}^k(t_o^k))$ in 2.3.1, will be simplified to $x_t$ and in the same way, $\mathcal{T}_k$ will be simplified into $\mathcal{T}$. The operating process of a single-cell LSTM with one hidden layer is then detailed by the following equations, recursively applied while incrementing $t, 1 \leq t \leq \mathcal{T}$:

(2.3)

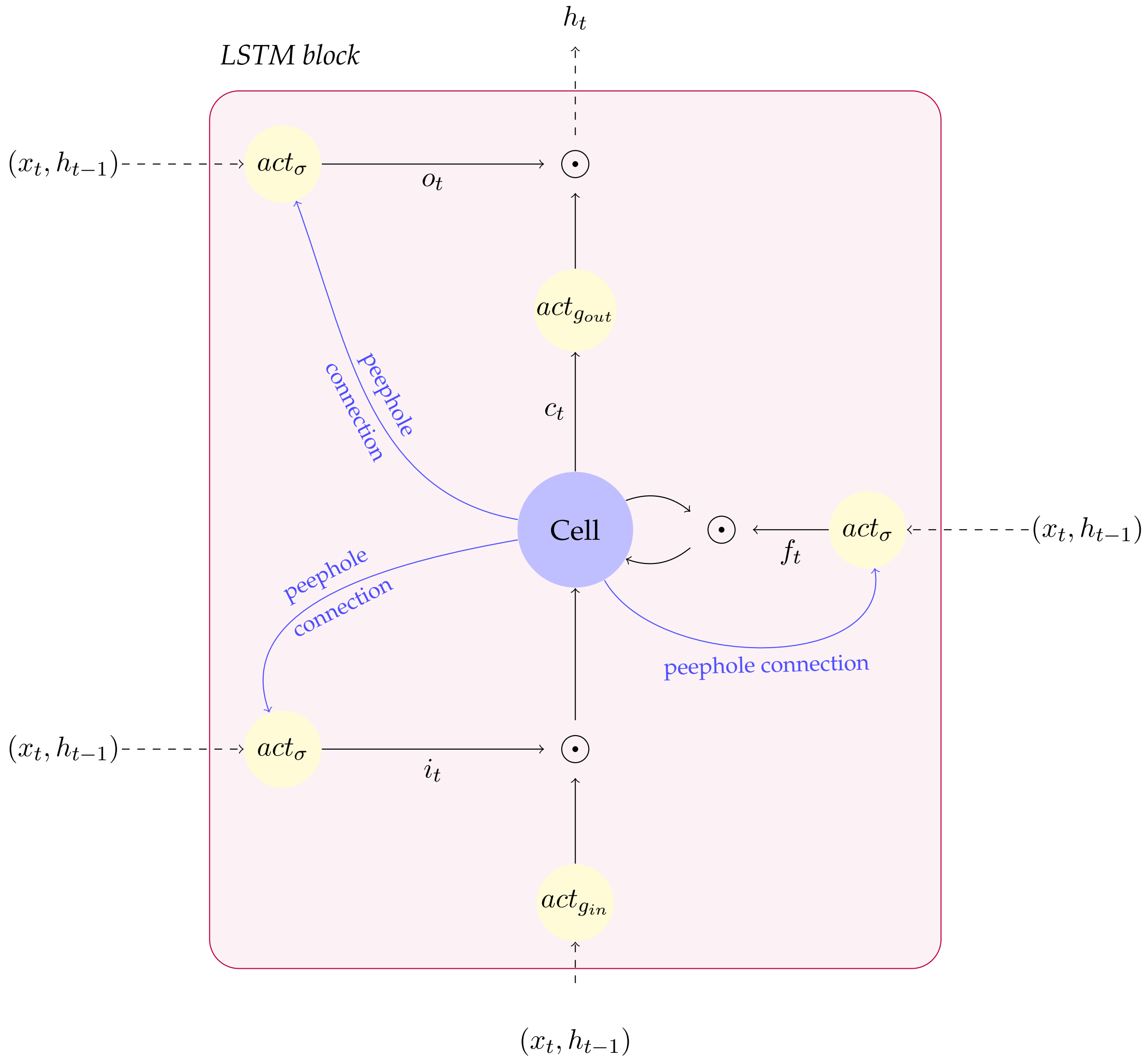

***Figure 2.5:* Representation of an extended single-cell LSTM memory block in one hidden layer network at time step $t$: The basic unit of an LSTM network is the memory block containing one or several memory cells (one in our case for the sake of clarity) and three gating units shared by all cells in one memory block. The weighted peephole connections from the cell to the three gates are shown with blue lines. $act$ is used to represent the gating, cell input, and output units activation.**

***At time $t$, the information from the input $x_t$ and the output at the previous time in the hidden layer $h_{t-1}$ enter the block. The flow of this information is controlled by three sigmoid gates via element-wise vector multiplication $\odot$: the forget gate $f_t$ updates the cell taking into account the cell's previous state, an external input gate $i_t$ updating the memory cell taking into account the activated block input, and an output gate $o_t$ controlling the LSTM block output taking into account the activated cell's output. The memory cell allows this information to persist through the cell state $c_t$.***

Input gates

$$i_t = \sigma(W_{ix}x_t + W_{ih}h_{t-1} + W_{ic}c_{t-1} + b_i) \tag{2.4}$$

Forget gates

$$f_t = \sigma(W_{fx}x_t + W_{fh}h_{t-1} + W_{fc}c_{t-1} + b_f) \tag{2.5}$$

Cell updating

$$\widetilde{c}_t = g_{in}(W_{cx}x_t + W_{ch}h_{t-1} + b_c) \tag{2.6}$$

$$c_t = f_t \odot c_{t-1} + i_t \odot \widetilde{c}_t \tag{2.7}$$

Output gates

$$o_t = \sigma(W_{ox}x_t + W_{oh}h_{t-1} + W_{oc}c_{t-1} + b_o) \tag{2.8}$$

Cell outputs

$$h_t = o_t \odot g_{out}(c_t) \tag{2.9}$$

Prediction

$$\hat{Y}_t = \phi(W_{yh}h_t + b_y) \tag{2.10}$$

$i$, $f$, and $o$ respectively refer to the input gate, forget gate and output gate. $h$ refer to the activation of hidden units (eg. at time $t$, $h_{t-1}$ is the activation of hidden units at the previous time) and $c$ is the activation of the cell unit.

$W_{\delta x}$ and $W_{\delta h}$ , $\delta = \{i, f, o\}$ are the matrices of the weighted connections from the $\delta$ gates to the input and from the $\delta$ gates to the hidden units, respectively. $W_{\delta c}$ are the matrices of the weighted connections from the cell $c$ to the $\delta$ gates, commonly known as the weighted "peephole" connections. As well, the $b_\gamma$ , $\gamma = \{i, f, c, o, y\}$ are the bias vectors.

$\sigma$ is the logistic sigmoid activation function so that the gates activations are between $0$ and $1$, this means, gates closed and gates open, respectively.

$g_{in}$ and $g_{out}$ are the cell input and output activation functions, usually tanh or logistic sigmoid functions. $\phi$ is the network output activation function, chosen, in our prediction context, as the softmax function to obtain probability distributions vector, where the j-th component that we will note $\left[\hat{Y}_t\right]_j$ is calculated by the equation 2.11. Note finally that $\odot$ means the element-wise vector product.

$$\left[\hat{Y}_t\right]_j = \frac{e^{\left[W_{yh}h_t + b_y\right]_j}}{\sum_{c=1}^{q+1} e^{\left[W_{yh}h_t + b_y\right]_c}}, \forall j \in 1, \ldots, q+1 \tag{2.11}$$

Where $[W_{yh}h_t + b_y]_j$ is the j-th component of the linear combinations vector result $W_{yh}h_t + b_y$. We recall that $q$ is number of studied crop types (thus $q + 1$ classification possibilities, considering a class corresponding to other cases), see Section 2.3.1.

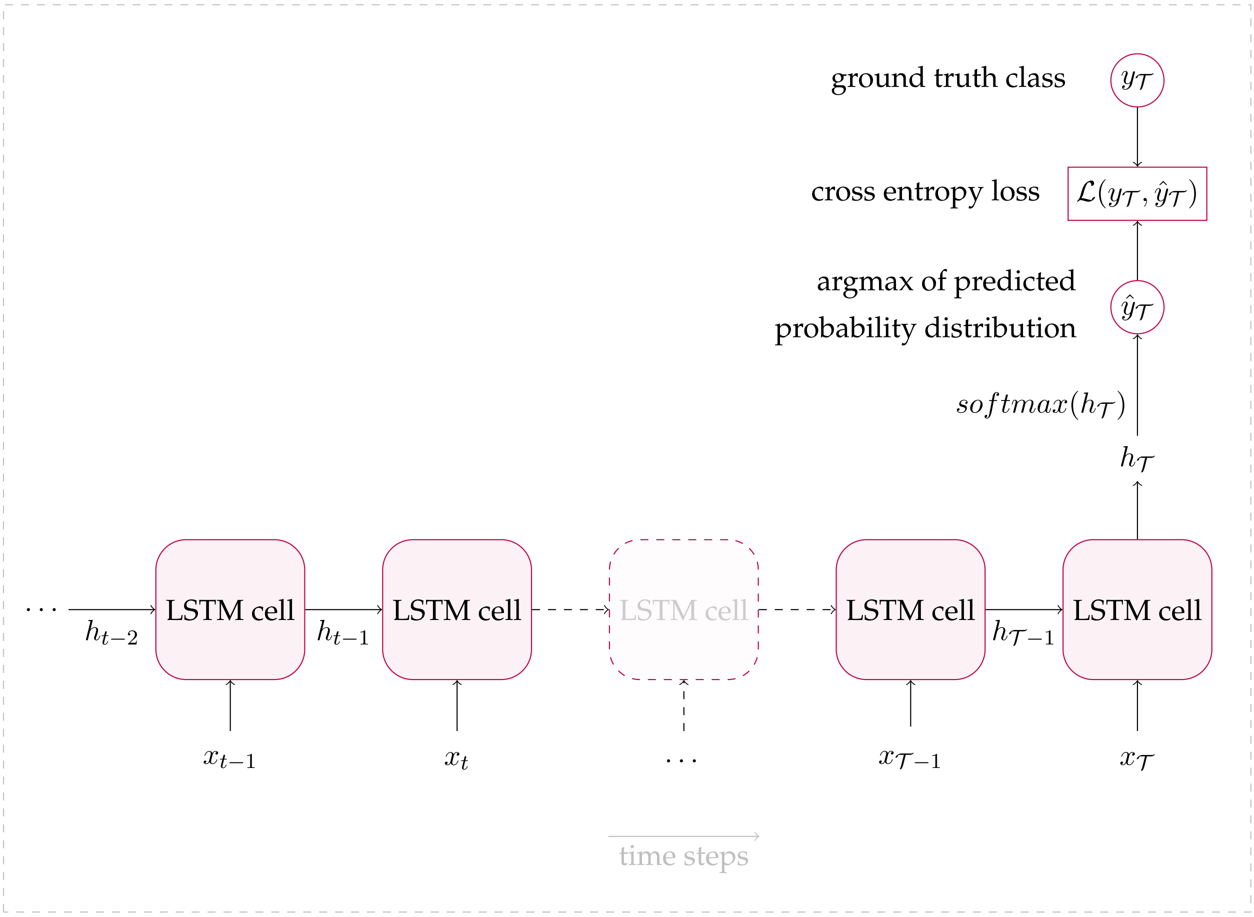

*Figure 2.6:* ***Information flow within the proposed LSTM model in its unfolded form. For clarity, the illustrated network contains a single hidden layer. An LSTM cell is composed of several recurrently connected LSTM blocks described in 2.5.***

The equations detailed above describe the functioning of an LSTM which calculates a mapping from $x = (x_1, \ldots, x_{\mathcal{T}})$ to $Y = (\hat{Y}_1, \ldots, \hat{Y}_{\mathcal{T}})$. In our particular case study, the crop type remains the same throughout the growing season, the prediction is then made at time $\mathcal{T}$ and therefore equation 2.10 becomes:

$$\hat{Y}_t = \phi(W_{yh}h_t + b_y) \text{ if } t = \mathcal{T} \tag{2.12}$$

Such an architecture is sometimes called the ”many-to-one” LSTM variant in the literature.

### 2.3.5 LSTM-based proposed crop classification approach

We train a model built from the LSTM network variant presented above to identify crop specie for each pixel using a temporal sequence of satellite images providing the variation of spectral response during crop development (Fig. 2.6).

A key objective for us is that the proposed LSTM model remains generic for both the input time series aligned according to the calendar time or aligned according to the thermal time (notably to test and compare the two cases). Therefore we introduce a common notation for both situation: for a scenario $k$ (evoked in 2.3.1), $\tilde{T}$ denotes the time step:

$$\begin{cases} 1 \leq \tilde{T} \leq \mathcal{T}_k & \text{in the case of a calendar time alignment;} \\ 1 \leq \tilde{T} \leq \lceil TT_k(t_{\mathcal{T}_k})/\alpha \rceil & \text{in the case of a thermal time alignment.} \end{cases}$$

(Let us recall that the definitions of $\mathcal{T}$, $\lceil TT_k(t_{\mathcal{T}_k}) \rceil$ and $\alpha$ are introduced in Section 2.3.1.) The observation vector $(x_1^k(\tilde{T}), \ldots, x_m^k(\tilde{T}))$ is injected in the model where $m$ is the number of pixels.

Equations 2.3 are then iteratively carried out at each $t$ and, at the last time step, the error between the predicted output probability vector for the instance $i$, $\widehat{Y}_i$, and the real one-hot coded output vector $Y_i$ is assessed by the cross entropy loss defined below:

$$\mathcal{L}(\hat{Y}_i, Y_i) = - \sum_{i=1}^{i=1+q} Y_i \log(\hat{Y}_i) \tag{2.13}$$

let us recall that one-hot coded vector is defined as follow: if there are $q$ crop labels to classify, each label is encoded as a vector of length $|q+1|$ (adding class 0 corresponding to none of the $q$ crops), taking the value $1$ at the position of the correct label and $0$ elsewhere.

The average cost function, which we denote by $\mathcal{J}$ will be defined by:

$$\mathcal{J} = \frac{1}{N} \sum_i \mathcal{L}(\hat{Y}_i, Y_i) \tag{2.14}$$

Where $N$ is the number of instances that will depend on the batch size in the training strategy.

Unless otherwise indicated, the update of network parameters is performed by the ADAM optimizer [Kingma and Ba, 2017] after computing the gradient of the loss function.

Note that a batch normalization [Ioffe and Szegedy, 2015] layer, which aims to normalize the distribution of input at each network's hidden layer, is inserted before the activation $f_l$ of the affine transformation $W_l.h_{l-1} + b_l$ as denoted earlier in 2.3.3. Indeed, this technique has been proposed to address the problem that, during training, the distribution of inputs in each layer evolves according to changes in the parameters of the previous layers (what [Ioffe and Szegedy, 2015] called "internal covariate shift").

This operation consists of normalizing the layer's inputs, by mini-batch, followed by an affine transformation allowing the result of the normalization to be scaled and shifted using two new parameters per layer ($\gamma$ and $\beta$ in 2.15), which will in their turn be learnt during training. An element in the mini-batch $B$, which can be denoted by $I_i$ is then mapped to $O_i$ as follows :

$$O_i = \gamma \left( \frac{I_i - \mu_B}{\sqrt{\sigma_B^2 + \epsilon}} \right) + \beta \tag{2.15}$$

Where $\mu_B$ and $\sigma_B^2$ are, respectively, the current mini-batch mean and variance. The constant $\epsilon$ is added for numerical stability.

Finally, it should be mentioned that we can find works in which this operation is applied after the activation functions, but we have opted, after various experiments and in keeping with most works in the literature, to apply it before the non-linear layer activation.

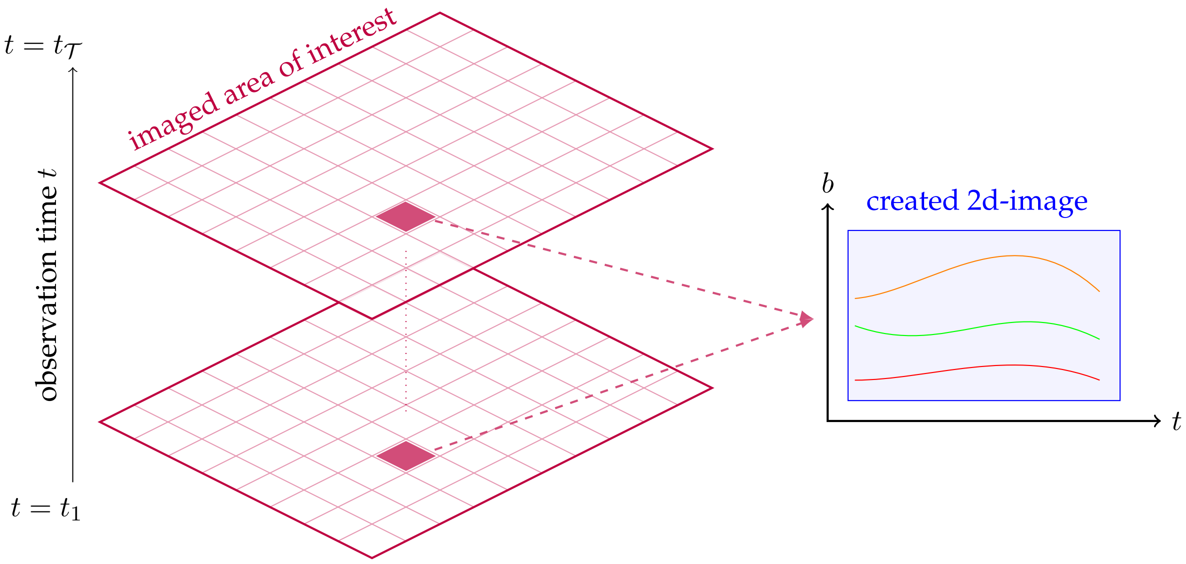

*Figure 2.7:* ***Method for the preparation of input data of the 2D-CNN convolution model: for a given scenario $k$, each pixel $i$ is expressed as an observation vector $X_i^k = (x_i^k(t_1^k), \ldots, x_i^k(t_{\mathcal{T}_k}^k))$ of size $\mathcal{T}_k$, where $\mathcal{T}_k$ is the length of the time series of observations for scenario $k$. Each pixel $i$, $1 \leq i \leq m$ where $m$ is the total number of pixels, is then transformed (as illustrated for the purple colored pixel) into a two-dimensional image: a temporal dimension denoted $t$ and a spectral/polarisation dimension denoted $b$. The set of created images is then injected into the convolution model.***

### 2.3.6 Convolutional Neural Network (CNN)

CNNs are defined as follows in [Goodfellow et al., 2016]: ”Convolutional networks are simply neural networks that use convolution in place of general matrix multiplication in at least one of their layers”. In at least one of the network’s layers, the transformation described in Equation 2.2, more generally known as the ”dense layer”, is replaced by a convolution layer.

The main motivation to use convolution layers instead of dense layers is the reduction of the number of weights in the neural network [LeCun and Bengio, 1998] by means of a technique called ”Parameter sharing” whereby the same linear combination is used all over the inputs. Indeed, each unit of a given layer $l$ receives input from a small set of units located in a small neighborhood in the previous layer $l-1$ instead of from all units in the classical dense layer, which considerably reduces the number of parameters to train while trying to learn the most important features in the data. We denote this reduced neighborhood by *LocalPatch*.
Typically, in our case study, an image created from the transformation of a time series of satellite responses in a given pixel into a 2D-image (as explained in Figure 2.7), such features can for example represent some distinctive behavior in the response variation curve over time like a strong increase, a strong decrease, or a stagnation.

The equation 2.2 is then transformed as follows to define this convolution layer:

$$h_l = f_l((W * h_{l-1})^{LocalPatch} + b_l) \tag{2.16}$$

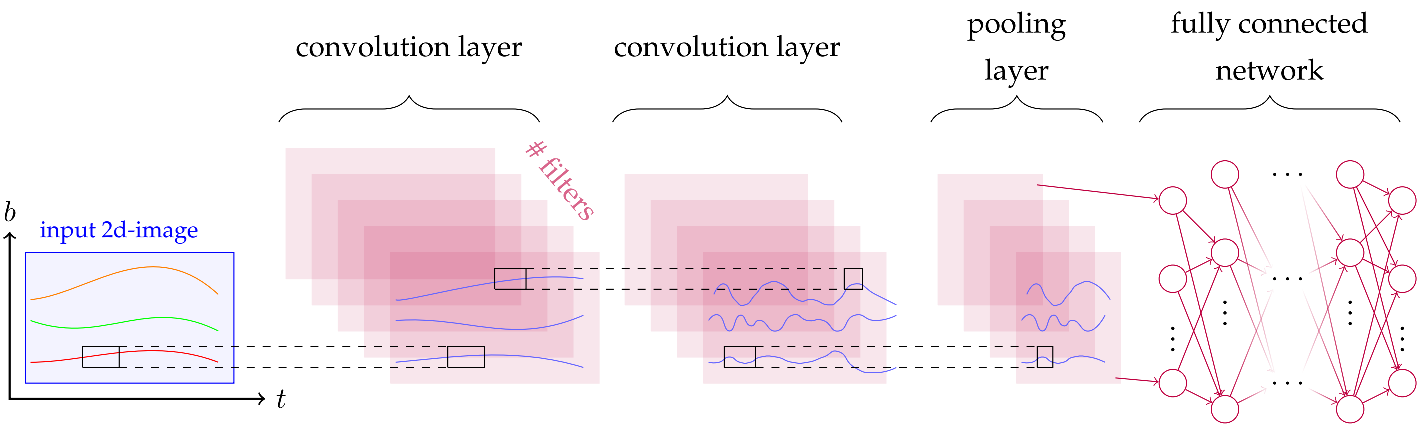

*Figure 2.8:* ***Global structure of the proposed 2D-CNN network architecture: this architecture illustrates the skeleton of the proposed network (the detailed model that is used in our work will be detailed later in this section). Each pixel created according to the transformation explained in figure 2.7 is injected into the network, convolution filters as well as pooling layers are applied, and the data from the last layer, in its flattened form, is then fed into a simple fully connected network, described at the beginning of 2.3.3, to make predictions.***

where $W$ denotes a kernel also known as filter and $*$ the convolution operation. The size of the kernel defines the spatial extension of this local neighborhood and a convolution layer can have several filters allowing to consider different characteristics from the input layer.

It is important to remember some language elements about convolution networks. The shape of the output of a convolution layer is controlled by the size of the convolution filters, but also by stride and padding. The stride represents the number of units of which the filter is shifted, and the padding is used to control the size of the data after the application of the convolution filters, generally by filling in the borders of the input data with zeros.

Another layer, which is widely used in a convolution network and which can be very efficient in some applications is the pooling layer. The pooling operation allows, by means of data subsampling, to ensure a form of robustness to the model by making it invariant or insensitive to small variations in the input data. The operation that we will use in our work is the max pooling [Zhou and Chellappa, 1988], which consists in keeping the maximum within a neighborhood window of size $k$. Generally, in a pooling layer, the stride is also equal to $k$.

### Overview of various works using convolutional networks in remote sensing

Convolutional neural networks (CNNs) have demonstrated their good performances across multiple applications, more particularly those that can be structured in the form of a grid allowing to take advantage of the notion of the neighborhood, such as time series (one-dimensional grid) and images (two or more dimensional grid) [LeCun and Bengio, 1998], or even videos (three or more dimensional grid) as in [Wu et al., 2015]. The most well-known application probably remains the recognition of handwritten digits [LeCun et al., 1999].

A variety of works have used convolution networks in applications that rely on remote sensing data. For the particular application of crop monitoring and land cover classification, CNNs have been used for pixel-based landcover classification of hyper-spectral images, as in [Midhun et al., 2014] and [Slavkovikj et al., 2015], where convolutions based only on the spectral dimension are applied, i.e. 1D-convolution. Afterward, research works started to focus on the pixel neighborhood, taking into account the spatial dimension in addition to the spectral one, but still with 1D-convolution filters, flattening the spectrum of the neighborhood as in [Chen et al., 2014], [Rustowicz, 2017] and [Chen et al., 2015].

[Maggiori et al., 2017] further proposed an approach based on a fully convolutional network to remote sensing image classification taking into account both spatial and spectral dimensions as for [Postadjian et al., 2017] who proposed a CNN-based framework for performing a large-scale landcover of multi-spectral satellite images.

Other works such as [Kussul et al., 2017] and [Scarpa et al., 2018] in which the temporal dimension of the data has been integrated into the convolution models, but without taking into account the chronological aspect of the data. Indeed, data within the same time series are considered as independent entities and the information vector generated by the sequencing of the data is not taken into account. In ([Kussul et al., 2017]), the authors aim to make a pixel-based classification of major agricultural crops in addition to water-based on multi-temporal optical and radar images, using CNNs with convolutions in the spatial domain in addition to the spectral dimension. However, the chronological aspect of the time series is not taken into account in the preparation phase of the models' input data. [Scarpa et al., 2018] have proposed a spatial CNN-based method for the estimation of spectral features, particularly the normalized difference vegetation index, when remote sensing data are missing (due to meteorological conditions for optical data for example) using multi-source data. A classical non-temporal CNN model is also used as a baseline for land cover classification, in addition to support vector machine(SVM) model, in [Rußwurm and Körner, 2017], with the aim of comparing the performances of the latter models with those achieved with recurrent networks.

To the best of our knowledge, our work is among the first to propose a supervised inter-annual approach for pixel-based major crops classification with a convolutional model in which both the spectral and temporal dimensions are taken into account, using Sentinel remote sensing data. [Pelletier et al., 2018] is the only similar work we found in which the authors adopted a similar methodology in the preparation of input data for a CNN, using Formosat optical data over the year 2006, with the objective of land cover classification.

### Proposed convolutional approach

The proposed model comprises two main phases :

1. A first step which consists in preparing the input samples of the convolution model (figure 2.7). The observation vector $X_i^k = (x_i^k(t_1^k), \dots, x_i^k(t_{T_k}^k))$ of a given pixel $i$ is transformed into a two-dimensional image with a spectral dimension $b$ which represents the

value in $i$ for all polarizations/spectral bands at a given acquisition time step $t$, and a temporal dimension $t$ consisting of the dynamics of the $p^{th}$ polarization/spectral band ($1 \leq p \leq b$) throughout the acquisition periods of the satellite images.

2. A second phase which consists in injecting the set of data created in the previous step into a convolution model whose basic global architecture is depicted in figure 2.8 and composed of:

   - Convolutional layers: in this layer defined in 2.16, each consists of several parallel convolution operations equal to the number of filters. To each filter, a non-linear activation function is applied (the rectified linear unit activation function (ReLu), calculated by Relu($x$)=$max(0, x)$, is used), which thus produces a set of non-linear activations whose size is the number of filters at each convolution layer.

     Batch normalization layers, detailed previously in page 53 by equation 2.15, will be applied after each activation function.

   - Pooling layers allowing, as explained above, for more robustness by sub-sampling the incoming data to these layers.

   - Dropout layer [Srivastava et al., 2014] helps prevent overfitting by randomly dropping a set of layers' input units during model training.

   - At the last layer of the network among the two previous layers, a flattening operation is then carried out to prepare the inputs of a classical fully connected network to obtain the final prediction probability distribution by way of the softmax function (equation 2.11). Cross entropy loss between the predicted probability and the one-hot coded ground truth is then computed as done in 2.13.

   More details on the configuration of each layer of the proposed model will be given in section 2.4.4.

One important point to evaluate and take into account in our various experiments is the shape of the different filters and their impact on the performance of the model. In fact, for the 2D-image at the input of the model, there are two possibilities concerning the shape of the convolution filters:

- We can separate the spectral features and consider that the spectral bands are independent of each other, the convolution filters will have a shape of (1, $\bar{t}$), $\bar{t}$ $<$ the number of time steps, in this case, and the same filters will then be applied, over the temporal dimension, on each polarization / spectral band.

- A second possibility consists in trying to link the temporal and spectral dimensions, by applying filters of shape ($\bar{b}$, $\bar{t}$), where $\bar{b} \leq$ to the number of spectral features.

The first and second cases will be denoted by **Temporal-convFilter** and **Spectral-Temporal-Conv**, respectively.

Note that a third choice may be possible, by applying filters of shape $(\bar{b}, 1)$, a possibility which will however be discarded because such a choice leads to ignoring the temporal aspect on which our approach is based.

## 2.4 Experiments

This part aims at evaluating the approaches proposed in 2.3.1 with the models detailed in section 2.3.3.

This part is organized as follows :

- Presentation of the first results obtained by applying the proposed LSTM and CNN models to the $U.S.A_1$ data set earlier presented in 2.2, over three corn growing seasons.
- As a proof of concept, presentation of some results obtained in study areas in France for an **intra-annual** approach.
- The results obtained with the models developed, for an **inter-annual** approach, on a selection of crops of interest, still in France located study areas, are then presented.
- These results will be finally discussed.

As previously mentioned in this document, the supervised learning of the proposed pixel-based models in France is carried out using the Sentinel-1 images as input data, and the French registre parcellaire graphique (RPG) as reference data by extracting the crop types associated with these pixels.

The RPG is a geographical information system that provides, based on declarations from the farmers, annual information on the occupation of agricultural soil in France. The data are made available with an annual latency of two years.

The parcels constitute the unitary classes of the RPG and are grouped into ”crop islands” which correspond to a group of contiguous parcels and are managed by the same farmer. In our work, we are interested in this smallest achievable unit, which is the parcel. Each parcel is characterized by different attributes, those of interest to us are the type of crop (coded with the attribute ”CODE_CULTU”, the group to which the crop belongs (represented by the ”CODE_GROUP” attribute, such as cereals) and eventually the surface area of the parcels in hectares (with the attribute ”SURF_PARC”).

Figures 2.10b and 2.10c further down in the document will provide an overview of vector layers of a set of parcels located in the east of France that has been extracted from the RPG by post-processing treatments that have been developed.

### 2.4.1 LSTM and CNN results in the $U.S.A_1$ test area

To study the impact of variability in temperature profiles between different years, we make experimental tests for both the proposed inter-annual approaches taking into account the thermal time and when the sequential data are synchronized with the calendar time. These first tests were carried out on $U.S.A_1$ test area using a temporal series of Sentinel-1 images covering a wide part of the corn growing season, from early June to late October over the three 2015, 2016, and 2017 farming years.

A series of three tests is performed: for each one, both LSTM and CNN models are trained on the data of two years (what will constitute the training data set), and tested on the third year data (test data set), which is thus not represented in the training data set. In order to prevent model overfitting, the training data set is randomly split into two subsets: a training subset (90%) and a validation subset (10%), this process is repeated $K$ times to perform a kind of K*2-fold cross-validation, $K$ was set to $5$ here.

Results are presented in tables 2.2 and 2.3 for the inter-annual approach with and without taking into account the thermal time for the three test configurations. We note that the performance measures retained for these initial tests in the $U.S.A_1$ area are overall accuracy and Area Under the Curve (AUC).

The results clearly show the superiority of the approach based on the thermal time, in all situations. But we particularly note the case in which models are trained on 2015 and 2017 data, and tested on 2016 data: a considerable gain is obtained when adding the thermal time in this test. Indeed, the study of the temperature data and the estimated evolution of the degree-days accumulated over the three years showed that 2016 was characterized by a very different temperature profile compared to 2015 and 2017. Actually, in South Dakota, it was warmer during the 2016 corn growing season compared to the 2015 and 2017 seasons.

*Table 2.2: Summary results of the proposed LSTM model*

| Training data | 2015 and 2016 | | 2015 and 2017 | | 2016 and 2017 | |
|---|---|---|---|---|---|---|
| Test data | 2017 | | 2016 | | 2015 | |
| | Calendar time | Thermal time | Calendar time | Thermal time | Calendar time | Thermal time |
| Overall Accuracy | 0.92 | 0.94 | **0.85** | **0.93** | 0.92 | 0.92 |
| AUC | 0.84 | 0.86 | **0.67** | **0.86** | 0.88 | 0.89 |

*Table 2.3: Summary results of the proposed CNN model*

| Training data | 2015 and 2016 | | 2015 and 2017 | | 2016 and 2017 | |
|---|---|---|---|---|---|---|
| Test data | 2017 | | 2016 | | 2015 | |
| | Calendar time | Thermal time | Calendar time | Thermal time | Calendar time | Thermal time |
| Overall Accuracy | 0.93 | 0.94 | **0.85** | **0.93** | 0.92 | 0.93 |
| AUC | 0.85 | 0.87 | **0.67** | **0.87** | 0.89 | 0.89 |

### 2.4.2 Data and materials for experiments in France

The second series of experiments, which represents the large majority of the tests conducted within the scope of our thesis work, was carried out on areas of interest located in France, for which we had a progressive availability of data, in particular training data.

Note that in experiments conducted in France, we have chosen to concentrate on convolutional models. Knowing that the work carried out in the framework of this thesis have purely research objectives, but also industrial purposes, this choice is mainly justified by the needs of the industrial partner of the thesis, CybeleTech, who works a lot on multi-source imaging, the convolutional models developed had more chances to be used on other projects and themes compared to the recurrent LSTM networks. Furthermore, the results obtained with convolutional models were slightly better than those obtained with LSTM networks according to the tests developed in the $U.S.A_1$ (see section 2.4.1).

To carry out these experiments in France, we have selected two large areas of interest whose location is illustrated by figure 2.9. The first area, outlined in orange in figure 2.9, which we will name **France-East** is located in the east of France, while the second, outlined in blue in the same figure, and which we will name **France-Center** is located in the Centre region. The choice of these areas was guided, in large part, by the availability of client information such as field knowledge and the possibility of obtaining training and/or validation data. The set of conducted experiences in these study areas will concern the 2016/2017, 2017/2018, and 2018/2019 agricultural seasons.

To have an idea about the dominant crop types in the France-East study area (resp. the France-Center study area), we have calculated the overall surface area per crop and we have displayed in figure 2.10a (resp. in figure 2.11a) the ten most important crops within this area.
Figures 2.10b and 2.10c (resp. 2.10b and 2.10c) provides an overview of parcel contours for a set of parcels located in France-East area (resp. in France-Center area). These data were extracted from the RPG.

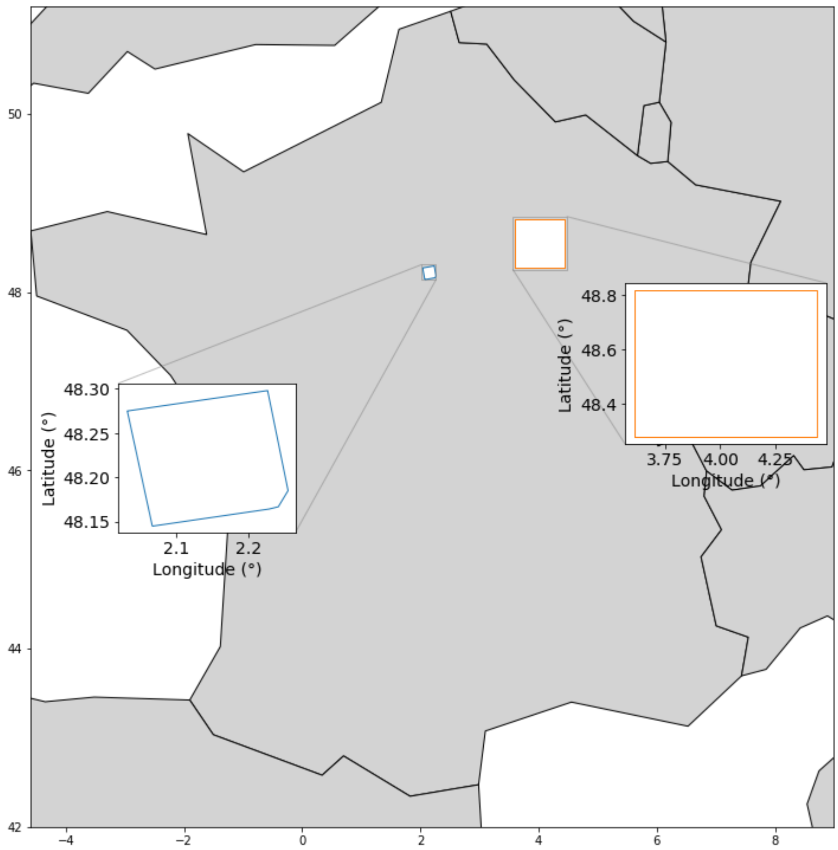

*(a) Coordinates of the areas of interest on France map.*

*(b) Study areas on open street map.*

*Figure 2.9: Location of study areas for crop recognition experiments.*

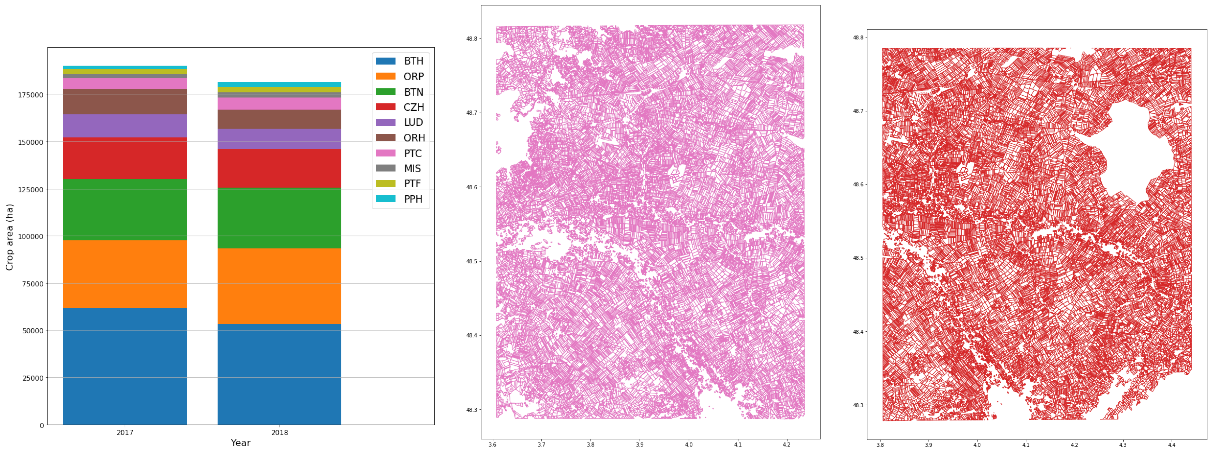

*(a)* *(b)* *(c)*

***Figure 2.10:*** *The ten majority crop statistics in the area of interest France-East (a) for the parcels of years 2017 (b) and 2018 (c). Figures (b) and (c) provides an overview of parcel contours for a set of parcels extracted from RPG. Crop codes according to the RPG naming are: BTH: Soft winter wheat, ORP: Spring barley, BTN: Beet, CZH: Winter rapeseed, LUD: Alfalfa, ORH: Winter barley, PTC: Ware potato, MIS: Corn, PTF: Starch potato, PPH: Grassland.*

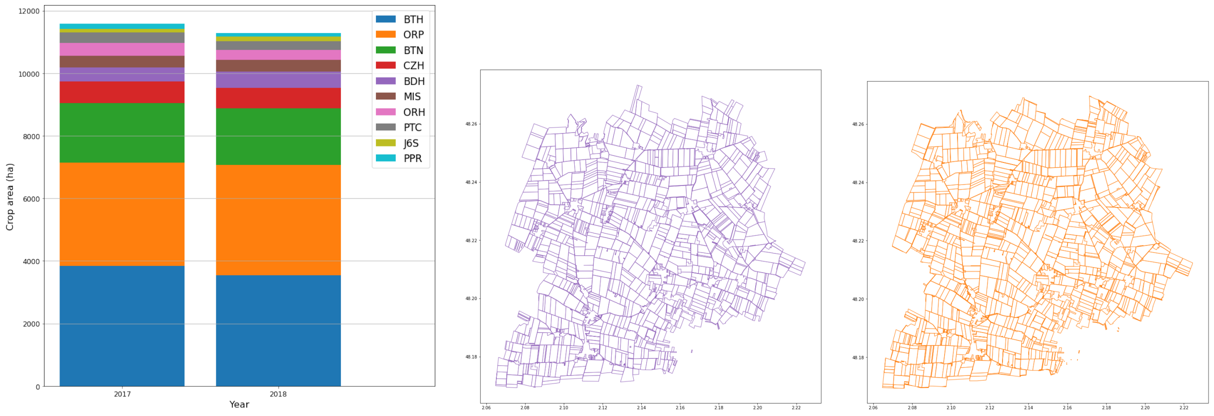

*(a)* *(b)* *(c)*

***Figure 2.11:*** *The ten majority crop statistics in the area of interest France-Center (a) for the parcels of the year 2017 (b) and 2018 (c). The same geographical location footprint is used for the two years. Figures (b) and (c) provides an overview of parcel contours for a set of parcels extracted from RPG and crop codes according to the RPG naming are: BTH: Soft winter wheat, ORP: Spring barley, BTN: Beet, CZH: Winter rapeseed, BDH: Winter durum wheat, MIS: Corn, ORH: Winter barley, PTC: Ware potato, J6S: Fallow land, PPR: Spring peas.*

### 2.4.3 Intra-annual experiments

The models developed were first tested for **intra-annual** crop recognition on a set of crops of interest. Concretely, knowing the crops in parcels $P_1, P_2, \ldots, P_N$ in a production basin for the agricultural season $S$, we aim at determining the crop rotation of parcels $P_{N+1}, P_{N+2}, \ldots, P_{N+M}$ for the same season $S$, using time series of Sentinel-1 images as input data, and RPG for ground truth data.

Table 2.4 summarises some results obtained with experiments carried out using the proposed multi-temporal 2D-convolutional model for the 2016/2017 agricultural campaign on some interesting crop types. For each of these, the crop-type prediction is made around two months before the harvest.

*Table 2.4:* ***Summary of results of the first phase of tests: Application of the proposed multi-temporal 2D-convolutional model for the classification of a selection of crops within the same production basin and for the same agricultural season.***

| Area | Crop | Training parcels number | Predicted parcels | Surface error based on real land coverage |
|---|---|---|---|---|
| Sub-area in France-East zone | Winter rapeseed | 93 parcels | 25 parcels | 1% pixel error (3.91 ha)<br>0 parcel not detected |
| 2 sub-areas in France-East and France-Center zones | Corn | 43 parcels in the north-east<br>25 parcels in the region centre | 49 parcels | 4% pixel error<br>03 parcels not detected (5.5 ha) |
| Sub-area in France-East zone | Soft winter wheat | 241 parcels | 66 parcels | 4.3% pixel error<br>1 parcel not detected (15ha) |
| Sub-area in France-East zone | Spring barley | 179 parcels | 32 parcels | 4% pixel error<br>1 parcel not detected (14ha) |

We present just below, in figure 2.12, some of the visual results obtained, the purpose being to get an idea, visually speaking, of this part of our work.

These results were obtained with multi-temporal convolutional models following the global framework of the approach we proposed in 2.3.6. However, the tuning of the hyper-parameters and, eventually, the network architecture (in terms of the number of convolution layers, use of pooling layer,... etc) is specific to each type of crop. The choice of these parameters and architecture is discussed in detail later starting from section 2.4.4 in the ”Training strategy and model configuration” paragraph.

*(a) Effective winter rapeseed parcels* *(b) Predicted winter rapeseed parcels*

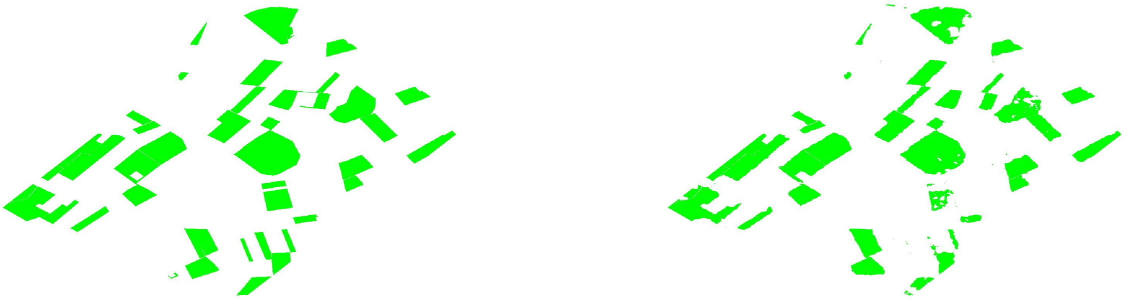

*(c) Effective corn parcels* *(d) Predicted corn parcels*

*(e) Effective soft winter wheat parcels* *(f) Predicted soft winter wheat parcels*

*(g) Effective spring barley parcels* *(h) Predicted spring barley parcels*

*Figure 2.12: Intra-annual approach results visualizations for a selection of crops.*

### 2.4.4 Inter-annual experimental design

#### Convolutional models

#### Target crop 1: soft winter wheat

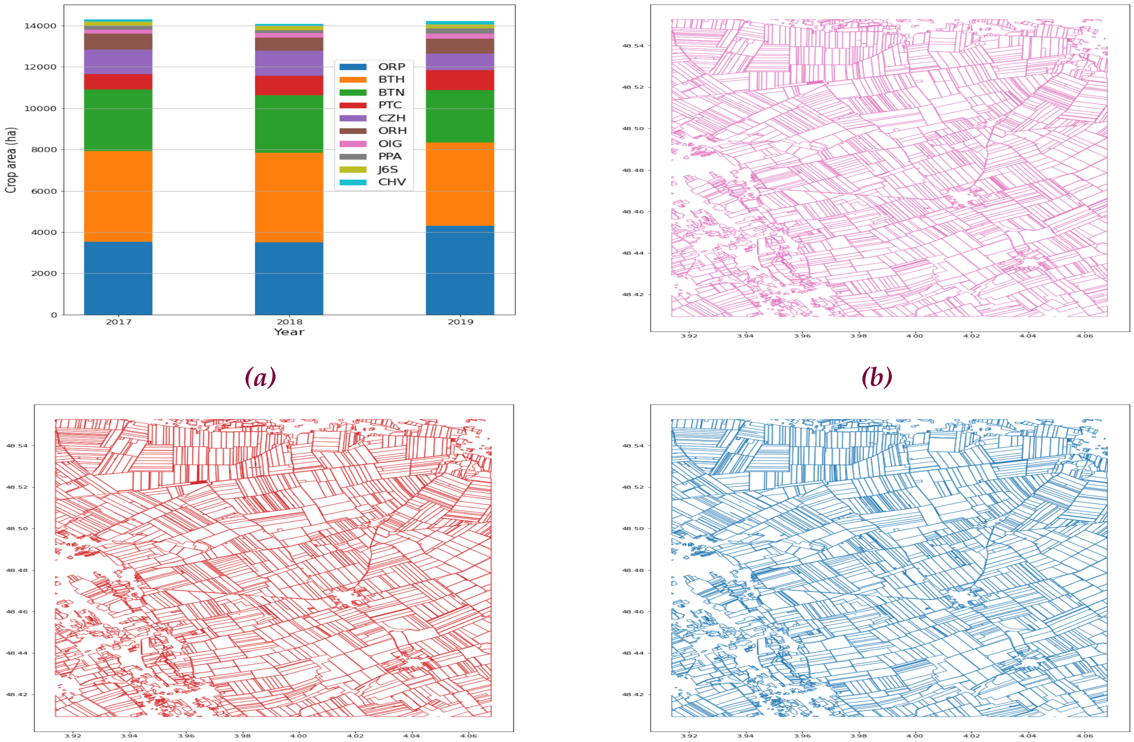

*(a)* *(b)*

*(c)* *(d)*

*Figure 2.13:* ***The ten majority crop statistics (a) in the study zone located within the area of interest France-East for the parcels of the 2017 (b), 2018 (c) and 2019 (d) seasons. Crop codes according to the RPG naming are: ORP: Spring barley, BTH: Soft winter wheat, BTN: Beet, PTC: Ware potato, CZH: Winter rapeseed, ORH: Winter barley, OIG: Onion, PPA: Perfume plant, J6S: Fallow land, CHV: Hemp.***

For the inter-annual approach, we wanted to start our experiments with soft winter wheat crop ("BTH" code in RPG), which appeared to be one of the most complex crops to discriminate by our models. In fact, the presence of another crop in the training database, winter barley, which is very close to winter wheat in several physiological characteristics related to the structure of the plant (volume, orientation, height,. . . , etc.), or to genetic / phenological characteristics developed during the growth cycle and resulting from backscatter signals that are almost similar at different stages of the growth cycles of the two crops, which may disrupt the learning of the binary soft winter wheat recognition model.

This is well illustrated in Figure 2.14 where, for two parcels of soft winter wheat and winter barley located within France-East area during the 2017/2018 season, there are clear overlaps in the backscatter distributions on at least three of the four dates showed beginning around the start of booting growth stage.

In addition, and at a similar level of complexity, the presence in the learning database of other

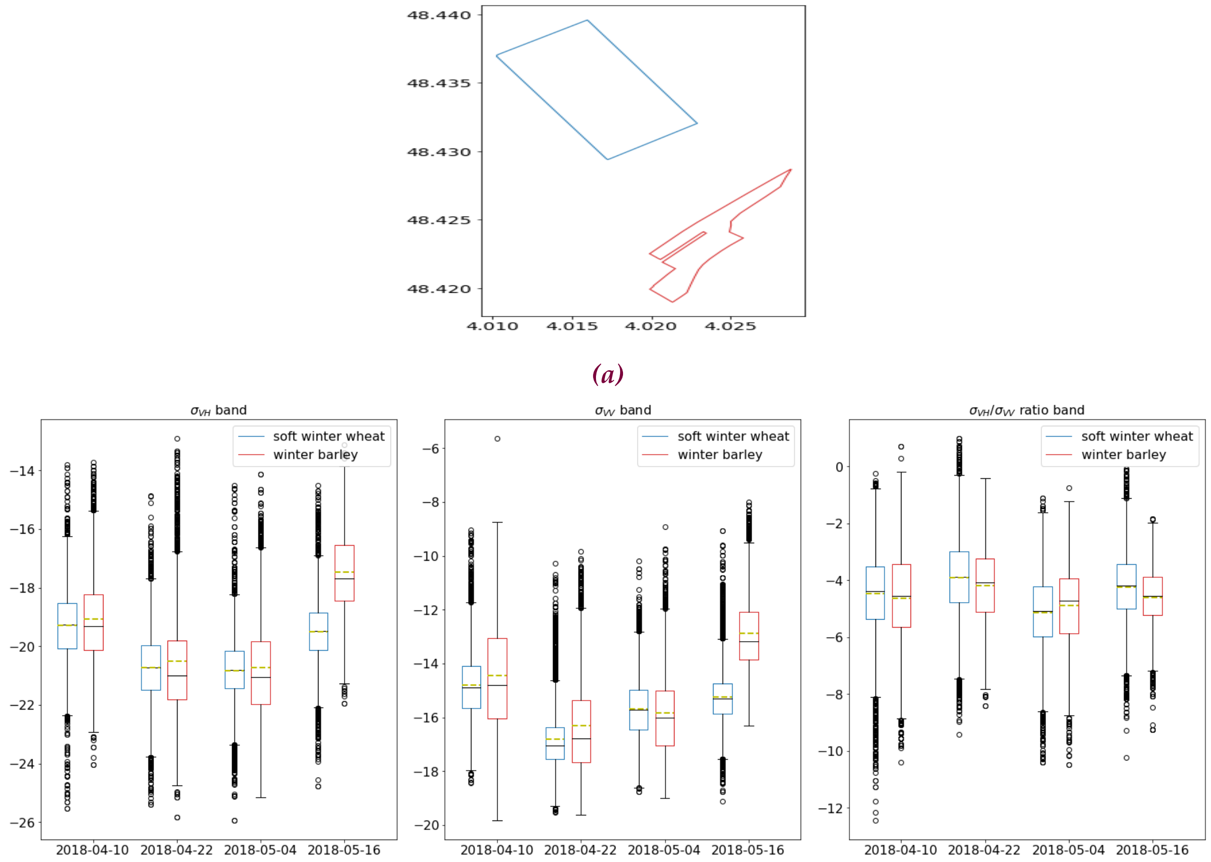

*(a)*

*(b)*

***Figure 2.14:* boxplots of backscatter variation for the Sentinel-1 $\sigma^0_{VH}$, $\sigma^0_{VV}$ and the ratio $\sigma^0_{VH}/\sigma^0_{VV}$ polarizations (b) on the two blue soft winter wheat and red winter barley parcels showed in (a). The black dashed lines represent the medians and those in yellow represent the mean values.**

types of cereals, which are not wheat but which are very close to it, makes training even more difficult. In fact, in the RPG, winter cereals of the type Hordeum, Secale, or Triticum as well as Winter Rye, Sorghum, Buckwheat, or winter Triticum are cataloged and considered. With the knowledge that these cereals (categorized as ”Other cereals” group in the RPG), as for winter barley, also share quite a few characteristics with winter wheat, such as orientation, height, or even the way in which the plant evolves during its growth cycle, the learning of our winter wheat models may be impacted, although they are a minority in the database.
It should be noted that, in principle, such a problem does not occur with spring cereals, including spring soft wheat crop, because there are seasonality differences, and thus in the periods of the time series, that the model is capable to distinguish and handle.

The proposed test phase is based on the evaluation of an inter-annual 2d-CNN model developed for the recognition of soft winter wheat crop (previously proposed in 2.3.6).
For a variety of practical reasons related to calculation times and simplifying the results visualization, but also for reasons related to the spatial resolution of environmental data [Hersbach et al., 2020] (about thirty kilometers, already evoked in 8 earlier in the document), we restricted

to working on sub-parts of the study areas we had chosen.

The sub-study areas during this stage of experiments on soft winter wheat are illustrated above in figure 2.13. The prevalence of cereal crops such as soft winter wheat, spring barley, but also beet (code ”BTN”), which will be studied in the rest of this experimental design, can be observed over the three seasons on the graphs (a) of this figure.

The experiments are conducted as follows :

- The 2d-CNN model for the soft winter wheat crop, which takes as input data a time series of S1 images aligned according to calendar time, is assessed on both 2017/2018 and 2018/2019 seasons.
  We will denote this experiment by **2d-CNN-CT** $_{\textbf{Temporal-Conv}}$ for the model trained with convolution filter of shape $(1, \bar{t})$, and **2d-CNN-CT** $_{\textbf{Spectral-Temporal-Conv}}$ for the one trained with convolution filter of shape $(\bar{b}, \bar{t})$, return to the last paragraph in 2.3.6 for more details on how to manage the convolution filter shape.
- This model is also tested over the two above-mentioned seasons, taking as input data, this once, a time series of S1 images aligned according to thermal time, an approach previously explained in section 2.3.2.
  In accordance with the notations in the previous item, we note this experiment by **2d-CNN-TT** $_{\textbf{Temporal-Conv}}$ and **2d-CNN-TT** $_{\textbf{Spectral-Temporal-Conv}}$.

### Training strategy and model configuration :

The objective of our work is not to propose the best possible convolutional model, but to reveal, through these experimental tests, the interest that the proposed inter-annual approach can offer, itself, but also by working with the thermal time in some particular temperature conditions that can directly impact the normal process of plant growth.

The construction of the proposed convolutional model is carried out according to the following procedure:

- In a preliminary step, the training data is divided into two subsets, training and test subsets with consecutive proportions of 90% and 10%. This splitting is done randomly, but in a stratified way to keep the same proportions of each class (soft winter wheat and other crop classes) in the two subsets. The training subset will be used for the model learning and the test subset will be used at the end of the process to validate the performances.
- The following step is the tuning of the model hyperparameters. Using the training subset (the 90% selected samples) and starting from a basic CNN architecture, described in 2.3.6, and composed of a single convolution layer (we remind that a convolution layer as we defined it in 2.3.6 is composed of a number of filters parallel convolution operations, followed by a batch normalization layers and the non-linear ReLu activation function), we aim to find which combination of hyper-parameters, whose list is specified in advance,

allows to achieve satisfying performances. This strategy, based on exhaustive research over a list of hyper-parameter candidates is commonly known as Grid Search method.

This research is done with a stratified K-Fold Cross-Validation : the training subset is split into $K$ consecutive folds in a stratified manner, the training is done on $K-1$ folds, and the validation is done on the remaining fold, at each time. The score retained is the average of the $K$ obtained scores and the hyper-parameters maximizing this score are then selected. The model is refitted on the whole training subset this time and evaluated one last time on the test subset data, the idea being to ensure the coherence of the results. Accuracy was chosen as a score metric over $K = 5$ folds, and the hyper-parameters on which this optimization is performed are : the batch size, optimizer, and the learning rate.

It should be noted that this procedure remains very expensive in terms of computing time. As an indication, it takes between 12 and 18 hours to build the soft winter wheat model, depending on the device and the data.

Once this baseline model has been elaborated, we apply a sort of exhaustive manual research on a relatively small number of candidates to define the architecture of the network in terms of depth, convolution filter size, and the use of pooling layers. In fact, we vary the number of convolution layers, the filter shape with candidates on both the temporal and spectral dimensions as explained in the last paragraph of 2.3.6, and, also, the use or not of pooling layers. The best architecture is selected according to the maximum score on the test subset, including an early stopping technique on a validation subset. We could have, again, used the K-fold cross-validation in this phase, but for reasons of computing cost, we preferred to use a simple procedure for choosing the network architecture.

The final convolutional model retained for soft winter wheat crop is composed of 2 convolution layers (16 2d-convolution operations each, with filters of shape (1, 3), followed by a batch normalization layer and a non-linear ReLu activation). Based on the test results, no pooling layers are used.

The flattened outputs of the second convolution layers are injected into a fully connected network by means of a dense layer composed of 512 units, followed by batch normalization and ReLu activation layers. These will, at last, be connected to a binary output layer, to which a softmax function is applied to obtain the final prediction probability distribution.

As well, and in order to prevent overfitting, two dropout layers, one after the second convolution layer and the other after the first dense layer, were used with 0.3 rate.

This network has been implemented with Tensorflow framework [Abadi et al., 2015] under Keras [Chollet et al., 2015] as a high-level API, and its parameters are trained using an RMPSProp optimizer [Tieleman and Hinton, 2012] with a learning rate equal to 0.0025, a batch size of 700 samples over 15 training epochs. The initialization of the network parameters is done with a Glorot uniform [Glorot and Bengio, 2010] initialization technique.

*Table 2.5:* ***Confusion matrix.***

| | | Observed ground truth | |
|---|---|---|---|
| | | Interest crop | Other crops |
| Predicted ground truth | Interest crop | True Positive ($TP$) | False Postitive ($FP$) |
| | Other crops | False Negative ($FN$) | True Negative ($TN$) |

The evaluation of the quality of the classifications produced by our models is based on accuracy and F1-score as performance metrics.

Accuracy, a measure widely used by the scientific community, is defined in the equation 2.17, where TP, FP, TN, and FN represent, consecutively, True Positive, False Positive, True Negative, and False Negative, which are defined in the confusion matrix presented in table 2.5.

$$Accuracy = \frac{TP + TN}{\text{total number of samples}} \tag{2.17}$$

F1-score, that we have chosen to display for each of the two studied classes, is on its turn defined as an harmonic mean of precision and recall in equation 2.18 :

$$F1{-}score = \frac{2 * precision * recall}{precision + recall} \tag{2.18}$$

with

$$precision = \frac{TP}{TP + FP} \tag{2.19}$$

and

$$recall = \frac{TP}{TP + FN} \tag{2.20}$$

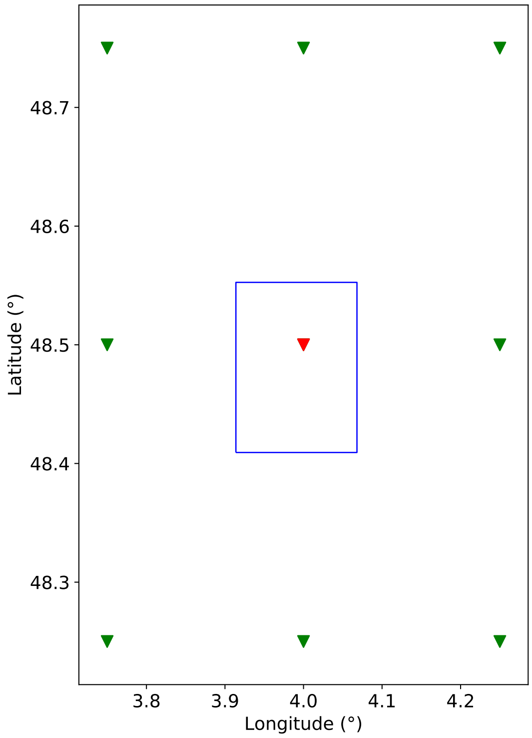

***Figure 2.15:* Green marked ERA5 points located close to the France-East area of interest, whose bounding box is showed in blue color. The point marked in red corresponds to the ERA5 point chosen for our study.**

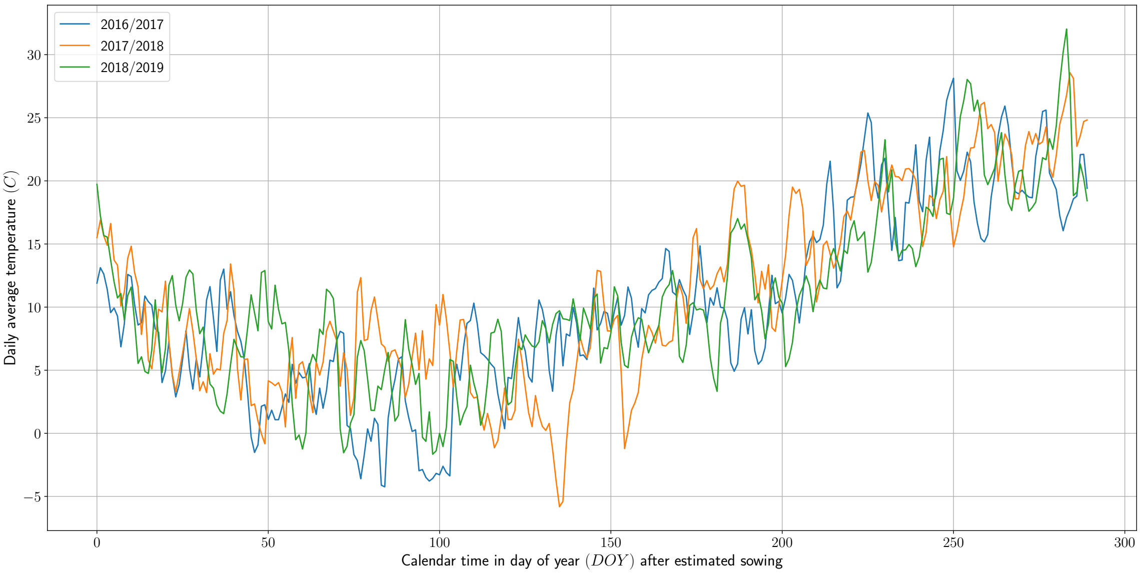

***Figure 2.16:* Average daily temperatures recorded in the France-East area over the three surveying seasons since the 15 October estimated sowing date of the target crop.**

On the basis of data from many field experiments, we defined for the purposes of our experiments on soft winter wheat, a sowing date that we had set at 15 October of each surveyed farming season.

The ERA5 reanalysis data [Hersbach et al., 2020] point retained in these experiments over the France-East study area is the one marked in red on figure 2.15 and the daily resampled temperatures curves for the three studied seasons are shown in figure 2.16.

An initial analysis of these temperatures data allows us to draw up an initial assessment. Indeed, according to figure 2.16, the most striking events are the two abrupt drops, at different magnitudes, of temperatures in the 2017/2018 season at 135 and 155 days after the estimated sowing date, around the tillering stage of the winter wheat growth cycle.
Knowing that we saw earlier in our work, in part 8, that this has an obvious impact on the radar signal by causing an abrupt drop in backscatter at these two periods, we, therefore, expect, as a first intuition, that the parcels of soft winter wheat in this season may be particularly difficult to classify with a model trained on the 2016/2017 season.

As a confirmation of this, four different parcels of soft winter wheat were selected over the two agricultural seasons 2016/2017 and 2017/2018, and the evolution of each of the radar polarization was traced. These graphs are shown in figure 2.17 and illustrate how the temperature conditions shown in figure 2.16 impacted the backscatter signal.

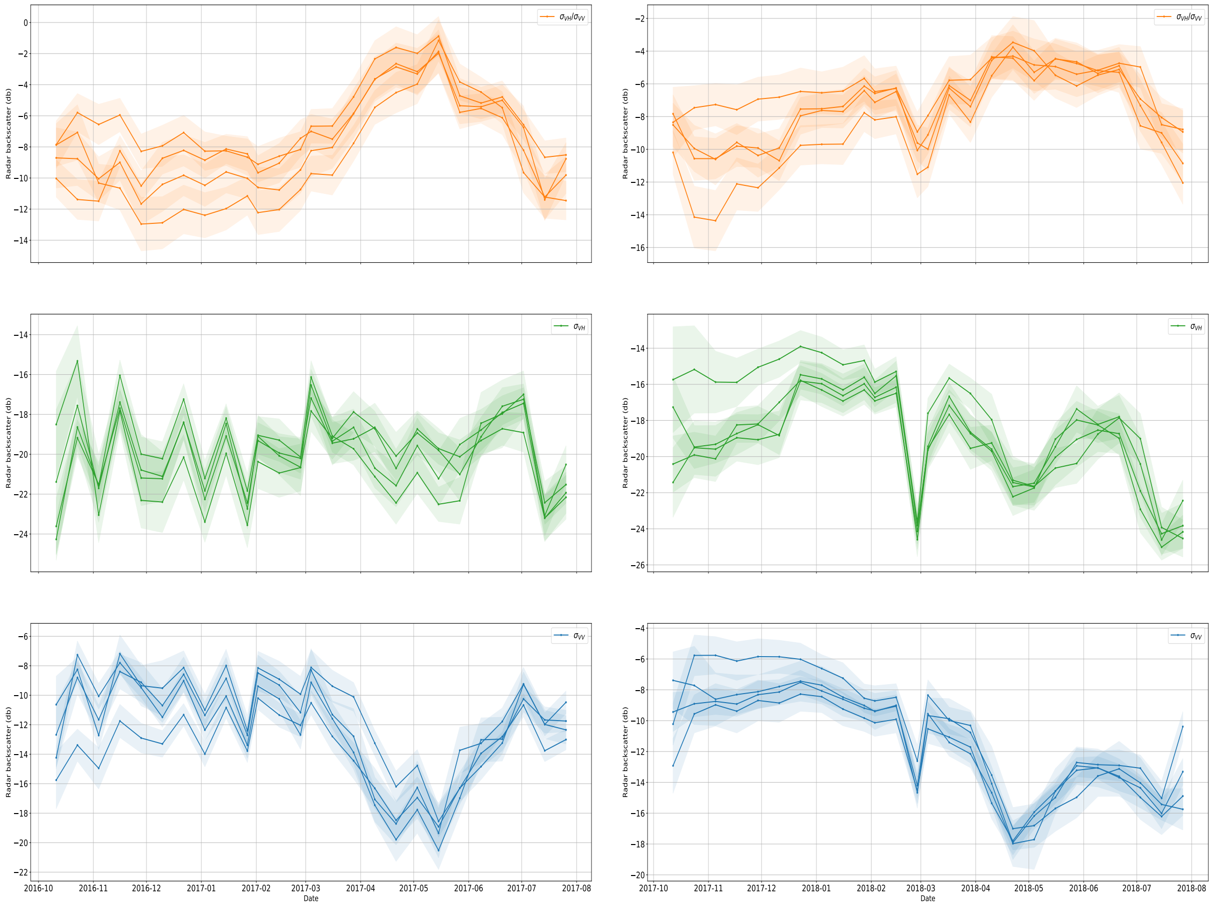

*(a) 2016/2017 farming season* *(b) 2017/2018 farming season*

*Figure 2.17: Average radar backscatter evolution of the three studied polarizations in four different soft winter wheat parcels located in the France-East area, across the farming seasons, 2016/2017 and 2017/2018.*

### Time series data preparation :

For the **2d-CNN-CT** experience, the dates composing the time series of the input images are chosen as follows : calendar dates covering the period from the beginning of November to the second half of May of the 2016/2017 farming campaign are chosen to be used as training data of the proposed model. The same calendar dates for the two campaigns 2017/2018 and 2018/2019 will then be requested to be used as test data.
However, as explained above in this document, and knowing that we restrict ourselves, as far as possible and for the reasons previously mentioned in the last paragraph on page 25, in particular the non-negligible effect of early morning dew, to images with the same orbit direction (ascending), the operating mode of the Sentinel-1 satellite makes it usually difficult to find exactly the same desired calendar dates. A delay of one (in the majority of cases) or even two days is often inevitable, depending, among other things, on the size of the area of interest. In fact, the more the zone of interest is large, the more difficult it is to find images with dates that match perfectly.

In the same reasoning logic, the alignment according to thermal time in the **2d-CNN-TT** experience is, on its side, done through the procedure explained in 2.3.2, based on the calendar dates previously chosen for the 2016/2017 campaign.

The calculation of the thermal times is done according to the procedure explained in 2.3.2 with a base temperature of $0°C$ and a saturation temperature of $28°C$ for wheat. An analysis, like the one made in 2.3.2 for the corn crop, illustrated by the graph 2.18, shows that for the different farming seasons, reference phenological stages (tillering and heading as for instance here) are reached at different dates, for the soft winter wheat crop.

The dates of the images used for the two inter-annual **2d-CNN-CT** and **2d-CNN-TT** experiments are summarized in Table 2.6.

Note an unavoidable derogation to the rule concerning the ascending orbit direction, where for image availability purposes, images with a descending orbit direction will be used when necessary; these are the dates noted with an asterisk in the cited above table.

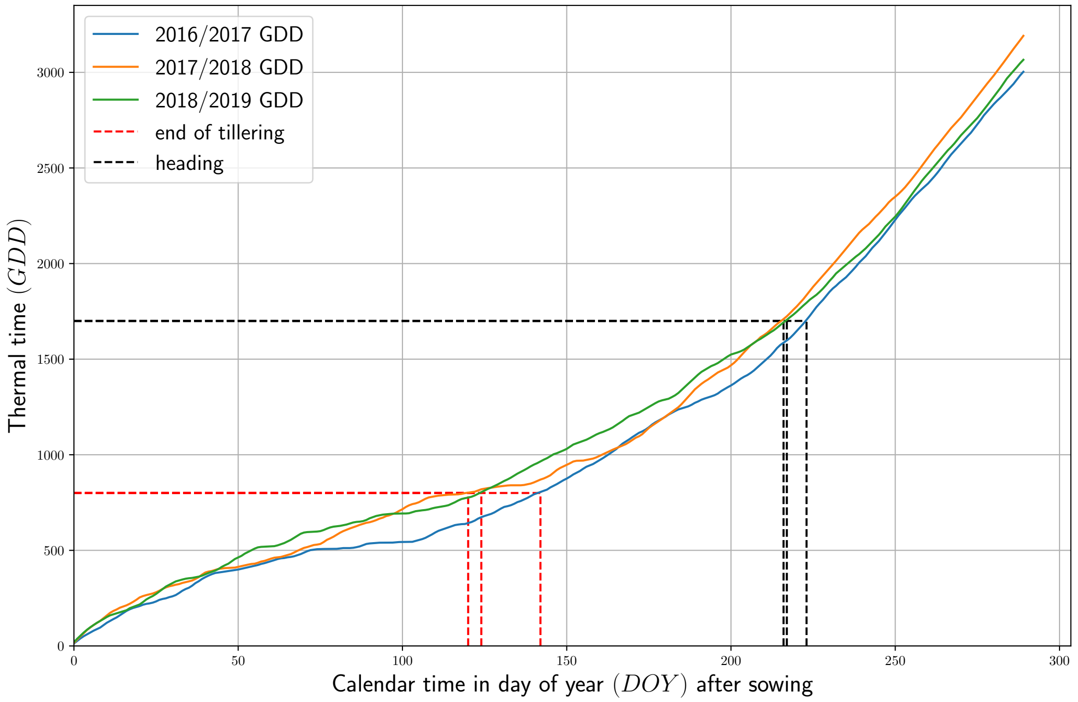

*Figure 2.18:* ***Evolution of soft winter wheat thermal time (growing degree day (GDD)) according to calendar time (Day of Year (DOY)) with*** $T_{Base} = 0^{\circ}C$ ***and*** $T_{Treshold} = 28^{\circ}C$ ***over three agricultural campaigns,*** 2016/2017, 2017/2018 ***and*** 2018/2019 ***in area France-East. For illustration purposes, soft winter wheat estimated temperature accumulation of end of tillering and heading stages are represented by red and black dotted curves, respectively.***

*Table 2.6:* ***Sentinel-1 acquisition dates in the France-East area of interest over the three study seasons.***

| **Usage** | **Campaign** | **2d-CNN-CT**<br>S-1 chosen dates (2016/2017) and corresponding calendar dates (2017/2018; 2018/2019) | **2d-CNN-TT**<br>S-1 estimated corresponding times in thermal time (2017/2018; 2018/2019) |
|---|---|---|---|
| **Train** | 2016/2017 | November 04, 16, 28; December 10, 22; January 03, 15, 27; February 02, 14, 26; March 04, 16, 28; April 09, 21; May 03, 15, 27. | – |
| **Test** | 2017/2018 | November 05, 17, 29; December 11, 23; January 04, 16, 28; February 03, 15, 27; March 05, 17, 29; April 10, 22; May 04, 16, 28. | October 30; November 08*, 23; December 08*, 20*, 23, 29, 29; January 04, 16, 25*; February 09; March 09*, 26*; April 10, 19*, 22; May 07*, 20*. |
| | 2018/2019 | November 05, 17, 29; December 12, 23; January 04, 16, 28; February 04, 16, 28; March 05, 17, 29; April 10, 22; May 04, 16, 28; | November 04*, 09*, 24, 30; December 06, 09*, 18, 18, 24; January 11; February 08*, 16, 28; March 12, 29; April 09*, 20*; May 02*, 23. |

* S1 images with descending orbit direction.

In order to have an idea of the shifting (in calendar dates) that can be created during a re-alignment operation according to thermal times for the **2d-CNN-TT** experiment, the scheme 2.19 has been established.

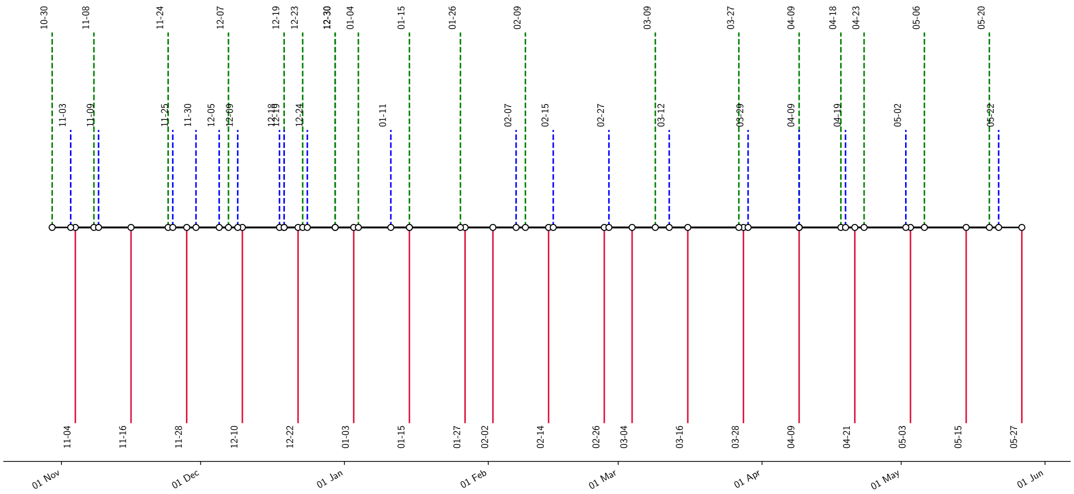

*Figure 2.19: The schematization of the expected acquisition dates for Sentinel-1 images: these dates are estimated based on a time series of calendar dates of the 2016/2017 farming campaign (dates chosen in advance, in red color). On the one hand, the thermal times corresponding to each of these dates are calculated. On the other hand, the thermal times between the beginning and the end of the 2017/2018 and 2018/2019 farming campaigns are calculated (with an estimated start date of 15 October for each season, the base and saturation temperature considered are those of wheat), then for each campaign, 2017/2018 (in green color) and 2018/2019 (in blue color), the calendar dates corresponding to the accumulated degree-days and coinciding with the degree-days of the 2016/2017 season previously calculated are deducted. Just mentioning that the dates written in bold are repeated twice or very close (30 December for 2017/2018, 18 and 19 December for 2018/2019 seasons), which corresponds to thermal times which evolved very slightly between the two dates because of the low temperatures.*

*Table 2.7: Summary results of proposed convolutional approach evaluated on soft winter wheat, trained over 2016/2017 campaign data. Just note that for experiments 2d-CNN-CT $_{\textit{Spectral-Temporal-Conv}}$ and 2d-CNN-TT $_{\textit{Spectral-Temporal-Conv}}$, since we use 3 bands in the case of the Sentinel-1 data, the reported results for each of the two experiments are the best between the one with model using a convolution filter of shape* $(2, \bar{t})$ *and the one with a model using a convolution filter shape of* $(3, \bar{t})$*, see the last paragraph in 2.3.6 for more details.*

| Test campaign | 2017/2018 | | 2018/2019 | |
|---|---|---|---|---|
| Metric | Overall accuracy | F1-score | Overall accuracy | F1-score |
| 2d-CNN-CT $_{\textbf{Temporal-Conv}}$ | 0.86 | (0.91, 0.73) | **0.96** | **(0.97, 0.92)** |
| 2d-CNN-TT $_{\textbf{Temporal-Conv}}$ | **0.94** | **(0.96, 0.89)** | 0.92 | (0.95, 0.85) |
| 2d-CNN-CT $_{\textbf{Spectral-Temporal-Conv}}$ | 0.85 | (0.91, 0.71) | 0.95 | (0.96, 0.89) |
| 2d-CNN-TT $_{\textbf{Spectral-Temporal-Conv}}$ | 0.93 | (0.95, 0.87) | 0.90 | (0.94, 0.83) |

Best result for each season shown in bold font.

The results obtained with the convolutional model trained on the 2016/2017 agricultural campaign data for the recognition of soft winter wheat are summarized in the table 2.7.

Figures 2.20 and 2.21 give a visual aspect to the prediction results of soft winter wheat pixels for the **2d-CNN-TT** $_{\textbf{Temporal-Conv}}$ and **2d-CNN-CT** $_{\textbf{Temporal-Conv}}$ approaches, respectively.

In each of the two figures, visual (a) represents the ground truth of the soft winter wheat cropland cover, extracted from the RPG, and visual (b) represents the output predicted by the model.

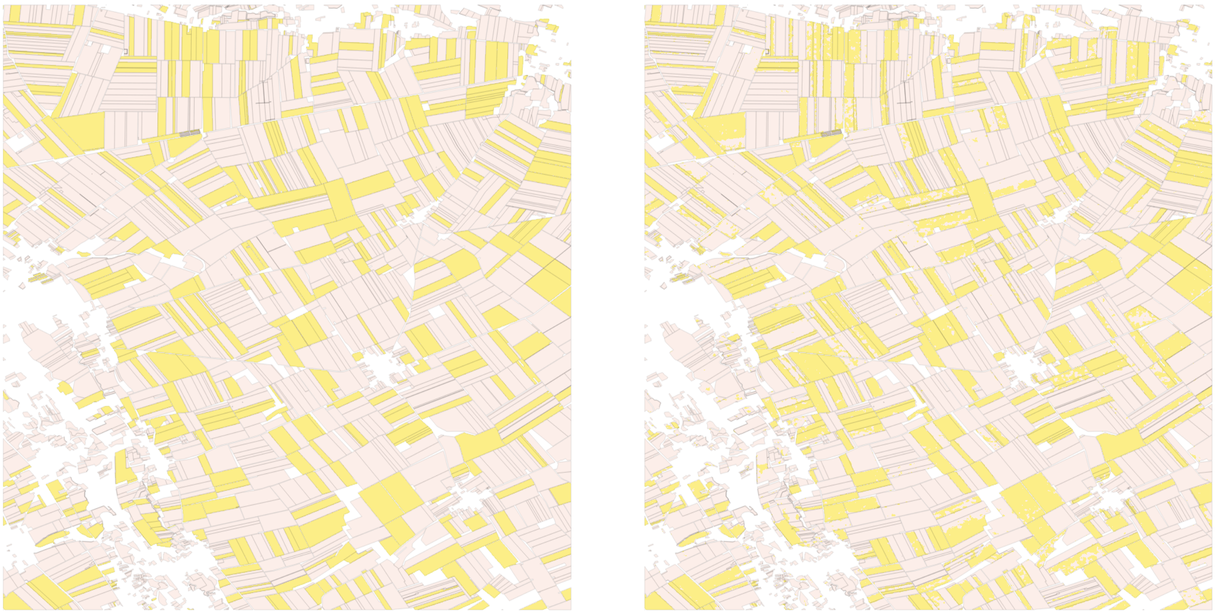

*(a) Effective land cover* *(b) Model prediction land cover*

***Figure 2.20:** Visualization of observed and predicted crop rotation of soft winter wheat parcels under the 2d-CNN-TT $_{Temporal\text{-}Conv}$ experiment in the studied sub-area of France-East zone over the campaign 2017/2018. Yellow pixels are those of soft winter wheat crop, the remaining pixels represent other crops.*

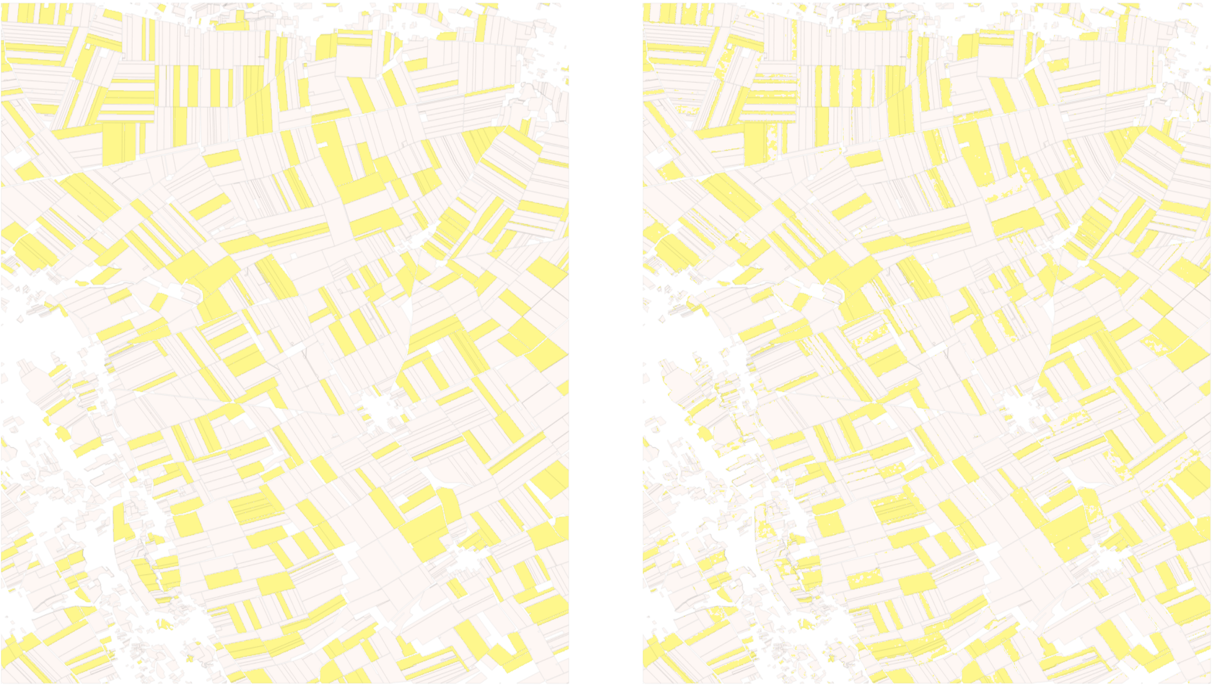

*(a) Effective land cover* *(b) Model prediction landcover*

***Figure 2.21:** Visualization of observed and predicted crop rotation of soft winter wheat parcels under the 2d-CNN-CT $_{Temporal\text{-}Conv}$ experiment in the studied sub-area of France-East zone over the campaign 2018/2019. Yellow pixels represent the soft winter wheat crop, the remaining pixels represent the rest of the crops.*

In order to evaluate the impact and the importance of the choice of the prediction date on the performance of the proposed models, the following experiment has been conducted : the 2d-CNN model is trained with time series starting at the beginning of November and going to dates between the first half of April and the second half of May (or the equivalent with the thermal time experiments). The results of this test with the experiments **2d-CNN-TT $_{\textbf{Temporal-Conv}}$** on 2017/2018 campaign and **2d-CNN-CT $_{\textbf{Temporal-Conv}}$** on 2018/2019 campaign are shown in figures 2.22 and 2.23, respectively.

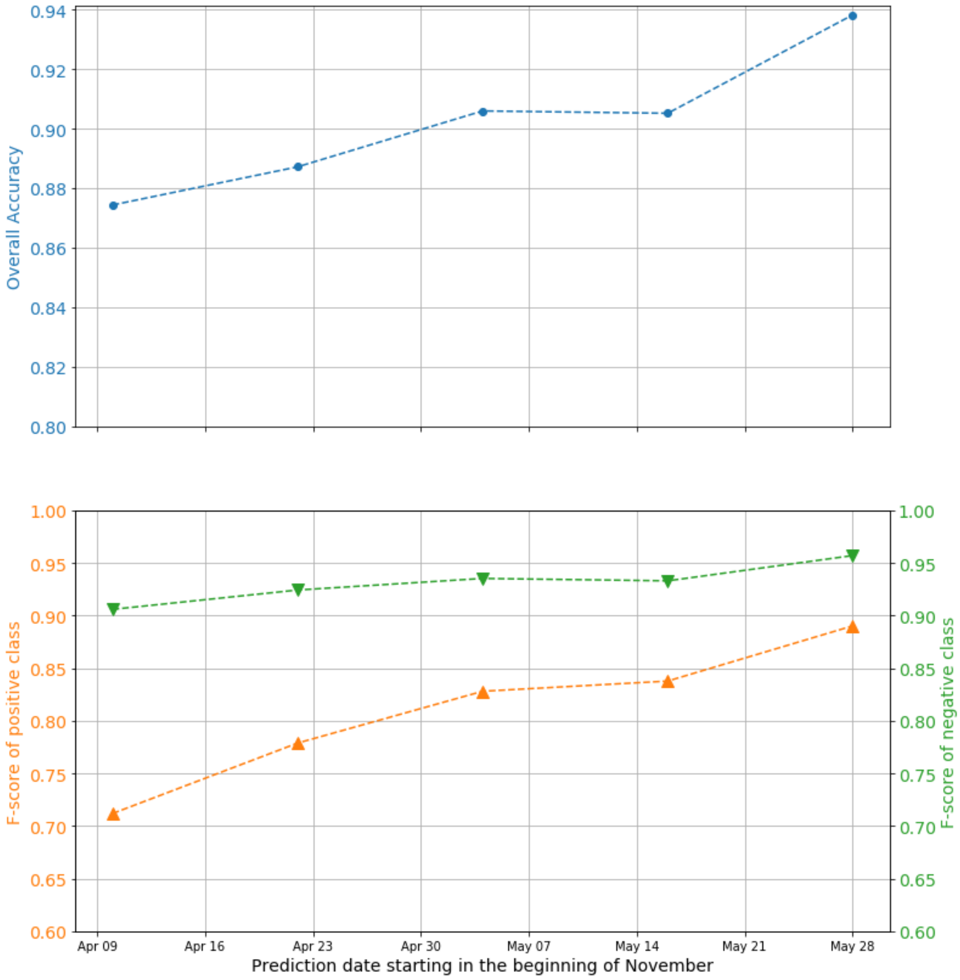

*Figure 2.22: Temporal precision evaluation for the experiment 2d-CNN-TT $_{\text{Temporal-Conv}}$ over the campaign 2017/2018.*

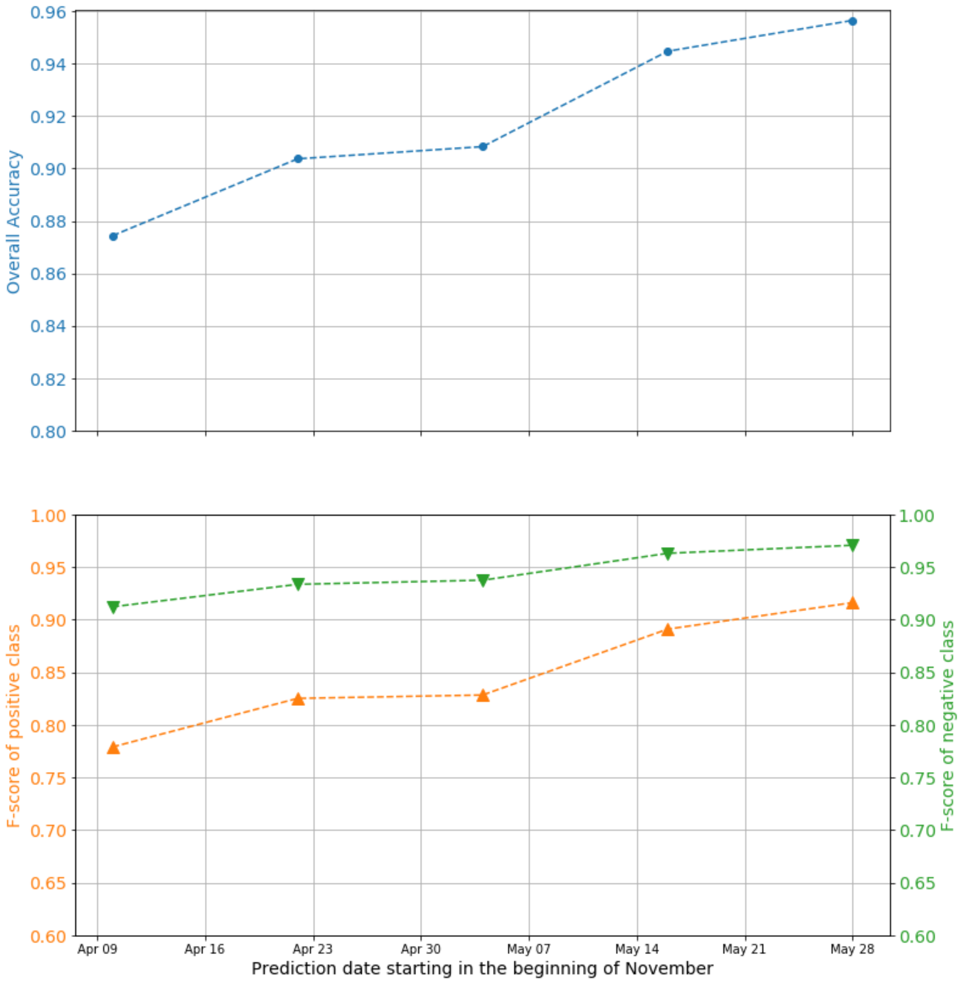

*Figure 2.23: **Temporal precision evaluation for the experiment 2d-CNN-CT $_{\text{Temporal-Conv}}$ over the campaign 2018/2019.***

As a global statement that can be deduced from these two graphs, the performance of the convolutional model improves with increasingly late prediction dates. this is due to the fact that at later dates, the plants of a given crop develop more properties that enable them to be distinguished from other crops. these characteristics are captured by the imagery and subsequently taken into account in the model. In fact, the accuracy of the models developed in our work will depend heavily on the desired prediction timing.

### Target crop 2: winter rapeseed

Winter rapeseed, present in almost all of the French territory, is another crop we have been interested in during our work. In addition to being a plant rich in oil and vegetable proteins, rapeseed has beneficial effects in cereal rotations by allowing a rupture in the cycle of cereal diseases and weeds as well as improving the organic state of the soil. Its high nitrogen requirements, particularly in autumn and winter, reduce nitrate losses through soil leaching during these very sensitive periods. Rapeseed also reduces the risk of erosion due to its relatively long soil cover. Refer to document [1] for more details

Experiments were conducted in the France-Center area of interest located in the region centre of France, whose geographical coordinates and statistics concerning the ten predominant crops, over the two agricultural campaigns of 2016/2017 and 2017/2018, were illustrated in the above-mentioned figure 2.11.

Winter rapeseed is planted at the end of the summer and harvested in July, it covers the soil for about 300 days. The sowing date can vary from the beginning of August for precocious sowing to the end of the first half of September for tardive sowing. This date depends on several parameters such as soil type, soil nitrogen availability, and climate, more particularly, temperature and rainfall. For the purposes of our study, and as we do not have information on exact sowing dates, we have estimated sowing to an arbitrary date of 1 September for each season studied.

The climatic ERA5 [Hersbach et al., 2020] points retained in these experiments over the France-Center area are the two points marked in red on figure 2.24, and we have created the intermediate point marked in yellow in the same figure, which represents the average of the data from the two red points taken.
An initial comparative analysis of the temperature curves between the three seasons of interest allows us to see, through figure 2.25, different temperature profiles. Globally, it can be said that the temperature profiles of the three seasons are more or less different. Also, abrupt drops in temperature near $-5°C$ are registered at different periods for the two seasons 2016/2017 and 2017/2018 particularly. The 2016/2017 season recorded two frost episodes in January, whereas such episodes occurred at the beginning and end of February for the 2017/2018 season, with slightly more intensity. These episodes of extreme frost are less intense for the 2018/2019 season, it is in fact the warmest season on average among the three seasons.

---

[1] Document Terresinovia, Les atouts du colza, Aurore BAILLET, 18 juin 2019

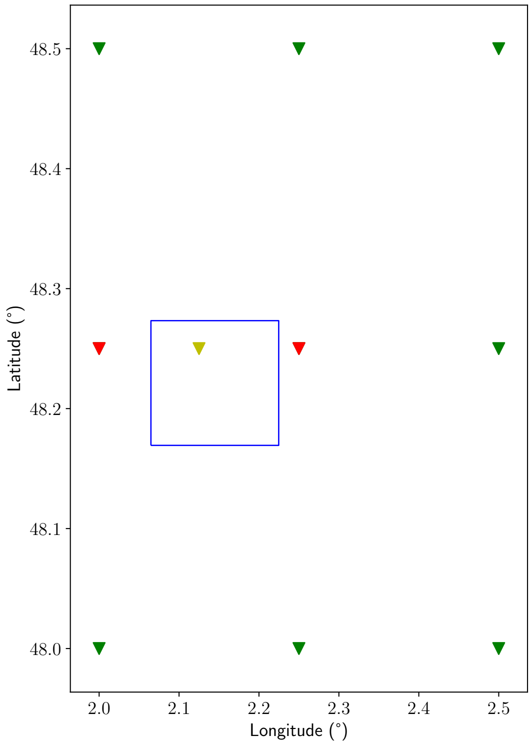

***Figure 2.24:* Green marked ERA5 points located close to the France-Center area of interest, whose bounding box is showed in blue color. The point marked as yellow corresponds to the chosen averaged both red ERA5 points.**

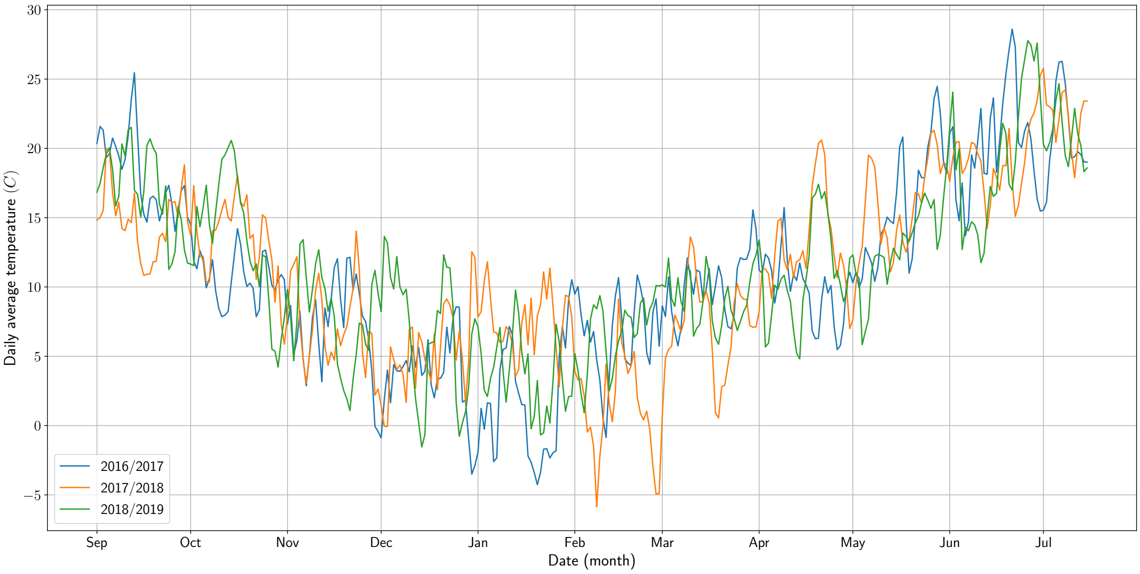

***Figure 2.25:* Average daily temperatures recorded in the France-Center area over the three 2016/2017, 2017/2018, and 2018/2019 seasons since the estimated sowing date of the target crop.**

With the aim of trying to understand how the winter rapeseed parcels studied could grow under such temperatures, the curves in figure 2.26 showing the evolution of thermal times in winter rapeseed parcels from the estimated sowing date for all seasons was plotted. The calculation

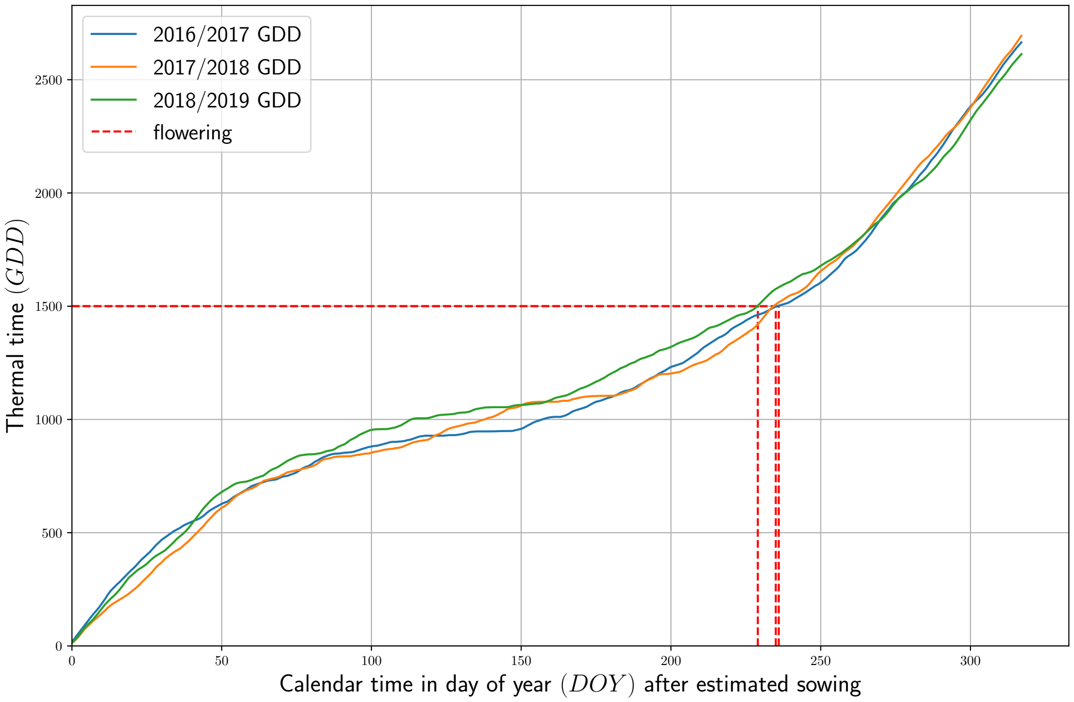

*Figure 2.26:* ***Evolution of winter rapeseed thermal time (growing degree day (GDD)) according to calendar time (Day of Year (DOY)) with $T_{Base} = 3°C$ and $T_{Treshold} = 28°C$ over the agricultural campaigns, 2016/2017, 2017/2018 and 2018/2019 in France-Center area. For illustration purposes, the winter rapeseed estimated temperature accumulation of F1 flowering stage (considered reached when at least 50% of the plants with an open flower) is represented by a red dotted curve. The time lag in calendar time is equal to 2 days between the two first seasons.***

of thermal times was made assuming a base temperature $T_{Base} = 3°C$ and a saturation temperature $T_{Treshold} = 28°C$. The red dashed lines represent the accumulated temperatures of winter rapeseed plants at the flowering stage, also called F1 (according to the works of [d'Andrimont et al., 2020], about 425 growing degree days are needed to reach flowering beginning on 1 January, this obviously remains an order of magnitude, as we are not working on the same regions and probably not the same cultural practices and rapeseed cultivars).

Two major phases can be seen through these curves. A first phase that starts at sowing and terminates around the beginning of flowering with curves of the thermal times of whole seasons that most often diverge. Then follows a second phase that starts at flowering (around day 240 after sowing), where the curves become smoother and closer to each other, especially for the first two seasons, until the end of the plant cycle.
This *"pivot"* period around flowering seems particularly interesting in a perspective of the choice of the time series dates for our winter rapeseed recognition models.

We, therefore, investigated the profiles of the Sentinel-1 radar backscatter on winter rapeseed parcels surveyed, whose geographical coordinates are shown in figure 2.27.

As an illustration, figure 2.28 describes the evolution of the average backscatter in $\sigma^0_{VV}$ polar-

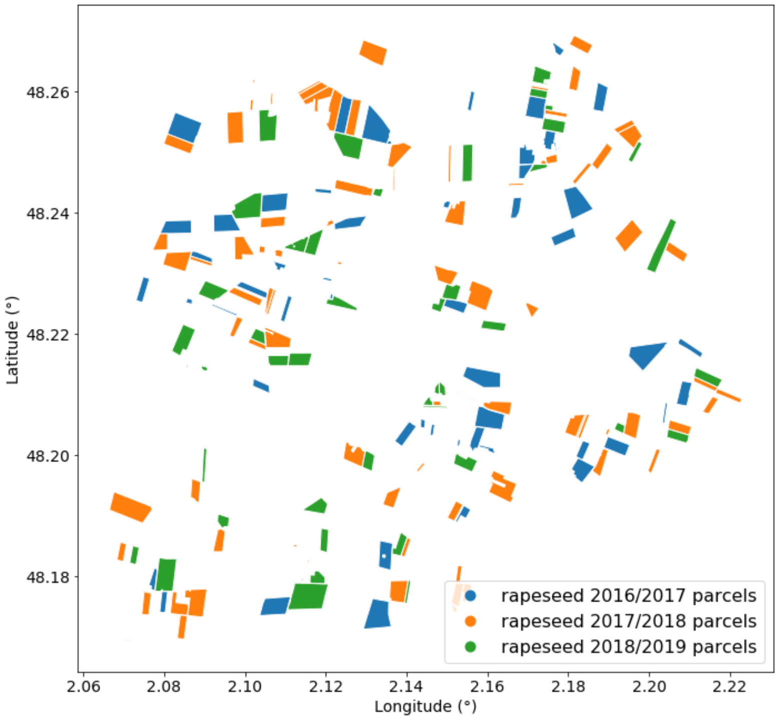

*Figure 2.27:* ***Location of the winter rapeseed parcels studied for the three farming seasons, 2016/2017 in blue color, 2017/2018 in orange color, and 2018/2019 in green color.***

ization of the winter rapeseed parcels over the three seasons. It can be seen that the two phases previously described based on the curves of thermal times in figure 2.26, are also present in the current figure, with relatively different profiles from sowing to the first half of April and then profiles of $\sigma^0_{VV}$ that vary in a quasi-similar way, at relatively different magnitude, however, since the second half of April.

According to [d'Andrimont et al., 2020], the flowering peak, they defined as when 50% of the plants are at this stage, occurs at the local minimum of the $\sigma^0_{VV}$ curve around this period of spring. This flowering peak is effectively observed around the last days of April in our study parcels, marked by the black dashed line in 2.28 and corresponds well to the 240 days after sowing as discussed above.

What these $\sigma^0_{VV}$ backscatter curves reveal is that, a priori, if one works with time series of images with dates around this flowering stage, a convolutional model with an alignment in calendar time, previously noted by 2d-CNN-CT $_{\textbf{Temporal-Conv}}$ and 2d-CNN-CT $_{\textbf{Spectral-Temporal-Conv}}$ approaches, should be sufficient to achieve satisfactory performance.

We, therefore, chose to work with Sentinel-1 data acquired during the flowering period. The dates taken into account in the training and testing of our convolutional winter rapeseed detection models are summarized in table 2.8.

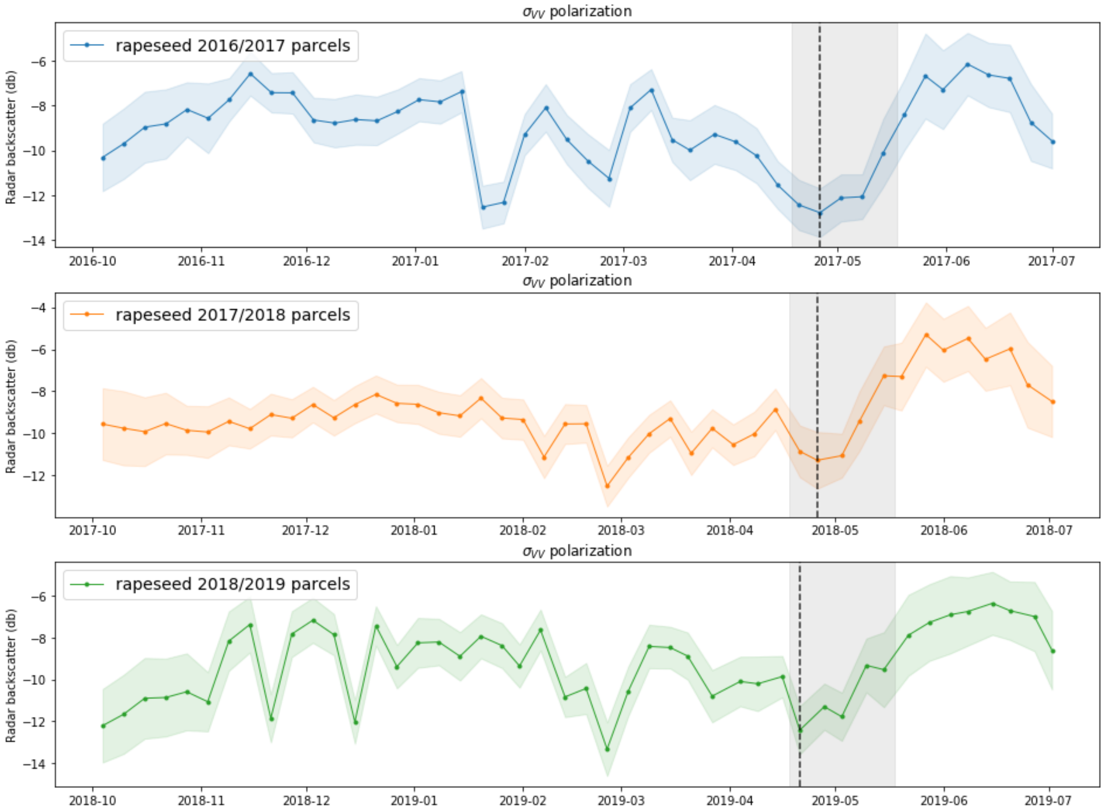

*Figure 2.28: Average radar backscatter evolution in $\sigma^0_{VV}$ polarisation over France-Center winter rapeseed parcels over the three study seasons. For each graph, the vertical black dashed line corresponds, eventually, to the date when the flowering peak occurs. The grey area corresponds to the interval of the dates, around the flowering stage, chosen for the winter rapeseed crop recognition models, this will be discussed below.*

The results of the evaluation of the convolutional approach are presented in table 2.9 and the comparative visuals, between ground truth and model prediction, obtained from the **2d-CNN-CT $_{\textbf{Temporal-Conv}}$** experiment over the 2017/2018 and 2018/2019 farming seasons are shown in figures 2.29 and 2.30, respectively.

*Table 2.8:* ***Sentinel-1 acquisition dates in the France-Center area of interest over the three study seasons.***

| **Usage** | **Campaign** | **2d-CNN-CT**<br>S-1 selected dates (2016/2017) and corresponding calendar dates (2017/2018; 2018/2019) |
|---|---|---|
| **Train** | 2016/2017 | April 18, 24, 30;<br>May 06, 12, 18. |
| **Test** | 2017/2018 | April 18, 24, 30;<br>May 06, 12, 18. |
| **Test** | 2018/2019 | April 19, 25;<br>May 01, 08, 13, 19. |

*Table 2.9:* ***Summary results of proposed convolutional approach evaluated on winter rapeseed, trained over 2016/2017 campaign data, and evaluated on both 2017/2018 and 2018/2019 campaigns. Note that for experiment 2d-CNN-CT $_{\text{Spectral-Temporal-Conv}}$, since we use 3 bands in the case of the Sentinel-1 data, the reported results are the best between the one with a model using a convolution filter of shape $(2, \bar{t})$ and the one with a model using a convolution filter shape of $(3, \bar{t})$, see the last paragraph in 2.3.6 for more details.***

| Test campaign | 2017/2018 | | 2018/2019 | |
|---|---|---|---|---|
| Metric | Overall accuracy | F1-score | Overall accuracy | F1-score |
| 2d-CNN-CT $_{\text{Temporal-Conv}}$ | **0.99** | **(0.996, 0.94)** | **0.99** | **(0.99, 0.915)** |
| 2d-CNN-CT $_{\text{Spectral-Temporal-Conv}}$ | 0.98 | (0.98, 0.93) | 0.98 | (0.98, 0.91) |

Best result for each season shown in bold.

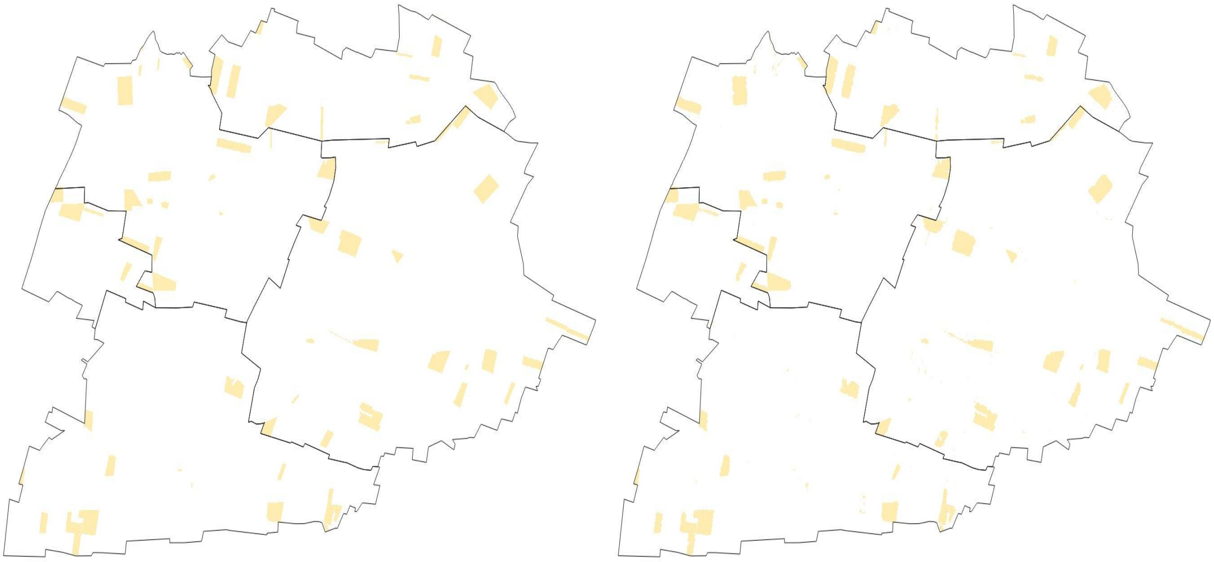

*(a) Effective land cover* *(b) Model prediction land cover*

*Figure 2.29: Visualization of observed and predicted crop rotation of winter rapeseed parcels under the 2d-CNN-CT$_{\text{Temporal-Conv}}$ experiment in France-Center zone over the farming campaign 2017/2018. Yellowish-brown pixels represent the winter rapeseed crop, the remaining pixels represent the rest of the crops.*

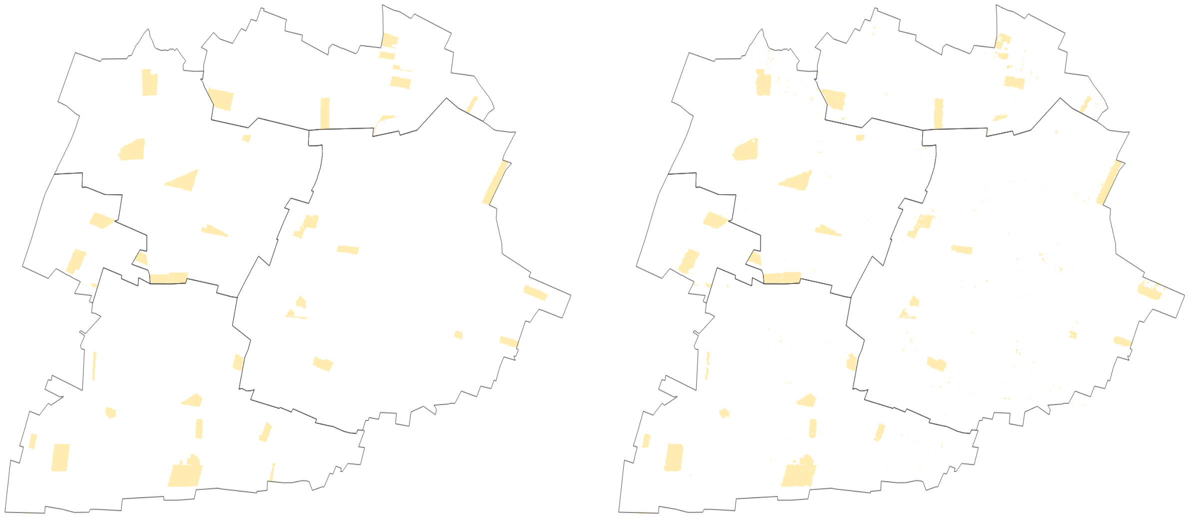

*(a) Effective land cover* *(b) Model prediction land cover*

*Figure 2.30: Visualization of observed and predicted crop rotation of winter rapeseed parcels under the 2d-CNN-CT$_{\text{Temporal-Conv}}$ experiment in France-Center zone over the farming campaign 2018/2019. Yellowish-brown pixels represent the winter rapeseed crop where the remaining pixels represent the other crop types.*

### Target crop 3: beet

*Table 2.10: Sentinel-1 acquisition dates in the France-Center area of interest for beet experiments.*

| **Usage** | **Campaign** | **2d-CNN-CT**<br>S-1 selected dates (2016/2017) and corresponding calendar dates of 2017/2018 season |
|---|---|---|
| **Train** | 2016/2017 | May 6, 12, 18, 24, 30; June 6, 12, 18, 24, 30; July 6, 12, 18, 24, 30; August 5, 11, 17. |
| **Test** | 2017/2018 | May 6, 12, 18, 24, 30; June 6, 12, 18, 24, 30; July 6, 12, 18, 24, 30; August 5, 11, 17. |

*Table 2.11: Summary results of proposed convolutional approach evaluated on beet, trained over 2016/2017 campaign data, and evaluated on 2017/2018 campaign in France-Center area. For experiment 2d-CNN-CT $_{\text{Spectral-Temporal-Conv}}$, and since we use 3 bands in the case of the Sentinel-1 data, the reported results are the best between the one with a model using a convolution filter of shape (2, $\bar{t}$) and the one with a model using a convolution filter shape of (3, $\bar{t}$), see the last paragraph in 2.3.6 for more details.*

| Test campaign | 2017/2018 | |
|---|---|---|
| Metric | Overall accuracy | F1-score |
| 2d-CNN-CT $_{\textbf{Temporal-Conv}}$ | **0.98** | **(0.988, 0.935)** |
| 2d-CNN-CT $_{\textbf{Spectral-Temporal-Conv}}$ | 0.96 | (0.97, 0.92) |

Best result for each season shown in bold.

*(a) Effective land cover* *(b) Model prediction land cover*

*Figure 2.31: Visualization of observed and predicted crop rotation of winter rapeseed parcels under the 2d-CNN-CT $_{Temporal\text{-}Conv}$ experiment in France-Center zone over the beet farming campaign 2017/2018. Purple pixels constitute the beet crop parcels where the remaining pixels represent the other crops.*

## 2.5 Discussion

We could see, through the preliminary tests of the **intra-annual** approach, how the proposed multi-temporal convolutional binary models, aimed at identifying crop types, perform on all the tested crops. In such an approach, a model is trained on a part of the parcels (more exactly pixels), and tested on another part of the parcels. The effect of climatic variability in this case study is limited, and very satisfying performances are achieved on all the crops studied.

Then, we aimed to reveal, through the presented experimental tests, the interest that the proposed **inter-annual** approach can provide, with a data preparation phase of the satellite time-series, either aligned along the calendar time or aligned according to the thermal time in some particular temperature conditions that can directly impact the normal process of plant growth.

Through the first stage of experimentation on soft winter wheat, we wanted to evaluate the capabilities of the proposed inter-annual convolutional approach in the recognition of this crop.

The obtained results show both the interest of the temporality of the satellite data in improving performance, as seen in the tests for the 2018/2019 farming campaign, but also the contribution of a thermal time alignment in particular temperature conditions, which differs at significant growth stages from the temperature conditions of the season over which the model was trained, as seen for the 2017/2018 soft winter wheat farming campaign.

It was also noted that globally, the test performances on data aligned in calendar time remain slightly higher than the test results on data aligned in thermal time. This is probably due to various reasons.
Indeed, as previously discussed, and to ensure maximum coherence and to avoid the effect of morning dew, we restrict ourselves to Sentinel-1 data with an ascending orbit direction. However, and contrary to a calendar time alignment, a thermal time alignment imposes, for reasons of data availability, to use the descending mode in addition to the ascending orbit direction, and this contributes to this performance reduction, even when compared to an alignment according to calendar time. Without neglecting the inevitable delay of one or two days between the date desired and the date available, as mentioned earlier in this section.

The experiments that followed on winter rapeseed revealed an important aspect : each crop has its own specific way to deal with particular climatic conditions such as frost. Evidently, this depends on the intensity of these climatic conditions, but also on the ability of each type of crop to resist/tolerate to/the climatic conditions.

In fact, winter rapeseed has a certain capacity to resist to extreme cold and to tolerate negative temperatures (until $-17°C$ [2]), a capacity acquired during the period extending from sowing to the rosette stage, also called 8-leaf stage, reached at approximately 600 GDD. This period is being followed by another phase, the vernalization, which is a process that usually takes place at the end of autumn and continues into winter, that allows the transition from the vegetative

---

[2] André Merrien et Nathalie Landé, Rencontres Techniques Régionales, ”PHYSIOLOGIE DU COLZA : mise en place du rendement”, CETIOM (2009).

phase to the reproduction phase, during which the plants requires a winter period with temperatures below $10°C$ in order to complete its vegetative cycle (the optimum winter rapeseed vernalization temperatures are between $3$ and $7°C$ [2]). Afterward, the floral transition phase takes place, marking the end of the vernalization and the progressive passage to the flowering stage, which can take 4 to 6 weeks [3] and requires relatively fresh temperatures (ideally between $10$ and $25°C$).

Through this information on the tolerance levels of winter rapeseed, and the results obtained by the convolutional winter rapeseed recognition models, it can be deduced that in an inter-season approach, if climatic disparities, notably of temperatures, are present but are not extreme, i.e. remains in the forks tolerated by the winter rapeseed plants, the latter finish by regaining similar levels of growth, as around flowering stage and the formation of siliques also known as pods, in our rapeseed case study in France-Center. This may contribute to the good performance of our winter rapeseed recognition models with input radar images aligned according to calendar times around these periods.
Of course, these good performances are mainly due to the fact that during these periods around flowering for our rapeseed first case study, winter rapeseed plants developed specific characteristics, particularly geometric such as plant height, foliage and flowers characteristics and orientation, which make the signal captured by the radar from these plants different from the signals from other crops plants present at the same time and in the same study area, at least in France.

Consequently, the winter rapeseed convolution model trained with a time series of dates around flowering during the 2016/2017 farming season performed very well while testing over the two following seasons, still with imagery data around flowering, even if it was noted that the test results for the last 2018/2019 season were slightly less good than those obtained in the test over the 2017/2018 season.
This is because the higher temperatures in the 2018/2019 season generated a potential slight advance in the growth of winter rapeseed plants compared to the two remaining seasons. This growth advance could be observed on the thermal time evolution in figure 2.26, and translated into a slight advance of the date of the local minimum of the backscatter signal at $\sigma^0_{VV}$ polarisation around flowering, on the green curve of the graph 2.28.

The proposed approach allows detection on a pixel level (with a spatial resolution of 10 meters in the case of Sentinel-1 radar images). The models can therefore operate without ”à priori” agricultural parcel delimitation, or be confronted with a given parcel delimitation to extract the most probable crop on the parcel with an uncertainty of identification of the crop (the type of crop on the parcel will then be that of the majority of pixels making up this same parcel), or even detect potential delimitation errors in the parcel provided.

As an example, the yellow parcel in figure 2.32 below within the 2017 parcel delimitation in

---

[3] Document of ”Institut national agronomique Paris-Grignon INA P-G, Département AGER” (2003) on rapeseed published via the Agroparistech course platform.

*Figure 2.32:* ***Example of a yellow-colored spring barley parcel in the 2016/2017 farming season, for which the proposed model detected a very clear change of disposition, with a passage to half beet, half spring barley in 2017/2018 season.***

the French region centre has visibly changed its disposition, switching from all spring barley in 2017 to half beet, half spring barley in 2018, this was effectively verified when the RPG for this latest year was made available online.

Moreover, the spatial resolution of the satellite images used induces parcel border effects and can impact, by underestimating or overestimating, the prediction results of our models.
In effect, with a pixel resolution of 10 meters, it is quite complex to differentiate between a field of a given crop type and its surroundings (which may be roads, constructions, etc.), this is one of the limitations of using Sentinel-1 data in the proposed pixel-based approach.

Furthermore, pixels adjacent to two (respectively, to several) different crop type fields, will necessarily be predicted as belonging to one crop type at the detriment of the other crop type (respectively, of other crop types). Therefore, the more spatial resolutions of the imagery data used are fine (i.e., smaller pixels), the better are the results, knowing that the proposed models are easily adaptable to imagery data that may come from other satellites or even other imagery sources.

## Chapter 3

# Estimation of plant bio-physical variables by satellite imagery : case of biomass of some major crops

## 3.1 Biomass estimation

### 3.1.1 Introduction to remote sensing for plant bio-physical variables estimation : Review and research problem description

The considerable potential of microwaves and Sentinel-1 backscatter for vegetation monitoring and estimation of Vegetation Water Content (VWC), biomass, Leaf Area Index (LAI), and height for winter cereals, corn, and oilseed-rape during two growing seasons was reported in [Vreugdenhil et al., 2018]. In another interesting study, Veloso et al. [Veloso et al., 2017] compared Sentinel-1 time series to optical NDVI time series for a variety of winter and summer crops (wheat, rapeseed, corn, soybeans, and sunflower) over several test sites in France. The time series of NDVI and radar backscatter are analyzed and physically interpreted with the support of rainfall and temperature data, as well as the destructive in situ measurements (green area index (GAI) and fresh biomass). A detailed study in two experimental sites of corn and barley showed that the Sentinel-1 and NDVI data correlate to GAI and fresh biomass. These studies point out the interest of radar data and particularly the $\sigma^0_{VH}/\sigma^0_{VV}$ ratio band for crop monitoring (irrigated crops and early crop identification) and biophysical parameters estimation using both radar and optical data).

In [Steele-Dunne et al., 2017], the authors provide a complete overview of the current state of knowledge concerning radar backscatter from vegetated agricultural landscapes and identify opportunities and challenges in this domain. They showed, among many other topics covered, how radar could be highly suitable for crop monitoring and several other applications. They also explained how the crop scattering mechanism varies due to changes in geometry and orientation. For instance, they highlight the fact that during the growing period of a given crop, the scattering mechanism varies due to changes in the geometry and orientation of leaves and branches around the stem about the radar line of sight, underneath soil surface roughness, and vegetation dielectric constant.

In [Kumar et al., 2017], Sentinel-1 radar analysis of time series data at C-band was carried out to estimate five winter wheat growth parameters (leaf area index, vegetation water content, fresh biomass, dry biomass, and plant height) using different regression algorithms. The study, carried out using crop growth parameters in-situ measurements in India, demonstrates the good capability of the Sentinel-1 data for monitoring agricultural areas, and the random forest regression model provides a useful predictive tool for estimating winter wheat growth parameters. For another type of vegetation cover, the potential of Synthetic Aperture Radar (SAR) radar data at several wavelengths for mapping of above-ground biomass at the provincial level in a Mediterranean forested landscape (area test in central Italy) was discussed in [Laurin et al., 2018].

We aim to develop statistical models capable of estimating the biomass of plants from radar imagery data, such approach may be important in different contexts. For example, for winter rapeseed plants, estimating biomass at specific periods of the growth cycle can help regulate nitrogen fertilization, an opportunity that is detailed later in this manuscript in chapter 3.2. Moreover, biomass estimation can constitute a source of real-time data for data assimilation methods aiming to improve the predictive power of plant growth models, this is the purpose of the work in part 4 of this manuscript on soft winter wheat crop.

The objective here is not to develop the most complex and efficient possible models, but to evaluate, with quite simple supervised models based on real field measurements data, the potential and opportunities that Sentinel-1 imagery data can provide for the estimation of above-ground biomass.

Let $x \in \mathbb{R}$ represent radar backscatter at different time steps and $y \in \mathbb{R}$ represent the above-ground plant biomass associated with the backscatter value.

The relationship between these two variables can be modeled through a widely used empirical approach : regression analysis. This relationship, where we want to predict $y$ from $x$ with the predicted value $\hat{y}$, can be formulated as follows :

$$\hat{y} = wx + b \tag{3.1}$$

where $w \in \mathbb{R}$ is the slope parameter and $b$ is the intercept term (or bias parameter).

The estimation of the parameters w and b is obtained by minimizing the sum of the squares of the differences between the observations and the model linear approximation predictions, it is the criterion of least squares (LS) defined as follows :

For an observation sequence $(x_i, y_i), i = 1, \ldots, n$, the LS criterion consists in :

$$\min_{w,b} \sum_{i=1}^{n} (y_i - \hat{y}_i)^2$$

where the parameters w and b are estimated by :

$$w = \frac{\sum_{i=1}^{n} (x_i - \bar{x})(y_i - \bar{y})}{\sum_{i=1}^{n} (x_i - \bar{x})^2} \quad \text{and} \quad b = \bar{y} - w\bar{x}$$

For the $n$ observations samples, $\bar{x}$ and $\bar{y}$ represent the backscatter and the above-ground biomass samples means, consecutively.

### 3.1.2 Study areas and data

The study area is located on the Limagne plain, in the center of the Auvergne region in the north-east of the Puy-de-Dôme department (Fig. 3.1). Ten agricultural parcels of soft winter wheat, covering a total area of 1.5 $km^2$, and spreading over an area of 342 $km^2$, are being studied during the 2014/2015 season. Five different varieties of soft winter wheat are planted in the studied parcels (one variety per pair of parcels).

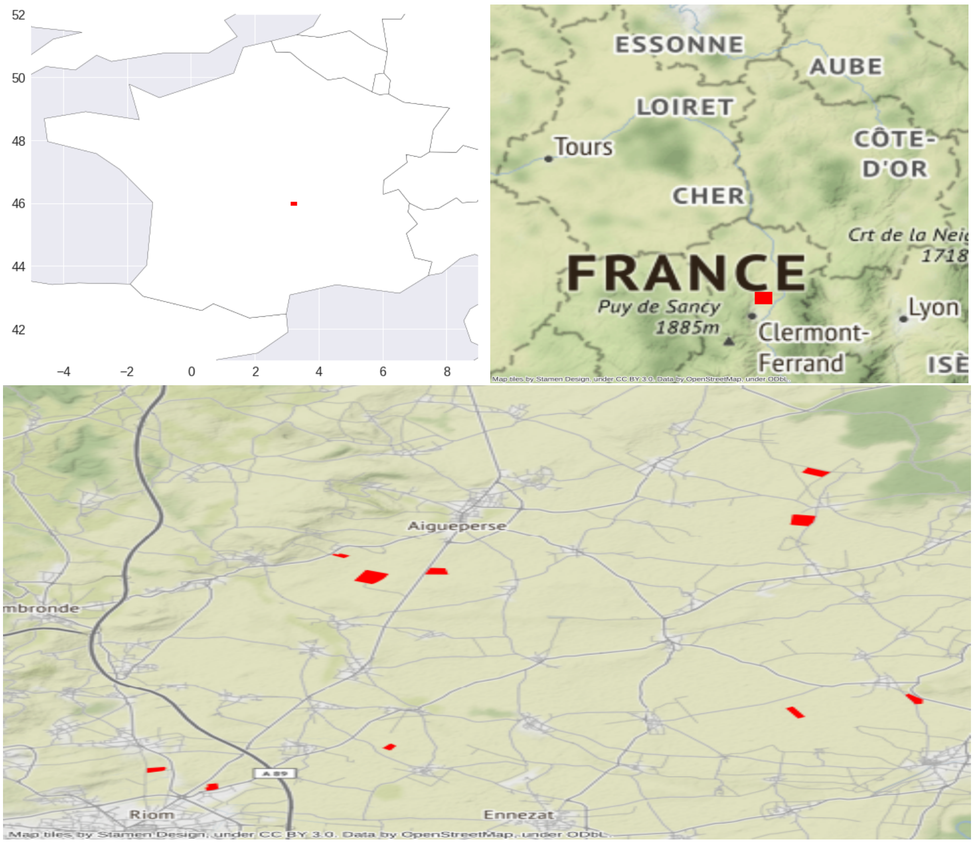

Map tiles by Stamen Design, under CC BY 3.0. Data by OpenStreetMap, under ODbL.

Map tiles by Stamen Design, under CC BY 3.0. Data by OpenStreetMap, under ODbL.

*Figure 3.1:* ***10 parcels of soft winter wheat in Limagne in the Auvergne region are being studied during the 2014/2015 agricultural season. Five varieties of soft winter wheat, one variety per pair of parcels, have been sown, with sowing dates ranging from 23 October to 23 December 2014.***

We are working with a time series of Sentinel-1 images, covering the studied parcels, acquired

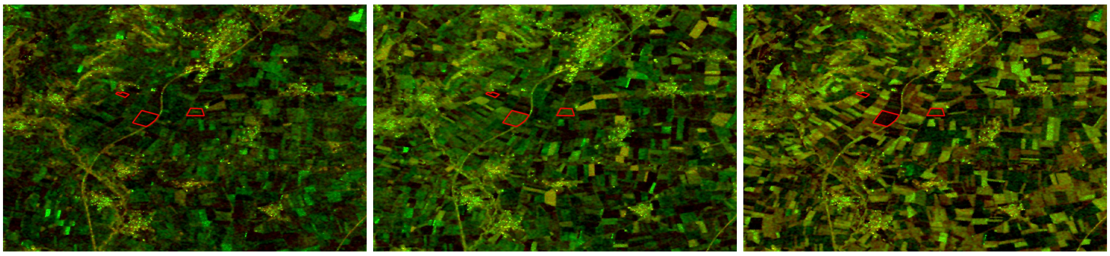

March 18, 2015 May 17, 2015 July 16, 2015

*Figure 3.2:* ***Illustration of the Sentinel-1 radar data used, a combination of $\sigma^0_{VH}$ and $\sigma^0_{VV}$ polarization, acquired at three different dates and covering three parcels, marked in red, in the study area.***

between the end of October 2014 and the end of July 2015 during the growth cycle of soft winter wheat (Table 3.1).

*Table 3.1:* ***Sentinel-1 acquisition dates in the studied area***

| Area of interest | Campaign | SAR Sentinel-1 acquisition dates |
|---|---|---|
| Limagne study area | 2014/2015 | October 25, November 01, 06, 14, 18, 25, 30 ;<br>December 08, 20, 31; January 01, 05, 13, 17, 29;<br>February 06, 17, 22; March 01, 06, 13, 18, 25, 30;<br>April 06, 11, 18, 23, 30; May 05, 12, 17, 24, 29;<br>June 05, 10, 18, 29; July 11, 16, 24, 28. |

The in situ biomass measurements data of the different plant compartments are measured according to a specific protocol of destructive biomass measurements per field (named *placette* in French in the biomass measurement protocol document).

Above-ground biomass data by plant compartments (total above-ground biomass, leaf, stem, and grain biomass, when possible) collected across 10 geo-located soft winter wheat parcels during the 2014/2015 crop year are available. Five varieties were sown, between 23 October and 23 December 2014, across these 10 parcels, with two varieties per parcel.

For 8 of the 10 parcels, the above-ground biomass was measured on 6 different dates between 2 March and 16 July 2015. For the remaining two plots, above-ground biomass was measured on 5 different dates between 24 March and 22 June 2015.

For the dates after 30 April 2015, total above-ground biomass, leaf biomass, and stem biomass were measured. For samples taken before 30 April, only the total above-ground biomass of the sample was measured, as it is difficult to accurately separate compartments in advanced stages.

For the grain biomass, these were measured for dates after 19 June 2015 (i.e. only 1 or 2 measurements for the parcels), on which samples were taken on 5 and 6 different dates respectively.

### 3.1.3 Methodology

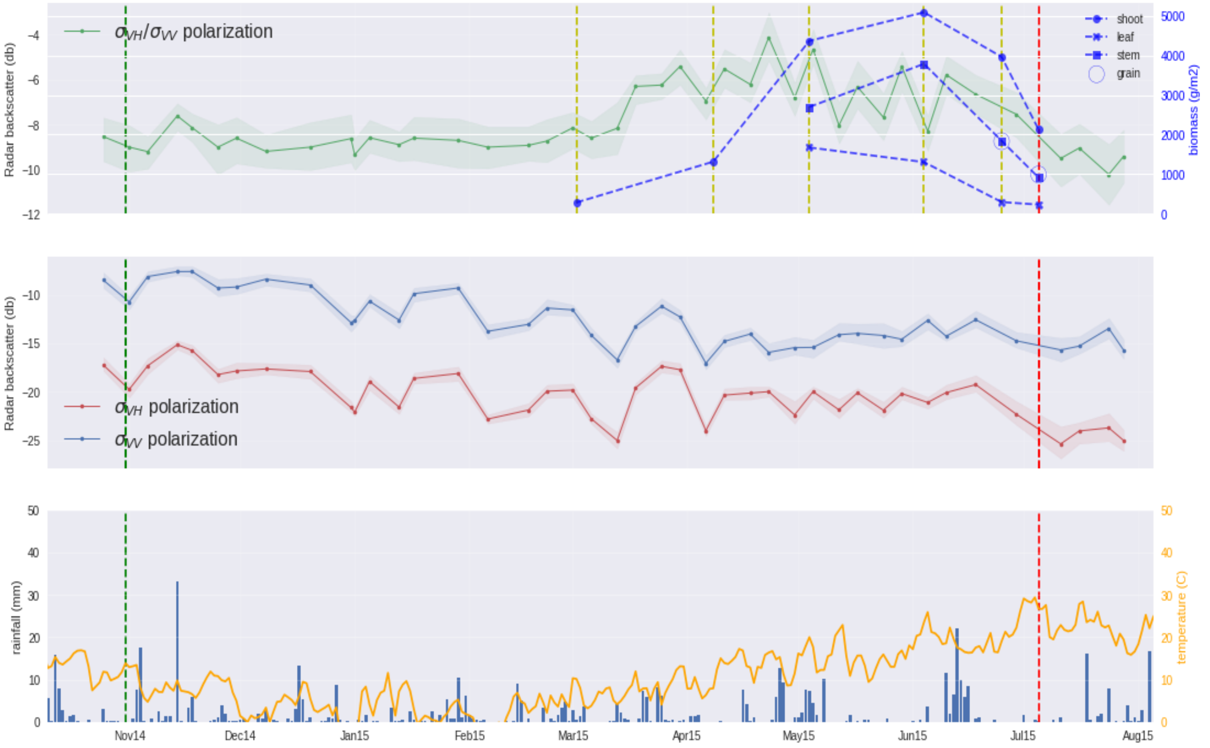

***Figure 3.3:* Temporal evolution of the signal ratio $\sigma^0_{VH}/\sigma^0_{VV}$, the two radar bands $\sigma^0_{VH}$ and $\sigma^0_{VV}$, biomass measurements, temperature, and precipitation for one of the study parcels. Sowing dates, different growth stages (early tillering, booting, 2 nodes, flowering, and senescence) as well as harvesting dates are indicated respectively by the green, yellow and red vertical lines.**

### Correlation study between biomass data and Sentinel-1 imagery data

To explore how the radar backscatter and above-ground biomass variables are related, we first perform a correlation analysis using Pearson's correlation coefficient $r$ defined using the following formula :

$$r = \frac{\sum_{i=1}^{n}(x_i - \bar{x})(y_i - \bar{y})}{(n-1)\ S_x S_y} \tag{3.2}$$

where $S_x$ and $S_y$ are the sample standard deviation of the two variables.

The results of the correlation study between the biomass data of the different plant compartments and the radar backscatter data from Sentinel-1 are presented.
First, variations in radar backscatter during the wheat growing season over the ten study parcels are analyzed. With the support of precipitation and temperature data, as well as biomass measurements of the different compartments and at different dates, an attempt was made to explain, physically in the field, the behavior of the radar backscatter on each of the ten parcels.

Figure 3.3 illustrates the variation of the $\sigma^0_{VV}$, $\sigma^0_{VH}$ and $\sigma^0_{VH}/\sigma^0_{VV}$ ratio bands during the wheat growing season on one of the studied parcels (Apache variety). Precipitation and temperature data, as well as the measured fresh biomass of the different plant compartments, are also shown in the figure.

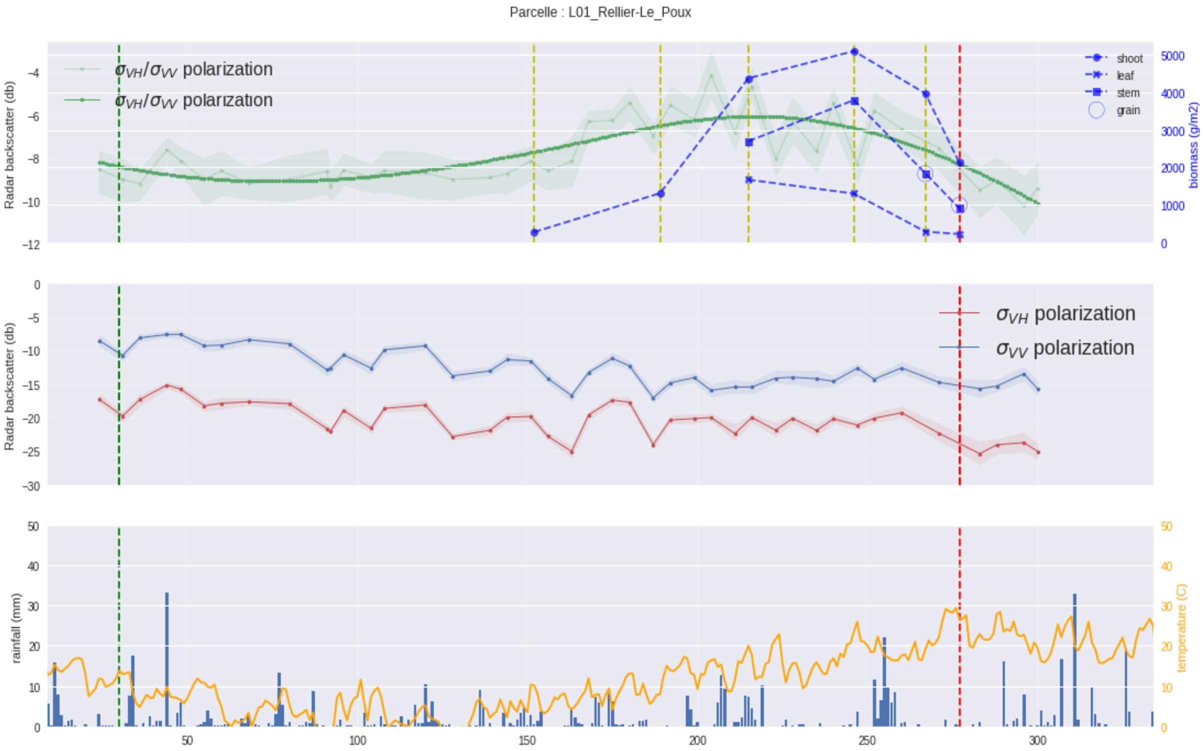

*Figure 3.4: **Filtering of the temporal evolution curve of the signal ratio $\sigma^0_{VH}/\sigma^0_{VV}$.***

The instability of the radar signal can be explained by variations in the structure, volume, and orientation of the plant, in addition to the impact of the soil (mainly the effect of soil smoothing due to rainfall, in addition to the roughness of the soil). For this reason, we proposed to apply a smoothing of the radar curve by interpolating the data with a cubic spline [Mckinley and Levine, 1998] as illustrated in the figure 3.4.

The basic idea of the cubic spline operation is that a series of unique cubic polynomials are fitted between each of the observations data points.
For $n$ data observations of variable $x$, the cubic spline function $S_i(x), i = \{1, \ldots, n-1\}$ can be defined by :

$$S_i(x) = a_i(x - x_i)^3 + b_i(x - x_i)^2 + c_i(x - x_i) + d_i$$

where $x$ ranges from $x_i$ to $x_{i+1}$ It is therefore about finding the parameters $a$,$b$,$c$ and $d$ for each interval of points. The procedure is detailed in the above cited paper [Mckinley and Levine, 1998]. Note that the implementation of such an interpolation has been done under the package *scipy.interpolate* of SciPy library [Virtanen et al., 2020].

As can be seen in Fig. 3.4, the ratio band $\sigma^0_{VH}/\sigma^0_{VV}$ is the one that best models the global dynamics of wheat during its growth cycle, with three essential phases : a first plateau corresponding to the pre-stem elongation growth cycle, an increase starting from the early stem elongation phases and a descent from the early senescence stage.

Figure 3.5, as well as Table 3.2 illustrate the results of the correlation study between the biomass of the different plant compartments and the radar ratio **smoothed** with a cubic interpolation on the 10 studied parcels.

*Figure 3.5: Scatter plot for the study of the correlation between the measured biomass data and the radar ratio averaged over each parcel, normalized and smoothed with a cubic spline interpolation.*

*Table 3.2: Pearson correlation coefficients between the measured biomass data and the normalized radar ratio averaged over each parcel and smoothed with a cubic spline. The values that are interesting for us are shown in bold.*

| | shoot | leaf | stem | grain | radar median |
|---|---|---|---|---|---|
| shoot | 1.0000 | 0.5586 | 0.8632 | 0.9438 | 0.5540 |
| leaf | 0.5586 | 1.0000 | 0.6523 | 0.6102 | **0.8230** |
| stem | 0.8632 | 0.6523 | 1.0000 | 0.8780 | **0.6697** |
| grain | 0.9438 | 0.6102 | 0.8780 | 1.0000 | **0.7158** |
| radar median | 0.5540 | **0.8230** | **0.6697** | **0.7158** | 1.0000 |

### Proposed statistical models and results

As explained earlier, linear regression analysis is performed using the simple model detailed in paragraph 3.1.1 with equation 3.1 and a second model emanating from the first with a logarithmic transformation, which involves switching to an exponential model by substituting $y$ by $ln(y)$ in the simple linear regression equation 3.1.

In fact, these two models are retained because they seem to be the most relevant for the level of simplicity we are looking for : the simple linear regression to be used as a baseline and a linear regression with logarithmic transformations will be also assessed.

For this analysis, above-ground biomass data are randomly divided into two subsets for training and testing ($2/3$ and $1/3$ respectively).

Note that the evaluation metric used here is the Mean Squared Error (MSE) defined by :

$$MSE = \frac{1}{n}\sum_{i=1}^{n}(y_i - \hat{y})^2$$

### Simple linear regression

Figures 3.6 and 3.7 summarise the results obtained by fitting the simple least squares linear regression model on the train and test data, respectively.

In each of the result figures below, each column corresponds to a plant compartment (shoot, leaf, stem, grain). Graphics in the first row represent the scatter plots of comparison between the field measured above-ground biomass data and those simulated by the regression model, the black dashed line corresponds to a perfect concordance between the measured and simulated biomass. The graphics in the second row represent the scatter plots of radar ratio band with in situ measured above-ground biomass and the red line corresponds to the fitted regression model line.

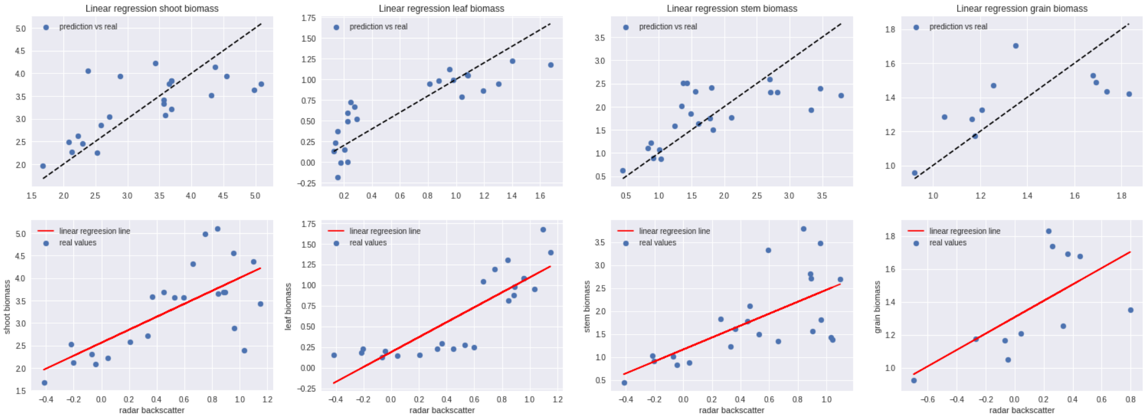

*Figure 3.6:* ***Results of the linear regression on the training set. Each column represents a plant compartment (shoot, leaf, stem, grain) and the MSE for the three compartments leaf, stem, grain is equal to : 0.07, 0.45, and 0.05 respectively. All biomass data are in (g/ha)/1000 to simplify the orders of magnitude of the MSE error.***

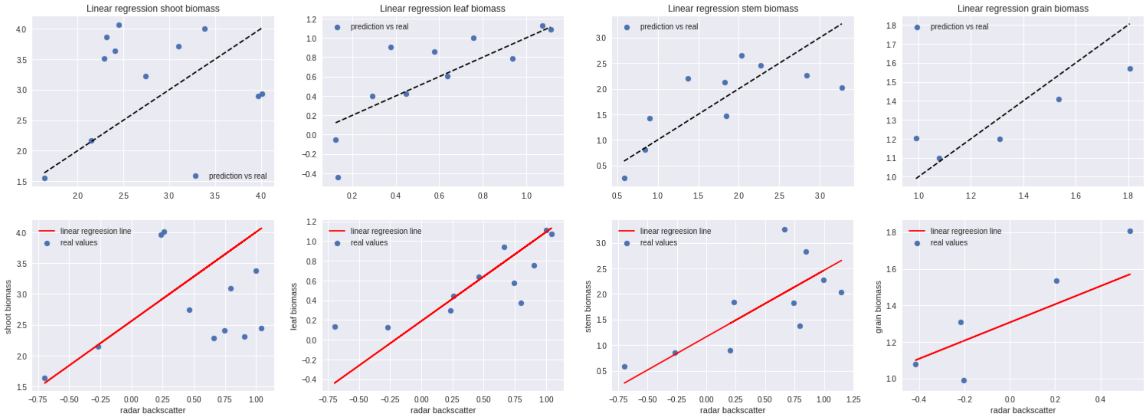

*Figure 3.7:* ***Results of the linear regression on the test set. MSE for the three compartments leaf, stem, grain is equal respectively to : 0.0744, 0.36, and 0.02.***

## Linear regression with logarithmic transformation

In order to have an exponential adjustment of the relationship between radar data and aerial biomass, the equation 3.1 was transformed to modelling the relationship between backscatter and the natural logarithm of the biomass, as follows :

$$ln(\hat{y}) = w'x + b' \tag{3.3}$$

Figures 3.8 and 3.9 summarise the results obtained by fitting the logarithmic transformed linear regression model on the train and test data, respectively.

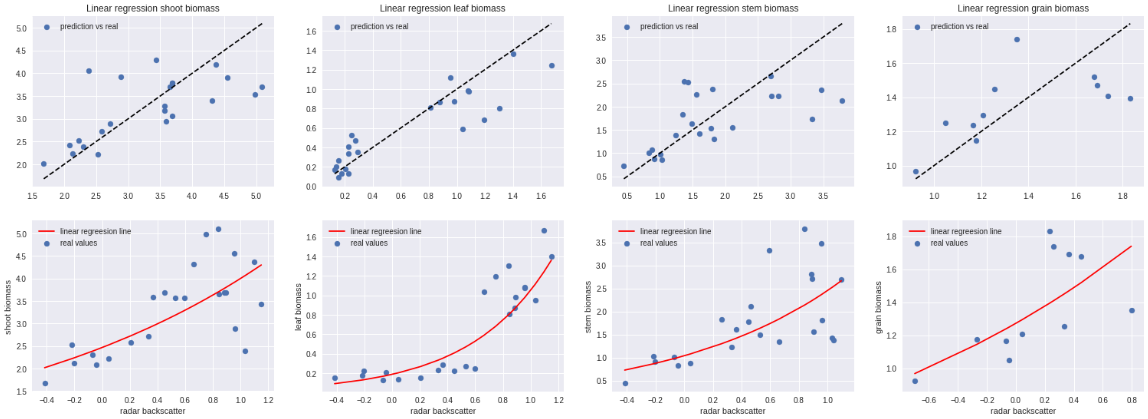

*Figure 3.8:* ***Results of the logarithmic linear regression on the training set. MSE for the three compartments leaf, stem, grain is equal respectively to : 0.05, 0.5, and 0.06.***

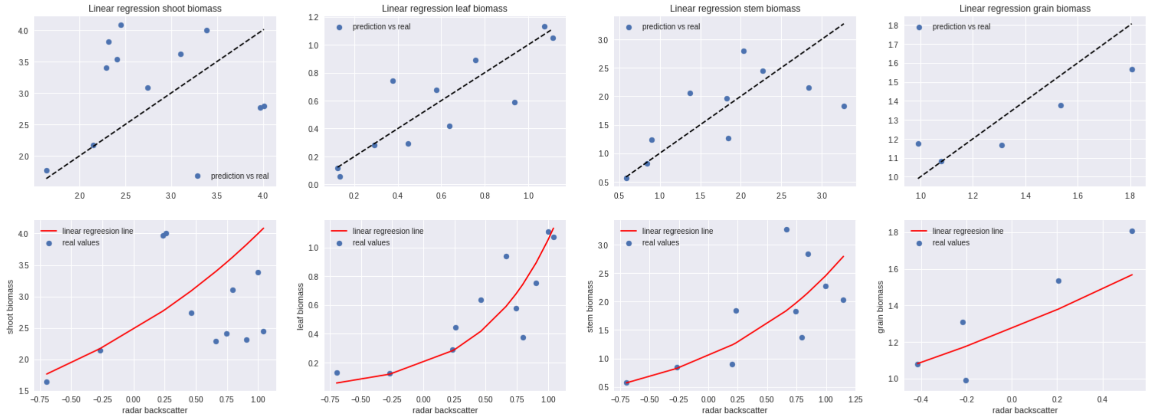

*Figure 3.9:* ***Results of the logarithmic linear regression on the test set. MSE for the three compartments leaf, stem, grain is equal respectively to : 0.03, 0.40, and 0.02.***

### 3.1.4 Discussion and conclusions

We aimed to evaluate in this work, using simple statistical concepts, the potential of Sentinel-1 radar data for the estimation of plant biophysical variables and growth dynamics monitoring. This evaluation was applied to a pilot crop, soft winter wheat, for which field data of an important biophysical variable, the above-ground biomass and that of each compartment, were available.

Through a first phase of the study, and in order to explore the existence of a relationship between radar backscatter and biomass, we performed correlation analysis with supporting scatter plots describing the nature of this relationship, as well as Pearson correlation coefficients to quantify it.
First, to compensate for the fact that the Sentinel-1 radar signal is noisy from one date of acquisition to another, a behavior that is reflected by a visible instability of the signal, we proposed filtering of the time series of the backscatter by interpolation type cubic spline.
In this correlation study, we could see through the scatter plots and correlation coefficients that there is a relation between the filtered backscatter and the biomass. Typically, the foliage is the compartment that most characterizes this relationship, the blue points in the figure 3.5 have a rather clear curved trend that can be explained with a simple model with an exponential tendency. This is probably due to the fact that in the radar signal captured from plants, leaves are the most exposed part of the plant, and therefore the most important contributor of the signal. This has already been discussed earlier in paragraph 8 of our manuscript.

Secondly, based on the earlier analysis and using the collected field biomass measurements and radar backscatter data, simple regression models were fitted : least squares and logarithmic-transformed linear regressions.
By opting for the mean squared error as a metric, the performance assessment of these models was done by splitting the available biomass data into two subsets : train to fit the models and test to validate the results.
We consider that the most interesting statement is to be drawn from the results obtained for the

leaf biomass, the compartment most correlated with the radar response as mentioned above. Indeed, by applying the logarithmic transformation model, we were able to improve the results on the test data set by passing from a MSE of $0.07$ obtained with the simple least squares linear regression to an MSE of $0.03$. This transformation was actually performed after the analysis of the scatter plot 3.5 of radar ratio band with in situ measured leaf biomass, in which the blue data have a curved trend that can be explained with an exponential model, hence the importance of the correlation analysis.
Furthermore, we also tested to fit a random forest model on the data at our disposition as done in [Vreugdenhil et al., 2018]. The results obtained in terms of MSE were largely worse than those obtained with the two main models mentioned earlier, so they are not reported here. It is nevertheless believed that the RF would have performed better with a larger data set.

This work also shows the interest that radar imagery data can have in estimating the periods of occurring of some plant growth stages. In fact, through figure 3.4 illustrating the evolution of the average radar responses signal in one of the studied parcels, we could see how each change of dynamics in the radar signal can be related to the beginning of a given growth stage. This is particularly visible for the early tillering stage (the first yellow vertical dashed line) where the signal starts a steady ascending phase and the early senescence (the last yellow vertical line) where the signal starts to decrease.

## 3.2 Study of the temporal heterogeneity of the radar signal : a tool for positioning rapeseed biomass measurements points for automated estimation by satellite imagery

### 3.2.1 Introduction

As winter rapeseed is a crop that requires a lot of nitrogen (between 200 and 250 nitrogen units for an average yield of 35 quintals per hectare [1]), fertilization is an important factor in optimizing the gross margin of the farmer. This involves finding a compromise between this economic aspect and the production, energy cost, and environmental impact aspects.

Winter rapeseed crop is usually sown in August-September and harvested around June-July. A large part of the vegetative biomass can be taken up during the autumn and a significant part of the nitrogen requirements, therefore, take place during this period, 10 to 25% of the final requirements, sometimes much more. The remaining nitrogen in the soil at the end of this period is therefore fairly or very low and is not taken into account in the nitrogen balance. It is thus considered that everything that has not already been taken up by the crop during the autumn will have to be provided via fertilization (minus a small amount of mineralization by soil organisms in the autumn and spring).

Biomass is an indicator of the amount of nitrogen absorbed by winter rapeseed. Actually, measuring the biomass at the end of the winter enables us to evaluate, by means of procedures for calculating provisional doses such as the ”Réglette Azote Colza” [2] tool, the quantity of nitrogen that has already been taken and to deduce what remains to be added to achieve the desired yield objective.
In regions where winter frost periods are frequent, a biomass measurement at the beginning of winter is also necessary to assess how much biomass has been lost during the winter. This biomass constitutes in fact organic matter that will be partially remobilized (about 50%) as soon as the vegetation recovers in spring, making a certain amount of nitrogen again available for the crop, meaning that less nitrogen fertilizer is needed.

Therefore, with the aim of collecting winter rapeseed biomass data in experimental parcels at our disposal, and with a perspective to developing supervised statistical models, as done in chapter 3.1, capable of estimating the winter entrance and exit biomass of winter rapeseed by satellite imagery, we have worked on a tool to define the points at which we will measure the biomass within each parcel, according to the intra-parcel heterogeneities that may exist within the latter, the overall objective is to ensure that the measurements describe the most variability possible.

---

[1] A. Baillet, 13 octobre 2009, Gestion de l’azote, document du CETIOM

[2] https://www.terresinovia.fr/p/la-reglette-azote-colza

### 3.2.2 Experimental fields and radar imagery data

For the development of the tool, we relied on four pilot parcels in the Beauce region of France. The geographical coordinates of the contours of the parcels, in longitude and latitude, are shown in figure 3.10.

For each parcel, a time-series of Sentinel-1 (S1) radar images is acquired, covering the period from early January to mid-February, approximately one and a half to two months from the winter output, the images are processed and clipped to the parcel. The dates of acquisition are summarized in table 3.3.

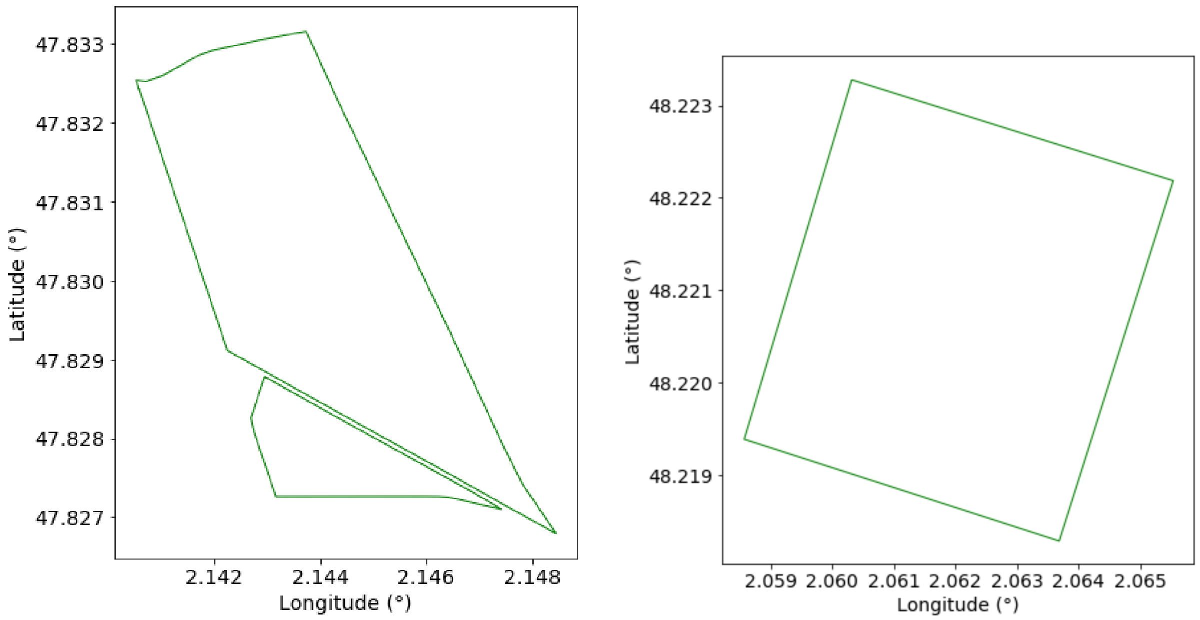

*(a) Parcel P1* *(b) Parcel P2*

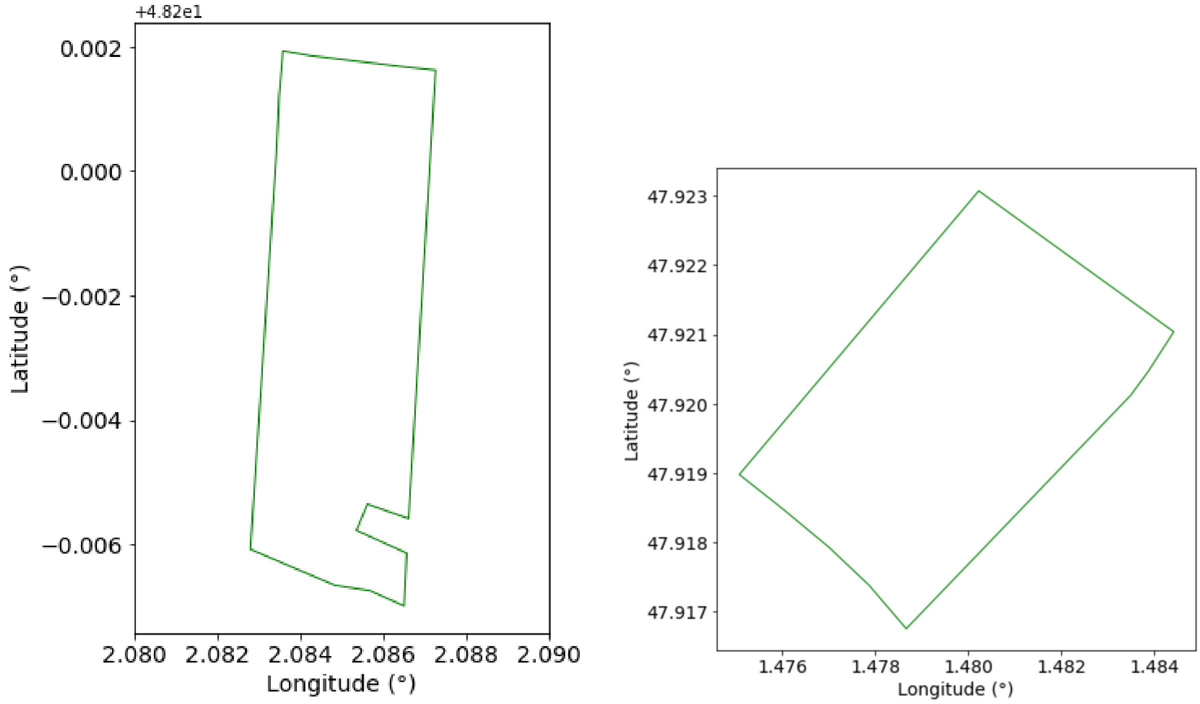

*(c) Parcel P3* *(d) Parcel P4*

*Figure 3.10: Geographical coordinates of the experimental parcels.*

*Table 3.3: Sentinel-1 acquisition dates in the studied fields*

| Area of interest | Rapeseed campaign | SAR Sentinel-1 acquisition dates |
|---|---|---|
| Each of the study parcels | 2019/2020 | January 04, 05, 10, 11, 16, 17, 22, 23 ; 28, 29; February 03, 04, 09, 10, 15, 16. |

### 3.2.3 Proposed approach

On each of the 4 parcels of interest, the choice of the intra-parcel areas in which the measurements will be carried out is made in the framework of a spatial-temporal classification approach as follows : from a time series of satellite radar images of the two months preceding the date scheduled for the measurements, pixel clustering is applied with the aim of grouping pixels with similar temporal profiles (signature of the radar response) into a single homogeneous group. We have chosen to work with the radar ratio band $\sigma^0_{VH}/\sigma^0_{VV}$ as a modality.
We will then try to define 3 measurement points per homogeneous area within each parcel (which will also serve to validate the clustering results). By integrating the effects of borders and GPS uncertainty when carrying out measurements in the field, the measurements will be positioned at least 30m from the parcel borders or from previous measurements.

Through the radar backscatter evolution graphs, a kind of stability in the profile of variation was observed as can be seen on the graph 3.12, which can potentially add difficulty to the classification model. In effect, this is due to the fact that during the period of acquisition of our images, which corresponds to the phase when the vegetation cover in the winter rapeseed parcels is relatively dense, the radar captures little variability in the texture.

Once the measurement points have been recommended according to intra-parcel heterogeneities, a specific protocol describing the acquisition of rapeseed biomass measurements in the field is established. On each previously identified point, three samplings spaced 3 to 5m around the recommended point are carried out, the aim being to better consider local heterogeneity.

#### Clustering algorithm

A given crop parcel is represented by a satellite image clipped to the contours of this parcel, grouping a set of $N$ pixels $p_i$, $i \in 1, \ldots, N$. Each pixel is a temporal vector of dimension $\mathcal{T}$, where $\mathcal{T}$ corresponds to the number of acquisition time steps. The set of these pixels is denoted by $P = \{p_1, p_2, \ldots, p_N\} \in \mathbb{R}^{\mathcal{T}}$.
Clustering operation then consists of partitioning $P$ into $K$ distinct groups (clusters) whose set is denoted by $\mathcal{C} = \{c_1, \ldots, c_K\}$.

We opted for a spatial-temporal clustering of the pixels based on the K-means method, a classical and widely used clustering technique, whose functioning is presented in the algorithm 2. It aims at partitioning data into distinct groups by minimizing an objective function of distances between the data points and the cluster centroids. The distance between two points $p_i$ and $p_j$ is denoted by distance($p_i$,$p_j$) in the algorithm.

In our work, where we consider time series data, we wanted to try two K-means clustering techniques.
The first one consists of a classical K-means with Euclidean distances to measure the similarity between the pixels which evolve over time and a standard averaging for the choice of the centroids.

The second technique consists of using a variant of the classical K-means with a new distance measure called dynamic time warping (DTW), introduced in [Sakoe and Chiba, 1971] and [Sakoe and Chiba, 1978] and which seems to be the most adapted to measure the similarity between the time series by taking into account the order of the sequences and their offset. Actually, DTW is able to find optimal global alignment between sequences and detecting so-called flexible similarities, by aligning the points inside both sequences. In this variant of K-means, called K-means-DTW Barycenter averaging (DBA-K-means) and detailed in [Petitjean et al., 2011], a new averaging method has been proposed. It consists of iteratively refining an initially (arbitrary) average sequence, to minimize its squared DTW distance to averaged sequences.

**Algorithm 2:** K-means

```
Input: The predefined number of clusters $K$
       The input data set $P$ composed of $N$ pixels, $P = \{p_1, p_2, \dots, p_N\} \in \mathbb{R}^{\mathcal{T}}$
1 Centroids initialization of the $K$ clusters producing the set of clusters $\mathcal{C} = \{c_1, \dots, c_K\}$;
2 $\forall i \in [1, N]$, assign each element $p_i$ to the closest centroid;
3 Compute the cost (inertia) function $J$
      $J = \sum_{j=1}^{N} \sum_{k=1}^{K} I(p_j \in c_k)\ distance(p_j, \bar{c}_k)^2$
    where I(X)=1 if X is true, 0 otherwise, until $J$ is below a certain desired threshold $\epsilon$;
4 Re-compute the new centroid of each cluster by mean vector as follow
      $\bar{c}_k = \frac{1}{|c_k|} \sum_{i=1}^{N} I(p_i \in c_k)\ \ p_i$
    where $|c_k|$ is the $k$th cluster number of elements;
5 Repeat steps 2, 3 and 4 until the centroids configuration $\mathcal{C}$ does not change;
```

For the initialization phase, which is an important step that can be determinate, instead of choosing the centroids of the clusters randomly, we opted for a strategy, known under an improved version of classical K-means noted K-means++ [Arthur and Vassilvitskii, 2007], which allows, by trying to keep the centroids far from each other, a better data spreading. This centroids initialization is done with the following steps:

- Choose an initial center $c_1$ uniformly at random from P.
- From remaining points of P, choose a new center $c_i$ with probability

  $$\frac{D(c_i)^2}{\sum_{p \in P} D(p)^2}$$

  where $D(p)$ is the shortest distance from a data point $p$ to the closest already chosen centroid.

- Repeat both previous steps until $K$ centroids are selected.

The threshold was set to $1e^{-6}$ and the final results correspond to the best inertia value over 20 runs with different centroid seeds.

### 3.2.4 Clustering results

Figure 3.12 shows the results of the pixel clustering into three distinct groups of time series within the P4 parcel, obtained using the standard Euclidean K-means (figure 3.12a) and DBA-K-means variant (figure 3.12b). The accompanying visuals are given in the figure 3.11.

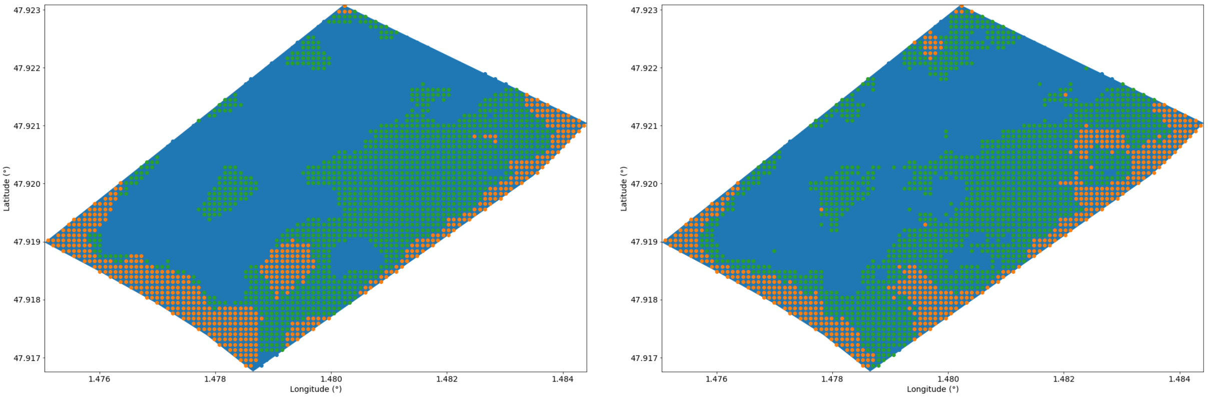

***(a)* Standard Euclidean K-means** ***(b)* DTW Barycenter Averaging K-means**

***Figure 3.11:* Visual comparison of the classification results obtained with both clustering strategies over the parcel P4.**

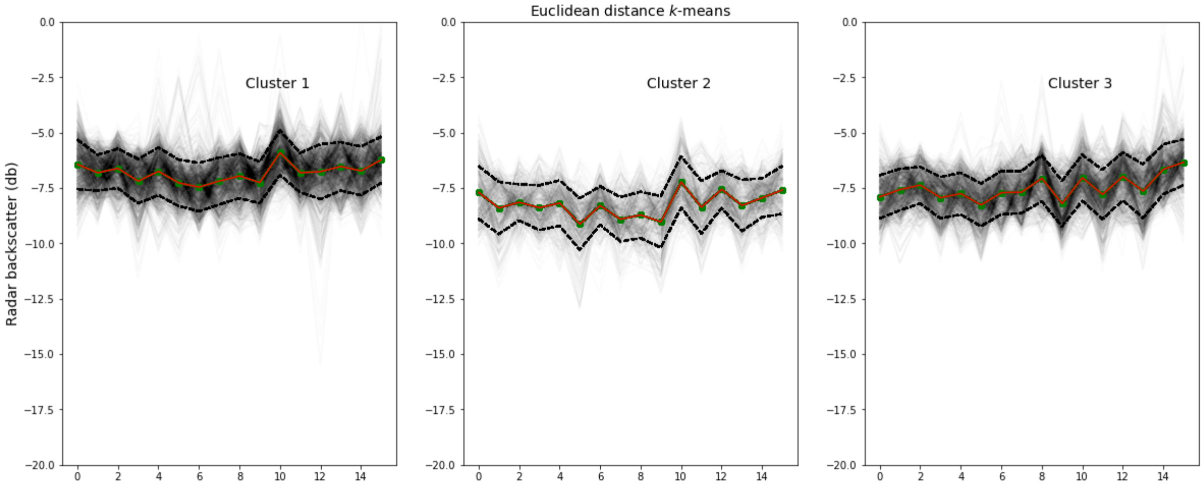

*(a) Clustering results in parcel P4 with euclidean distance strategy*

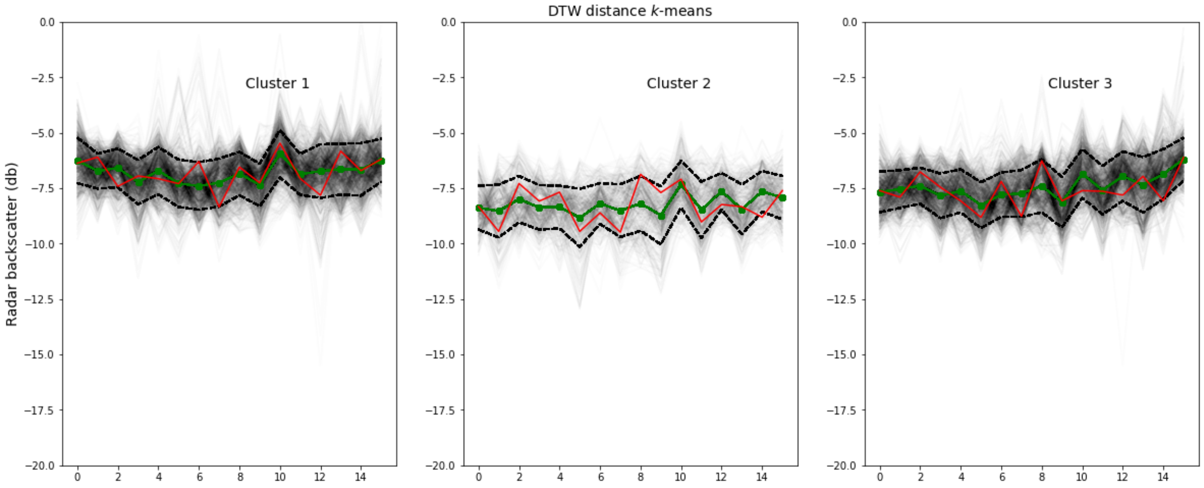

*(b) Clustering results in parcel P4 with DTW-DBA distance strategy*

***Figure 3.12:** Example results of pixel temporal evolution clustering in three clusters over one of the four parcels studied, P4 parcel. Clustering is applied to the radar ratio band $\sigma^0_{VH}/\sigma^0_{VV}$. For each cluster whose time series are represented in light black and the two dashed black curves indicate the dispersion (mean $\pm$ standard deviation), the green graph represents the time-series average, while the red graph represents the cluster center.*

Figure 3.13 shows some visualizations of the classification results obtained on the four parcels.

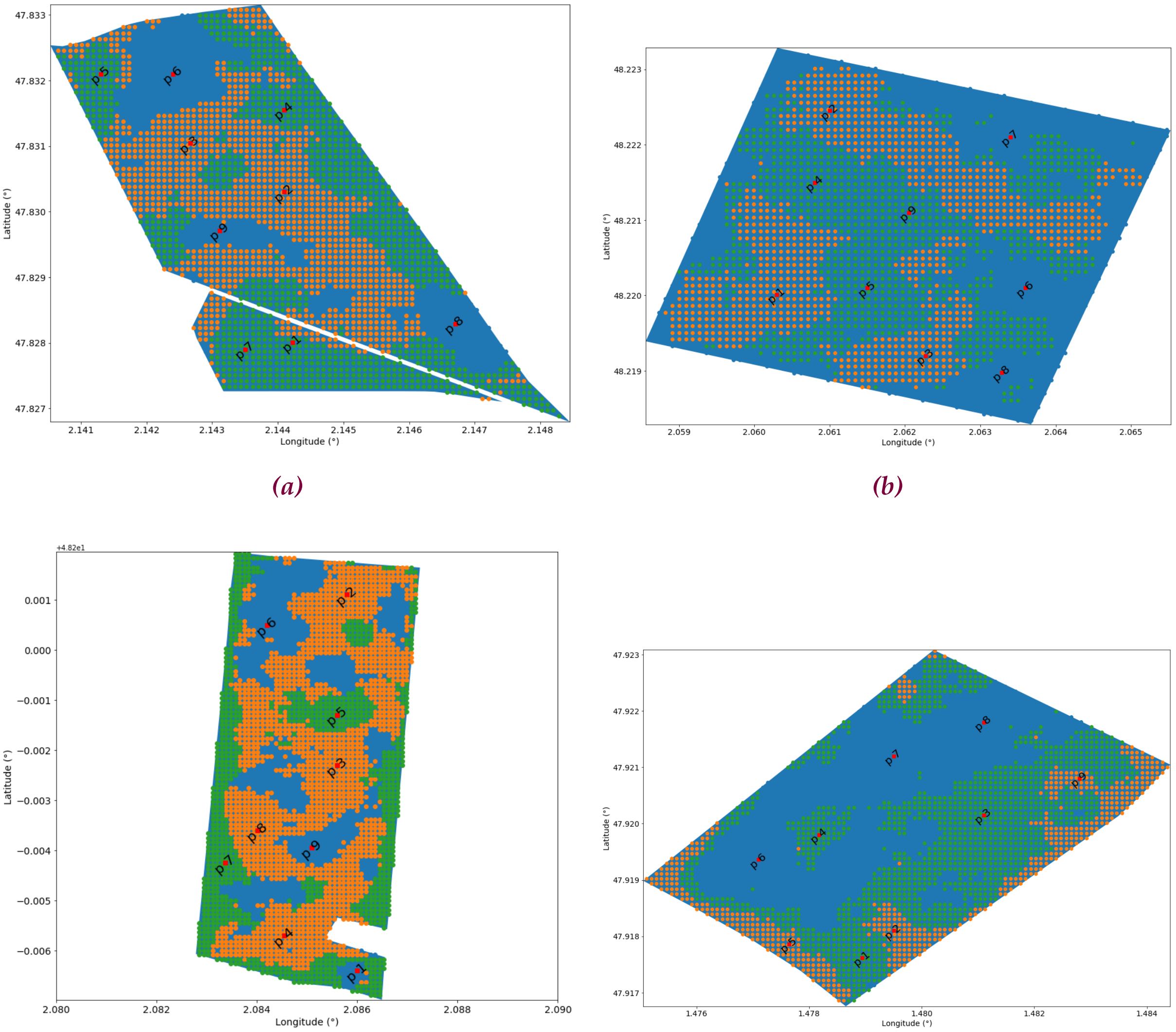

*(a)* *(b)*

*(c)* *(d)*

*Figure 3.13: Final results visualization for the location of biomass measurement points according to intra-parcel heterogeneities. The points $p_i$ correspond to the points designated for the biomass measurements, based on 3 distinct points per cluster.*


(a) (b)

*Figure 3.14:* ***Pictures were taken in the P4 field in order to check the coherency in the clustering results. picture 3.14a was taken in an area in the centre of the field, while picture 3.14b was taken at the border of the field.***

### 3.2.5 Discussion

In this work, a tool was proposed to recommend the locations in the parcel where winter rapeseed biomass measurements can be collected, in order to enrich the database for developing statistical models for biomass estimation. These locations are defined in terms of intra-parcel disparities, allowing the measurements taken to be as representative as possible in terms of the covered variability.

An unsupervised approach of clustering pixels that vary over time was used, using a K-means algorithm. Two measures of similarity of each time series were tested, the most classical measure being the Euclidean distance, and another measure, more adapted to sequential data, dynamic time warping (DTW).
Globally, both approaches give relatively similar results in terms of inertia, with, however, a slight advantage for the DTW distance. Indeed, this latter measure would have been much more efficient than the classical Euclidean distance if the pixels varied with different profiles, which is not the case for the Sentinel-1 data, as it is able to detect shifts in the alignment of the sequences.

The results also show that, in general, the algorithm tends to group the pixels at the borders of the parcel into a common group. This tendency can be clearly observed, through the orange-colored cluster, in figure 3.13d of the parcel P4.

Therefore, and in order to understand what happens in the field and to check the consistency of the clustering results with the field heterogeneities, the plants' vegetation cover was closely studied. As an example, in the parcel P4, Figure 3.14 illustrates the difference in winter rapeseed canopy cover, reflected in the classification of these points into different clusters.

In effect, picture 3.14a below was taken in a point belonging to the blue coloured cluster (more exactly close to the point p3 of figure 3.13d ), while image 3.14b was captured from a point located at the border of the parcel.

# Chapter 4

# Data assimilation methods to improve the predictive power of mechanistic plant growth models: application to a mechanistic winter wheat model

## 4.1 Introduction

Data assimilation contributes to the development of so-called precision agriculture [Jin et al., 2018b]. As experimental measurements carried out in the field can be costly or even imprecise, the resulting varietal characterization is often insufficient to extrapolate a yield forecast of sufficient quality in a distinct environmental context. Data assimilation leverages data available in new contexts to extrapolate and make more specific the prediction of a generic model (or a model calibrated in a different condition), in order to provide a much more reliable forecast. In addition, data assimilation has proved to be suitable for the acquisition of data from automated sources, more particularly remote sensing, thus allowing the forecasting tool to be dynamically updated each time new data are available.

The basic principle of data assimilation consists of characterizing the parameters of the model to be estimated by probability distributions (the so-called Bayesian viewpoint) and updating these probability distributions according to the experimental data collected. This protocol requires, within the framework of filtering methods, to sample the initial probability distributions using 'particles', then to propagate these particles independently of each other utilizing of the dynamic model equations, before selecting them according to their pertinence regarding the experimental data [Wikle and Berliner, 2007b].
In the scope of our thesis, we implemented and used a method derived from [Chen and Cournède, 2014], in which the particle selection process is enhanced by a convolution step ensuring a better diversity in the particle population and thus a better exploration of the space of the parameters to be estimated.

In this section, we will first briefly describe the functioning of the deterministic mechanistic model adapted to the growth of soft winter wheat. The data assimilation algorithm used in the statistical framework of a general state-space model will then be described, before presenting some results of the application of the assimilation method on the mechanistic model. We will then conclude with a discussion phase.

## 4.2 Winter wheat plant growth model: Mechanistic Modelling of Plant-Environment Interaction (MMPE)

We developed a version of the STICS model [Brisson et al., 2003] (Simulateur mulTIdisciplinaire pour Cultures Standards) adapted to soft winter wheat. It consists in the mechanistic and deterministic modeling of the plant-environment interaction, characterized by a detailed consideration of biophysical and physico-chemical processes, cultural practices and soil characteristics. This approach relates the carbon, water and nitrogen balances within the plant organs to its environment, enabling the prediction of the yield, simulated at compartment level per unit of land surface area, as well as the protein content of the crop. In addition to the phenological stages, the growth in STICS is driven by an empirical law for the Leaf Area Index (LAI) growth. This index represents, for a given surface, the cumulative area of leaf blades located above a given surface by projection onto the ground.

Figure 4.1 below illustrates, in a global manner, the main processes involved in the STICS model adapted to the winter wheat crop.

In this mechanistic model, the growth of soft winter wheat is given in the form of a discrete dynamical system (4.1), with function $f$, describing the transition from the state variables at time $n$ denoted by $x_n$ (compartments biomass, leaf area index, ...etc.) to their states at time $n+1$, denoted by $x_{n+1}$ with a daily time step. This transition depends on the previous state, but also on the environment variables $u_n$ at instant $n$ (cultural conditions, climate, ...etc.) and the plant physiological parameters denoted by $\theta$.

$$x_{n+1} = f(x_n, u_n, \theta) \tag{4.1}$$

All the details concerning the processes and equations of the STICS model can be found in [Brisson et al., 2008], where the precise growth equations are given.

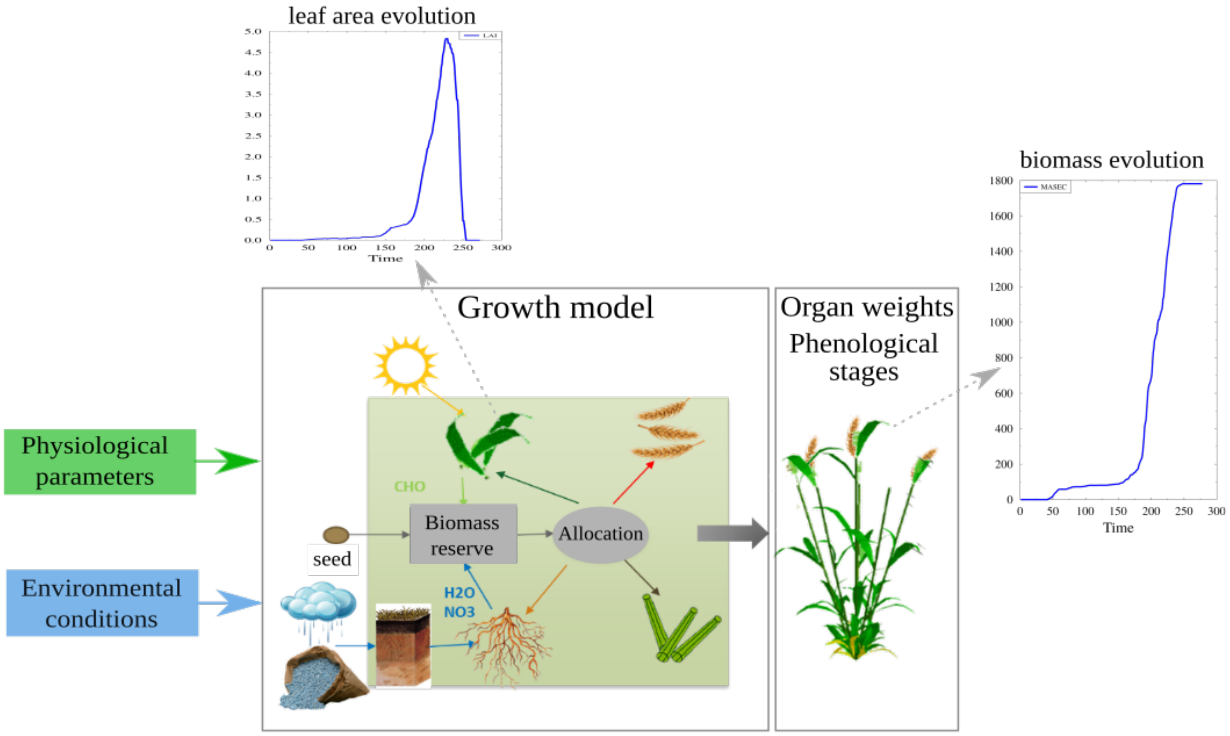

*Figure 4.1: Global scheme of the mechanistic modelling of the soft winter wheat growth in interaction with the environment.*

## 4.3 Data assimilation approach

### 4.3.1 The filtering problem in the context of Bayesian inference

To introduce filtering and the issues that we want to address in this part, let us start by recalling the concept of general state-space model, on which the used mechanistic model of wheat growth can be based, with a few adjustments.

Given augmented state variables $x$ (augmented, in the sense that the vector of parameters, which we denote by $\theta$, is incorporated in the state equation by considering that it has a constant evolution, the aim is to estimate jointly the parameters and the states), parameters $\theta$, environmental variables $u$, noisy observations $y$, and a discrete-time step $n$, the general state-space model dynamics is defined by the following system of equations:

$$\begin{cases} x_n = f_n(x_{n-1}, \theta, u_n, \epsilon_n) \\ y_n = g_n(x_n, \theta, \eta_n) \end{cases} \tag{4.2}$$

where the random variables $\epsilon$ and $\eta$ are the modeling and observation noises, respectively. $f_n$ and $g_n$ encode time-dependent model and observation functions.

Equations 4.2 can represent dynamic systems, whether they are probabilistic such as hidden Markov model (HMM) [Cappe et al., 2005] on which some plant growth models can be built [Cournède et al., 2013], or deterministic such as the STICS model that we use in this work. In the deterministic model we simply consider that the $\epsilon$ and $\eta$ noises are zero with probability 1.

Starting from a prior distribution $p(x_0)$ on the initial state, state variables follow a a dynamic evolution characterized by a sequence of transition functions $f_n(x_n|x_{n-1})$. Observations are considered conditionally independent and described by a conditional probability density function $g_n(y_n|x_n)$. The problem that we want to address in the following is to determine the posterior distribution $p(x_k|y_{1:n})$, given a sequence of experimental observations $y_{1:n} = y_1, \ldots, y_n$.

In the case where $k < n$, we face a smoothing problem, while if $k > n$ it represents a prediction problem. In our work, our interest is the case where $k = n$, which is called a filtering problem and falls within the framework of Bayesian inference, whose aim is to use prior knowledge to infer the conditional probability given limited observations, through the application of Bayes rule [Bayes, 1763] which we recall below.

$$p(\theta|y) = \frac{p(y|\theta)p(\theta)}{\int p(y|\theta)p(\theta)d\theta} \tag{4.3}$$

The posterior distribution $p(\theta|y)$ is expressed as a function of the prior distribution $p(\theta)$ and the likelihood $p(y|\theta)$.

### 4.3.2 Convolution Particle Filter

#### Sequential Monte Carlo in a Particle Filter framework

Sequential Monte Carlo (SMC) methods [Del Moral, 2004, Arnaud Doucet and Gordon, 2001] are powerful algorithms to perform Bayesian inference in dynamic systems. These methods, also known under the heading of particle filters in the context of dynamic systems, have become extremely popular way beyond the borders of the statistics community.

The idea of such methods is to represent the probability distributions by particles, i.e. independent identically distributed samples of the distributions, and to propagate and update them using the general state-space model equations, hence the equivalent nomenclature of particle filter methods.
One of the main challenges is to circumvent the famous particle degeneracy problem [Gordon et al., 1993] and to ensure that parameter space is widely explored to enable accurate estimation.
Several methods have been proposed to address this challenge, among which iterated filtering [Ionides et al., 2011] and particle Markov chain Monte Carlo [Andrieu et al., 2010] in the specific context of joint parameter/hidden state estimation. They constitute batch or offline methods, however, in that they are unable to take into account new observations dynamically. A distinct idea is to allow freedom in parameter space by regularizing the posterior density using a mixture, these are the so-called Regularized Particle Filter methods.

### Regularized Particle Filtering and Convolution Particle Filtering

Regularized particle filter methods [Musso and Oudjane, 1998] [Oudjane and Musso, 1998] represent an interesting variation of traditional particle filters. They rely on kernel-based posterior density estimation at each filtering step, with particle resampling performed from the reconstructed density.
In many situations, this method was proven to help prevent sample impoverishment in the resampling step and thereby enhance the robustness of particle filtering.

Inspired by the Regularized methods, the objective of Convolution Particle method, proposed by [Campillo and Rossi, 2009], is to estimate simultaneously the parameters $\theta$ and the state $x_n$ based on the observations $y_{1:n} = \{y_1, \ldots, y_n\}$.

The filtering process is performed recurrently in two steps and occurs only at time steps when observations are available.

The first step, called **prediction** stage, aims to provide a kernel estimate $\hat{p}(x_n, y_{1:n})$ of $p(x_n, y_{1:n})$. $M$ particles $\{\tilde{x}_{n-1}^{(i)},\ i = 1, \ldots, M\}$ are sampled from $\hat{p}(x_{n-1}, y_{1:n-1})$ and propagated through the dynamical model until the next available measurement, leading to a sample $\{\tilde{x}_n^{(i)}, \tilde{y}_{1:n}^{(i)}, i = 1, \ldots, M\}$ from $p(x_n, y_{1:n})$.

The empirical kernel estimation of the joint density of $(x_n, y_{1:n})$, $\hat{p}(x_n, y_{1:n})$ is deduced using the Parzen-Rosenblatt [Parzen, 1962] Gaussian kernels $\mathcal{K}_{h_M^x}^x$ and $\mathcal{K}_{h_M^y}^y$ with bandwidth parameters

$h^x_M$ and $h^y_M$ as follows:

$$\hat{p}(x_n, y_{1:n}) = \frac{1}{M} \sum_{i=1}^{n} \mathcal{K}^x_{h^x_M}(x_n - \tilde{x}^{(i)}_n) \mathcal{K}^{\bar{y}}_{h^{\bar{y}}_M}(y_{1:n} - \tilde{y}^{(i)}_{1:n}) \tag{4.4}$$

where

$$\mathcal{K}^{\bar{y}}_{h^{\bar{y}}_M} = \prod_{s=1}^{n} \mathcal{K}^y_{h^y_M}(y_s - \tilde{y}^{(i)}_s)$$

In the next step, called the **correction** stage, we aim to provide a kernel estimate of the optimal filter $p(x_n|y_{1:n})$, $\hat{p}(x_n|y_{1:n})$, is deduced from the prediction step and Bayes' law as follows:

$$\hat{p}(x_n|y_{1:n}) = \frac{\sum_{i=1}^{M} \mathcal{K}^x_{h^x_M}(x_n - \tilde{x}^{(i)}_n) \mathcal{K}^{\bar{y}}_{h^{\bar{y}}_M}(y_{1:n} - \tilde{y}^{(i)}_{1:n})}{\sum_{i=1}^{M} \mathcal{K}^{\bar{y}}_{h^{\bar{y}}_M}(y_{1:n} - \tilde{y}^{(i)}_{1:n})} \tag{4.5}$$

The part $(\mathcal{K}^{\bar{y}}_{h^{\bar{y}}_M}(y_{1:n} - \tilde{y}^{(i)}_{1:n})/(\sum_{i=1}^{n} \mathcal{K}^{\bar{y}}_{h^{\bar{y}}_M}(y_{1:n} - \tilde{y}^{(i)}_{1:n}))$ can then be considered as the normalized weight $\tilde{w}^{(i)}_n$ of the particle $\tilde{x}^{(i)}_n$.

The new set of particles $\{\tilde{x}^{(i)}_n,\ i = 1, \ldots, M\}$ are samples from $\hat{p}(x_n|y_{1:n})$ to perform the correction at the next time $n + 1$ with available observation and so on. The convolution particle filtering algorithm used in this thesis is presented in 3 pseudo code.

Finally, other SMC-based data assimilation approaches have been discussed in various research papers. In [Chen et al., 2013], the authors have tested the performance of three data assimilation approaches to predict biomass production and allocation in a dynamically evolving probabilistic plant-growth model. In addition to CPF, the Unscented Kalman filter (UKF) and the ensemble Kalman filter (EnKF) were investigated and assessed in the context of sequential data assimilation problems for a plant growth model.

**Algorithm 3:** Convolution Particle Filter

```
Result: posterior distribution $\hat{p}(x_{\mathcal{T}}|y_{1:\mathcal{T}})$
Initialization phase :
At time step $t = 0$;
for i = 1 : M do
    Initial sampling of $x_t^{(i)}$ from the parameters prior distribution;
end
for t = 1 : $\mathcal{T}$ do                          ⇒ loop over observation timeline
    for i = 1 : M do                                  ⇒ loop over particles
        Prediction phase :
        State sampling $\tilde{x}_t^{(i)} \sim p(x_t|\tilde{x}_{t-1}^{(i)})$;
        Observation sampling $\tilde{y}_t^{(i)} \sim p(y_t|\tilde{x}_t^{(i)})$;
        Weight computing and normalization :
        $w_t^{(i)} = \mathcal{K}_{h_M^{\bar{y}}}^{\bar{y}}(y_{1:n} - \tilde{y}_{1:n}^{(i)})$;
        $\tilde{w}_t^{(i)} = \frac{w_t^{(i)}}{\sum_{k=1}^{M} w_t^{(k)}}$;
    end
    Correction phase :
    $\hat{p}(x_t|y_{1:t}) = \sum_{i=1}^{M} \tilde{w}_t^{(i)} \mathcal{K}_{h_M^x}^{x}(x_t - \tilde{x}_t^{(i)})$;
    New particle sampling $\tilde{x}_t^{(i)} \sim \hat{p}(x_t|y_{1:t})$
end
Return samples from the posterior distribution $\hat{p}(x_{\mathcal{T}}|y_{1:\mathcal{T}})$ ;
```

## 4.4 Method implementation on mechanistic winter wheat growth model

*Figure 4.2:* ***Localization of two experimental parcels of the same soft winter wheat variety (Apache cultivar). For each parcel, the information on agricultural grain yield at 12% of humidity is given in*** $g/m^2$**.**

Our objective in this experiment is to study the performance of the CPF-based data assimilation algorithm applied to the mechanistic winter wheat growth model described in section 4.2, the aim being to improve the predictive power of such a model with the support of experimental data which may represent different state variables of the mechanistic model and that can be collected in fields or estimated from different sources such as remote sensing.

In [Chen and Cournède, 2014], a data assimilation approach using the Convolution Particle Filtering algorithm has been proposed and applied to a mechanistic STICS-type wheat growth model with the objective of improving the model prediction, based on field measurements of LAI and soil averaged water content. The results obtained were promising and the filtering method demonstrated its robustness.

In our work, and in the same perspective of using the CPF-based data assimilation method to improve the predictive power of our winter wheat growth model which is an adaptation of the STICS model, we want to test a slightly different approach, by calibrating the soil parameterization of the model using a sequence of synthetic biomass data, more precisely above-ground dry matter data.

Indeed, we started from a first observation established through experimental agricultural yield data in soft winter wheat parcels in France over the 2014/2015 agricultural campaign. Figure 4.2 illustrates two of these winter soft wheat parcels.

We thus noted strong differences in yields on parcels of the same variety of soft winter wheat, namely Apache cultivar, with, in principle, similar environmental conditions, since the parcels are located in the same production basin, or even very close to each other.

For readers who are familiar with STICS model notations recalled in detail in [Brisson et al., 2008], note that yield is usually represented by the state variable MAGRAIN, which represents the dry matter of grain yield. In our work, experimental yield data are reported in grain fresh matter, at 12% of humidity.

Based on available experimental field-measured soil parameters data, it appeared that these differences in yield are most probably explained, in large part, by the fact that the two parcels have different soil potentials, which reveals the importance of data related to soil parameters in mechanistic growth models, notably for soft winter wheat.

The soil potential also called the useful plant reserve represents the soil water content and is expressed by the state HUR in the STICS model, which corresponds to the difference between water content at field capacity in the seedbed and the wilting point water content in the seedbed (the humidity at the wilting point is the quantity of water below which the plant no longer has access to water because it is too difficult to extract from the soil). These last two parameters are represented in STICS by HXS and HNS, respectively, and expressed in mm water/cm soil unit.

Therefore, the approach that we chose to evaluate the contribution of the CPF-based data assimilation algorithm is explained below.

In order to assess the application potential of the CPF-based data assimilation algorithm to the mechanistic model, we generated simulated biomass data (more precisely above-ground dry matter data, denoted by MASEC state in STICS) using the mechanistic wheat growth model with a given soil potential (HUR and the soil layers depth over three horizons) and pre-calibrated variety parameters, using a sensitivity analysis and a simple calibration step. This alternative of using simulated biomass data is dictated by the lack of field data.

Figure 4.3 illustrates the evolution of the simulated data: above-ground dry matter (4.3a) as well as some yields of the different winter wheat compartments (4.3b). We kept the same STICS notations nomenclature in the legends of the two graphs.

The prior distributions of soil parameters were derived from the literature ([Brisson et al., 2008]), and the generated biomass data generated were used to correct dynamically the model's soil calibration during the season to improve model yield prediction.

### CPF-based data assimilation application and discussion

Convolutional Particle Filter data assimilation algorithm was performed using 10,000 particles. Eight dates among the simulated above-ground dry matter data were selected for recalibration and evaluation. The recalibration phase was performed using the first five data. Afterwards, the model was simulated to give the predictions, which were then compared to the validation data given by the three remaining experimental data. Note that simulations are performed for each of the 10000 particles $\tilde{x}_5^{(i)}$ obtained after the fifth date as samples of $\hat{p}\left(x_5|y_{1:5}\right)$, thus allowing to obtain samples of the distribution $\hat{p}\left(y_k|y_{1:5}\right)$, with $k = 6, 7, 8$, and 95% credibility intervals.

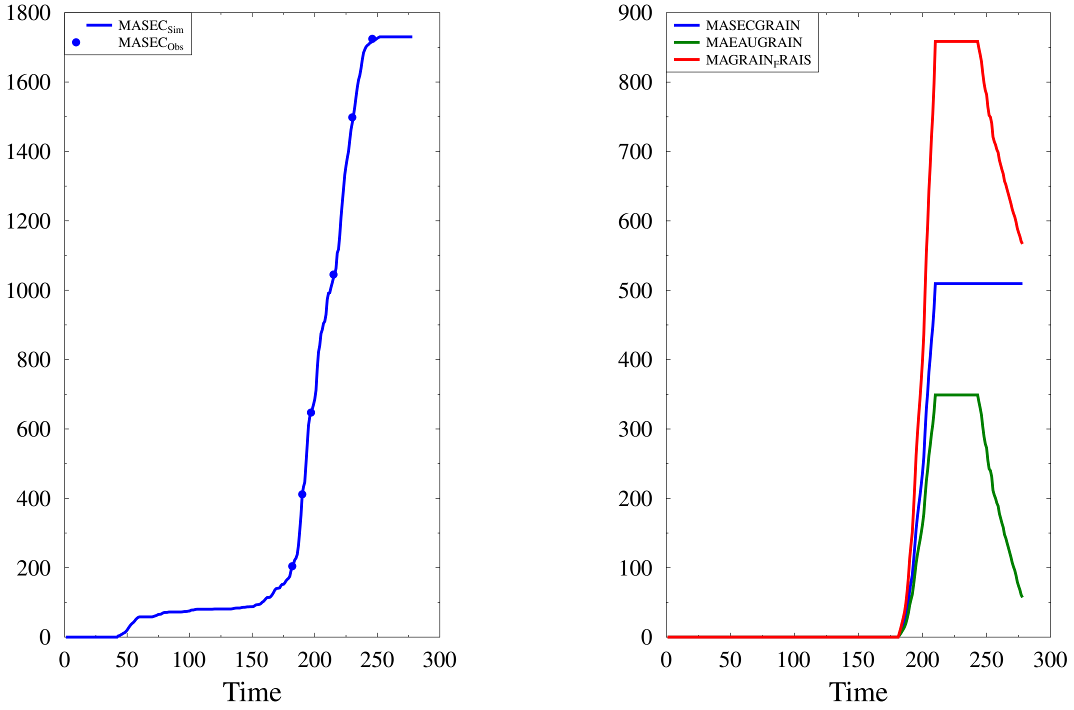

*(a)* *(b)*

***Figure 4.3:*** ***Generation of simulated biomass data (expressed as above-ground dry matter MASEC in $g/m^2$ in 4.3a and the biomass of the different wheat yield compartments in $g/m^2$ (the grain dry mass MASECGRAIN, the grain humidity MAEAUGRAIN, and the grain fresh mass, MAGRAIN) in 4.3b) using the mechanistic plant growth model adapted to soft winter wheat with known soil potential and variety parameters.***

An example of the results obtained is shown in Figure 4.4. It can be stated that, with this dynamic estimation of soil-related parameters, data assimilation has allowed a good predictive capacity of the model with respect to the simulated validation data. These results remain however clearly improvable with more precise data, either field measured or statistically estimated with the help of remote-sensing imagery.

Below, we present some more experiments to illustrate the impact of the dates of the observations used for model recalibration or the number of observations.

Subsequently, and in order to study the impact and importance of the observation times, the data assimilation algorithm was run, using as recalibration data some above-ground dry matter data simulated at precocious time-steps, potentially before the winter soft wheat second node visible stage. The obtained results are presented in figure 4.5.

It can be seen that the results obtained are not satisfactory. It appears that the data used for the recalibration phase, taken at dates before the soft winter wheat mounting stage, do not carry

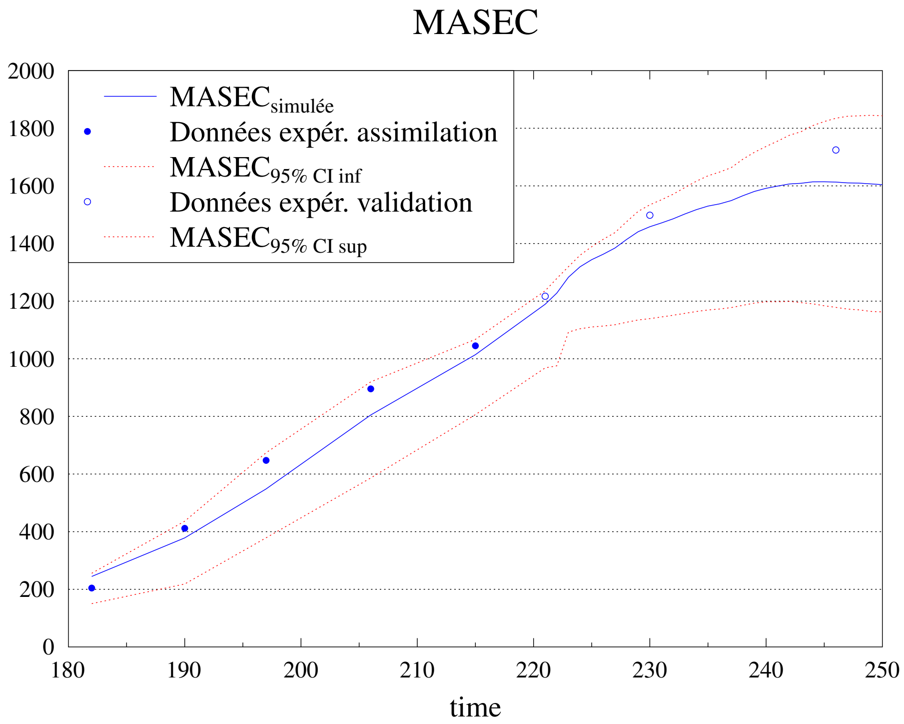

***Figure 4.4:*** ***Result of averaged prediction of soft winter wheat above-ground dry matter by the convolutional particle filter data assimilation algorithm in blue curve, based on experimental data of the Apache variety. The dark blue dots represent the data used for the assimilation, the light blue dots represent the data used for the validation of the method. The two red curves correspond to the 95% credibility interval (CI) limits at each time step.***

enough information for the parameterization of the soil parameters. During this early stage, there is not yet any soil water stress and therefore the soil parameters do not have any impact, at this stage, on the simulated growth of the wheat.

Another experiment, aimed at assessing the importance of the number of observations dates, was carried out. For the recalibration phase, instead of taking 5 simulated experimental data, only the first 3 dates were considered. The results are presented in figure 4.6.

We can clearly observe that we perform less well than the results shown in figure 4.4, hence the importance of having more data to assimilate.

Finally, a perspective of this work would be to use the evaluation of biomass or biophysical variables from satellite images (presented in Chapter 3 ) as inputs of the data assimilation algorithm, with a clear advantages in terms of costs and scalability compared to approaches as in [Chen and Cournède, 2014] where data assimilation was performed from field measurements.

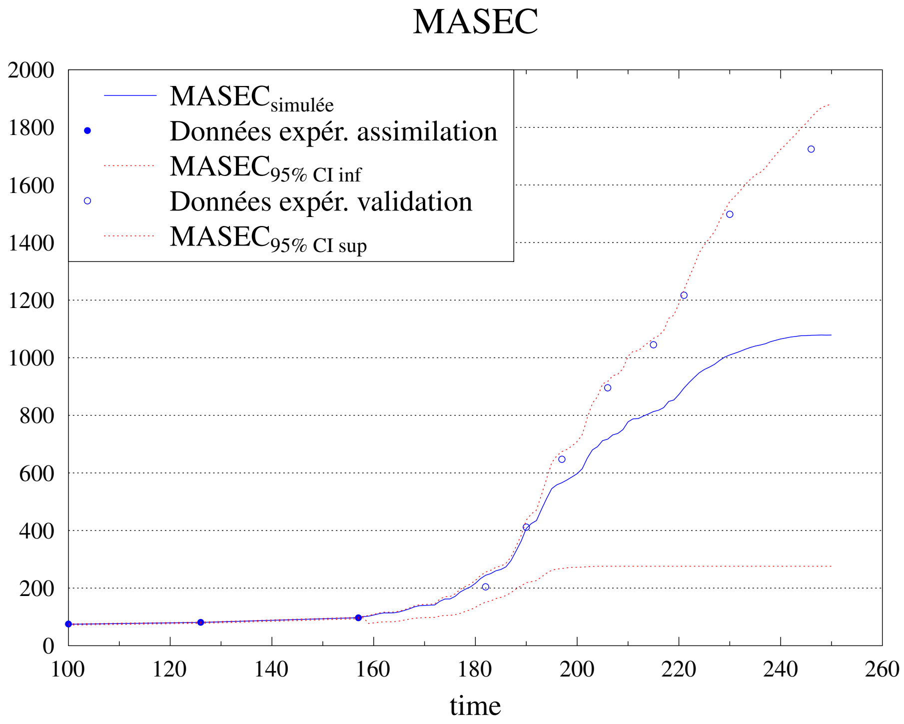

***Figure 4.5:*** ***Importance of the timing of observations: the result of prediction of soft winter wheat above-ground dry matter by the convolutional particle filter data assimilation algorithm, based on simulated observation data of the Apache variety chosen at dates before the molting stage of soft winter wheat. The dark blue dots represent the data used for the assimilation, the light blue dots represent the data used for the validation of the method.***

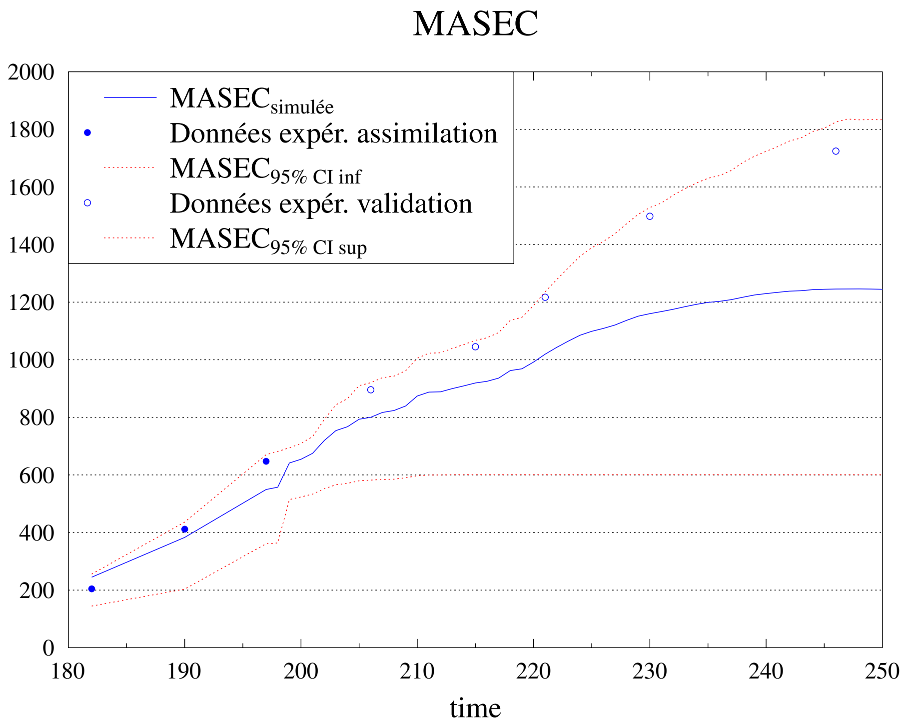

*Figure 4.6: The importance of the number of observation dates: the result of prediction of soft winter wheat above-ground dry matter by the convolutional particle filter data assimilation algorithm, based on simulated observation data of the Apache variety. The dark blue dots represent the data used for the assimilation, the light blue dots represent the data used for the validation of the method.*

# Conclusion & Perspectives

In this work, we discussed topics that can contribute to answering some of the requirements of today's agriculture, a field in constant search of improvement through new technologies. The first application that we studied concerns the identification of crop types in a production basin. We have used satellite imagery coupled with statistical learning to build models capable of providing better visibility on crop rotation and agricultural surfaces of field crops. Our second application concerns agricultural yield forecasting. We only studied some specific parts of this vast research domain. We started by evaluating the potential of satellite imagery, more specifically radar imagery, for the estimation of plant biophysical variables and growth dynamics monitoring using simple statistical models. Then, we proposed a tool, still based on satellite imagery, to determine the optimal locations of measurement points at the parcel scale. Finally, we presented an implementation of a Convolution Particle Filter data assimilation algorithm, which was applied to a mechanistic wheat growth model in order to improve the predictive power of such a model, based on field measurements of Leaf Area Index and averaged Soil Water Content. We detail in the following the main contributions of our work as well as the perspectives that could emanate from our results.

## Contributions

### Radar remote sensing for crop monitoring

We started by recalling the basic concepts of how radar technology works and the various operations to calibrate a radar image so that it is ready for exploitation. We then conducted a statistical experimental plan with the objective of evaluating the effect of the interaction between incidence angles and pedo-climate on the radar response of vegetation areas. In fact, we tried through this study to answer a more global question: at what point statistical models trained on imagery data acquired in a given area/year remain valid for another area/year? Also, through this experimental design, we tried to analyze and interpret the elements that drive the radar signal's evolution during the plant growth cycle.

### Crop type recognition by machine learning methods using satellite images

We have proposed an approach allowing the recognition of crop types at the scale of a production basin days or even a few months before the harvest. This subject bears several interests and applications that we largely developed in the introduction but also within the part dedicated to crop recognition in our manuscript. This approach is based on the temporal dynamics of the radar signal returned by the vegetation coverage from each satellite image pixel during the growth cycle of the plants, as a particular signature allows the identification of each crop type. For this purpose, we chose to use two supervised deep learning models: Long Short-Term Memory (LSTM) recurrent and Convolutional Neural Network (CNN) models. The functioning of these models were presented. We also detailed the proposed approaches to manage inputs and outputs in the context of crop identification at the pixel level of the satellite image.

Our proposal is conceived such that the models may be able to produce an evaluation of the cropland cover without having to label parcels at the beginning of the campaign. For this purpose, we used models calibrated using data from previous campaigns. We called it ”inter-annual” approach.

We also presented an ”intra-annual” approach, which consists in recognizing the main crops during a given campaign with models trained on a few parcels during the same campaign. This task is easier since it avoids the problem caused by the variability of the growth dynamics of the same plant from one season to another, but also from one region to another if the training fields are located in the prediction production basin. However, such an approach raises other difficulties from a feasibility point of view. Indeed, having training parcels requires either being in contact with farmers who can tell us what they have sown, or going out into the field to manually label a certain number of parcels. To all this is added an additional level of difficulty, the training data collected must ensure a certain level of precision and as much variability as possible. As a matter of fact, depending on the cultural practices, the development of a given crop may be different from one exploitation to another, or even from one parcel to another. These processes remain very complicated to achieve if one wants to develop automatic and large-scale tools. To remedy all these obstacles, the approach we propose allows us to produce an evaluation of cropland cover through statistical models trained on crop occupation data from previous farming seasons, data that are reasonably available.

In the proposed approach, our first intuition was to rely on the growth dynamics captured by satellite imagery, expressed in calendar time, to differentiate crops. However, this growth dynamic can vary from one campaign to another and is strongly driven by the pedoclimatic environment, cultural practices, as well as the concerned crop characteristics, such as its frosts resistance. Therefore, the dynamic in calendar time of the radar images can be very different from one campaign to another, either with the same evolutionary dynamic but shifted in time, or with a quite different dynamic evolution.

We then proposed an approach in which the phenological development of the plant was considered to identify its species. Instead of using calendar time series of the radar response, we proposed to use time series aligned with the thermal time, a key concept in plant science, to readjust the shift and/or difference in the dynamics of the radar response. It allows a better synchronization of the radar backscatter evolution between different years. This idea was motivated by the fact that a priori, independently of the pedoclimatic conditions, the cultivation practices or the crop degree of resistance, a specific phenological stage of a given crop is reached at a given level of temperature accumulation, hence of thermal time, ensuring the robustness of the inter-annual variation of crop development dynamics.

Note that I also integratd the methods developed in this chapter into an industrial application module at CybeleTech, which is now used to deliver services to several clients, and has thus broadly demonstrated the validity of the approach.

### Estimation of plant bio-physical variables by satellite imagery

We discussed the large potential of microwaves for the estimations of plant biophysical variables. Based on biomass data of the different soft winter wheat compartments measured in the field, we investigated the interest of Sentinel-1 imagery for the estimation of these variables by fitting some simple statistical models. We started by performing a Pearson's correlation coefficient analysis in order to assess the relationship between backscatter and above-ground biomass field measurements. First, to compensate for the fact that the Sentinel-1 radar signal is noisy from one date of acquisition to another, a behavior that is reflected by a visible instability of the signal, we proposed filtering of backscatter time series using the cubic spline interpolation method. We observed that there is a relation between the filtered backscatter and the biomass. Typically, the foliage is the compartment that most characterizes this relationship. It is probably due to the fact that in the radar signal captured from plants, leaves are the most exposed part of the plant, and therefore the most important contributor to the signal. This has already been discussed earlier in paragraph 8 of the present manuscript.

Then, based on the earlier analysis, simple regression models were fitted: least squares and logarithmic-transformed linear regressions. Using the mean squared error as a metric, the performance assessment of these models was done by splitting the available biomass data into two subsets: train to fit the models and test to validate the results.

We have considered that the most interesting statement should be obtained for the leaf biomass, the compartment most correlated with the radar response as mentioned above. Indeed, by applying the logarithmic transformation model, we were able to improve the results on the validation data set compared to the simple least-squares linear regression. This transformation was performed after the analysis of the scatter plot of the radar ratio band with in situ measured leaf biomass. It showed a curved trend that can be explained with an exponential model, hence the importance of the correlation analysis.

Furthermore, we also trained a random forest model on the data at our disposition and the results obtained in terms of MSE were worse than those obtained with the two previous models, so they are not reported here. It is however probable that the RF would have performed better with a larger data set.

In the second part of this chapter, we presented a tool providing recommendations on the positioning of measurement points in parcels considering the intra-parcel heterogeneity. These locations leverage intra-parcel disparities, aiming to make the measurements as representative as possible.

We proposed an approach based on unsupervised K-means clustering of the radar response dynamic in each pixel. Two measures of similarity of each time series were tested, the most classical Euclidean distance measure, and another measure, more adapted to sequential data, dynamic time warping (DTW). Globally, both approaches provided relatively similar results in terms of inertia, with, however, a slight advantage for the DTW distance. This latter measure would have been much more efficient than the classical Euclidean distance if the pixels varied with completely different variation typology, which is not the case for the Sentinel-1 data, as it can detect shifts in the alignment of the sequences. Finally, we observed that, in general, the algorithm tends to group the pixels at the borders of the parcel into a common group.

### Data assimilation methods to improve the predictive power of mechanistic plant growth models

We presented an implementation of data assimilation methods to show how they can be used to improve the predictive powers of plant growth models, by leveraging observation data that could be estimated thanks to satellite imagery, thus opening perspectives of our work towards large-scale yield predictions.

We started by describing the general functioning of mechanistic plant growth models. We then discussed the interest of data assimilation as well as the general principle and operating details of this approach. An experimental part was presented, in which we present an implementation of a Convolution Particle Filter based data-assimilation algorithm and apply it to a mechanistic model of wheat growth adapted from the STICS model. The objective was to calibrate the soil parameters of the model using a sequence of synthetic simulated above-ground biomass data. We relied on biomass simulated data as the few biomass data sets that were available to us were incomplete and not very reliable. Starting with prior distributions of the most important soil parameters in the model, and dynamically correcting model calibration using experimental biomass data, data assimilation has allowed good predictive capacity, when compared with the simulated validation data. We also investigated the impact and the importance of the observation times as well as the number of available observations dates in the model calibration.

Finally, we believe that this feasibility study opens interesting perspectives for large-scale yield prediction, notably by coupling the results of biophysical data estimation from satellite imagery with the proposed data assimilation method.

## Perspectives

### Crop type recognition by machine learning methods using satellite images

The crop recognition tool that we have worked on is now integrated in a wider platform of agricultural services. In this context, improving its reliability and robustness at large scales is crucial. Because, even if the proposed models have shown quite satisfactory results on the evaluations we have conducted Prediction errors still exist. For example, pixels covering a subarea of a parcel that has endured vegetation accidents may not be well identified. Similarly, there are errors related to parcel border effects, where the spatial resolution of the satellite images used does not allow for differentiation between a field and its surroundings, and this may lead to incomplete georeferenced prediction renderings. To face these issues, we have started to work on two approaches. In the first one, we use the parcel contours over a set of previous years from an existing crop rotation database, such as the RPG, to establish the smallest common parcel for these years. Then, parcels are reconstructed by expanding the predictions to the most probable crop on the parcel presenting uncertainties/anomalies in crop identification. The second approach, which is necessary when there are no previous rotation data, consists in developing parcel segmentation models based on optical satellite imagery.

Furthermore, the final renderings of predictions are usually analyzed visually. We have thus started to work on a tool allowing an automatic diagnosis of the results of the predictions, the idea being to establish a metric that we have called ”filling rate” and that allows us to indicate how compact/dense the identified parcels are because we believe that it is an important indicator of the quality of the predictions.

The purpose of this work is to know instantaneously if, for example, a model trained on area A is acceptably portable on area B or not. In the case where the results on area B are not good enough (for example in terms of the filling rate previously mentioned), for reasons that may be related to unlearned variabilities or to imagery effects, the models must be re-trained on this new zone for a better prediction quality. It leads to another perspective. Indeed, we can imagine to re-train an already trained model instead of starting from scratch.

By way of medium and long-term perspectives, we believe that the proposed approach is prone to be used to discriminate varieties (cultivars) of the same crop. Nevertheless, our first impression is that radar will not be enough and that it will be necessary to integrate other sources of imagery such as optical, or even other imaging technologies. In this regard, we can mention, for instance, works of [Schmitt et al., 2017] where challenges and contributions of the fusion of SAR and optical remote sensing data have been discussed. Future trends in multi-sensor data fusion are also discussed.

Also, it would be interesting to extend our proposal to the so-called perennial crops which do not have an annual cycle and occupy the soil permanently, such as cotton or coffee. The challenge would then be to determine the periods to consider in the study of temporal satellite signals.

### Estimation of plant bio-physical variables by satellite imagery

In addition to allowing the generation of logistically cost-effective, non-destructive, and increasingly accurate measurement estimations, biophysical variable estimation using satellite imagery can provide a source of quasi-real-time data to adjust the calibration of plant growth models during the season via data assimilation methods. It promises more and more reliable forecasts. The statistical models we proposed can thus be used as a complement to plant growth models. Also, we believe that the diversification of imagery sources, such as the combination of radar and optical, can allow the design of more robust statistical models for biophysical and agronomic variables estimation such as Leaf Area Index, a widely important variable in plant modeling.

### Data assimilation methods to improve the predictive power of mechanistic plant growth models

As detailed above, a close perspective would be to use plant biophysical variables estimation such as biomass or LAI through statistical models and remote-sensing as input data for data assimilation. We concentrated on soil parameter characterization, but the idea of specifying a generic model to a particular situation is far more general. Data assimilation can be used to adapt to a new soil type, a new variety, or to new climatic conditions (e.g. severe stresses) not taken into account by the model for example. As such, it bears similarity to the whole scientific of ”domain adaptation” in statistical learning.

### Conclusion

Through this work, we have recourse to a mixture of technologies to address some concrete problems of today’s agricultural world. Benefiting from the availability of satellite imagery with a reasonable spatial and temporal resolution and using artificial intelligence methods, we have developed models allowing us to establish large-scale vegetation cover maps, particularly for major crops. This mix of technologies also allowed us to address topics related to agricultural yields. We discussed the contribution of satellite imagery in issues associated with the estimation of plant biophysical variables, as well as the interest in data assimilation methods for the improvement of agricultural yield predictions.

This thesis was prepared in an industrial context, in partnership with Cybeletech company, allowing us to interact permanently with the different agricultural actors. From closer up, we were able to assess the requirements, but also the issues and challenges of agriculture today and tomorrow, which we might resume like this: how to improve productions and their quality while ensuring sustainable development of agriculture in an increasingly diversified and complex context, marked by climate change.
Besides, we believe that this interaction with agricultural actors was and is essential to provide the most accurate and appropriate answers to their needs through tools designed with them. Also, this work has highlighted the crucial importance of data if we wish to propose increasingly accurate tools. Rightly so, this interaction with the agricultural actors can allow us to obtain data in quantity and of satisfactory quality because an agricultural actor who better understands the interest of what we propose to him is an actor who is ready to provide the maximum of data possible.

At last, we would like to underline that our work aims at accompanying the different actors of the agricultural chain; in any case, the digital and the new technologies can replace the farmer and his know-how.

# Bibliography

[Abadi et al., 2015] Abadi, M., Agarwal, A., Barham, P., Brevdo, E., Chen, Z., Citro, C., Corrado, G. S., Davis, A., Dean, J., Devin, M., Ghemawat, S., Goodfellow, I., Harp, A., Irving, G., Isard, M., Jia, Y., Jozefowicz, R., Kaiser, L., Kudlur, M., Levenberg, J., Mané, D., Monga, R., Moore, S., Murray, D., Olah, C., Schuster, M., Shlens, J., Steiner, B., Sutskever, I., Talwar, K., Tucker, P., Vanhoucke, V., Vasudevan, V., Viégas, F., Vinyals, O., Warden, P., Wattenberg, M., Wicke, M., Yu, Y., and Zheng, X. (2015). TensorFlow: Large-scale machine learning on heterogeneous systems. Software available from tensorflow.org.

[Abendroth et al., 2011] Abendroth, L. J., Elmore, R. W., Boyer, M. J., and Marlay, S. K. (2011). *Corn Growth and Development*. Iowa State University.

[Andrieu et al., 2010] Andrieu, C., Doucet, A., and Holenstein, R. (2010). Particle markov chain monte carlo methods. *Journal of the Royal Statistical Society: Series B (Statistical Methodology)*, 72(3):269–342.

[Angel et al., 2017] Angel, J. R., Widhalm, M., Todey, D., Massey, R., and Biehl, L. (2017). The u2u corn growing degree day tool: Tracking corn growth across the us corn belt. *Climate Risk Management*, 15:73 – 81. Useful to Usable: Developing Usable Climate Science for Agriculture.

[Arnaud Doucet and Gordon, 2001] Arnaud Doucet, N. d. F. and Gordon, N. (2001). *Sequential Monte Carlo Methods in Practice*. Springer, New York, NY.

[Arthur and Vassilvitskii, 2007] Arthur, D. and Vassilvitskii, S. (2007). K-means++: The advantages of careful seeding. In *Proceedings of the Eighteenth Annual ACM-SIAM Symposium on Discrete Algorithms*, SODA '07, page 1027–1035, USA. Society for Industrial and Applied Mathematics.

[Bayes, 1763] Bayes, T. (1763). An essay towards solving a problem in the doctrine of chances. *Philosophical Transactions*, 53:370–418.

[Bengio et al., 1994] Bengio, Y., Simard, P., and Frasconi, P. (1994). Learning long-term dependencies with gradient descent is difficult. *IEEE Transactions on Neural Networks*, 5(2):157–166.

[Blaes et al., 2006] Blaes, X., Defourny, P., Wegmuller, U., Della Vecchia, A., Guerriero, L., and Ferrazzoli, P. (2006). C-band polarimetric indexes for maize monitoring based on a validated radiative transfer model. *Geoscience and Remote Sensing, IEEE Transactions on*, 44:791 – 800.

[Boutarfa et al., 2013] Boutarfa, S., Bouchemakh, L., and Smara, Y. (2013). Application of improved sigma filter to polarimetric sar images. *Teledetection*, 11(2):307–323.

[Brisco et al., 1993] Brisco, B., Bedard, D., Naunheimer, J., and Brown, R. J. (1993). Environmental effects on radar data of agricultural areas. In *Canadian Symposium on Remote Sensing, Proceedings, 16th*, Earth Sciences Sector, Contribution Series 20041172, pages 283–288, 8th, Sherbrooke, Québec,. Association Québécoise de télédétection.

[Brisson et al., 2003] Brisson, N., Gary, C., Justes, E., Roche, R., Mary, B., Ripoche, D., Zimmer, D., Sierra, J., Bertuzzi, P., Burger, P., Bussière, F., Cabidoche, Y., Cellier, P., Debaeke, P., Gaudillère, J., Hénault, C., Maraux, F., Seguin, B., and Sinoquet, H. (2003). An overview of the crop model stics. *European Journal of Agronomy*, 18(3):309–332. Modelling Cropping Systems: Science, Software and Applications.

[Brisson et al., 2008] Brisson, N. N., Launay, M., Mary, B. B., and Beaudoin, N. N. (2008). *Conceptual basis, formalisations and parameterization of the STICS crop model*. Editions Quae.

[Campillo and Rossi, 2009] Campillo, F. and Rossi, V. (2009). Convolution particle filter for parameter estimation in general state-space models. *Aerospace and Electronic Systems, IEEE Transactions on*, 45:1063 – 1072.

[Cappe et al., 2005] Cappe, O., Moulines, E., and Rydén, T. (2005). *Inference in Hidden Markov Models*. Springer, New York, NY.

[Cazals, 2017] Cazals, C. (2017). *Apport des données Sentinel-1 pour la cartographie des milieux humides*. PhD thesis, Université Paris-Est.

[Chen and Cournède, 2014] Chen, Y. and Cournède, P.-H. (2014). Data assimilation to reduce uncertainty of crop model prediction with convolution particle filtering. *Ecological Modelling*, 290:165–177. Special Issue of the 4th International Symposium on Plant Growth Modeling, Simulation, Visualization and Applications (PMA'12 ).

[Chen et al., 2014] Chen, Y., Lin, Z., Zhao, X., Wang, G., and Gu, Y. (2014). Deep learning-based classification of hyperspectral data. *Selected Topics in Applied Earth Observations and Remote Sensing, IEEE Journal of*, 7:2094–2107.

[Chen et al., 2013] Chen, Y., Trevezas, S., Gupta, A., and Cournède, P.-H. (2013). Some sequential Monte Carlo techniques for Data Assimilation in a plant growth model. In *Applied Stochastic Models and Data Analysis International Conference (ASMDA) 2013*, page in press, Spain.

[Chen et al., 2015] Chen, Y., Zhao, X., and Jia, X. (2015). Spectral-spatial classification of hyperspectral data based on deep belief network. *IEEE J. Sel. Top. Appl. Earth Obs. Remote. Sens.*, 8(6):2381–2392.

[Chollet et al., 2015] Chollet, F. et al. (2015). Keras. `https://keras.io`.

[Chu and Yu, 2020] Chu, Z. and Yu, J. (2020). An end-to-end model for rice yield prediction using deep learning fusion. *Computers and Electronics in Agriculture*, 174:105471.

[Cournède et al., 2013] Cournède, P.-H., Chen, Y., Wu, Q., Baey, C., and Bayol, B. (2013). Development and evaluation of plant growth models: Methodology and implementation in the pygmalion platform. *Mathematical Modelling of Natural Phenomena*, 8(4):112–130.

[Cross and Zuber, 1972] Cross, H. Z. and Zuber, M. S. (1972). Prediction of flowering dates in maize based on different methods of estimating thermal units1. *Agronomy Journal*, 64(3):351–355.

[Dalsasso et al., 2021a] Dalsasso, E., Denis, L., and Tupin, F. (2021a). SAR2SAR: a semi-supervised despeckling algorithm for SAR images. *IEEE Journal of Selected Topics in Applied Earth Observations and Remote Sensing*, pages 1–1. Article accepted for publication to IEEE Journal of Selected Topics in Applied Earth Observations and Remote Sensing. Code is made available at https://gitlab.telecom-paris.fr/RING/SAR2SAR.

[Dalsasso et al., 2021b] Dalsasso, E., Meraoumia, I., Denis, L., and Tupin, F. (2021b). Exploiting multi-temporal information for improved speckle reduction of Sentinel-1 SAR images by deep learning. In *IGARSS 2021*, Bruxelles (virtual), Belgium.

[Dalsasso et al., 2020] Dalsasso, E., Yang, X., Denis, L., Tupin, F., and Yang, W. (2020). SAR Image Despeckling by Deep Neural Networks: from a Pre-Trained Model to an End-to-End Training Strategy. *Remote Sensing*, 12(16):2636.

[Del Moral, 2004] Del Moral, P. (2004). *Feynman-Kac Formulae: Genealogical and Interacting Particle Systems With Applications*. Probability and its Applications. Springer, New York, NY.

[Deledalle et al., 2017] Deledalle, C.-A., Denis, L., Tabti, S., and Tupin, F. (2017). MuLoG, or How to apply Gaussian denoisers to multi-channel SAR speckle reduction? *IEEE Transactions on Image Processing*, 26(9):4389–4403.

[Delécolle et al., 1992] Delécolle, R., Maas, S., Guérif, M., and Baret, F. (1992). Remote sensing and crop production models: present trends. *ISPRS Journal of Photogrammetry and Remote Sensing*, 47(2):145–161.

[Denis et al., 2021] Denis, L., Dalsasso, E., and Tupin, F. (2021). A review of deep-learning techniques for SAR image restoration. In *IGARSS 2021*, Bruxelles (virtual), Belgium.

[Denis et al., 2019] Denis, L., Deledalle, C.-A., and Tupin, F. (2019). From Patches to Deep Learning: Combining Self-Similarity and Neural Networks for Sar Image Despeckling. In *2019 IEEE International Geoscience and Remote Sensing Symposium (IGARSS 2019)*, IGARSS

2019 - 2019 IEEE International Geoscience and Remote Sensing Symposium, pages 5113–5116, Yokohama, Japan. IEEE.

[Desgranges et al., 2007] Desgranges, C., Pennetier, A., Delor, G., and Fleurat-Lessard, F. F. (2007). Base de données multifactorielle de l'incidence des facteurs agro-climatiques sur l'intensité de la fusariose et sur les teneurs en fusariotoxines. In *Mycotoxines fusariennes des céréales*, Progrès et perspectives de la recherche sur les mycotoxines de Fusarium dans les céréales, Arcachon, France. Editions Quae.

[Dodge, 2008] Dodge, Y. (2008). *Fisher Table*, page 204. Springer New York, New York, NY.

[Dong et al., 2020] Dong, T., Liu, J., Qian, B., He, L., Liu, J., Wang, R., Jing, Q., Champagne, C., McNairn, H., Powers, J., Shi, Y., Chen, J. M., and Shang, J. (2020). Estimating crop biomass using leaf area index derived from landsat 8 and sentinel-2 data. *ISPRS Journal of Photogrammetry and Remote Sensing*, 168:236–250.

[Dorigo et al., 2017] Dorigo, W., Wolfgang, W., Clement, A., Franziska, A., Gianpaolo, B., Luca, B., Daniel, C., Martin, E., Matthias, F., Alexander, G., Eva, H., Paul, D. H., Martin, H., Jaakko, I., Richard, d. J., Richard, K., William, L., Yi, Y. L., Diego, M., Thomas, M., Nadine, N.-S., Robert, P., Chiara, P., Christoph, R., Robin, v. d. S., Sonia, I. S., Tuomo, S., and Pascal, L. (2017). Esa cci soil moisture for improved earth system understanding: State-of-the art and future directions. *Remote Sensing of Environment*, 203:185 – 215. Earth Observation of Essential Climate Variables.

[Dorigo et al., 2007] Dorigo, W., Zurita-Milla, R., de Wit, A., Brazile, J., Singh, R., and Schaepman, M. (2007). A review on reflective remote sensing and data assimilation techniques for enhanced agroecosystem modeling. *International Journal of Applied Earth Observation and Geoinformation*, 9(2):165–193. Advances in airborne electromagnetics and remote sensing of agro-ecosystems.

[Dowd, 2007] Dowd, M. (2007). Bayesian statistical data assimilation for ecosystem models using markov chain monte carlo. *Journal of Marine Systems*, 68(3):439–456.

[Duflot et al., 2022] Duflot, R., San-Cristobal, M., Andrieu, E., Choisis, J.-P., Esquerré, D., Ladet, S., Ouin, A., Rivers-Moore, J., Sheeren, D., Sirami, C., Fauvel, M., and Vialatte, A. (2022). Farming intensity indirectly reduces crop yield through negative effects on agrobiodiversity and key ecological functions. *Agriculture, Ecosystems and Environment*, 326:107810.

[d'Andrimont et al., 2020] d'Andrimont, R., Taymans, M., Lemoine, G., Ceglar, A., Yordanov, M., and van der Velde, M. (2020). Detecting flowering phenology in oil seed rape parcels with sentinel-1 and -2 time series. *Remote Sensing of Environment*, 239:111660.

[Elachi, 1988] Elachi, C. (1988). *Polarimetric SAR Radar Imaging: From Basic to Applications*. IEEE Press.

[Elman, 1990] Elman, J. L. (1990). Finding structure in time. *Cognitive Science*, 14(2):179 – 211.

[Fassnacht et al., 2021] Fassnacht, F. E., Poblete-Olivares, J., Rivero, L., Lopatin, J., Ceballos-Comisso, A., and Galleguillos, M. (2021). Using sentinel-2 and canopy height models to derive a landscape-level biomass map covering multiple vegetation types. *International Journal of Applied Earth Observation and Geoinformation*, 94:102236.

[Ferrazzoli et al., 1997] Ferrazzoli, P., Paloscia, S., Pampaloni, P., Schiavon, G., Sigismondi, S., and Solimini, D. (1997). The potential of multifrequency polarimetric sar in assessing agricultural and arboreous biomass. *IEEE Transactions on Geoscience and Remote Sensing*, 35(1):5–17.

[Fischer et al., 2002] Fischer, R., Santiveri, F., and Vidal, I. (2002). Crop rotation, tillage and crop residue management for wheat and maize in the sub-humid tropical highlands: Ii. maize and system performance. *Field Crops Research*, 79(2):123–137.

[Forkuor et al., 2020] Forkuor, G., Benewinde Zoungrana, J.-B., Dimobe, K., Ouattara, B., Vadrevu, K. P., and Tondoh, J. E. (2020). Above-ground biomass mapping in west african dryland forest using sentinel-1 and 2 datasets - a case study. *Remote Sensing of Environment*, 236:111496.

[Fowler et al., 1999] Fowler, D. B., Limin, A. E., and Ritchie, J. T. (1999). Low-temperature tolerance in cereals: Model and genetic interpretation. *Crop Science*, 39(3):cropsci1999.0011183X003900020002x.

[Fracastoro et al., 2020] Fracastoro, G., Magli, E., Poggi, G., Scarpa, G., Valsesia, D., and Verdoliva, L. (2020). Deep Learning Methods For Synthetic Aperture Radar Image Despeckling: An Overview Of Trends And Perspectives. *arXiv e-prints*, page arXiv:2012.05508.

[Gasnier et al., 2021] Gasnier, N., Dalsasso, E., Denis, L., and Tupin, F. (2021). Despeckling Sentinel-1 GRD images by deep learning and application to narrow river segmentation. In *IGARSS 2021*, Bruxelles, Belgium.

[Geiger et al., 2010] Geiger, F., Bengtsson, J., Berendse, F., Weisser, W. W., Emmerson, M., Morales, M. B., Ceryngier, P., Liira, J., Tscharntke, T., Winqvist, C., Eggers, S., Bommarco, R., Pärt, T., Bretagnolle, V., Plantegenest, M., Clement, L. W., Dennis, C., Palmer, C., Oñate, J. J., Guerrero, I., Hawro, V., Aavik, T., Thies, C., Flohre, A., Hänke, S., Fischer, C., Goedhart, P. W., and Inchausti, P. (2010). Persistent negative effects of pesticides on biodiversity and biological control potential on european farmland. *Basic and Applied Ecology*, 11(2):97–105.

[Gers, 2001] Gers, F. (2001). Long short-term memory in recurrent neural networks.

[Gers and Schmidhuber, 2001] Gers, F. and Schmidhuber, E. (2001). Lstm recurrent networks learn simple context-free and context-sensitive languages. *IEEE transactions on neural networks*, 12(6):1333—1340.

[Gers et al., 2000] Gers, F., Schmidhuber, J., and Cummins, F. (2000). Learning to forget: Continual prediction with lstm. *Neural computation*, 12:2451–71.

[Gers et al., 2002] Gers, F., Schraudolph, N., and Schmidhuber, J. (2002). Learning precise timing with lstm recurrent networks. *Journal of Machine Learning Research*, 3:115–143.

[Glorot and Bengio, 2010] Glorot, X. and Bengio, Y. (2010). Understanding the difficulty of training deep feedforward neural networks. In Teh, Y. W. and Titterington, M., editors, *Proceedings of the Thirteenth International Conference on Artificial Intelligence and Statistics*, volume 9 of *Proceedings of Machine Learning Research*, pages 249–256, Chia Laguna Resort, Sardinia, Italy. JMLR Workshop and Conference Proceedings.

[Goodfellow et al., 2016] Goodfellow, I., Bengio, Y., and Courville, A. (2016). *Deep Learning*. MIT Press. `http://www.deeplearningbook.org`.

[Goodman, 1976] Goodman, J. W. (1976). Some fundamental properties of speckle∗. *J. Opt. Soc. Am.*, 66(11):1145–1150.

[Gordon et al., 1993] Gordon, N., Salmond, D., and Smith, A. (1993). Novel approach to nonlinear/non-gaussian bayesian state estimation. *IEEE Proceedings F, Radar and Signal Processing*, 140(2):107–113.

[Graves, 2012] Graves, A. (2012). *Supervised Sequence Labelling with Recurrent Neural Networks*, volume 385. Springer, Berlin, Heidelberg.

[Graves et al., 2007] Graves, A., Liwicki, M., Bunke, H., Schmidhuber, J., and Fernández, S. (2007). Unconstrained on-line handwriting recognition with recurrent neural networks. In Platt, J., Koller, D., Singer, Y., and Roweis, S., editors, *Advances in Neural Information Processing Systems*, volume 20. Curran Associates, Inc.

[Graves et al., 2013] Graves, A., Mohamed, A.-r., and Hinton, G. (2013). Speech recognition with deep recurrent neural networks. *ICASSP, IEEE International Conference on Acoustics, Speech and Signal Processing - Proceedings*, 38.

[Gregor et al., 2015] Gregor, K., Danihelka, I., Graves, A., Rezende, D. J., and Wierstra, D. (2015). Draw: A recurrent neural network for image generation.

[Gruber et al., 2017] Gruber, A., Dorigo, W., Crow, W., and Wagner, W. (2017). Triple collocation-based merging of satellite soil moisture retrievals. *IEEE Transactions on Geoscience and Remote Sensing*, PP:1–13.

[Gruber et al., 2019] Gruber, A., Scanlon, T., van der Schalie, R., Wagner, W., and Dorigo, W. (2019). Evolution of the esa cci soil moisture climate data records and their underlying merging methodology. *Earth System Science Data*, 11(2):717–739.

[Guerif et al., 1988] Guerif, M., Delecolle, R., Gu, X. F., Guinot, J., Jappiot, M., Leblon, B., Steinmetz, S., and Seguin, B. (1988). Utilisation de la teledetection par satellite pour le suivi des cultures dans la basse vallee du Rhone. Estimation de la biomasse et du rendement des cultures a partir du satellite SPOT : resultats d'une experimentation sur ble dur en Camargue. Rapport final 1987.

[Gómez et al., 2016] Gómez, C., White, J. C., and Wulder, M. A. (2016). Optical remotely sensed time series data for land cover classification: A review. *ISPRS Journal of Photogrammetry and Remote Sensing*, 116:55–72.

[Han et al., 2012] Han, W., Yang, Z., Di, L., and Mueller, R. (2012). Cropscape: A web service based application for exploring and disseminating us conterminous geospatial cropland data products for decision support. *Computers and Electronics in Agriculture*, 84:111 – 123.

[Hersbach et al., 2020] Hersbach, H., Bell, B., Berrisford, P., Hirahara, S., Horányi, A., Muñoz-Sabater, J., Nicolas, J., Peubey, C., Radu, R., Schepers, D., Simmons, A., Soci, C., Abdalla, S., Abellan, X., Balsamo, G., Bechtold, P., Biavati, G., Bidlot, J., Bonavita, M., De Chiara, G., Dahlgren, P., Dee, D., Diamantakis, M., Dragani, R., Flemming, J., Forbes, R., Fuentes, M., Geer, A., Haimberger, L., Healy, S., Hogan, R. J., Hólm, E., Janisková, M., Keeley, S., Laloyaux, P., Lopez, P., Lupu, C., Radnoti, G., de Rosnay, P., Rozum, I., Vamborg, F., Villaume, S., and Thépaut, J.-N. (2020). The era5 global reanalysis. *Quarterly Journal of the Royal Meteorological Society*, 146(730):1999–2049.

[Hochreiter et al., 2001] Hochreiter, S., Bengio, Y., Frasconi, P., and Schmidhuber, J. (2001). Gradient flow in recurrent nets: the difficulty of learning long-term dependencies. In Kremer, S. C. and Kolen, J. F., editors, *A Field Guide to Dynamical Recurrent Neural Networks*. IEEE Press.

[Hochreiter and Schmidhuber, 1997] Hochreiter, S. and Schmidhuber, J. (1997). Long short-term memory. *Neural computation*, 9:1735–80.

[Inglada et al., 2017] Inglada, J., Vincent, A., Arias, M., Tardy, B., Morin, D., and Rodes, I. (2017). Operational high resolution land cover map production at the country scale using satellite image time series. *Remote Sensing*, 9(1).

[Ioffe and Szegedy, 2015] Ioffe, S. and Szegedy, C. (2015). Batch normalization: Accelerating deep network training by reducing internal covariate shift. *CoRR*, abs/1502.03167.

[Ionides et al., 2011] Ionides, E. L., Bhadra, A., Atchadé, Y., and King, A. (2011). Iterated filtering. *The Annals of Statistics*, 39(3):1776 – 1802.

[Jin et al., 2018a] Jin, X., Kumar, L., Li, Z., Feng, H., Xu, X., Yang, G., and Wang, J. (2018a). A review of data assimilation of remote sensing and crop models. *European Journal of Agronomy*, 92:141–152.

[Jin et al., 2018b] Jin, X., Kumar, L., Li, Z., Feng, H., Xu, X., Yang, G., and Wang, J. (2018b). A review of data assimilation of remote sensing and crop models. *European Journal of Agronomy*, 92:141–152.

[Jones et al., 2017] Jones, J. W., Antle, J. M., Basso, B., Boote, K. J., Conant, R. T., Foster, I., Godfray, H. C. J., Herrero, M., Howitt, R. E., Janssen, S., Keating, B. A., Munoz-Carpena, R., Porter, C. H., Rosenzweig, C., and Wheeler, T. R. (2017). Brief history of agricultural systems modeling. *Agricultural Systems*, 155:240–254.

[Jullien et al., 2011] Jullien, A., Mathieu, A., Allirand, J.-M., Pinet, A., De Reffye, P., Cournède, P.-H., and Ney, B. (2011). Characterization of the interactions between architecture and source–sink relationships in winter oilseed rape (brassica napus) using the greenlab model. *Annals of botany*, 107(5):765–779.

[Kang et al., 2011] Kang, F., Galinier, T., Cournède, P.-H., and Lecoeur, J. (2011). Parameterization of plant growth models to characterize genotype by environment interactions: a methodology adapted to breeding programs. In Halford, N., Semenov, and M., editors, *Aspects of Applied Biology 107: Systems Approaches to Crop Improvement*, pages 27–35. The Association of Applied Biologists.

[Keating et al., 2003] Keating, B., Carberry, P., Hammer, G., Probert, M., Robertson, M., Holzworth, D., Huth, N., Hargreaves, J., Meinke, H., Hochman, Z., McLean, G., Verburg, K., Snow, V., Dimes, J., Silburn, M., Wang, E., Brown, S., Bristow, K., Asseng, S., Chapman, S., McCown, R., Freebairn, D., and Smith, C. (2003). An overview of apsim, a model designed for farming systems simulation. *European Journal of Agronomy*, 18(3):267–288. Modelling Cropping Systems: Science, Software and Applications.

[Khaldoune et al., 2011] Khaldoune, J., van Bochove, E., Bernier, M., and Nolin, M. (2011). Mapping agricultural frozen soil on the watershed scale using remote sensing data. *Applied and Environmental Soil Science*, 2011.

[Khatami et al., 2016] Khatami, R., Mountrakis, G., and Stehman, S. (2016). A meta-analysis of remote sensing research on supervised pixel-based land-cover image classification processes: General guidelines for practitioners and future research. *Remote Sensing of Environment*, 177:89–100.

[Kingma and Ba, 2017] Kingma, D. P. and Ba, J. (2017). Adam: A method for stochastic optimization.

[Kumar et al., 2017] Kumar, P., Prasad, R., . Gupta, D., Mishra, V., Vishwakarma, A., Yadav, V., Bala, R., Choudhary, A., and Avtar, R. (2017). Estimation of winter wheat crop growth parameters using time series sentinel-1a sar data. *Geocarto International*, pages 1–24.

[Kussul et al., 2017] Kussul, N., Lavreniuk, M., Skakun, S., and Shelestov, A. (2017). Deep learning classification of land cover and crop types using remote sensing data. *IEEE Geoscience and Remote Sensing Letters*, 14(5):778–782.

[Laur et al., 2004] Laur, H., Bally, P., Meadows, P., Sanchez, J., Schaettler, B., Lopinto, E., and Esteban, D. (2004). Derivation of backscattering coefficient sigma 0 in esa ers sar pri products. Technical report, ESA.

[Laurin et al., 2018] Laurin, G. V., Balling, J., Corona, P., Mattioli, W., Papale, D., Puletti, N., Rizzo, M., Truckenbrodt, J., and Urban, M. (2018). Above-ground biomass prediction by Sentinel-1 multitemporal data in central Italy with integration of ALOS2 and Sentinel-2 data. *Journal of Applied Remote Sensing*, 12(1):1 – 18.

[LeCun and Bengio, 1998] LeCun, Y. and Bengio, Y. (1998). *Convolutional Networks for Images, Speech, and Time Series*, page 255–258. MIT Press, Cambridge, MA, USA.

[LeCun et al., 1999] LeCun, Y., Haffner, P., Bottou, L., and Bengio, Y. (1999). *Object Recognition with Gradient-Based Learning*, pages 319–345. Springer Berlin Heidelberg, Berlin, Heidelberg.

[Lee, 1983] Lee, J.-S. (1983). Digital image smoothing and the sigma filter. *Computer Vision, Graphics, and Image Processing*, 24(2):255–269.

[Lee, 1986] Lee, J. S. (1986). Speckle suppression and analysis for synthetic aperture radar images. *Optical Engineering*, 25(5):636.

[Lee et al., 2009] Lee, J.-S., Wen, J.-H., Ainsworth, T. L., Chen, K.-S., and Chen, A. J. (2009). Improved sigma filter for speckle filtering of sar imagery. *EEE Transactions on Geoscience Remote Sensing*, 47(1):202–213.

[Legrand et al., 2017] Legrand, F., Picot, A., Cobo-Díaz, J. F., Chen, W., and Le Floch, G. (2017). Challenges facing the biological control strategies for the management of fusarium head blight of cereals caused by f. graminearum. *Biological Control*, 113:26–38.

[Lemaire et al., 2009] Lemaire, S., Maupas, F., Cournède, P.-H., and De Reffye, P. (2009). A morphogenetic crop model for sugar-beet (beta vulgaris l.). In *Crop modeling and decision support*, pages 116–129. Springer.

[Maggiori et al., 2017] Maggiori, E., Tarabalka, Y., Charpiat, G., and Alliez, P. (2017). Convolutional Neural Networks for Large-Scale Remote Sensing Image Classification. *IEEE Transactions on Geoscience and Remote Sensing*, 55:645–657.

[Maiorano et al., 2008] Maiorano, A., Blandino, M., Reyneri, A., and Vanara, F. (2008). Effects of maize residues on the fusarium spp. infection and deoxynivalenol (don) contamination of wheat grain. *Crop Protection*, 27(2):182–188.

[Makowski et al., 2004] Makowski, D., Jeuffroy, M.-H., and Guerif, M. (2004). Bayesian methods for updating crop-model predictions, applications for predicting biomass and grain protein content. *Frontis*, 3.

[Mansaray et al., 2020] Mansaray, L. R., Zhang, K., and Kanu, A. S. (2020). Dry biomass estimation of paddy rice with sentinel-1a satellite data using machine learning regression algorithms. *Computers and Electronics in Agriculture*, 176:105674.

[Matton et al., 2015] Matton, N., Canto, G. S., Waldner, F., Valero, S., Morin, D., Inglada, J., Arias, M., Bontemps, S., Koetz, B., and Defourny, P. (2015). An automated method for annual cropland mapping along the season for various globally-distributed agrosystems using high spatial and temporal resolution time series. *Remote Sensing*, 7(10):13208–13232.

[Mckinley and Levine, 1998] Mckinley, S. and Levine, M. (1998). Cubic spline interpolation. *College of the Redwoods*, 45(1):1049–1060.

[McMaster and Wilhelm, 1997] McMaster, G. S. and Wilhelm, W. (1997). Growing degree-days: one equation, two interpretations. *Agricultural and Forest Meteorology*, 87(4):291 – 300.

[Midhun et al., 2014] Midhun, M. E., Nair, S. R., Prabhakar, V. T. N., and Kumar, S. S. (2014). Deep model for classification of hyperspectral image using restricted boltzmann machine. In *Proceedings of the 2014 International Conference on Interdisciplinary Advances in Applied Computing*, ICONIAAC '14, New York, NY, USA. Association for Computing Machinery.

[Miranda and Meadows, 2015] Miranda, N. and Meadows, P. (2015). Radiometric calibration of s-1 level-1 products generated by the s-1 ipf. Technical report, ESA.

[Musso and Oudjane, 1998] Musso, C. and Oudjane, O. (1998). Regularisation schemes for branching particle systems as a numerical solving method of the nonlinear filtering problem. *OFFICE NATIONAL D ETUDES ET DE RECHERCHES AEROSPATIALES ONERA-PUBLICATIONS-TP*.

[Oudjane and Musso, 1998] Oudjane, N. and Musso, C. (1998). Regularized particle schemes applied to the tracking problem. *OFFICE NATIONAL D ETUDES ET DE RECHERCHES AEROSPATIALES ONERA-PUBLICATIONS-TP*.

[Parzen, 1962] Parzen, E. (1962). On Estimation of a Probability Density Function and Mode. *The Annals of Mathematical Statistics*, 33(3):1065 – 1076.

[Pelletier et al., 2016] Pelletier, C., Valero, S., Inglada, J., Champion, N., and Dedieu, G. (2016). Assessing the robustness of random forests to map land cover with high resolution satellite image time series over large areas. *Remote Sensing of Environment*, 187:156–168.

[Pelletier et al., 2018] Pelletier, C., Webb, G. I., and Petitjean, F. (2018). Temporal convolutional neural network for the classification of satellite image time series. *CoRR*, abs/1811.10166.

[Peters et al., 2003] Peters, R., Sturz, A., Carter, M., and Sanderson, J. (2003). Developing disease-suppressive soils through crop rotation and tillage management practices. *Soil and Tillage Research*, 72(2):181–192. Soil Agroecosystems: Impacts of Management on Soil Health and Crop Diseases.

[Petitjean et al., 2011] Petitjean, F., Ketterlin, A., and Gancarski, P. (2011). A global averaging method for dynamic time warping, with applications to clustering. *Pattern Recognition*, 44:678–.

[Peña-Barragán et al., 2011] Peña-Barragán, J. M., Ngugi, M. K., Plant, R. E., and Six, J. (2011). Object-based crop identification using multiple vegetation indices, textural features and crop phenology. *Remote Sensing of Environment*, 115(6):1301–1316.

[Postadjian et al., 2017] Postadjian, T., Le Bris, A., Sahbi, H., and Mallet, C. (2017). Investigating the Potential of Deep Neural Networks for Large-Scale Classification of Very High Resolution Satellite Images. *ISPRS Annals of Photogrammetry, Remote Sensing and Spatial Information Sciences*, 41W1:183–190.

[Ritchie and Nesmith, 2015] Ritchie, J. T. and Nesmith, D. S. (2015). *Temperature and Crop Development*, chapter 2, pages 5–29. John Wiley & Sons, Ltd.

[Romero et al., 2013] Romero, J. R., Roncallo, P. F., Akkiraju, P. C., Ponzoni, I., Echenique, V. C., and Carballido, J. A. (2013). Using classification algorithms for predicting durum wheat yield in the province of buenos aires. *Computers and Electronics in Agriculture*, 96:173–179.

[Rosich and Meadows, 2004] Rosich, B. and Meadows, P. (2004). Absolute calibration of asar level 1 products generated with pf-asar. Technical report, ESA.

[Ruder, 2017] Ruder, S. (2017). An overview of gradient descent optimization algorithms.

[Rumelhart et al., 1986] Rumelhart, D., Hinton, G. E., and Williams, R. J. (1986). Learning representations by back-propagating errors. *Nature*, 323:533–536.

[Rußwurm and Körner, 2017] Rußwurm, M. and Körner, M. (2017). Multi-Temporal Land Cover Classification with Long Short-Term Memory Neural Networks. *ISPRS - International Archives of the Photogrammetry, Remote Sensing and Spatial Information Sciences*, 42W1:551–558.

[Rustowicz, 2017] Rustowicz, R. (2017). Crop classification with multi-temporal satellite imagery. Final Reports. Univ. Stanford.

[S. Lee, 2009] S. Lee, E. P. (2009). *Polarimetric SAR Radar Imaging: From Basic to Applications*. CRC Press, Taylor & Francis Group.

[Sakoe and Chiba, 1971] Sakoe, H. and Chiba, S. (1971). A dynamic programming approach to continuous speech recognition. In *Proceedings of the Seventh International Congress on Acoustics, Budapest*, volume 3, pages 65–69, Budapest. Akadémiai Kiadó.

[Sakoe and Chiba, 1978] Sakoe, H. and Chiba, S. (1978). Dynamic programming algorithm optimization for spoken word recognition. *IEEE Transactions on Acoustics, Speech, and Signal Processing*, 26(1):43–49.

[Scarpa et al., 2018] Scarpa, G., Gargiulo, M., Mazza, A., and Gaetano, R. (2018). A cnn-based fusion method for feature extraction from sentinel data. *Remote Sensing*, 10:236.

[Schmider et al., 2010] Schmider, E., Ziegler, M., Danay, E., Beyer, L., and Bühner, M. (2010). Is it really robust? *Methodology*, 6(4):147–151.

[Schmitt et al., 2017] Schmitt, M., Tupin, F., and Zhu, X. x. (2017). FUSION OF SAR AND OPTICAL REMOTE SENSING DATA - CHALLENGES AND RECENT TRENDS. In *IGARSS*, Fort-Worth, United States.

[Serra and Pons, 2008] Serra, P. and Pons, X. (2008). Monitoring farmers' decisions on mediterranean irrigated crops using satellite image time series. *International Journal of Remote Sensing*, 29(8):2293–2316.

[Slavkovikj et al., 2015] Slavkovikj, V., Verstockt, S., De Neve, W., Van Hoecke, S., and Van de Walle, R. (2015). Hyperspectral image classification with convolutional neural networks. In

*Proceedings of the 23rd ACM International Conference on Multimedia*, MM '15, page 1159–1162, New York, NY, USA. Association for Computing Machinery.

[Small and Schubert, 2019] Small, D. and Schubert, A. (2019). Guide to sentinel-1geocoding. Technical report, University of Zurich / RSL.

[Srivastava et al., 2014] Srivastava, N., Hinton, G., Krizhevsky, A., Sutskever, I., and Salakhutdinov, R. (2014). Dropout: A simple way to prevent neural networks from overfitting. *Journal of Machine Learning Research*, 15(56):1929–1958.

[Steele-Dunne et al., 2017] Steele-Dunne, S. C., McNairn, H., Monsivais-Huertero, A., Judge, J., Liu, P. W., and Papathanassiou, K. (2017). Radar remote sensing of agricultural canopies: A review. *IEEE Journal of Selected Topics in Applied Earth Observations and Remote Sensing*, 10(5):2249–2273.

[Tardieu, 2003] Tardieu, F. (2003). Virtual plants: modelling as a tool for the genomics of tolerance to water deficit. *Trends in Plant Science*, 8(1):9–14.

[Thenkabail et al., 2000] Thenkabail, P. S., Smith, R. B., and De Pauw, E. (2000). Hyperspectral vegetation indices and their relationships with agricultural crop characteristics. *Remote Sensing of Environment*, 71(2):158 – 182.

[Tieleman and Hinton, 2012] Tieleman, T. and Hinton, G. (2012). Lecture 6.5-rmsprop: Divide the gradient by a running average of its recent magnitude. *COURSERA: Neural networks for machine learning*, 4(2):26–31.

[Tomaz et al., 2021] Tomaz, A., Palma, J. F., Ramos, T., Costa, M. N., Rosa, E., Santos, M., Boteta, L., Dôres, J., and Patanita, M. (2021). Yield, technological quality and water footprints of wheat under mediterranean climate conditions: A field experiment to evaluate the effects of irrigation and nitrogen fertilization strategies. *Agricultural Water Management*, 258:107214.

[Tupin et al., 2019] Tupin, F., Denis, L., Deledalle, C.-A., and Ferraioli, G. (2019). TEN YEARS OF PATCH-BASED APPROACHES FOR SAR IMAGING: A REVIEW. In *IGARSS (International Geoscience and Remote Sensing Symposium)*, Yokohama, Japan.

[Ulaby, 1982] Ulaby, F. R. M. A. F. (1982). *Microwave Remote sensing active and passive; V. 2 - Radar remote sensing and surface scattering and emission theory*. Addison-Wesley.

[Valero et al., 2016] Valero, S., Morin, D., Inglada, J., Sepulcre, G., Arias, M., Hagolle, O., Dedieu, G., Bontemps, S., Defourny, P., and Koetz, B. (2016). Production of a dynamic cropland mask by processing remote sensing image series at high temporal and spatial resolutions. *Remote Sensing*, 8(1).

[van Klompenburg et al., 2020] van Klompenburg, T., Kassahun, A., and Catal, C. (2020). Crop yield prediction using machine learning: A systematic literature review. *Computers and Electronics in Agriculture*, 177:105709.

[Veloso et al., 2017] Veloso, A., Mermoz, S., Bouvet, A., Le Toan, T., Planells, M., Dejoux, J.-F., and Ceschia, E. (2017). Understanding the temporal behavior of crops using sentinel-1 and sentinel-2-like data for agricultural applications. *Remote Sensing of Environment*, 199:415–426.

[Venugopalan et al., 2015] Venugopalan, S., Rohrbach, M., Donahue, J., Mooney, R., Darrell, T., and Saenko, K. (2015). Sequence to sequence – video to text.

[Virtanen et al., 2020] Virtanen, P., Gommers, R., Oliphant, T. E., Haberland, M., Reddy, T., Cournapeau, D., Burovski, E., Peterson, P., Weckesser, W., Bright, J., van der Walt, S. J., Brett, M., Wilson, J., Millman, K. J., Mayorov, N., Nelson, A. R. J., Jones, E., Kern, R., Larson, E., Carey, C. J., Polat, İ., Feng, Y., Moore, E. W., VanderPlas, J., Laxalde, D., Perktold, J., Cimrman, R., Henriksen, I., Quintero, E. A., Harris, C. R., Archibald, A. M., Ribeiro, A. H., Pedregosa, F., van Mulbregt, P., and SciPy 1.0 Contributors (2020). SciPy 1.0: Fundamental Algorithms for Scientific Computing in Python. *Nature Methods*, 17:261–272.

[Vreugdenhil et al., 2018] Vreugdenhil, M., Wagner, W., Bauer-Marschallinger, B., Pfeil, I., Teubner, I., Rüdiger, C., and Strauss, P. (2018). Sensitivity of sentinel-1 backscatter to vegetation dynamics: An austrian case study. *Remote Sensing*, 10(9):1396.

[Vuolo et al., 2018] Vuolo, F., Neuwirth, M., Immitzer, M., Atzberger, C., and WaiTim, N. (2018). How much does multi-temporal sentinel-2 data improve crop type classification? *International Journal of Applied Earth Observation and Geoinformation*, 72:122–130.

[Wang et al., 2021] Wang, J., Barański, M., Hasanaliyeva, G., Korkut, R., Kalee, H. A., Leifert, A., Winter, S., Janovska, D., Willson, A., Barkla, B., Iversen, P. O., Seal, C., Bilsborrow, P., Leifert, C., Rempelos, L., and Volakakis, N. (2021). Effect of irrigation, fertiliser type and variety on grain yield and nutritional quality of spelt wheat (triticum spelta) grown under semi-arid conditions. *Food Chemistry*, 358:129826.

[Wikle and Berliner, 2007a] Wikle, C. K. and Berliner, L. M. (2007a). A bayesian tutorial for data assimilation. *Physica D: Nonlinear Phenomena*, 230(1):1–16. Data Assimilation.

[Wikle and Berliner, 2007b] Wikle, C. K. and Berliner, L. M. (2007b). A bayesian tutorial for data assimilation. *Physica D: Nonlinear Phenomena*, 230(1-2):1–16.

[Wood et al., 2002] Wood, D., McNairn, H., Brown, R., and Dixon, R. (2002). The effect of dew on the use of radarsat-1 for crop monitoring: Choosing between ascending and descending orbits. *Remote Sensing of Environment*, 80(2):241–247.

[Wu et al., 2015] Wu, Z., Wang, X., Jiang, Y., Ye, H., and Xue, X. (2015). Modeling spatial-temporal clues in a hybrid deep learning framework for video classification. *CoRR*, abs/1504.01561.

[Yin and Struik, 2010] Yin, X. and Struik, P. C. (2010). Modelling the crop: from system dynamics to systems biology. *Journal of Experimental Botany*, 61(8):2171–2183.

[Zhou and Chellappa, 1988] Zhou, Y. and Chellappa, R. (1988). Computation of optical flow using a neural network. *IEEE 1988 International Conference on Neural Networks*, pages 71–78 vol.2.

université
PARIS-SACLAY

ÉCOLE DOCTORALE
**INTERFACES**
**Approches Interdisciplinaires : Fondements, Applications et Innovation**

**Titre:** Méthodes d'apprentissage statistique pour la classification automatique des cultures et la prévision de rendement à grande échelle

**Mots clés:** Reconnaissance des cultures, Propriétés réflectives des plantes, Télédétection radar, Sentinel-1, Temps Thermique, Réseaux de neurones récurrent LSTM, Réseaux de convolution CNN, Biomasse, Prévision des réndements, Assimilation de données.

**Résumé:**

La principale thématique étudiée dans ce travail concerne l'identification des types de cultures par imagerie satellite radar avec des modèles d'apprentissage statistique. L'identification des cultures permet le suivi automatique de la couverture du sol et l'estimation des surfaces plantées ainsi que l'amélioration de la prévision des rendements agricoles, c'est l'autre sujet traité dans ce travail. Pour ces travaux, nous avons pu compter sur un allié majeur, l'imagerie satellitaire qui fournit des images multi-temporelles à haute résolution offrant une réelle opportunité de suivre l'évolution des propriétés réflectives des plantes durant leur croissance, en fonction des variations liées à la phénologie et au pédoclimat. Nous utilisons l'imagerie radar Sentinel-1 assurant une indépendance vis-à-vis des conditions climatiques. Notre approche pour la reconnaissance des cultures est basée sur l'utilisation de la dynamique de croissance des plantes pouvant être capturée par l'imagerie satellite pour discriminer les cultures. Il s'agit d'une approche par pixels pour laquelle nous avons choisi d'utiliser deux modèles supervisés d'apprentissage statistique, les réseaux de neurones récurrents LSTM et les réseaux de convolution CNN. Notre approche est conçue de telle sorte que le modèle puisse produire une évaluation du couvert végétal sans avoir à labelliser des parcelles en début de campagne, opération complexe à réaliser. Nous avons donc cherché à calibrer les modèles en utilisant les données des campagnes précédentes. Nous proposons une méthode dans laquelle le développement phénologique de la plante est considéré pour l'identifier en utilisant le concept du temps thermique. Cela permet de compenser la variabilité inter-annuelle, qu'elle soit pédo-climatique, liée aux caractéristiques de la culture comme la résistance aux épisodes de gel, ou due aux pratiques culturales. L'identification des cultures peut servir l'amélioration des prévisions de rendement résultant d'une meilleure connaissance des surfaces plantées. C'est une autre thématique de recherche de notre thèse. La reconnaissance des cultures peut constituer un élément essentiel dans le processus visant à obtenir des prévisions de rendements les plus précis possible. En identifiant le type de culture dans le champ, nous connaissons les caractéristiques phénotypiques de cette culture pour pouvoir estimer les paramètres biophysiques, ce qui, couplé aux données pédoclimatiques et aux pratiques culturales, nous permet d'aller vers une prévision précise des rendements agricoles en utilisant les modèles de croissance des plantes, les méthodes de calibration et d'assimilation de données. Cette méthodologie pour la prévision des rendements à l'échelle de la parcelle ou de la région est également étudiée dans cette thèse. En effet, la connaissance anticipée des rendements agricoles est un enjeu majeur en agriculture: dans un bassin de production, pour le chef de silo afin de prévoir la logistique de culture et de stockage des grains ou à plus grande échelle, pour anticiper les crises agricoles. Dans ce contexte, nous avons commencé par évaluer le potentiel de l'imagerie radar pour le développement de modèles statistiques permettant l'estimation des variables biophysiques des plantes telles que la biomasse. Nous avons également proposé un outil permettant de conseiller le positionnement des points de mesure dans les parcelles agricole en fonction des hétérogénéités intra-parcellaires et en utilisant un clustering non supervisé de type K-means de la dynamique de la réponse radar de chaque pixel. Ensuite, nous présentons une mise en œuvre des méthodes d'assimilation de données pour montrer comment elles peuvent être utilisées pour améliorer les pouvoirs prédictifs des modèles de croissance des plantes. Nous utilisons un algorithme d'assimilation de données basé sur le filtre particulaire par convolution appliqué à un modèle mécaniste de croissance du blé dérivé du modèle STICS.

**Title:** Machine learning methods for automatic crop classification and prediction of yields on a large scale

**Keywords:** Crop Recognition, Plant's Reflective Properties, Rradar Remote Sensing, Sentinel-1 SAR data, Thermal Time, Long Short-Term Memory recurrent neural networks, Convolutional Neural Networks, biomass, crops yield forecasting, Data Assimilation.

**Abstract:** The main thematic studied in this work concerns the identification of crop types using radar satellite imagery by using statistical learning models. Crop type identification allows the automatic monitoring of land cover and the estimation of planted areas as well as the improvement of the prediction of agricultural yields, this is the other topic that will be addressed in this work. For these works, we could count on a major ally, the satellite imagery which provides multi-temporal images with high resolution offering a real opportunity to track the evolution of the reflective properties of plants during their growth, according to the variations related to the phenology and the pedoclimate. We use radar remote sensing imagery ensuring independence from climatic conditions, more precisely, images from the Sentinel-1 satellite. Our approach for crop recognition is based on the use of plant growth dynamics that can be captured by satellite imagery to discriminate crops. It is a pixel-based approach for which we have chosen to use two supervised statistical learning models, LSTM recurrent and CNN convolutional neural networks. Our approach is designed so that the model can produce a vegetation coverage assessment without having to label parcels at the beginning of the season, which is a very complex operation to perform. We, therefore, sought to calibrate the models using data from previous seasons. We propose a method in which the phenological development of the plant is considered to identify its species using the concept of thermal time. This allows compensating the inter-annual variability, whether it is pedo-climatic, related to the characteristics of the crop such as the resistance to frost episodes, or due to the cultivation practices. Crop type identification can be useful for several applications, such as improving yield forecasting through a better knowledge of the planted areas. This is another research theme of our thesis. Crop recognition can be an essential element in the process of obtaining the most accurate crop yield forecasts possible. By identifying the type of crop in the field, we know the phenotypic characteristics of that crop to be able to estimate the biophysical parameters, which, coupled with soil-climate data and cultivation practices, allows us to move towards accurate crop yield forecasting using plant growth models, calibration and data assimilation methods. This methodology for yield forecasting at the scale of the parcel or the region is also studied in this thesis. The anticipated knowledge of agricultural yields is a major challenge in agriculture: in a production basin, for the silo manager to predict the logistics of cultivation and storage of grains or on a larger scale, to anticipate agricultural crises. In this context, we started by evaluating the potential of radar imagery for the development of statistical models allowing the estimation of plant biophysical variables such as biomass. We also proposed a tool allowing to recommend the positioning of measurement points in agricultural parcels according to intra-parcel heterogeneities and using an unsupervised K-means clustering of the radar response dynamics of each pixel. Next, we present an implementation of data assimilation methods to show how they can be used to improve the predictive powers of plant growth models. We use a data assimilation algorithm based on the particle convolution filter applied to a mechanistic wheat growth model derived from the STICS model.

**Université Paris-Saclay**

Espace Technologique / Immeuble Discovery

Route de l'Orme aux Merisiers RD 128 / 91190 Saint-Aubin, France